Characterization of the partially premixed combustion of Acetone-Butanol-Ethanol bio- fuel for thermal engines

Tung Lam Nguyen

UNIVERSITÉ D'ORLÉANS

ÉCOLE DOCTORALE

ENERGIE, MATERIAUX, SCIENCES DE LA TERRE ET DE L'UNIVERS

LABORATOIRE PRISME

THÈSE présentée par :

Tung Lam NGUYEN

soutenue le : **16 Décembre 2021**

pour obtenir le grade de : **Docteur de l'université d'Orléans**

Discipline/Spécialité : Mécanique et Energétique

Characterization of the partially premixed combustion of Acetone-Butanol-Ethanol bio-fuel for thermal engines

THÈSE dirigée par :

Christine MOUNAÏM-ROUSSELLE	Professeur, Université d'Orléans – PRISME
Dinh Long HOANG	Professeur, HUST
Camille HESPEL	Maître de conférences, Université d'Orléans – PRISME

RAPPORTEURS :

Marc BELLENOUE	Professeur, ENSMA – Pprime
Alan KEROMNES	Maître de conférences, Université de Limoges

JURY :

Marc BELLENOUE	Professeur, ENSMA – Pprime, Président du Jury
Alan KEROMNES	Université de Limoges
Dinh Long HOANG	Professeur, HUST
Christine MOUNAÏM-ROUSSELLE	Professeur, Université d'Orléans – PRISME
Camille HESPEL	Maître de conférences, Université d'Orléans – PRISME
Ob NILAPHAI	Docteur, Université Kasetsart

RÉSUMÉ

Aujourd'hui, en raison des exigences législatives et politiques en matière de réduction des émissions de NOx, de particules (PM) et de CO_2 (liés à la consommation de carburant), de nouveaux concepts de combustion avancés, tels que la combustion à basse température (LTC), sont à considérer. Les bio-alcools, en particulier le méthanol, l'éthanol et le butanol, ont reçu beaucoup d'attention en tant que futurs carburants potentiels alternatifs à l'essence pure. Comme le bio-butanol contient 30 % d'énergie de plus que l'éthanol, l'utilisation du n-bio-butanol comme carburant pour les moteurs peut permettre d'économiser 39 à 56 % d'énergie fossile tout en réduisant les émissions de gaz à effet de serre jusqu'à 48 % à partir d'une analyse du cycle de vie. De plus, le bio-butanol peut être plus facilement mélangé à l'essence ou au diesel que le méthanol ou l'éthanol. Mais même si le bio-butanol présente plusieurs avantages par rapport à l'éthanol et au méthanol, le principal problème qui empêche l'utilisation du n-butanol dans les moteurs modernes reste son coût de production élevé.

L'acétone-butanol-éthanol (ABE), le produit intermédiaire du processus de fermentation pour la production de bio-butanol, est de plus en plus considéré comme un autre carburant alternatif. Le butanol pur est obtenu à partir du solvant de fermentation de l'ABE, qui perd beaucoup d'énergie lors de la distillation en raison de la température élevée du point d'ébullition (118°C) du butanol.

L'éthanol produit à partir de matières premières renouvelables a une qualité d'auto-allumage plus faible avec un effet de refroidissement par évaporation élevé que l'essence, ce qui contribue à augmenter le délai d'allumage, comme l'indiquent les caractéristiques d'allumage : indice d'octane de recherche élevé (RON = 108,6) et indice de cétane très faible (5∼15). Le n-butanol est le principal produit de la fermentation de l'ABE. Il contient des atomes d'oxygène dans sa structure moléculaire, ce qui entraîne une diminution des émissions, notamment des particules de suie. De plus, le butanol a une densité énergétique et une chaleur latente de vaporisation plus élevés, de meilleures propriétés de miscibilité avec l'essence que le bioéthanol mais une réactivité plus faible (RON supérieur à 100). L'acétone est l'espèce la plus volatile du mélange ABE, avec le point d'ébullition le plus bas (56°C) et la pression de saturation la plus élevée.

Par la suite, le mélange utilisé est indiqué de la façon suivante : NomXX avec Nom soit éthanol, butanol, ABE et XX la quantité de carburant en volume mélangée au carburant conventionnel.

L'étude de Cheng et al. [1] a montré que Bu10 et Bu20 (10 % et 20 % en volume) peuvent réduire simultanément les émissions de NOx et de suie avec peu d'effet sur les HC, le CO et la consommation de carburant dans le cas d'un moteur fonctionnant en mode combustion partiellement prémélangée (PPC). Les résultats de Zhang et al. [2] ont montré que Bu20 et Bu40 retardent l'allumage, augmentant ainsi le rendement thermique indiqué alors que les émissions de HC et de CO peuvent être réduites à l'aide de la recirculation des gaz d'échappement. Les performances et les émissions d'un moteur à combustion interne turbocompressé avec Bu20 et Bu40 en mode PPC ont également été étudiées par Valentino et al. [3]. L'étude de Han et al. [5] présente des résultats à plus forte charge sous une combustion à basse température, indiquant que le n-butanol est plus adapté à la combustion de type PPC que le diesel lui-même, grâce à son très faible niveau d'émissions de suie et de NOx par rapport à la combustion diesel. Cet avantage peut être obtenu, mais seulement dans une plage de charge étroite du moteur et avec une pénalité considérable dans les émissions de CO et de HC.

Les effets combinés de la teneur en n-butanol et de l'EGR sur les moteurs à combustion interne en mode PPC ont été étudiés par [5], mais en mélange avec de l'essence. L'impact principal dû à l'indice d'octane plus élevé et à la volatilité de l'essence par rapport au carburant diesel est de retarder les temps d'auto-inflammation. Ils ont constaté que l'ajout de n-butanol améliore légèrement l'oxydation des émissions de CO et de HC, mais a peu d'impact sur les émissions de NOx. Les effets combinés de l'EGR et de l'additif n-butanol sur les émissions réglementées et non réglementées d'un moteur à combustion interne, étudiés par Yang et al. [6], ont montré une amélioration des émissions de suie.

Wu et al. [7] et Zhou et al. [8] ont étudié l'effet des mélanges ABE-diesel sur les caractéristiques de la combustion diffusive dans des conditions similaires au moteur à allumage par compression et dans des conditions de combustion à basse température dans une chambre à volume constant.

Les résultats ont montré que, dans ces conditions, les mélanges ABE-diesel avaient un retard à l'inflammation et une durée de combustion plus longs que le diesel pur. Dans d'autres études, Wu et al. [8] ont étudié l'effet de la teneur en acétone et en butanol des mélanges ABE20-diesel sur les caractéristiques de combustion, avec des carburants ABE de différents rapports volumétriques de composants (A:B:E de 6:3:1, 3:6:1, 0:10:0 (butanol pur)) et un mélange diesel. Ils ont trouvé que l'ABE 6:3:1 a des caractéristiques de combustion plus proches de celles du diesel.

Nilaphai et al. [9] ont étudié l'effet des propriétés physiques et chimiques de l'ABE et des mélanges de type diesel (n-dodécane) à un rapport volumique de 20% en comparaison avec le mélange d'éthanol et le mélange de butanol sur les caractéristiques d'évaporation et de combustion. Ces expériences ont été réalisées dans le dispositif expérimental 'New One Shot Engine' dans des conditions de spray A et à différentes températures ambiantes de 800 K et 850 K, avec des conditions inertes et réactives. Les résultats ont montré que l'ABE20 avait la longueur de pénétration liquide et un délai d'allumage plus courts que ceux du mélange d'éthanol et du mélange de butanol, mais plus longs que ceux du n-dodécane. En résumé, les chercheurs ont conclu que les solutions d'ABE peuvent être appliquées aux moteurs à allumage par compression, dans des conditions de combustion classiques et à basse température.

Cependant, jusqu'à présent, les caractéristiques de combustion des mélanges ABE - essence ou similaires à l'essence dans une chambre de combustion à volume constant n'ont pas été étudiées. C'est l'objectif de cette étude d'examiner les propriétés des carburants acétone-butanol-éthanol (ABE) et des alcools (éthanol/butanol) mélangés avec un carburant de substitution à l'essence (PRF80) sur 2 modes du concept de combustion avancée: le mode de combustion HCCI (Homogeneous Charge Compression Ignition) et le mode GCI (Gasoline Compression Ignition).

La première partie de la thèse présente l'étude réalisée afin de comprendre l'effet chimique du mélange Ethanol/Butanol et ABE dans le carburant de substitution, PRF80, sur le mode de combustion HCCI de deux manières : (1) par des résultats expérimentaux sur le délai d'allumage, le processus de combustion, les performances et les émissions dans un moteur à allumage par compression monocylindre et (2) par des simulations cinétiques du délai d'allumage (avec le cadre OpenSmoke++). L'effet des propriétés du carburant sur le mode de combustion HCCI des mélanges ABE/Et/Bu-PRF80 a été étudié sur les caractéristiques de performance, de combustion et d'émissions. Les résultats montrent que les mélanges d'alcools ont un délai d'allumage plus long et peuvent donc prolonger la charge élevée du moteur en mode HCCI. En revanche, le délai d'allumage plus long et la phase de combustion plus tardive d'une fraction d'alcools plus élevée entraînent une émission plus importante de HC et de CO ainsi qu'un COV élevé. Par conséquent, la faible charge est difficile à atteindre.

Les nouvelles expériences pour les mélanges d'éthanol, de butanol et d'essence ABE en mode de combustion HCCI sont fournies pour une gamme de conditions d'admission : température, pression et rapport d'équivalence, y compris les effets du mélange sur la région LTR, HRR, la

performance du moteur, la combustion et les caractéristiques d'émissions avec également l'évaluation de l'effet du rapport EGR. Plusieurs observations expérimentales clés ont été faites :

- La région LTR a été observée avec des mélanges de carburants contenant plus de 20 % de butanol, d'ABE et de tous les mélanges d'éthanol dans les conditions du moteur testé.

- Sous une température d'admission élevée (plus de 150°C), en augmentant la fraction d'éthanol de 0 à 20%, le délai d'auto-allumage augmente, mais de 20 à 60%, le délai d'auto-allumage avance légèrement.

A partir de ces résultats de simulation, on peut clairement observer que l'augmentation de la température ou de la richesse diminue le délai d'allumage aux deux pressions initiales, avec une tendance typique pour le carburant de référence [10]. A 25 bars, le carburant PRF80 présente un comportement caractéristique NTC (Negative Temperature Coefficient) significatif dans une gamme de température de 850 à 900 K pour une richesse de 0.3, étendu à des températures plus basses de 820 K et 780 K pour des richesses plus élevés de 0.4 et 0.5, respectivement.

Dans la deuxième partie de cette thèse, l'effet des propriétés du carburant sur les caractéristiques du spray et de la combustion a été étudié en fonction de la teneur en ABE, éthanol et butanol dans le PRF80 lors d'une injection simple ou fractionnée. La compréhension approfondie des processus physico-chimiques complexes qui se produisent à l'intérieur de chambres de combustion peut conduire à une plus grande précision des modèles numériques prédictifs, comme le rappelle Engine Combustion Network. Cette étude fournit une base de données expérimentale unique pour valider la précision des modèles actuels de CFD dans la prédiction de la longueur de pénétration liquide et vapeur, du délai d'inflammation, de la zone de stabilisation de la flamme (Lift-off-length) et de la formation de suie pour ce type de carburants non habituels.

Des défis ont été relevés durant ce travail, comme l'estimation expérimentale de la masse de suie pour des carburants à fort indice d'octane (plus de 80). L'impact de la division de l'injection en 2 injections a été étudié pour les carburants à essence dans des conditions GCI à haute température et haute pression. Les résultats détaillés ont été analysés sur la base des conditions inertes (débit massique, longueur du liquide et pénétration de la vapeur), dans des conditions réactives (taux de dégagement de chaleur, délai d'allumage et longueur où la flamme se stabilise) et du processus de production de suie.

La conclusion de la partie sur les stratégies d'injections fractionnées est résumée comme suit :

*) Pour la mesure du débit massique des stratégies d'injection fractionnée, l'injection pilote et l'injection principale ont une vitesse de pointe similaire pour chaque carburant testé.

*) Pour les conditions inertes, les pénétrations de liquide et de vapeur du spray principal sont plus rapides avec une dynamique plus élevée que l'injection pilote, ce qui contribue à un bon mélange air-carburant de l'injection principale. Ce comportement est observé pour tous les carburants testés et sa sensibilité ne dépend pas du mélange de carburants testés.

*) En combustion, le dégagement de chaleur se fait en deux étapes ou en une seule selon l'indice d'octane du mélange de carburant, ou lorsque l'oxygène ambiant est plus faible.

- Les délais d'inflammation de l'injection principale diminuent pour ces conditions d'oxygène quelque soit le carburant testé, comme prévu, en raison de la température élevée des gaz brûlés de l'injection pilote ou des espèces réactives dans les réactions à basse température.

*) La masse de suie, est quant à elle fortement réduite lorsque l'indice d'octane du carburant est plus élevé, ou lorsque l'oxygène ambiant est faible, en raison d'une période de mélange plus longue. Dans le cas du carburant PRF80, la concentration de suie a été significativement réduite sous 18% d'oxygène ambiant. La principale amélioration de l'auto-inflammation est obtenue en cas de faible teneur en oxygène ambiant pour les mélanges à indice d'octane élevé tels que Bu20 et ABE20, avec une très faible production de suie. Cependant, pour les carburants à faible indice d'octane, comme le PRF60 et le PRF70, l'allumage et la longueur de levée de l'injection principale se déplacent vers l'amont, ce qui entraîne une formation de suie plus importante en amont et une production de suie plus élevée.

D'après les résultats obtenus avec la stratégie d'injection fractionnée, ce mélange plus efficace de l'injection principale avec une dynamique plus élevée, combiné à la présence d'espèces issues de la réaction de combustion de l'injection pilote favorise l'allumage de l'injection principale et la diminution de la zone de stabilisation de la flamme.

Ces mesures ont permis de développer une base de données nouvelles dans le but d'améliorer la précision des modèles CFD et d'envisager la stratégie d'injection

multiples dans le cas des biocarburants, tels que l'éthanol, le n-butanol et l'ABE. Les résultats ont montré un avenir prometteur pour le mélange ABE-essence en tant que carburant alternatif pour le transport, avec un coût plus faible de production de l'ABE. Certaines caractéristiques clés du mélange ABE-essence pour le mode LTC sont les suivantes :

- Les délais d'allumage globalement plus longs des injections simples et principales conduisent à l'augmentation de la fraction de la phase de combustion prémélangée.

- L'allongement des délais d'inflammation que ce soit de toute la charge ou de la charge liée à l'injection principale dans le cas d'une double injection conduit à un mélange plus pauvre dans la région où a lieu l'inflammation menant à une concentration de suie plus faible.

Sur la base des recherches mentionnées dans cette thèse, les perspectives d'études peuvent être les suivantes :

- Réaliser des expériences dans des conditions encore plus proches du moteur, sur des moteurs à accés optiques par exemple.

- Les performances et les émissions du moteur en mode GCI avec l'ABE60 doivent être étudiées en comparaison avec l'essence pure.

- D'autres alcools avec une réactivité, une viscosité et une densité énergétique plus élevées et plus d'atomes de carbone, comme l'heptane et l'octane, pourraient également être mélangés à l'essence.

Bibliographie

[1] Cheng X, LI S, Yang J, Dong S, Bao Z. Effect of N-butanol-Diesel Blends on Partially Premixed Combustion and Emission Characteristics in a Light-duty Engine. SAE Tech Pap 2014;2014-Octob. https://doi.org/10.4271/2014-01-2675.

[2] Zhang Q, Yao M, Zheng Z, Liu H, Xu J. Experimental study of n-butanol addition on performance and emissions with diesel low temperature combustion. Energy 2012;47:515–21. https://doi.org/10.1016/j.energy.2012.09.020.

[3] Valentino G, Corcione FE, Iannuzzi SE, Serra S. Experimental study on performance and emissions of a high speed diesel engine fuelled with n-butanol diesel blends under premixed low temperature combustion. Fuel 2012;92:295–307. https://doi.org/10.1016/j.fuel.2011.07.035.

[4] Han X, Zheng M, Wang J. Fuel suitability for low temperature combustion in compression ignition engines. Fuel 2013;109:336–49. https://doi.org/10.1016/j.fuel.2013.01.049.

[5] Yang B, Yao M, Cheng WK, Zheng Z, Yue L. Regulated and unregulated emissions from a compression ignition engine under low temperature combustion fuelled with gasoline and n-butanol/gasoline blends. Fuel 2014;120:163–70. https://doi.org/10.1016/j.fuel.2013.11.058.

[6] Wu H, Nithyanandan K, Zhang J, Lin Y, Lee TH, Lee C fon F, et al. Impacts of Acetone-Butanol-Ethanol (ABE) ratio on spray and combustion characteristics of ABE-diesel blends. Appl Energy 2015;149:367–78. https://doi.org/10.1016/j.apenergy.2014.11.053.

[7] Zhou N, Huo M, Wu H, Nithyanandan K, Lee C fon F, Wang Q. Low temperature spray combustion of acetone-butanol-ethanol (ABE) and diesel blends. Appl Energy 2014;117:104–15. https://doi.org/10.1016/j.apenergy.2013.11.035.

[8] Wu H, Nithyanandan K, Zhou N, Lee TH, Lee CFF, Zhang C. Impacts of acetone on the spray combustion of Acetone-Butanol-Ethanol (ABE)-Diesel blends under low ambient temperature. Fuel 2015. https://doi.org/10.1016/j.fuel.2014.10.009.

[9] Nilaphai O, Hespel C, Chanchaona S, Mounaïm-Rousselle C. Spray and combustion characterizations of ABE/Dodecane blend in comparison to alcohol/Dodecane blends at high-pressure and high-temperature conditions. Fuel 2018;225:542–53. https://doi.org/10.1016/j.fuel.2018.03.184.

[10] Vuilleumier D, Atef N, Kukkadapu G, Wolk B, Selim H, Kozarac D, et al. The Influence of Intake Pressure and Ethanol Addition to Gasoline on Single- and Dual-Stage Autoignition in an HCCI Engine. Energy and Fuels 2018;32:9822–37. https://doi.org/10.1021/acs.energyfuels.8b00887.

ABSTRACT

Nowadays, due to legislative demands reduction the emissions of NO_x, Particulate Matter (PM) and CO_2 (reduce fuel consumption), new advanced combustion concepts, such as Low-Temperature combustion (LTC) are being researched and developed. Moreover, due to the future lack of fossil fuels and their impact on the environment, the use of bio-fuels will be one issue. Bio-alcohols, especially methanol, ethanol, butanol have received a lot of attention as potential future alternative fuels to pure gasoline. As bio-butanol contains 30% more energy than ethanol, to use n-bio-butanol as a transportation fuel can save 39-56% fossil energy while reducing greenhouse gas emissions by up to 48% on a life cycle analysis [1]. Moreover, bio-butanol can be easily mixed with gasoline or diesel in higher proportion than methanol or ethanol. But even if bio-butanol has several advantages compared to ethanol and methanol, the main issue preventing n-butanol's use in modern engines is its relatively high production and energy costs. Acetone-Butanol-Ethanol (ABE), the intermediate product from the fermentation process for bio-butanol production, is more and more considering as another alternative fuel. Therefore, this study investigates the fuel properties of Acetone-Butanol-Ethanol (ABE) and alcohols (Ethanol/Butanol) fuels blended with gasoline surrogate fuel (PRF80) on 2 modes of advanced combustion concept: Homogeneous Charge Compression Ignition (HCCI) combustion mode and Gasoline Compression Ignition (GCI).

In the first part of thesis, the effect of fuel properties on the HCCI combustion mode of ABE/Et/Bu-PRF80 blends were investigated on the performance, combustion and emission characteristics. The results show that the alcohols blends have longer ignition delay and hence can extend the high load of engine under HCCI mode. In contrast, the longer ignition delay and later combustion phasing of higher alcohols fraction cause higher emission of HC and CO and also high COV. Therefore, low load is difficult to reach.

In the second part of this thesis, the effect of fuel properties on the spray and combustion parameters were investigated as a function of ABE, ethanol and butanol content in PRF80 under single and split injection. The stringency of emission regulations for diesel engines required the better understand the physical and chemical phenomena inside the cylinder chamber, especially with new concept combustion mode, such as GCI mode. The deeper understanding the complex physicochemical processes occurring inside the Constant Volume Combustion Chamber (CVCC) can be leaded to higher accuracy of predictive numerical models, as recommended by Engine Combustion Network. This study provides unique

experimental database to validate accuracy of current Computational Fluid Dynamic models in prediction of liquid length, vapor spray penetration, ignition delay time, fuel-air mixing prior to combustion (LOL), soot formation for this kind of non-usual fuels.

Keywords: Acetone-Butanol-Ethanol blend, Alcohol blend, HCCI mode, GCI mode, Spray Characteristics, Lift-Off Length, Ignition Delay, High-Pressure High-Temperature Conditions.

ACKNOWLEDGEMENTS

The time has come to complete my thesis by writing acknowledgments – one of the most important parts. This journey has not been easy, it has been filled with ups and downs, thrills and scares but towards the end, I manage to escape from it with feeling stronger, wiser, and surely humbler.

I would like to thank those who have supported me throughout the years. Any successes I have obtained and any obstacles I have overcome would not have been possible without them.

First of all, I would like to send my deepest gratitude to my supervisor, Prof. Dr. Christine Rouselle, who developed me as a professional. Christine, you were always patient, supportive, and allowed me the freedom to pursue my goals. And I'm sorry if I gave you a hard time with my work. Working with you has undeniably been my great fortune.

I would like to express my appreciation to Dr. Camille Hespel - my co-supervisor because of her patience and kind support given to my PhD work and for being my photophysics guru during the experimental campaign which we performed together. Her active participation at every stage of my study and advice have shaped my overall research outlook. I cherish the time I have spent under her guidance.

I also want to thank Prof. Fabrice Foucher, the head of the division Energie Combustion Moteur. He did so much work for everyone in the lab, creating a welcoming research environment. Working at one of the best combustion research labs in the world was truly a unique experience for me.

I would also like to extend my gratitude to the jury members, Prof. Marc BELLENOUE and Dr. Alan KEROMNES, for taking the time to examine my research work.

Experimental tasks need teamwork for trying to run every single aspect. Therefore, I would like to thank technicians Bruno, Julien, and Yahia who kept the engine and vessel running and made my stay incredibly productive.

Additionally, I would like to thank all my co-musketeers in the ECM group at Orleans University, including PhD candidates and postdocs (Pierre, Ida, Chetal, Pietro, Nicola, Marco, Ob, Mehdi, Anthony, Charles, Ricardo, Richard, Cah, and others).

Ida, Pietro and Nicola, thank you for sharing their knowledge, experience, ideas, and providing me with a collaborative research environment. As well as this, a special thank to Ob and Chetal

for sharing theirs experimental findings and expertise on a novel diagnostic technique with me. I am truly thankful for theirs friendship and cooperation, the interesting results obtained so far a largely because of your hard work. The fact that we still communicate on a regular basis confirms the pleasant cooperation.

Prof. Long, Bau, Khanh, and Chau need to be mentioned here owing to fruitful discussions about the internal engine combustion domain.

Although sometimes challenging, staying abroad for longer periods was by far the most interesting part of the PhD. project. The social interactions outside work: dinners, wine tasting and the Orleans lifestyle in general, largely contributed to this truly positive experience.

Luckily for me, I was not the only “expat” in Orleans. Life outside work got so much better because of all the friends I met during my PhD. project, too many to all be listed here: Hung, Duy, Lam, Linh, Binh, Chau, Hieu, Toan, Hung, Duc, Thanh, Hieu, Trung, Bang, etc. All dinners, long evenings, weekend trips and sometimes even sport activities have been extremely important to me to overcome research pressure. I would also like to thank all my friends at Orleans and in France, who have made these PhD years considerably more enjoyable.

The meaning “being at home” is something you learn to understand when you are away from it too often. Going back to Viet Nam to “hang out” with the friends, it is great to have you as my friends especially since you always make me feel so welcome: Tam, Ha, Anh, … With the colleagues in UTC (University of Transport and Communications), Pr. Duc, Dr. Ha,…. Thank for the great support.

Many special thanks to my beloved parents, first of all for teaching me what’s right and wrong, to learn me what true principles in life are and especially how to stick to them, for their unconditional support and their firm belief in the power of education.

I acknowledge the financial support from the Project 911 Scholarship (Vietnam scholarship Council) and BCS (bourses de couverture sociale) from The French Embassy in Vietnam that funded me during my study in France. The Vietnam scholarship Council paid my living cost while The French Embassy in Vietnam waived my tuition fees. This generous financial support enabled me to focus on my study.

Last, my greatest appreciation is for my wife (Thu) and my daughter (Phuong) for their patience and sacrifice when I were studying in France. They are among the prime motivation for me to complete my thesis.

CONTENTS

TABLE

FIGURES

NOMENCLATURE

Initials and acronyms

ASOI After Start of Injection

ATDC After Top Dead Center

BTDC Before Top Dead Center

BDC Bottom Dead Center

CDC Conventional Diesel Combustion

CFR Cooperative Research Engine

CFD Computational Fluid Dynamics

COV Covariance (Coefficient of Variation)

CHRR Cumulative heat release rate

CI Compression Ignition

CN Cetane Number

CR Compression Ratio

CVCV Constant Volume Combustion Vessel

DBI Diffused Back-Illumination

DNS Direct Numerical Simulation

DPF Diesel Particulate Filter

DOE Design Of Experiments

ECN Engine Combustion Network

EGR Exhaust Gas Recirculation

EOC End of Combustion

EOI End Of Injection

ER Equivalence Ratio

EVC Exhaust Valve Closure

EVO Exhaust Valve Open

GCI/GDCI Gasoline Compression Ignition/ Gasoline Direct Compression Ignition

GDI Gasoline Direct Injection

GHG Green house gases

HC Hydrocarbon

HCCI Homogeneous Charge Compression Ignition

HCHO Formaldehyde

HRR Heat Release Rate

HP High Pressure

HT High Temperature

ICE Internal Combustion Engine

ICCD Intensified Charge Couple Device

ID Ignition Delay

IE Indicated Efficiency

IMEP Indicated Mean Effective Pressure

IVC Intake Valve Closure

IVO Intake Valve Open

KI Knock Intensity

LED Light Emitting Diode

LES Large Eddy Simulation

LHV Lower Heating Value

LL Maximum liquid length

LOL Lift-Off Length

LTC Low Temperature Combustion

LTHR Low Temperature Heat Release

MFC Mass Flow Controller

MON Motor Octane Number

NL Natural Luminosity

NO_x Oxides of Nitrogen

ORE Optical Research Engine

PAH Polycyclic aromatic hydrocarbon

PDF Probability Density Function

PFI Port Fuel Injection

PM Particulate matters

PT Pressure Transducer

PPM parts per million

PIV Particle Image Velocimetry

PM Particulate Matter

PMT Photomultiplier Tube

PN Particulate Number

PPC/PPCI Partially Premixed Combustion/ Partially Premixed Compression Ignition

PCI Premixed Compression Ignition

RCM Rapid Compression Machine

RI Ringing Intensity

RON Research Octane Number

ROI Rate of Injection

RPM Revolutions per minute

RCCI Reactivity Controlled Compression Ignition

SCR Selective Catalytic Reduction

SCCI Stratified Charge Compression Ignition

SOC Start of Combustion

SOI Start of Injection

SI Spark Ignition

TDC Top Dead Centre

VVT Variable Valve Timing

Symbols

Avg Average

BuOH Butanol

C_p Specific heat capacities at constant pressure

C_v Specific heat capacities at constant pressure

C_d Discharge coefficient

C_a Area coefficient

CA02	Crank angle where 2% of the fuel burnt
CA05	Crank angle where 5% of the fuel burnt
CA10	Crank angle where 10% of the fuel burnt
CA50	Crank angle where 50% of the fuel burnt
CA90	Crank angle where 90% of the fuel burnt
EtOH	Ethanol
fps	Frames per second
h	Enthalpy
L	Orifice length
M	Momentum flux
m	Mass flow rate
I	Light intensity measured
I_o	Reference light intensity
R	specific gas constant
Re	Reynolds number
Std	Standard deviation
t	Time
T	Temperature

Greek

Δ	Increment
θ	Spreading spray angle
ρ	Density
σ	Surface tension
γ	Ratio of specific heats
λ	Air-excess ratio
φ	Equivalence ratio

Subscripts and Superscripts

air	Air
amb	Relative to ambient
eq	Equivalent
eff	Effective
evap	Relative to evaporative conditions
f	Relative to fuel
g	Relative to Gas
l	Relative to fuel liquid phase
p	Pressure
st	Stoichiometric
th	Theoretical conditions
v	Volume

Chapter 1. INTRODUCTION

1.1. Background

1.1.1. Global warming and greenhouse gases

Global warming is defined as the increase in the average temperature of the Earth near land and ocean surface. According to the Intergovernmental Panel on Climate Change, most of the increase in temperature since the middle of the last century is due to the increase in the concentration of greenhouse gases in the atmosphere caused by human activities, as the deforestation and the burning of fossil fuels [2]. The change in the Earth's average temperature between 1949 and 2010 is shown in Figure 1.1.

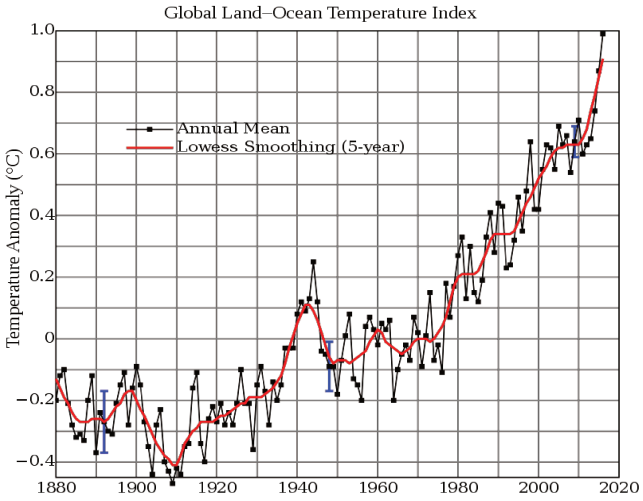

Figure 1.1. Global variation in average surface temperature relative to the average temperature between 1961 and 2020 [3]

Climate models predict an increase in the average global temperature between 1.1 and 6.4 K at the end of the current century as a function of the models. This average increase in the Earth's temperature will lead to a rise in sea level (due to the melting of Arctic and Antarctic glaciers) [4], an increase in precipitation and desert expansion but also extreme weather events, species extinction and changes in agricultural yields.

The Greenhouse effect is the process by which the Earth's lower atmosphere is warmed by the absorption and emission of infrared radiation by gases in the atmosphere. This effect is vital for the existence of living blooms and fauna on planet Earth, as it maintains the average global temperature at 306 K. The main greenhouse gases in the atmosphere are: water vapor, carbon

dioxide, methane, ozone and clouds.

Since the beginning of the industrial revolution, the amount of greenhouse gases caused by human activities has increased considerably; for example, the amount of CO_2 and methane is 36% and 148% higher than in the 18th century. On the other hand, the anthropogenic methane production is mainly due to an increase in livestock (enteric fermentation) and the decomposition of organic compounds, for example in landfills. Natural methane production is caused by clathrates in ocean floors, methane leakage from the earth's crust and methanogenesis. Therefore, the global warming could be mitigated by mainly limiting the amount of CO_2 released into the atmosphere either by reducing its production or by using capture and storage techniques [4], due to the fact that most of the main greenhouse gas emissions are due to CO_2 in Figure 1.2. The combustion of fossil fuels (such as natural gas, oil and coal) to produce power for residential, commercial, industrial and transportation purposes has been responsible for 75% of the increase in CO_2 in the atmosphere over the past 20 years; the remaining 25% is mainly due to deforestation [2]. Figure 1.3 indicates the repartition as a function of the sectors.

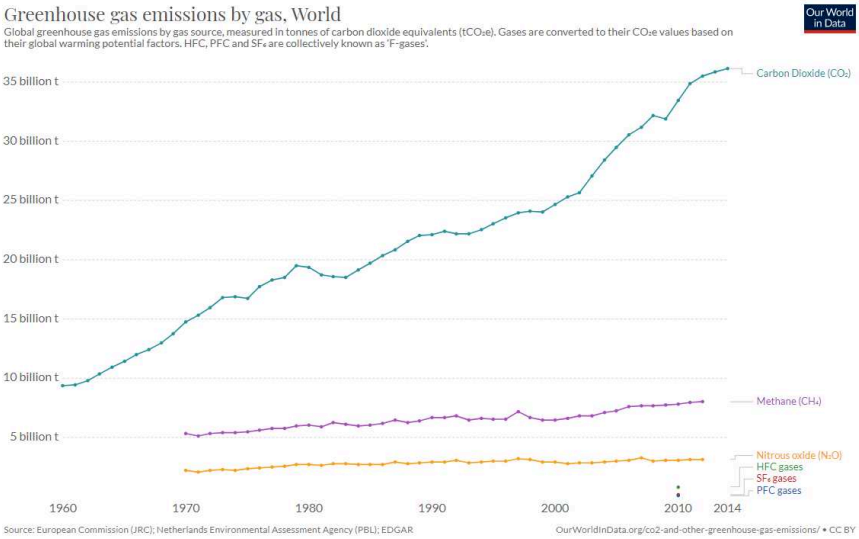

Figure 1.2. Top-three global GHG emissions, measured as billions of carbon dioxide equivalents per year. Gases are converted to their CO_2 eq values based on their global warming potential

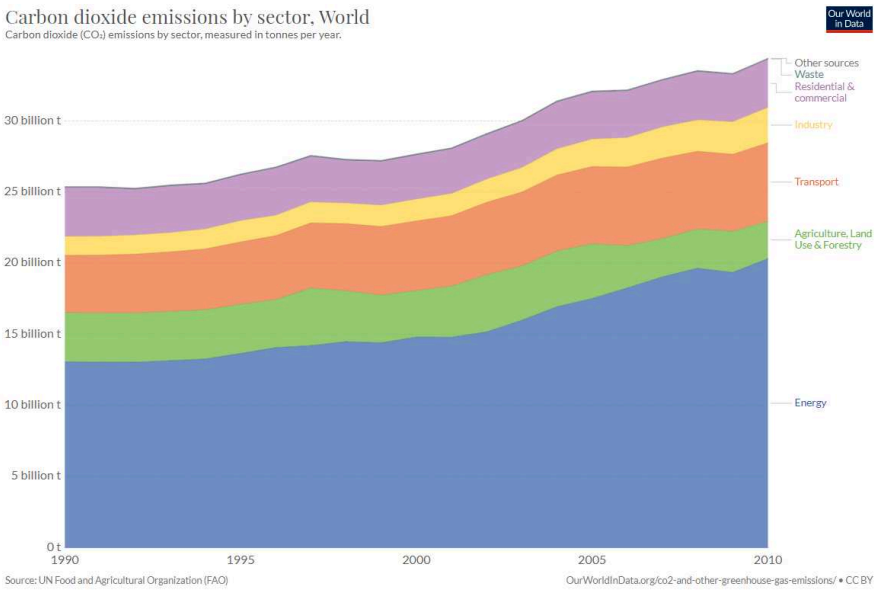

Figure 1.3. Global CO_2 emissions by economic sectors [5]. Sector fractions for 2010 are listed on the right side

1.1.2. Energy demand and supply

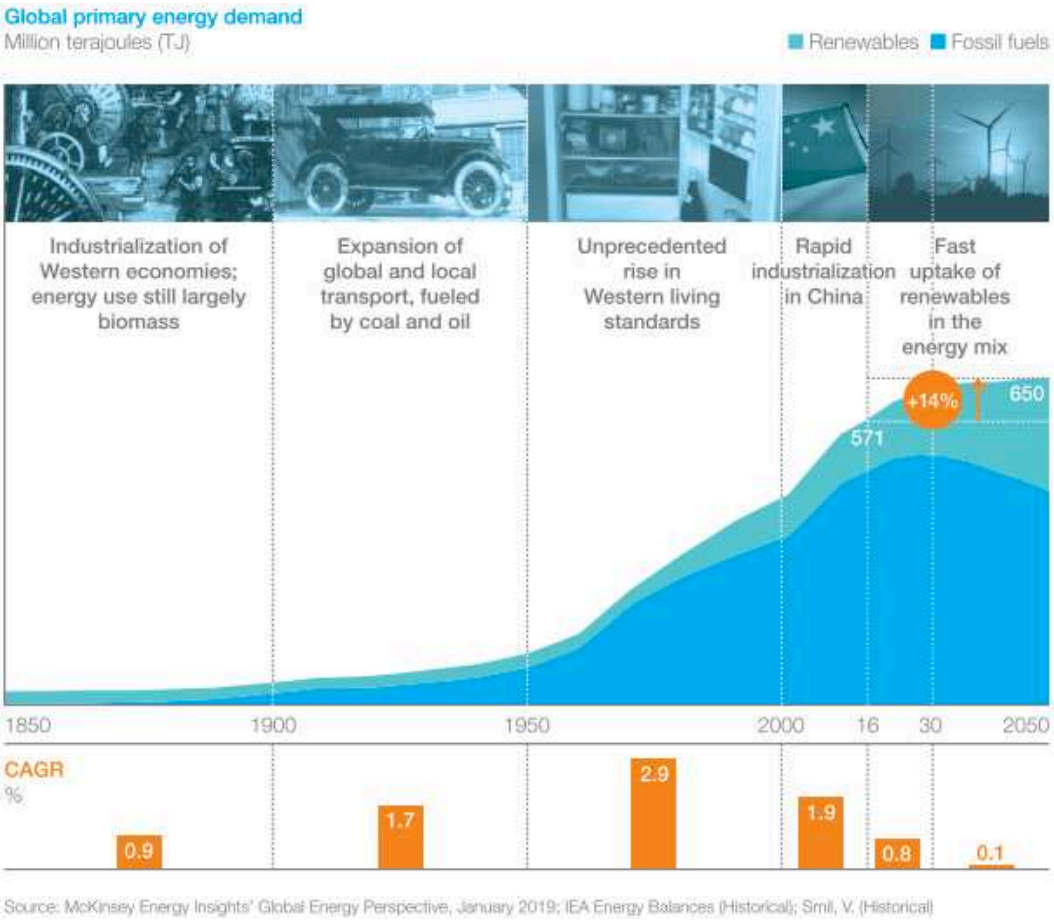

Figure 1.4. Primary Energy demand [6]

Figure 1.4 shows the historical and projected primary energy demand to 2050. According to [6], most of the energy will continue to be supplied by liquid fossil fuels even if a peak is assumed near 2030. According to the Hubbert Peak theory, in the worst case scenario, oil should be available until 2050 [7]. Therefore, in the future, beyond 2050, the main problems will be the increase of oil costs, due to the increase of the demand and of the extraction cost itself and, as consequence CO_2 emissions. New types of oil as oil sands, shale oil or coal liquefaction are more intense in terms of carbon emissions.

1.1.3. Reduction CO_2

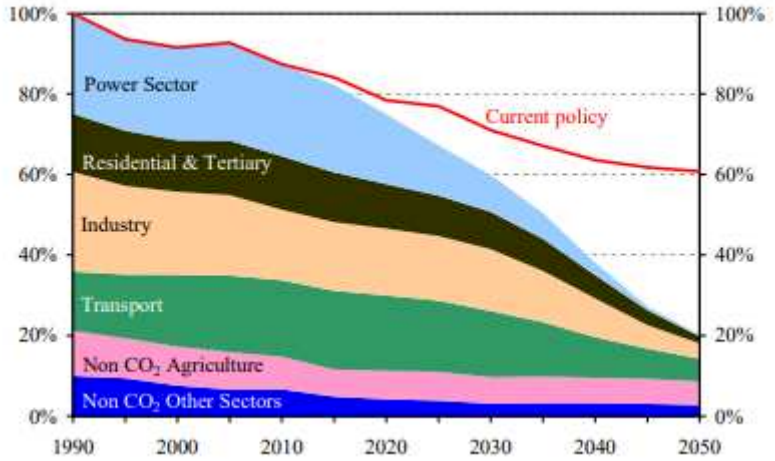

Figure 1.5. The European Union's vision for reducing GHG emissions by 2050 (100%=1990)

To reduce drastically the carbon footprint for the transportation and power sections as predicted in Figure 1.5, main alternatives are deployment of electrical vehicles or efficient internal combustion engines filled with bio-fuels.

Bio-fuels are normally oxygenated hydrocarbon fuels, which induce not only CO_2 reduction due to the vegetal grows but by the combustion of them. In term of improve the efficient of ICE, with thermal efficiency of engine increased from 40% to 50% cause to output power CO_2 reduced up to 20%.

1.1.4. Internal combustion engine

ICE have two types: diesel engine with compression ignition and gasoline engine with spark ignition. Diesel engines have advantages of thermal efficiency afforded by the higher

compression ratios than gasoline spark ignition engine but some disadvantages of particulate matter (PM) and nitro oxide (NO_x) emissions. The development of different combustion modes and engine technologies to reach high brake efficiency and therefor low emissions is shown in Figure 1.6.

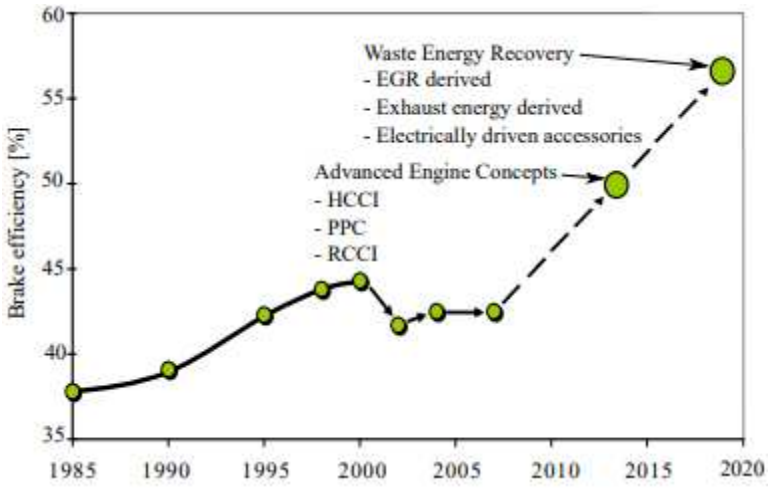

Figure 1.6. Historical perspective of heavy-duty diesel engine brake thermal efficiency [8]

The new combustion concepts, based on Homogeneous Charge Compression Ignition (HCCI), as Partial Premixed Combustion (PPC) or Gasoline Partial Premixed Combustion (GPPC), can allow high thermal efficiency with decrease of pollutant emissions [9–11]. In addition, by using the bio-fuel, as alcohols, both combustion and emission can be improved [12].

Concerns over demands of future petroleum supply and environmental degradation from fossil fuel have led to substantial interest in the production and usage of biomass-derived fuels, due to the global impact on CO_2 production. Two types of biofuel are developed: first generation from agricultural crops for human and animal foods (i.e. ethanol and biodiesel) and the second-generation biofuel - manufactured from various types of biomass (wood, vegetable waste, and more generally lignocellulose material). The second-generation biofuels are superior the first generation in terms of energy balances, reduction of greenhouse gas emission and completion for food.

Renewable energy in the Europe global and in France especially have positioned ethanol addition to gasoline squarely into the long-term view. Currently, gasoline in France contains up to 10% ethanol by volume (E10), on the future, the contents of ethanol on fuel should be increased.

In comparison with ethanol, bio-butanol is one of these second-generation biofuels, well suited

for ICE due to its similar in physical properties to gasoline. N-butanol is more compatible with existing engines when blended with convention gasoline or diesel fuels avoiding phase separation and increasing cost effective ness in the existing transportation infrastructure. However, the main issue preventing n-butanol's use in modern engines is its relatively high production costs.

ABE, the intermediate product in the ABE fermentation process for producing bio-butanol, is being studied as an alternative fuel recovery for individual component during fermentation. ABE fuel could be used for clean combustion, the separation costs would be mitigated.

Several research studies about n-butanol and ABE as fuels for ICEs have been conducted due to its properties that closely similar to those of gasoline [13]. Yu et al. [14] investigated the effect of n-butanol blends on emissions and combustion characteristics of a spark ignition (SI) engine with direct injection engine. The results showed that NO_x and CO emissions decline continuously and particle number significantly reduce with increasing n-butanol blending ratios while the indicated mean effective pressure (IMEP) and engine torque small changes. Karthick et al. [15] were investigated the combustion characteristics and emission behavior of ABE-gasoline blends in port-fuel injected (PFI) SI engine at medium load, the main results concluded that ABE can improve both power output and emissions behaviors. In [16] the comparison of performance and emissions for different ABE – gasoline blends indicate that a small amount of ABE addition could enhance efficiency and reduce emissions of HC while the combustion characteristics did not change.

1.2. Motivation

As ABE seems to be considered, from recent studies, as a fuel itself, the motivation of this study was to provide data not available for the moment, about the physical and chemical aspects of ABE combustion in the case of alternative engine combustion mode as Gasoline Compression Ignition (GCI). GCI was selected as it could be a very high potential strategy to achieve higher specific power and higher fuel efficiency, as well as lower soot and NO_x emissions than PPC, as gasoline like fuels allows a better mixing in the cylinder with the ambient air prior the combustion.

For that, two different but complementary steps were followed:

- First, the ignition process of ABE/PRF blend was characterized by using perfect HCCI

process and compared with ethanol and butanol to better understand the autoignition process and to improve the accuracy of kinetics modelling.

- The experiments of spray combustion under engine-relevant condition recommended from Engine Combustion Network were performed to characterize and understand the behavior of spray and combustion development of ABE/PRF blend also compared with Ethanol and Butanol/PRF mixtures. Last, to approach GCI conditions, the final part was dedicated to the physical process occurred in the case of double injections.

Chapter 2. BIBLIOGRAPHY

As the objective of this study is to evaluate the potential of ABE for GCI engine, one important part of this work is dedicated to the macroscopic features of the spray under engine relevant condition. Indeed, the spray is the process which provides the required amount of liquid fuel from injection. The interaction with ambient gases leads to the decomposition and detachment from periphery of fuel jet, the fuel-air mixture by entrainment of ambient gas and then vaporization of fuel. The spray processes are complex, namely: the breakup, atomization and evaporation are separated to three group (1) spray shape (temporal and special morphology development), (2) the microscopic features (droplet diameter, velocity and momentum flux) and (3) macroscopic features (breakup, atomization, penetration and spreading angle).

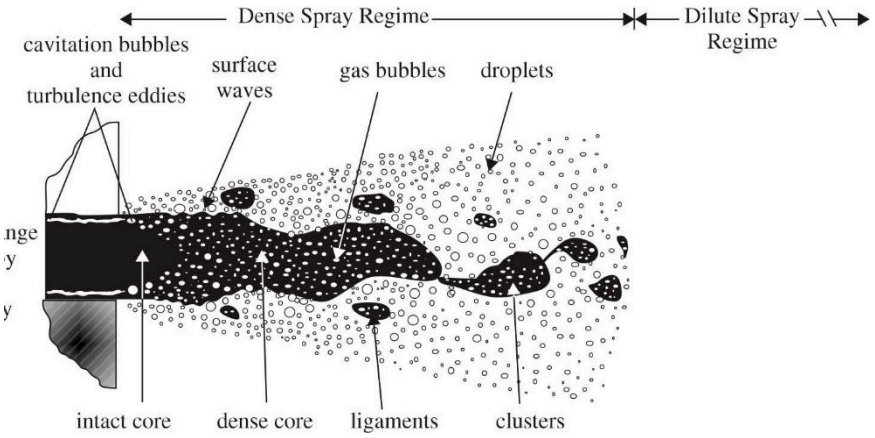

Figure 2.1. Characteristic parts of a liquid spray in the atomization breakup regime [17]

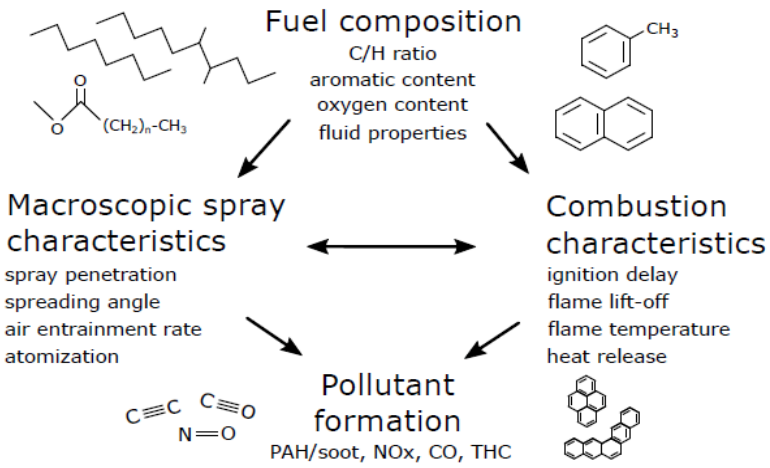

Figure 2.2. Fuel component effect on spray combustion and pollutant formation [18]

The equations describing the physical processes governing mixture formation are mainly established by empirical equations from the experimental results on diesel sprays. The

improvement of the empirical equations provides more understanding of the diesel spray processes in order to validate the accuracy of CFD simulation.

The main parameters on macroscopic atomization of spray are (1) injector structure (hole geometry and internal structure), (2) injection conditions (injection pressure, duration, time delay of open and close the injector, injected fuel temperature and injection strategy), (3) fuel properties (density, viscosity, surface tension and volatility) and (4) ambient gas conditions (temperature, density (or pressure) and air movement with engine optical experimental).

2.1. Inert process

2.1.1. Liquid spray penetration length

After the start of injection, the liquid-phase fuel reaches a maximum penetration length, which is nearly constant during the steady period of injection and the spray vapor phase of fuel continues to penetrate downstream. The liquid length (LL) is generally defined by the maximum axial penetration distance from injector tip of liquid-phase fuel penetration in the evaporating fuel spray [19,20]. In terms of improvement of the in-cylinder combustion processes in diesel engine, liquid-phase fuel penetration is important as a compromise has to be founded between the optimization of local air-fuel mixture and the fuel impingement along the cylinder and piston walls. The value of LL is one fundamental parameter to improve spray model liquid breakup, evaporation and mixing controlled [21–23] to increase the accuracy of CFD simulations. Browne et al. [24] conducted firstly to observed the initial data of liquid fuel penetration in diesel spray with a diffuse back-light technique in an optically accessible engine. They highlighted the reduction of LL as a function of the fuel volatility and the orifice diameter size. Espey and Dec [19] showed that ambient temperature and density strongly affect liquid length. Higgins et al. [25] conducted the experiment measured liquid length for several three-component blends under both inert and combustion conditions, i.e. in reactant gases. They concluded that LL in reacting conditions is slightly shorter than that of inert ones. Canaan et al. [26] investigated the effect of fuel volatility on liquid penetration under compression ignition condition. They showed that the strong effect of mid-boiling point and higher-boiling point of fuel on liquid length. Dernotte et al. [27] conducted experiments to investigate the influence of fuel properties on liquid length and vapor spray penetration. They concluded the fuel volatility increase or the density decrease lead to a reduction of liquid length. Siebers [20]

presented first the investigation of the liquid length over wide range of ambient conditions not in an optical engine but in constant volume chamber vessel in order to better control all parameters with as operating conditions, the injection pressure, orifice diameter, ambient gas temperature and density and fuel temperature. Matsuoka et al. [28] conducted the experiment to investigate of diesel fuel properties (kinetic viscosity and distillation characteristic) on liquid spray penetration under high-temperature and high-pressure conditions within combustion. They concluded that an increase of liquid length leads to higher level of soot emissions. Higgins et al. [29], Pastor et al. [30] and Kook and Pickett [31] focused also their studies on impact of fuel physical properties on liquid length under high-temperature and high-pressure condition, especially by considering 90% or 50% boiling point of fuel.

From all these experimental data, many authors tried to assess and estimate the liquid length under steady-state as a function of the parameters that they focused. Some of them are summarized in the table below in order to highlight the effect of fuel and ambient density, ambient temperature and fuel pressure.

Table 2.1. Some expressions of liquid penetration length

Equation	**Constant parameter**	**Author**
$LL = Cd_o\left(\frac{\rho_l}{\rho_g}\right)^{0.5}$	C: empirical constant $7<C<16$	Chehroudi et al. [32]
$LL = 0.5B_1 d_o\left(\frac{\rho_l}{\rho_g}\right)^{0.5}$	B_1: breakup constant of Kelvin Helmholtz, B_1=60.	Beale and Reitz [33] Su et al. [34].
$LL = 7.0d_o\left(1+0.4\frac{r_o}{d_o}\right)\left(\frac{P_g}{\rho_l V_{inj}^2}\right)^{0.05}\left(\frac{l_o}{d_o}\right)^{0.13}\left(\frac{\rho_l}{\rho_g}\right)^{0.5}$		Hiroyasu and Arai [35]
$LL = 93\left(\frac{294}{T_g}\right)^{1.43} d_o\left(\frac{\rho_l}{\rho_g}\right)^{0.5}$		Dos Santos and Le Moyne [22]
$LL = \frac{b}{a}\left(\frac{\rho_l}{\rho_g}\right)^{0.5}\frac{d_o C_a^{0.5}}{\tan(\theta/2)}\left(\left(\frac{2}{B}+1\right)^2-1\right)^{0.5}$	a et b: two constant value of 0.66 and 0.41. B: ratio of fuel and ambient gas mass flow rates.	Siebers [36]
$LL = cd_f\rho^{-0.5}T_a\Delta P^b$		Lopez et al. [37]

Equation	Constant parameter	Author
$LL \propto \rho_f^{0.5} \rho_g^b \rho_{amb}^c T_f^d \Delta p^e$		Payri et al. [38]

It can be concluded that a lot of studies were and are conducted in order to investigate liquid length as a function of physical parameters but only few are focused on multiple injections and the interaction between first injection and second ones.

2.1.2. Vapor spray penetration length

The vapor spray penetration length is defined as the furthest spray distance along the spray axis from the injector tip. It is also a function of operating condition and fuel properties. Different expressions had been suggested as a function of different theories or from the best fit of experimental date. Some of them are summarized in the Table 2.2.

Table 2.2. Some expressions of vapor penetration length

Theory or from experimental data	Expression	Ref.
Momentum	$S_v(t) = 1.189 C_a^{0.25} \left(\frac{\Delta P}{\rho_g}\right)^{0.25} \left(\frac{d_0 t}{\tan(\theta/2)}\right)^{0.5}$	[39]
Jet mixing theory	$S_v(t) = 3.07 C_a^{0.25} \left(\frac{\Delta P}{\rho_g}\right)^{0.25} \left(\frac{294}{T_g}\right)^{0.25} (d_0 t)^{0.5}$	[40]
Jet disintegration theory t_b: jet breakup time. $t_b = 28.65 \frac{\rho_l d_o}{(\rho_g \Delta P)^{0.5}}$	For $t_b>t>0$: $S_v(t) = 0.39 \left(\frac{2\Delta P}{\rho_l}\right)^{0.25} t$ For $t>t_b$: $S_v(t) = 2.95 \left(\frac{\Delta P}{\rho_g}\right)^{0.25} (d_o t)^{0.5}$	[41], [35]
Cone penetration length	$S_v(t) = 1.1414 C_v^{0.5} \left(\frac{\Delta P}{\rho_g}\right)^{0.25} \left(\frac{d_o t}{\tan(\theta/2)}\right)^{0.5}$	[42]
Exp. fit	$S_v(t) = d_o^{0.608} P_{inj}^{0.283} \rho_g^{-0.242} \tan(\theta/2)^{-0.5} t^{0.523}$	[43]
Exp. fit	$S_v(t) \propto (2C_a)^{0.25} C_v^{0.5} \rho_{amb}^{-0.25} \tan(\theta/2)^{-0.5} \Delta p^{0.25} D_o^{0.5} t^{0.5}$	[44]

Pastor et al. [45] developed the 1D model of prediction the spray behavior for understand the relationship between fuel-air mixing and spray penetration.

2.2. Reactive process

In the case of spray combustion, two parameters can characterize the state of the combustion: the time and the location of the Start of Combustion (SOC), i.e. the ignition timing and the lift of length. The mixing process and the combustion kinetics process are both involved. In most of the configurations, one first stage can be observed due to the cool flame chemistry (mainly observed by means of OH* radical chemiluminescence. The ignition occurs where locally the mixture is partially premixed. The schema of a conceptual jet combustion model from injection to stabilized diffusion flame is presented in Figure 2.3.

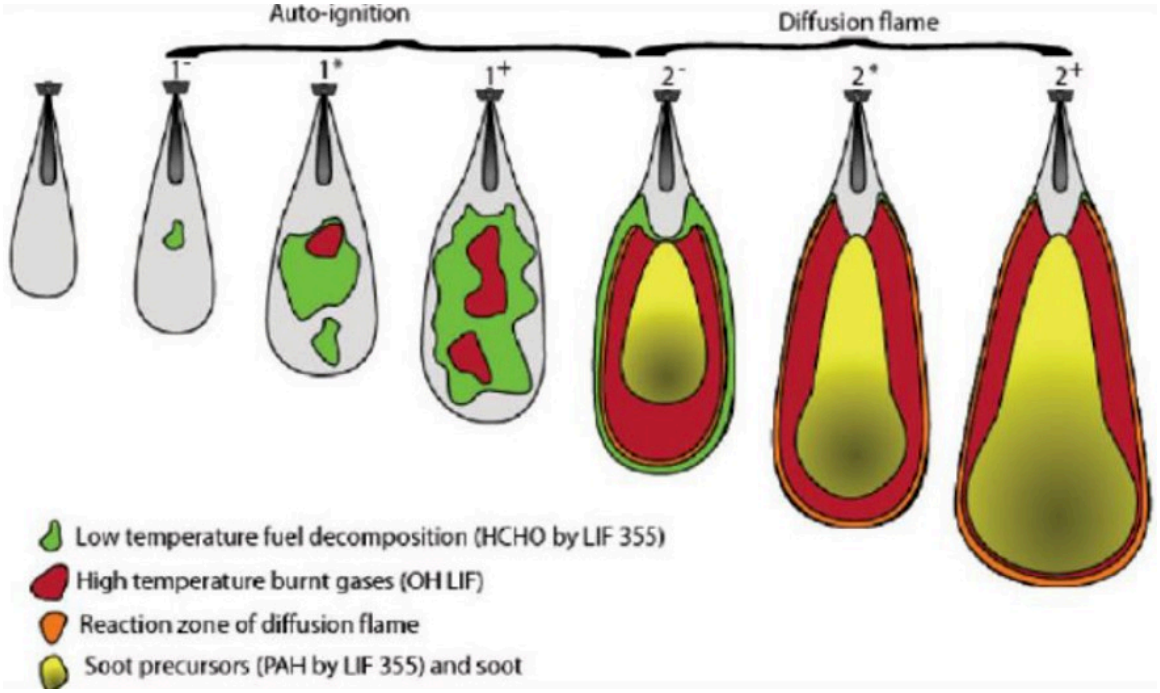

Figure 2.3. Schema of a conceptual jet combustion model from injection to stabilized diffusion flame [46]

2.2.1. Ignition timing

The ignition delay represents the time between the real start of injection and the beginning of the Heat Release Rate, due to mixing process and the chemical ignition itself. The chemical ignition delay, τ_{Arr} is usually described by an Arrhenius equation [47], with E_A the activation energy [kJ/mol], as $\tau_{Arr} = A.P_{back}^{-n}.\exp\left(\frac{E_A}{R.T}\right)$. But in the case of spray combustion, Payri et al. [48] suggested another correlation to take into account the acceleration of the ignition process

due to the increase of the injection and back pressures, (respectively P_{inj} and P_{back}) as: $\tau_{Arr} = A.P_{back}^{-n}.\exp\left(\frac{E_A}{R.T}\right).P_{inj}^{-m}$. Liu et al. [49] added the oxygen concentration of ambient gases: $\tau_{Arr} = A.P_{back}^{-n}.\exp\left(\frac{E_A}{R.T}\right).P_{inj}^{-m}.[O_2]^{-c}$.

In fact, the total ignition delay is the sum of Arrhenius one plus a physical one, related to the time needed for the air-vapor fuel mixing process, τ_{mv}, expressed as:

$$\tau_{mv} = \frac{k.\left(\frac{1}{4}\right)^{0.5}.\left(\frac{\pi}{4}\right)^{0.5}.d_f}{C_{mv}^2.U_{eff}.\tan\left(\frac{\theta_{eff}}{2}\right)}\left(\frac{\rho_f}{\rho_a}\right)^{0.5}$$

It can be considered as the elapsed time between the moment fuel parcels leaving from the injector hole exit and when those parcels reach the axis position of liquid length.

2.2.2. Flame Lift off length

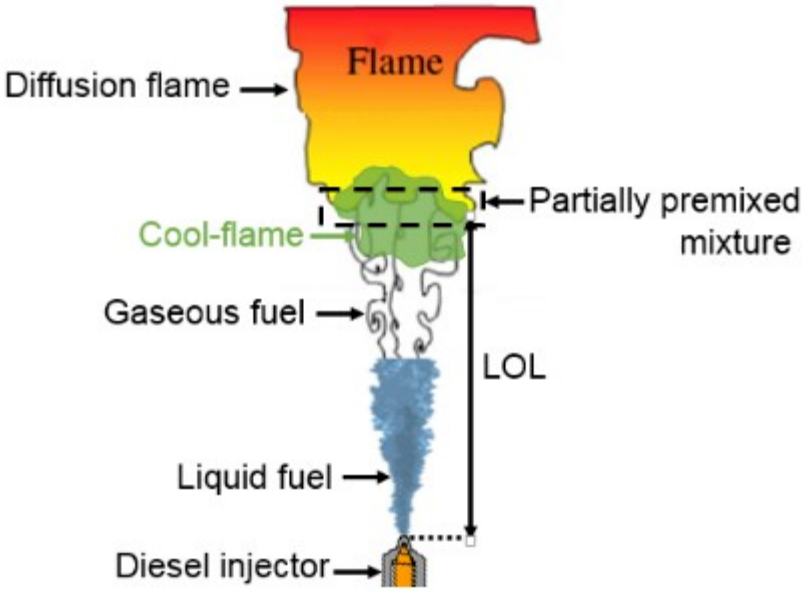

Figure 2.4. Illustration of a stabilization of Diesel spray flame [54]

An important feature of the mixing-controlled phase which occurs in Compression Ignition Combustion is the physical location of the flame stabilization, named the Flame Lift-Off Length (LOL). The stabilization process can be explained following two different points of

views: first, the stabilization of LOL in a diffusion flame is reached where there is the balance between the jet velocity and 'one' turbulent premixed stoichiometric flame speed at one distance of the injector (Burgess and Lawn [50], Peters [51]). But in this case, the effect of density difference between the fuel and the air is not considered. Second, introduced by Siebers, Higgins and Pickett [52,53], the LOL is governed by an ignition chemistry based mechanism: an increase in ignition delay time leads to a longer LOL even if the premixed stoichiometric flame speed is the same and is affected by the ambient gas oxygen concentrations.

The LOL in the case of compression ignition combustion mode is controlled by diffusion phase, so by the mixing occurred when the reacting fuel jet becomes a typical lifted turbulent diffusion flame. The LOL allows the fuel jet and air ambient to be premixed before reaching the initial auto-ignition region in the reacting jet. The Lift-Off Length is defined as the distance between the injector tip to the most upstream locations of the flame spray in a lifted turbulent diffusion under quiescent condition stabilizes [52,55].

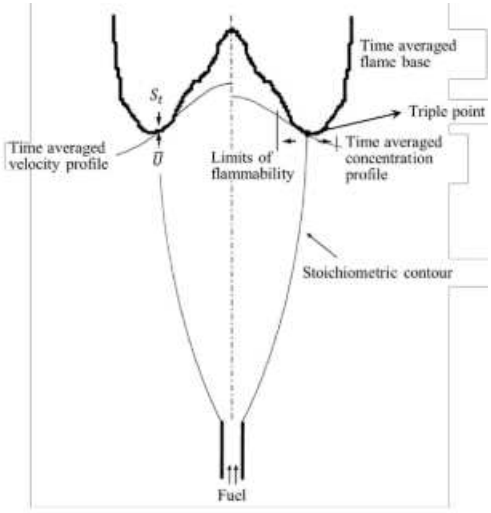

Figure 2.5. Schema of Lift-Off diffusion flame model [50]

To express the dependency of the LOL as a function of ambient temperature, oxygen concentration and nozzle diameter as obtained experimentally and seen in Figure 2.4 for a single hole injector, Pickett, Siebers and Higgins [53,55] proposed an experimental correlation of LOL for stabilized flame as:

$$LOL = CT_a^a \rho_a^b D_0^c u_0 Z_{st}^{-1} \qquad \textit{Eq. 2.1}$$

With C, a, b, c constant, set from their experimental data at 7.04×10^8, -3.74, -0.85, 0.34.

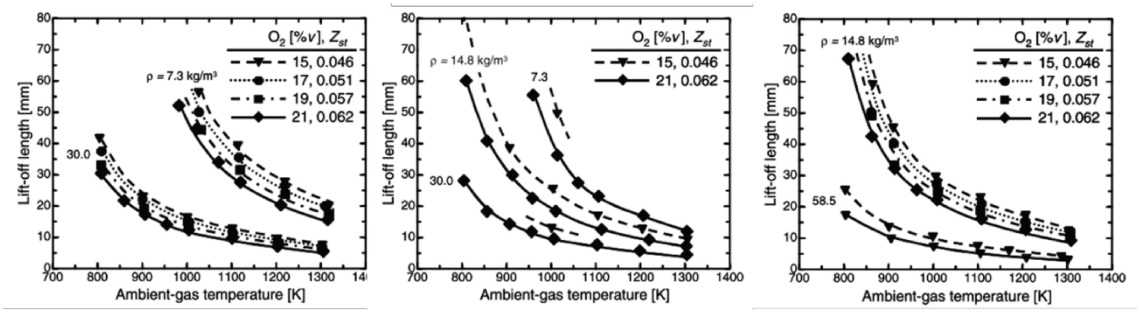

Figure 2.6. LOL variation versus ambient temperature, oxygen concentration and nozzle diameter [53]

Other studies (Payri et al. [56], Benajes et al. [73], Payri et al. [57,58]) improved this correlation by means of other experimental data without any convergence on constant and exponent values and no universal exponents have been found. Payri et al. [59] investigated the impact of multi-holes injector with same specifications than single hole and concluded slightly shorter LOL are obtained with more realistic injectors as it can be seen in Figure 2.7.

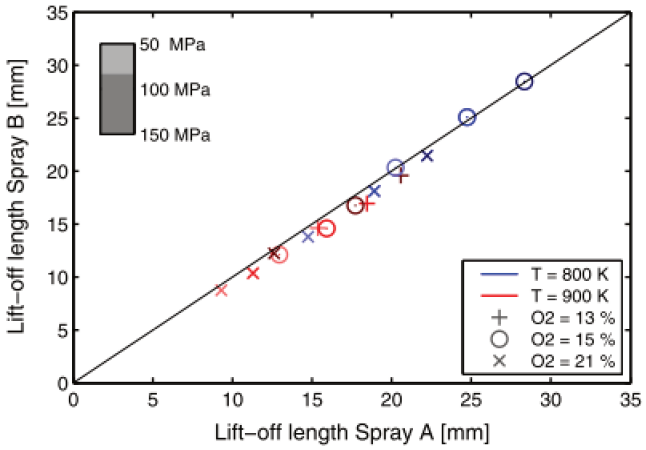

Figure 2.7. LOL comparison between a single orifice injector and multi-orifice one [59]

Persson et al. [60], Musculus [61], Rusly et al. [62], Lequien et al. [63] performed studies in optical heavy duty engines to investigate the effect of in-cylinder environment (such as the wall temperature, the in-cylinder gas flows, the interactions between adjacent jets, between jets and wall) on Lift-off length and validate the LOL experimental correlation but by adding the characteristics of the global flow motion inside the combustion chamber.

*) Effect of fuel properties on LOL

In [64], the effect of the reactivity of fuel, identified by the Cetane number was studied and as expected, the more reactive the fuel is, the less LOL is, as the example in Figure 2.8.

By considering the reactivity of the fuel through the octane number, Pastor et al. [65]

investigated in high pressure/high temperature vessel, that high octane fuel (low reactive fuel) provides longer LOL, as expected if one compares gasoline to diesel type fuel, as also did Lundgren et al. [66]. Moreover, they showed that longer LOL favors non-sooting conditions with equivalence ratio value below approximately 2. Therefore, as from kinetics point of view (Kitamura et al. [67], Westbrook et al. [68]), the oxygen content in the fuel also reduces soot formation; Manin et al. [69] showed experimentally that an increased amount of oxygen in the fuel leads to longer LOL for the same ignition delay times.

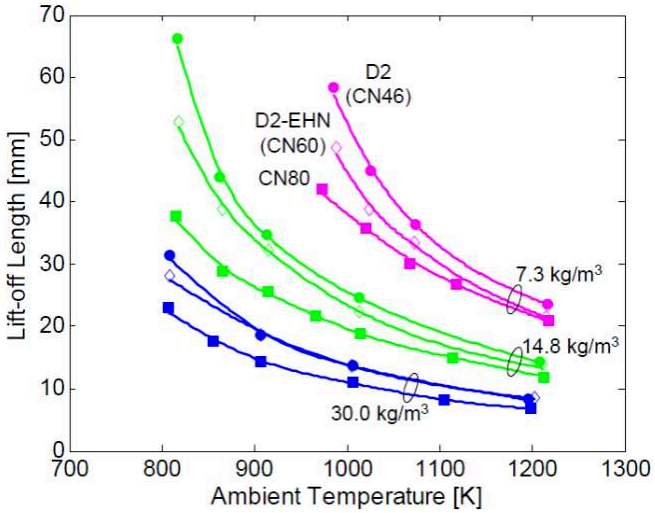

Figure 2.8. Effect of cetane number of fuel on LOL under variation of ambient gas temperature and density [64]

Jain and Aggarwal [70] also conducted the effect of low octane gasoline surrogate (n-heptane, iso-octane and toluene) fuels with RON of 70 and 80 on spray combustion characteristics under compression ignition condition. The results confirm the effect of octane number to increase the ignition delay but the effect of toluene is also to increase the first stage ignition delay (Low temperature ignition delay) and decrease second main ignition delay. Moreover, the spray flame lift-off length is mainly controlled by the ignition behavior.

2.2.3. Soot process

The soot particles formation from hydrocarbons fuel is complex process for different steps (pyrolysis, nucleation, coalescence, surface growth, agglomeration and oxidation process) as summarized in Figure 2.9.

To characterize soot during (or after) combustion process, several measurement techniques can be used to provide soot temperature, soot volume fraction or soot particle sizing. All techniques

have some advantages and drawbacks. Most of studies on soot for ECN are mainly based on the use of high-speed Back-Illumination extinction [72–75] as temporal evolution of soot amount can be obtained in harsh conditions.

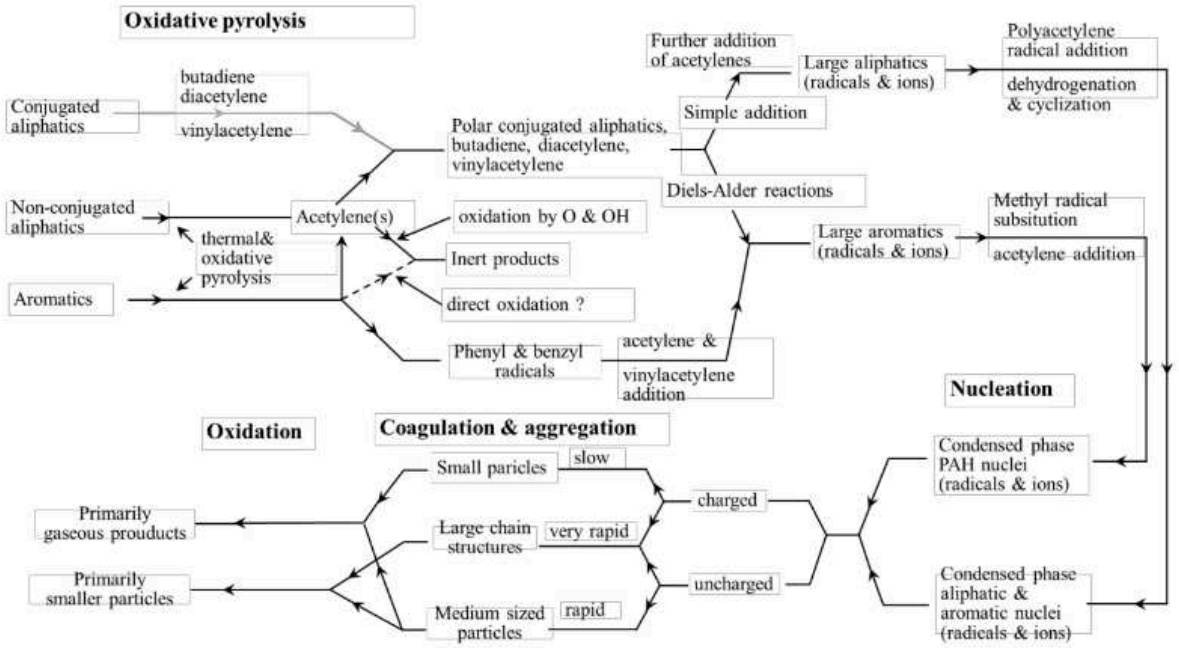

Figure 2.9. Pathway of soot production mechanism [71]

The soot formation rates and its oxidation process depend on the fuel structure, ambient gas oxygen concentration, ambient gas temperature [76,77]. Idicheria et al. [78] conducted experiments with ambient gas oxygen concentration variation and concluded that the region of soot formation and oxidation move upstream by increasing ambient oxygen. Pickett et al. [79], pointed out that the variation of ambient temperature induces the displacement of the soot formation zone toward the tip injector in the fuel-rich region, an increase of the peak soot mass with the soot formation occur in more fuel-rich regions while increasing ambient temperature. Payri et al. [80] concluded from experiments with real Diesel injectors that high ambient gas temperatures lead to higher peak in soot formation and high ambient gas density leads to a combustion process closer to injector tip, so in richer fuel-air region inducing high soot formation. In other hand, the increase of injection pressure reduces soot production in the flame jet. Xuan et al. [81] investigated soot formation of fossil diesel and blend with 50% hydrogenated catalytic biodiesel (B50) fuels as a function of injection pressure, ambient gas temperature and oxygen concentration and concluded also that the soot onset time of B50 appears earlier than with fossil diesel and the soot production location is closer to the injector tip. The total soot mass of both simulation and experiment under single injection are similar,

reported by Skeen et al. [74].

**) Effect of fuel on soot process*

Pickett et al. [82,83], conducted the soot processes in diesel fuel jets for four fuels: T70 (a fuel blend containing the oxygenate tetraethoxy-propane), BM88 (a fuel blend containing the oxygenate dibutyl-maleate), GE80 (a fuel blend containing the oxygenate tri-propylene-glycol-methyl-ether) and CN80 (a diesel reference fuel composed of an n-hexadecane and heptamethyl-nonane mixture), under 3 engine conditions. The results show the soot levels decrease by increasing oxygen ratio at LOL (with more air entrainment, oxygen of ambient gas or oxygen of fuel).

Menkiel et al. [84] investigated the combustion and soot processes the ultra-low sulphur diesel (ULSD) and rapeseed methyl ester (RME) and concluded the RME, which contains more oxygen than ULSD, have lower overall soot distribution.

Ito et al. [85] concluded that oxygenated fuel could induce soot suppression of spray under diesel compression ignition conditions and Donkerbroek et al. [86], that the premixed fuel and air upstream (include oxygen ratio of fuel) of the reaction zone of LOL affect soot formation processes downstream.

As may be inferred Table 2.3 and Table 2.4, the trends in the reviewed literature are qualitative for influence of operating and fuel properties, respectively, on macroscopic spray and combustion spray process.

Table 2.3. Summary the influence of operating on macroscopic spray and combustion spray process

Parameters	**Inert atmosphere**			**Reacting atmosphere**		
	Liquid Length	**Spr. Angle**	**Vapor Spray pen.**	**Ignition delay**	**Lift Off Length**	**Soot mass fraction**
	(*LL*)	(θ)	(S_v)	(*ID*)	(LOL)	(m_{soot})
Ambient gas Temperature (T_{amb})	⇓ [20,29, 30,87,8 8]	⇑ [87]	⇓ [87,89]	⇓ [58,64,74,8 0,90,91]	⇓ [58,64,74, 78,80,85,9 1,92]	⇑ [74,79–81,85,91–93]
Ambient gas density (ρ_{amb})	⇓ [20,29, 30,87,8	⇓ [44,94, 95]	NE [44,94, 95]	⇓ [58,64,80]	⇓ [58,64,80]	⇑ [79,80]

	8]					
Injection Pressure (P_{inj})	NE/⇓ [20,88]/ [30]	⇑ [94]	⇑ [89,94]	⇓ [58,59,80]	⇑ [58,59,80]	⇓ [79–81]
Fuel injection temperature (T_{inj})	⇓ [96]	-	-	⇓ [96]	⇓ [96]	
Orifice diameter (D_{nozz})	⇑ [20,87, 88]	⇑/NE [95] /[44]	⇑ [44,87, 95]	-	⇑ [64]	⇑ [74,78,80]
Ambient gas Oxygen concentration (Z_{st})	-	-	-	⇓ [58,59,64,9 0]	⇓ [58,59,64, 85,92]	⇓/⇑ [85,92,93]/ [74,78,80,8 1]

Note: ⇑: same direction; ⇓: inverse direction; NE: no effect

Table 2.4. Summary the influence of fuel properties on macroscopic spray and reacting spray

Parameters	**Inert atmosphere**			**Reacting atmosphere**		
	Liquid Length	**Spr. Angle**	**Vapor Spray pen.**	**Ignition delay**	**Lift Off Length**	**Soot mass fraction**
	(LL)	(θ)	(S_v)	(ID)	(LOL)	(m_{soot})
Fuel density (ρ_f)	⇑ [31]	⇑/NE [94]/ [31]	⇑/NE [94]/ [31]	-	-	-
Fuel viscosity (ν_f)	-	NE [31]	⇑/NE [94]/ [31]	-	-	-
Fuel volatility (⇓Boiling point) (⇑Vapor pressure)	⇓ [20,29, 31]	-	NE [31]	-	-	-
T50	⇑ [30]	-	-	-	-	-

Parameters	Inert atmosphere			Reacting atmosphere		
	Liquid Length	**Spr. Angle**	**Vapor Spray pen.**	**Ignition delay**	**Lift Off Length**	**Soot mass fraction**
	(*LL*)	(θ)	(S_v)	(*ID*)	(LOL)	(m_{soot})
T90	⇑ [31]	-	-	-	-	-
Oxygen content in molecule	-	-	-	⇓ [69]	⇑ [69,86]	⇓ [81,85]
Cetane number of fuel (C_t)	-	-	-	⇓ [69,86]	⇓ [69,86]	-
Octane number of fuel (*ON*)	-	-	-	⇑ [65,70]	⇑ [65]	-

Note: ⇑: same direction; ⇓: inverse direction; NE: no effect

2.3. Butanol/ABE fuel

2.3.1. Butanol/ABE fermentation production

Bio-butanol is a bio-fuel, which was produced through an anaerobic process with a fermentation microorganism from biomass 2nd generation resources such as corn, wood hydrolysate, ... Clostridium acetobutylicum and clostridium beijerinckii are the most commonly used micro-organism to convert the sugars or starch to butanol [97,98], Metabolic pathway of Clostridium acetobutylicum employed ABE fermentation is shown in Figure 2.10. ABE (Acetone – Butanol - Ethanol) fermentation, in 3:6:1 of volume of Acetone : Butanol : Ethanol, is obtained [99]. Pure butanol is obtained from ABE fermentation solvent, which is lost high-energy to distillation because of high boiling point temperature (118^{o}C) of butanol. ABE mixture is an intermediate product of the fermentation process without distillation to pure chemicals (such as butanol, ethanol), which can be is considered as a bio-fuel itself, and therefore one solution to operation internal combustion engines can save the bio-fuel production.

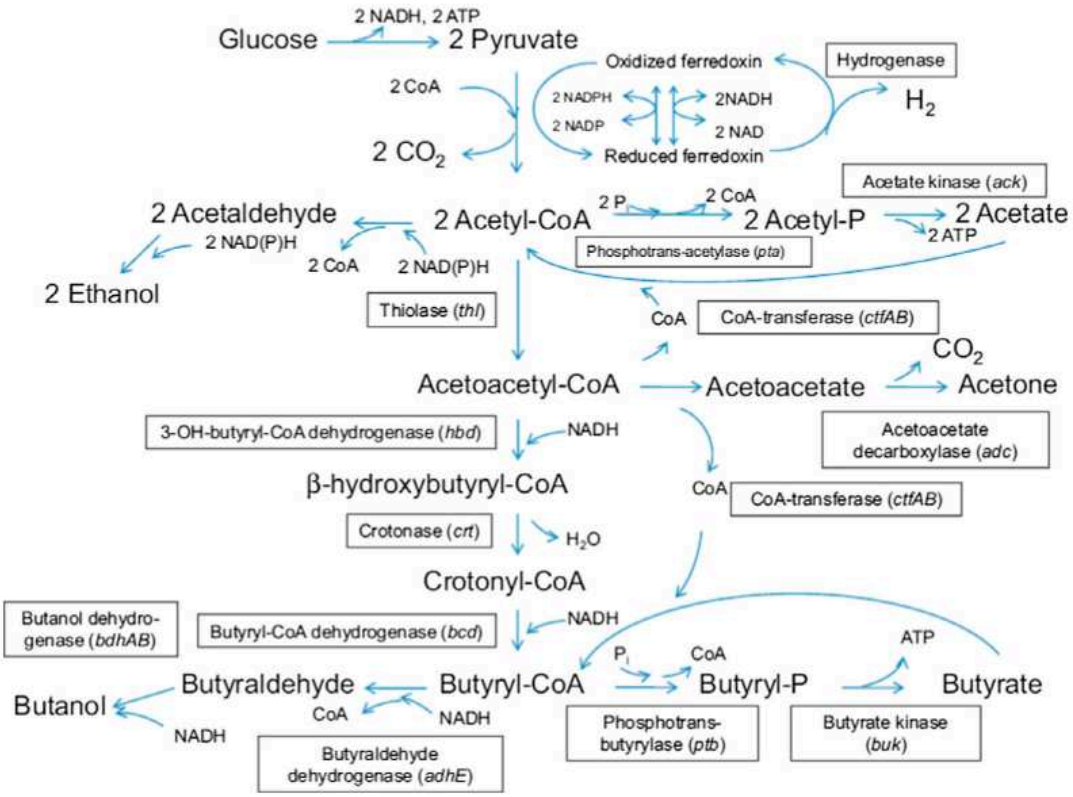

Figure 2.10. Metabolic pathway of Butanol by ABE fermentation [100]

2.3.2. Ethanol, Butanol, ABE properties

Due to the variation of the gasoline composition and its complexity, gasoline surrogate fuels are used to investigate novel combustion mode concepts without confounding factor from the effects of fuel composition changes but also to help improvement of models. Simple ones are named Primary Referenced Fuels, a mixture of iso-octane and n-heptane, PRF80 corresponds to 80% in volume of iso-octane. The properties of one gasoline surrogate, i.e. PRF80, ethanol, n-butanol, and acetone are presented in Table 2.5. Ethanol produced from renewable feed stocks has lower auto-ignition quality with high evaporative cooling effect than gasoline, which contributes to increase the ignition delay time, as indicating by the ignition characteristics: high research octane number (RON) of 108.6 and very low cetane number of 5∼15. Butanol has four different forms of isomer: n-butanol, sec-butanol, iso-butanol and tert-butanol, but n-butanol is the main product from ABE fermentation. N-butanol has oxygen atoms in its molecular structure, potentially leading to decrease of emissions, especially soot [101]. Moreover, butanol has higher energy density, higher LHV, lower reactivity and better miscible properties with gasoline than bio-ethanol fuel. N-butanol has a research octane number higher

than 100. Acetone is the most volatile species among the ABE mixture, with the lowest boiling point (56°C) and the highest saturation pressure.

Table 2.5. Pure fuel properties

No.	Properties	PRF80	Ethanol	Butanol	Acetone	Unit
1	Formula	$C_{7.8}H_{17.6}$	C_2H_5OH	$C_4H_{10}O$	C_3H_6O	
2	Molar weight	112	46	74	58	g/mol
3	Oxygen content	0	34.8	21.6	27.6	% wt
4	Density at 15°C	0.6904	0.795	0.810	0.791	g/ml
5	Lower heating value	44.36	26.8	33.1	29.6	MJ/kg
6	Latent heat of vaporization	31.13	904	43.07	518	kJ/mol
7	A/F stoichiometric ratio	15.10	9.02	11.21	9.54	-
8	RON/MON	80/80	108.6/89	96/78	110/-	-
9	Viscosity at 15°C	0.452	1.08	4.142	0.35	$mm^2.s^{-1}$
10	Vapor pressure at 298 K		7.9	0.56	30	kPa
11	Boiling point at 1 atm	99	78.4	117.7	56.1	°C

2.3.3. Butanol or ABE fuel for new combustion modes

In following 'Name of the Fuel (i.e. ethanol, butanol, ABE) XX' indicates the amount of fuel (XX) in volume blended in conventional fuel (diesel or gasoline as a function of the fuel used).

The effect of n-butanol-diesel fuel blends on PPC for reducing NO_x and soot emissions simultaneously was investigated by Cheng et al. [102] in a light duty engine. Bu10 and Bu20 (10% and 20% in volume content) can reduce soot and NO_x simultaneously, while a little effect on HC, CO and fuel consumption. They suggested that the engine performance with medium EGR could be optimized by adapting the injection strategy with higher injection and intake pressures, using oxygenated blend fuel. The results of Zhang et al. [103] showed that Bu20 and Bu40 have higher ignition delay than pure diesel fuel with a slightly higher indicated thermal efficiency while HC, CO emissions can be reduced with help of higher EGR level. Performance and emission of a turbocharged CI engine with Bu20 and Bu40 under PPC mode were also investigated by Valentino et al. [104]. The investigation of Han et al. [105] presents results at high load operations under low temperature combustion indicated n-butanol fuel is more suitable to enable PPC than the diesel fuel due to its ultra-low level of soot and NO_x emission compared to diesel combustion. This advantage can be obtained, but only in a narrow engine load range and with a considerable penalty in CO and HC emissions.

The combined effects of n-butanol contents and EGR on CI engine under PPC mode were investigated by [105] but by blending with gasoline. The main impact due to the higher-octane number and volatility of gasoline than Diesel fuel is to delay the auto-ignition timings. They found that n-butanol addition improves the oxidation of CO and HC emissions slightly, while little impact on NO_x emissions. The combined effects of EGR and n-butanol additive on the regulated and unregulated emissions from a CI engine, studied by Yang et al. [106], proved an improvement on soot emissions.

Wu et al. [107] and Zhou et al. [108] investigated the effect of ABE-diesel blends on spray combustion characteristics under both conventional compression ignition and low temperature combustion conditions in a Constant Volume Chamber (CVC. The results shown that under those conditions the ABE-diesel blends had longer both ignition delay and lift off length than neat diesel. In other studies, Wu et al. [109] studied the effect of acetone and butanol content of ABE20-diesel blends on the combustion characteristics, with ABE fuels of different component volumetric ratio (A:B:E of 6:3:1, 3:6:1, 0:10:0 (pure butanol)) and diesel mixture. They found that ABE of 6:3:1 ratio of component has combustion characteristics close to its of diesel.

Nilaphai et al. [110] investigated effect of properties of physical and chemical of ABE and diesel-like (n-dodecane) blends at volume ratio of 20% in comparison with ethanol blend and butanol blend on the spray and combustion characteristics. These experiments were performed in New One Shot Engine under Spray A condition and various ambient temperatures of 800 K and 850 K, with inert and reactive conditions. The results showed that ABE20 had shortest liquid length, shorter ignition delay and lift off length than those of both ethanol blend and butanol blend while longer than its of n-dodecane.

In summary, the researchers concluded that ABE solutions can be applied to compression ignition engine, under both conventional combustion and low temperature combustion conditions. However, up to date, combustion characteristics of ABE – gasoline or gasoline-like blends in constant volume combustion chamber have not been investigated.

Chapter 3. ABE/GASOLINE BLEND IN HCCI CONFIGURATION

This chapter presents the study performed in order to understand the chemical effect of Ethanol/Butanol and ABE blend in surrogate fuel, PRF80, on HCCI combustion mode by two ways: (1) through experimental results on ignition delay, combustion process, performance and emission performed in a single-cylinder compression ignition engine and (2) through kinetics simulations of ignition delay time (with OpenSmoke++ framework [111]).

3.1. Experimental setup and operating conditions

3.1.1. Experimental set-up

The experiments were performed in a research single-cylinder engine modified from the original four cylinders compression ignition engine (PSA DW10 engine) by fuelling only one cylinder. The displacement is of 0.5 l with a compression ratio of 16:1 and other specifications are given in Table 3.1. This engine is fully described in [112]. The engine was directly driven by an electric motor to keep a constant engine speed, fixed for this work at 1500 rpm. The engine oil and coolant were set at 95^{o}C by means of electrical heaters.

Table 3.1. Main characteristics of the single cylinder HCCI engine

No.	Parameter	Description	Unit
1	Engine model	Peugeot PSA DW10 light duty compression ignition	
2	Bore x Stroke	85 x 88	mm
3	Connecting rod length	145	mm
4	Displacement	499	cm^3
5	Geometric compression ratio	16:1	
6	Number of valves	4	
7	IOV – IVC – EVO – EVC	351; -157; 140; 366	CAD

As seen in Figure 3.1, the intake air was supplied from an air compressor and heated up to desired temperature by electrical heaters inside the plenum volume. Additional nitrogen was used to simulate exhaust gases recirculation (EGR). Each gas was supplied and controlled by a Brooks gas mass flow controller (MFC). For operation without dilution, the air flow was adjusted to achieve the desired intake pressure. For operation with dilution, the air flow was

reduced from amount required to achieve the desired intake pressure as with air alone. The intake air temperature and pressure were measured by two thermocouples (type K) with an accuracy of ± 2 K and a piezo-resistive pressure sensor (Kistler 4075A) with the accuracy of ± 0.3% of the full scale, respectively.

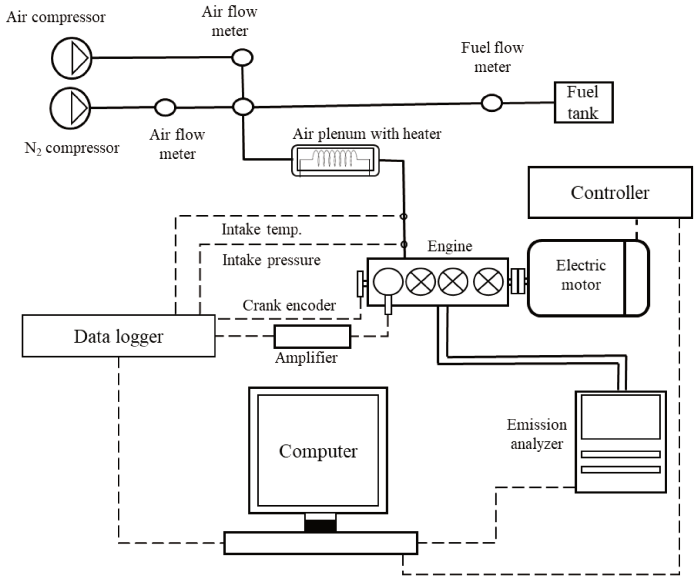

Figure 3.1. Scheme of the experimental setup

The fuel flow was supplied and measured by a liquid MFC (Bronkhorst M13-CORI-FLOW) that has an accuracy of ± 0.2%. The fuel vapor is mixed with the intake air inside the plenum. The crank angle position was identified by an optical crank encoder with an accuracy of ± 0.1 CAD. The in-cylinder pressure was measured by means of a piezo-electric pressure transducer (Kistler 6043A) mounted in the cylinder head with an accuracy of ± 2% and recorded with 0.1 CAD resolution. For all the experimental results, the in-cylinder pressure data was recorded and averaged for 100 consecutive cycles to calculate combustion characteristics using thermodynamic analysis. The measured in-cylinder pressure traces were used to calculate the Pressure Rise Rate (*PRR*), Heat Release Rate (*HRR*), Combustion phasing (*CA50*), Indicated Mean Engine Efficiency (*IMEP*) and its covariance (COV_{IMEP}) and Ringing Intensity (*RI*).

3.1.2. Combustion analysis

The heat release rate was calculated with an energy balance by considering heat transfer through Woschni's model [113] was used to consider the heat transfer, determined from the average pressure data as:

$$\frac{dQ}{d\theta} = \frac{\gamma}{\gamma - 1} P \frac{dV}{d\theta} + \frac{1}{\gamma - 1} V \frac{dP}{d\theta} + \frac{dQ_w}{d\theta} + \frac{dQ_{crevice}}{d\theta} \qquad \textbf{Eq. 3.1}$$

With Q the net heat release, P the instantaneous in-cylinder pressure, V the instantaneous combustion chamber volume, γ the ratio of specific heats ($\gamma = C_p / C_v$) and θ the crank angle. Here, heat loss through the crevices was assumed to be sufficiently small to be neglected.

The heat loss rate is written as follows: $\frac{dQ_w}{d\theta} = A_c h_c (T_g - T_w) / \omega$, With Q_w the wall heat loss, A_c the area in contact with the gases, T_g (K) the gas temperature, T_w (K) the cylinder wall temperature and ω (rad/s) the angular speed. With HCCI combustion process, the heat transfer coefficient h_c (W/m^{2}K) is based on the correlation formula given by [114]: $h_c(t) = \alpha L(t)^{-0.2} p(t)^{0.8} T(t)^{-0.73} v(t)^{0.8}$, With α the scaling factor, is used to tune the coefficient to match a specific engine geometry.

Combustion induced gas velocity is a function of the difference between motoring and firing pressure:

$$v(t) = C_1 \overline{S_p} + \frac{C_2}{6} \frac{V_d T_r}{p_r V_r} \left(p - p_{motoring} \right) \qquad \textbf{Eq. 3.2}$$

Subscript *r* denotes a reference crank angle, such as the intake valve closing.

The accumulated apparent heat release was calculated by integrating *HRR*, *CA10*, *CA50*, *CA90* being defined as the crank angles of 10%, 50% and 90% of the max accumulated apparent heat release. The combustion duration (*CD*) is defined as: *CA90* - *CA10*.

The combustion efficiency, η_c is calculated as:

$$\eta_c = \frac{\sum HRR}{Q_{in}} = 1 - \frac{\sum x_i Q_{LHV_i}}{\left[\dot{m}_f / (\dot{m}_{air} + \dot{m}_f) \right] Q_{LHV_f}} \qquad \textbf{Eq. 3.3}$$

With $\sum HRR$ the integrated value of heat release rate, Q_{in} the total heat content of the introduced fuel, x_i the mass fraction of *THC* and *CO* in the exhaust gas, Q_{LHVi} the lower heating values of these species and Q_{LHVf} the lower heating value of the fuel.

The Ringing Intensity (*RI*) is a factor to assess the combustion noise in HCCI mode, due to knock phenomenon. A correlation based on fundamental ware dynamics [115] is defined by the equation:

$$RI = \frac{1}{2\gamma} \frac{\left[\beta\left(\frac{dP}{dt}\right)_{\max}\right]^2}{P_{\max}} \sqrt{\gamma R T_{\max}} [MW / m^2] \qquad \textit{Eq. 3.4}$$

With γ the ratio of specific heats, $(dP/dt)_{max}$ the peak pressure rise rate (kPa/ms), P_{max} the peak cylinder pressure (kPa), R the universal gas constant, T_{max} the peak in-cylinder temperature (K) and β the constant with value of 0.05 (ms).

3.1.3. Experimental Conditions

The experimental conditions for this study are summarized in Table 3.2. In the present study, the Indicated Mean Effective Pressure (*IMEP*) is used as a measure of the engine load. The ratio between IMEP and the chemical fuel energy input represents the indicated efficiency. The operating condition is considered stable if $COV_{IMEP} < 5\%$ and $RI < 5$ MW/m^2.

Table 3.2. Engine operating conditions

Nº	**Parameter**	**Value**	**Unit**
1	Intake conditions		
	Air temperature	30 to 190	ºC
	Pressure	1 to 1.3	atm
2	Equivalence ratio	0.2 to 0.6	-
3	Dilution ratio	0 to 50	%

The objective of this study was to characterize ABE as fuel blended in gasoline surrogate, PRF80, for Low Temperature Combustion Mode and to compare it to other alcohols blend (Ethanol and Butanol) and to the surrogate itself. The properties of the mixtures as a function of alcohols blends are presented in Table 3.3-Table 3.5. In this study, the RON (Research Octane Number) was predicted by using linear volumetric weighting models as indicated in references [116–119].

First, the temperature at the intake and the mixture are two main parameters that directly affect the kinetics in LTC mode, so by consequence, the combustion, performance and emissions. The intake pressure and the dilution are used to control combustion phasing and knock in order to reach some IMEP levels. Before comparing ABE/PRF blend to ethanol/PRF and

Butanol/PRF, first part of results is focused on PR80 to highlight how LTC is sensitive to the variations of these parameters.

Table 3.3. Ethanol Blend fuel properties

No.	Properties	PRF80	Et20	Et40	Et60	Unit
1	Formula	$C_{7.8}H_{17.6}$	$C_{5.4}H_{12.9}O_{0.41}$	$C_{4.0}H_{10.1}O_{0.65}$	$C_{5.4}H_{12.9}O_{0.41}$	
2	Molar weight	111.2	84.6	68.9	58.7	g/mol
3	Density at 15°C	0.6904	0.710	0.730	0.750	g/ml
4	Lower heating value	44.36	40.92	37.66	34.57	MJ/kg
5	A/F stoichiometric ratio	15.06	13.70	12.42	11.20	-
6	RON/MON	80/80	85.6/-	91.2/-	96.8/-	-

Table 3.4. Butanol Blend fuel properties

No.	Properties	PRF80	Bu20	Bu40	Bu60	Unit
1	Formula	$C_{7.8}H_{17.6}$	$C_{6.6}H_{15.3}O_{0.31}$	$C_{5.8}H_{13.5}O_{0.54}$	$C_{6.3}H_{14.4}O_{0.33}$	
2	Molar weight	111.2	99.8	91.1	84.2	g/mol
3	Density at 15°C	0.6904	0.714	0.738	0.762	g/ml
4	Lower heating value	44.36	41.80	39.41	37.16	MJ/kg
5	A/F stoichiometric ratio	15.06	14.17	13.30	12.60	-
6	RON/MON	80/80	83.2/-	86.4/-	89.6/-	-

Table 3.5. ABE Blend fuel properties

No.	Properties	PRF80	ABE20	ABE40	ABE60	Unit
1	Formula	$C_{7.8}H_{17.6}$	$C_{6.3}H_{14.4}O_{0.33}$	$C_{5.3}H_{12.2}O_{0.57}$	$C_{4.5}H_{10.5}O_{0.75}$	
2	Molar weight	111.2	95.8	84.7	76.5	g/mol
3	Density at 15°C	0.6904	0.713	0.735	0.757	g/ml
4	Lower heating value	44.36	41.50	38.80	36.27	MJ/kg
5	A/F stoichiometric ratio	15.06	14.02	13.03	12.12	-
6	RON/MON	80/80	84.2/-	88.6/-	92.8/-	-

3.2. LTC characteristic for PRF80 as a function of intake temperature and pressure, air/fuel and EGR mixture

In this part, main characteristics of LTC are given by considering PRF80 as the reference fuel. The effect of intake pressure and temperature, equivalence ratio and EGR is shown for low-partial load, i.e. with an equivalence ratio around 0.30 - 0.40.

3.2.1. Effect of intake parameters variation on the combustion development

The effect of the intake pressure, the mixture itself as the equivalence ratio and the dilution rate on the in-cylinder pressure and the heat release rate is highlighted in Figure 3.2 in the case of PRF80. As well known, the intake pressure and the equivalence ratio control the engine load (IMEP) and the intake temperature and the dilution rate the start of the combustion and therefore the combustion phasing. The increase of the intake temperature leads to an early kinetics reaction occurrence as it can be seen in Figure 3.2 (c) as highlighted in the small window, this low temperature reaction phase is called 'cool flame'. The change of the intake temperature from 50 to 110°C delays the Low Temperature ignition timing from -10 to -25 CAD ATDC, inducing also an earlier main combustion phasing. But as the other configurations were set at 100°C intake temperature, due to also that the LTC part for a gasoline fuel type is very low, the effect of intake pressure, equivalence ratio and dilution rate is very low, without delay of cool flame ignition. It has to be noted that in the case of intake pressure higher than 1.15 bar, the dilution rate was set to 40% (and not 20%) to limit ringing intensity.

Performance, combustion phases and CO and unburnt HC emissions for each condition are presented in Figure 3.3. The results in Figure 3.3 (a) and (b) show that IMEP increases with equivalence ratio or intake pressure increase since more fueling rate is provided to maintain constant the equivalence ratio, advanced auto-ignition timing (indicated by CA10) and combustion phasing (CA50) further. The higher output power is caused by the higher in-cylinder pressure peak (see Figure 3.3 (a) and (b)). Hence, the combustion and indicated efficiencies also increase with a reduction of HC and CO emissions as a function of the equivalence ratio. For the effect of intake pressure, the curve is separated in two phases due to the change of dilution rate for $P_{int} > 1.15$ bar.

The results in Figure 3.3 (c) indicate that with the intake temperature increase, IMEP slightly decreases unlike the combustion efficiency, with an auto-ignition timing (CA10) and combustion phasing (CA50) nearer TDC. This effect is caused by several factors [120,121]: (1) the increase of heat losses due to high temperature peak, (2) the increase of heat loss due to high ringing intensity, (3) some negative works prior to the piston reaches TDC due to advanced combustion phasing and (4) lower charge density.

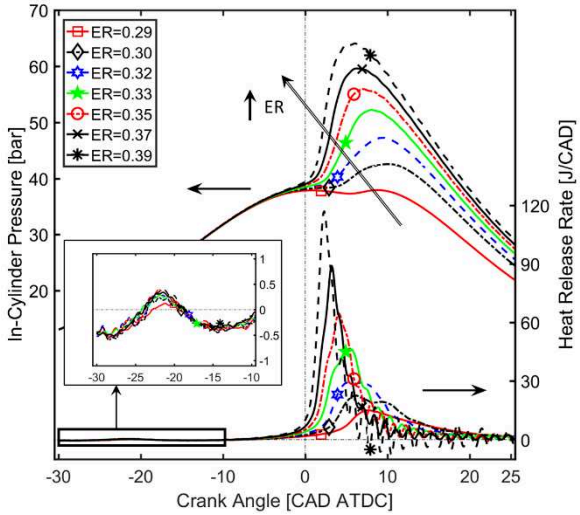

(a) Equivalence ratio variation, P_{int}=1bar, 0% EGR, T_{int}=110°C

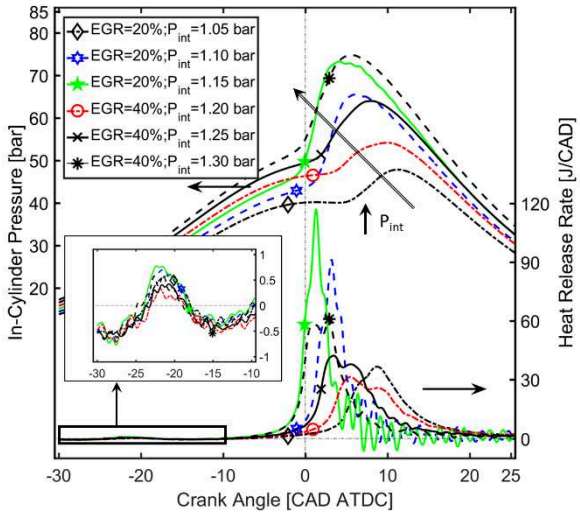

(b) Intake pressure variation, ER=0.35, 20% EGR/ 40% EGR, T_{int}=100°C

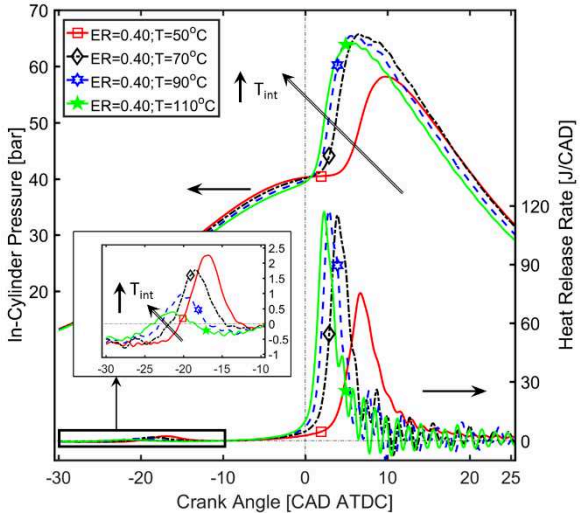

(c) Intake temperature variation, P_{int}=1bar, 0% EGR, ER=0.40

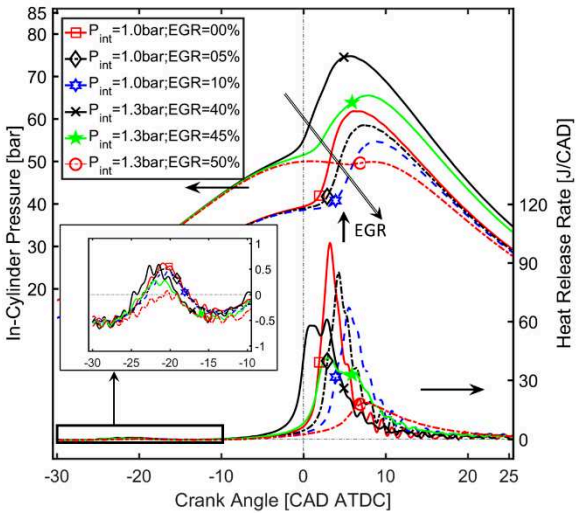

(d) EGR variation, T_{int}=100°C, P_{int}=1bar, ER=0.3 and P_{int}=1.3bar, ER=0.30

Figure 3.2. In-cylinder pressure and HRR for PRF80 fuel as a function of equivalence ratio (a), intake pressure (b), intake temperature (c) and EGR (d)

The influence of EGR under 2 intake pressure conditions is shown in Figure 3.3 (d): at P_{int} = 1.0 bar EGR variation was set until 10%, and for P_{int} = 1.3 bar, from 40% to 60%. At a given equivalence ratio, as the EGR is simulated by 100% N_2, the oxygen mole fraction is reduced by increasing amount of EGR, with also the quantity of fuel. Hence, EGR increase retards the auto-ignition timing and combustion phasing sufficiently to lead to an acceptable Ringing intensity. The EGR under higher intake pressure can extend the IMEP range from 3.0 to 3.3 bar and from 2.8 to 3.5 bar for 1.0 and 1.3 bar of intake pressure, respectively.

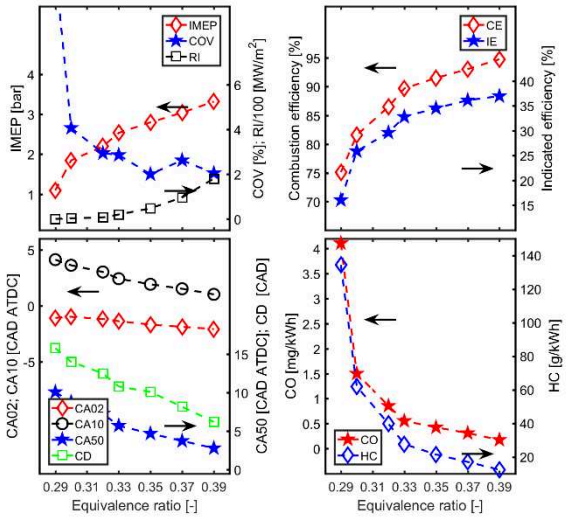

(a) Equivalence ratio variation, P_{int}=1bar, 0% EGR, T_{int}=110°C

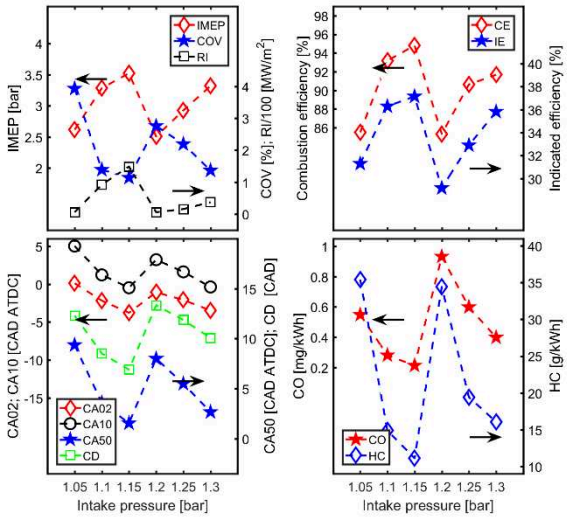

(b) Intake pressure variation, ER=0.35, 20% EGR/ 40% EGR, T_{int}=100°C

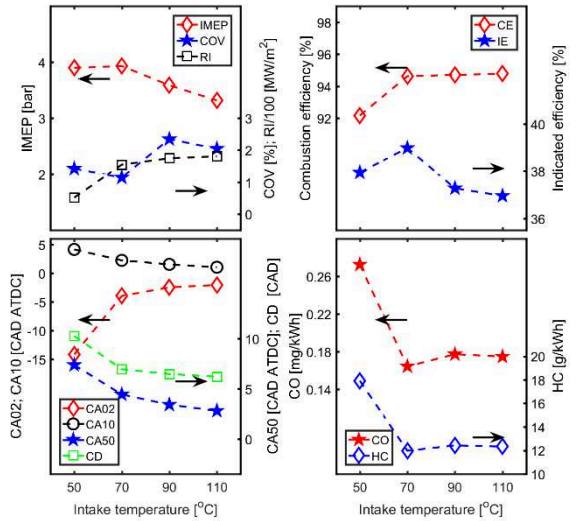

(c) Intake temperature variation, P_{int}=1bar, 0% EGR, ER=0.40

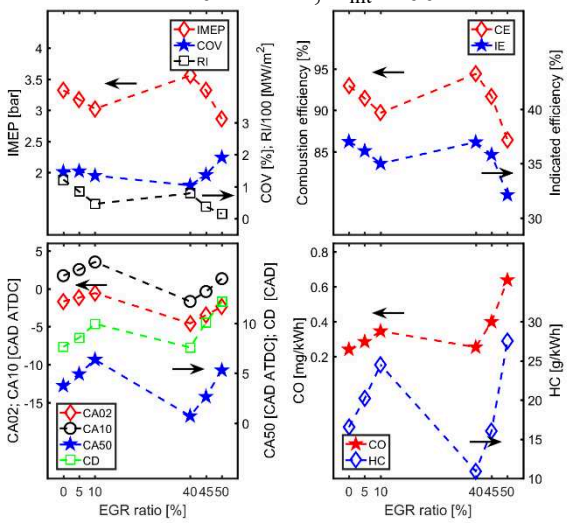

(d) EGR variation, T_{int}=100°C, P_{int}=1bar and P_{int}=1.3bar, ER=0.35

Figure 3.3. Performance, combustion phases and pollutant emission of HCCI mode for PRF80 fuel as a function of equivalence ratio (a), intake pressure (b), intake temperature (c) and EGR (d)

Correlation between performance, combustion process and emissions (Y) and intake conditions (X) as the formula of linear regression in Eq. 3.5 to evaluate the sensitivity.

$$Y=a*X+b \qquad \textit{Eq. 3.5}$$

The summary of the correlations is listed in Table 3.6, for CA10 and CA50 (CAD ATDC), IMEP (bar), CE and EI (%), RI (MW/m^2), CO and HC (mg/kW.h), T (ºC), ER (-), P (bar) and EGR (%). Under intake temperature variations, the effect on CO and HC emissions is non-linear, as shown in Figure 3.3 c.

Table 3.6. Coefficients for Eq. 3.5

	Coef.	Variable parameters					
		T	ER	P		EGR	
				0%EGR	20%EGR	1.0bar P	1.3bar P
CA10	A	-0.05	-32.56	-55.0	-36.0	0.18	0.30
	B	6.22	13.3	62.42	46.5	1.69	-13.75
	R^2	0.903	0.960	0.995	0.996	0.996	0.994
CA50	A	-0.074	-75.49	-78.2	-53.4	0.26	0.46
	B	10.42	31.49	90.85	72.13	3.72	-17.69
	R^2	0.896	0.940	0.960	0.999	0.996	0.992
IMEP	A	-0.01	21.24	9.09	8.13	-0.03	-0.07
	B	4.52	-4.63	-6.85	-7.24	3.322	6.394
	R^2	0.867	0.898	0.945	0.999	0.999	0.966
CE	A	0.071	331.5	93.12	63.58	-0.326	-0.796
	B	77.75	-28.7	-11.28	9.73	930	126.7
	R^2	0.577	0.752	0.954	0.986	0.998	0.991
IE	A	0.023	189.0	58.6	66.6	-0.2	-0.48
	B	39.7	-320	-29.6	-50.6	37.1	56.7
	R^2	0.802	0.759	0.985	0.995	0.998	0.986
RI	A	2.03	1853.6	1428.9	316.2	-7.60	-6.38
	B	-22.12	-563.3	-1489.5	-375.5	122.6	331.2
	R^2	0.723	0.893	0.992	0.924	0.999	0.988
CO	A		-0.031	-0.003	-0.005	$11*10^{-6}$	$38*10^{-6}$
	B		0.011	0.004	0.007	$238*10^{-6}$	$-1.3*10^{-3}$
	R^2		0.754	0.805	0.952	0.997	0.995
HC	A		-1002.1	-243.4	-183.9	0.796	1.661
	B		376.7	288.3	253.2	16.42	-56.58
	R^2		0.632	0.865	0.752	0.998	0.992

The results in Table 3.6 show the influence of the intake condition including temperature, pressure and dilution gas, and air-fuel mixture quantity on the operation, combustion process and emissions of HCCI mode. Some general trends, with regard to sensitivity of the intake parameters, were identified for PRF80 fuel under HCCI mode:

- The increasing the equivalence ratio, intake temperature or pressure can increase the combustion efficiency and indicated efficiency, reduced the CO and HC emissions through advanced of auto-ignition timing and combustion phasing and reverse for impact of EGR.

- The impact of intake pressure on auto-ignition timing, combustion phasing, combustion efficiency, RI and HC emission of higher EGR ratio is lower and reverse on indicated efficiency

and CO emission.

- The impact of EGR ratio on auto-ignition timing, combustion phasing, combustion efficiency, indicated efficiency, CO and HC emissions of higher intake pressure is higher and reverse on RI.

Consider the performance of HCCI mode, the IMEP is modeled as a linear function of energy content, lowest heat value per cycle (LHV, in Joule/cycle) by Eq. 3.6, with the coefficients in Table 3.7.

$$IMEP=a*LHV+b \qquad \textbf{Eq. 3.6}$$

Table 3.7. Coefficients for Eq. 3.6. IMEP in bar and LHV in Joule/cycle

	Coef.	Variable parameters					
		T	ER	P		EGR	
				0%EGR	20%EGR	1.0bar P	1.3bar P
IMEP	a	0.010	0.019	0.016	0.024	0.018	0.019
	b	-1.09	-5.16	-4.22	-7.81	-4.55	-5.64
	R^2	0.960	0.924	0.955	0.923	0.974	0.915

The coefficient obtained for each parameter is significantly different, hence the correlation can be established for one variation of each condition. For each case tested, IMEP has a good correlation with fuel energy injected per cycle, with 91% confidence level. Under higher EGR ratio case of 20% and the intake pressure variation, the sensitivity of energy content on IMEP is highest. Under case of intake temperature variation, the sensitivity of energy content on IMEP is lowest.

Correlation between CA10 and CA50, see Eq. 3.7, with the coefficients in Table 3.8.

$$CA50=a*CA10+b \qquad \textbf{Eq. 3.7}$$

Table 3.8. Coefficients for Eq. 3.6. CA10 and CA50 in CAD ATDC.

	Coef.	Variable parameters						All cases
		T	ER	P		EGR		
				0%EGR	20%EGR	1.0bar P	1.3bar P	
CA50	a	1.793	2.371	1.438	1.481	1.444	1.527	1.413
	b	1.196	0.185	2.069	3.180	1.280	3.274	2.334
	R^2	0.999	0.998	0.997	0.999	0.999	0.999	0.860

The positive coefficient of a value and high R^2 highlights the similar trends of CA10 and CA50. The higher coefficient of a for intake temperature and ER variation indicates that these

conditions affects significantly the combustion phasing, hence the control of the HCCI mode by intake temperature and equivalence ratio is perspective.

**) Ignition delay time from chemical kinetic Simulation*

OpenSMOKE++ chemical kinetics simulation package developed by CRECK Modeling Lab [111] was used to calculate ignition delay time of PRF80 and air (79% N_2 and 21% O_2) mixture under homogeneous condition with Polimi mechanism [122]. Ignition delay is defined as the time at which the maximum slope of Temperature as time (dT/dt). Ignition delay times computations were done to further analyze the impact of the temperature, pressure and equivalence ratio on the combustion of PRF80 fuel. The initial pressure was set at 25 bar and 40 bar, respectively for equivalence ratio of 0.3, 0.4 and 0.5, to represent operating conditions in the HCCI mode where low temperature combustion and main combustion are occurred.

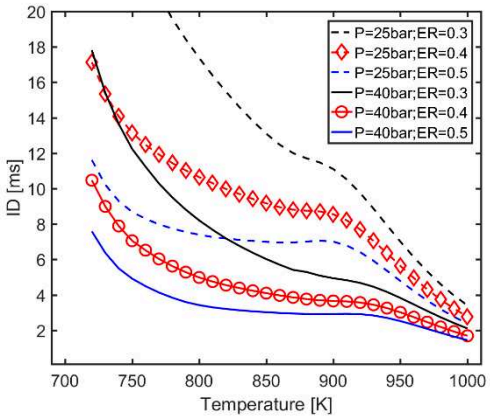

Figure 3.4. Ignition delays of PRF80-air mixture homogeneous as a function of temperature, under 3 equivalence ratios with 25 and 40 bar ambient pressure

Figure 3.4 shows the ignition delay times obtained as a function of temperature at different pressure and equivalence ratio. From these simulation results, it may clearly observe that the increase of the temperature or the equivalence ratio decreases ignition delay at both initial pressures, with typical trend for primary reference fuel [123]. At 25 bar condition, the PRF80 fuel exhibits significant NTC (Negative Temperature Combustion) behavior in the temperature range from 850 to 900 K for 0.3 equivalence ratio, extended to lower temperature of 820 K and 780 K for higher equivalence ratio of 0.4 and 0.5, respectively.

**) Controlling combustion phasing*

Another way to identify the influence of parameters on engine performance is to plot IMEP,

COV, RI, indicated efficiency, combustion efficiency as a function of the combustion phasing (CA50) as in Figure 3.5 and Figure 3.6.

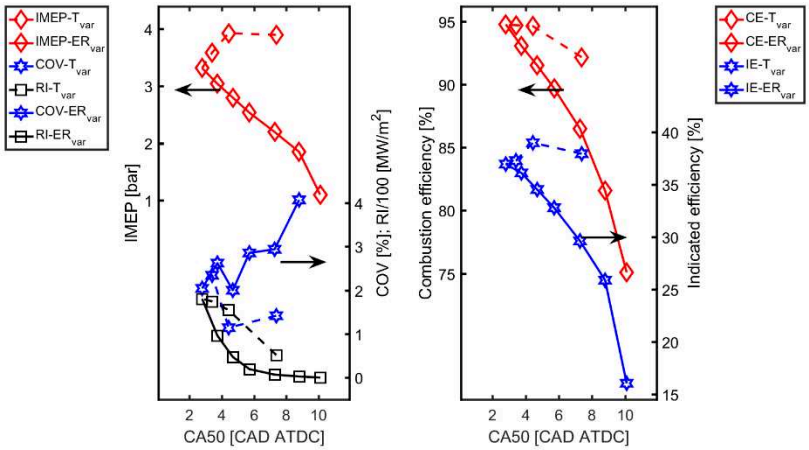

Figure 3.5. The performance parameters as a function of combustion phasing: for different intake temperatures (Dashed line) and equivalence ratio (Solid line)

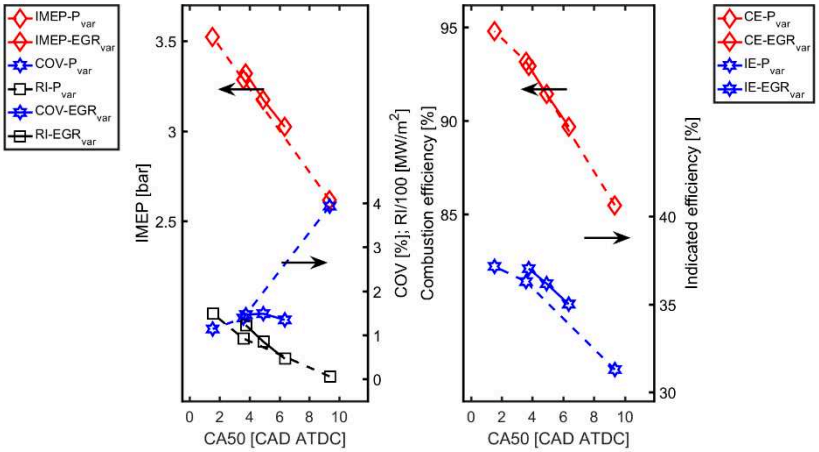

Figure 3.6. The operating and combustion parameters as a function of combustion phasing under intake pressure (Dashed line) and EGR ratio (Solid line) variation

These figures highlight in fact the trade-off between best combustion and indicated efficiencies and the stability and limits; the highest efficiencies are obtained for highest ringing intensity but lowest covariance when the CA50 is nearer TDC. In the other hand, to delay a little the combustion induces less high-pressure gradient impact but a slight decrease of the efficiency. A CA50 around 5 CAD ATDC could be this compromise value.

From Figure 3.6, it is less evident to identify this compromise as IMEP continuously drops with delayed combustion phasing, while intake pressure decreases or EGR ratio increases. The intake pressure and EGR ratio can be used to control the combustion phasing to extend the high load of HCCI mode, with intake pressure to increase the fueling rates and EGR ratio to retard

the combustion timing to avoid the knock combustion, as examined by Sjöberg and Dec [124].

Correlation between performance, efficiencies and combustion phasing is presented in Eq. 3.8, with coefficients in Table 3.9.

$$Y=a*(CA50)+b \qquad \textbf{Eq. 3.8}$$

Table 3.9. Coefficient for Eq. 3.8. CA50 in CAD ATDC

	Coef.	Variable parameters					
		T	ER	P		EGR	
				0%EGR	20%EGR	1bar P	1.3bar P
IMEP	a	0.108	-0.280	-0.116	-0.152	-0.114	-0.154
	b	3.196	4.131	3.702	3.735	3.746	3.692
	R^2	0.867	0.974	0.999	0.997	0.997	0.996
RI	a	-29.24	-20.91	-17.55	-5.96	-29.15	-13.61
	b	272.26	179.33	167.16	51.79	230.80	83.46
	R^2	0.975	0.707	0.756	0.988	0.997	0.995
CE	a	-1.031	-4.304	-1.222	-1.173	-1.25	-1.76
	b	88.076	100.941	97.05	95.51	97.6	95.9
	R^2	0.745	0.893	0.825	0.854	0.999	0.999
EI	a	0.19	-2.60	-0.78	-1.24	-0.78	-1.09
	b	36.9	46.31	38.7	39.3	40.0	38.1
	R^2	0.823	0.897	0.896	0.956	0.999	0.992

The impact of combustion phasing on performance, efficiencies based on the following observations:

- The IMEP, CE and IE are strongly influenced by the combustion phasing, as delayed CA50 leads to higher load.

- The IMEP and IE in the case of temperature variation have positive constants, while other case negative, that suggest the increase intake temperature to control the auto-ignition timing and decrease intake temperature to increase the load.

- The RI mainly depends on the combustion phasing (CA50), as delayed CA50 leads to lower RI, especially when intake temperature and EGR vary without boosted. RI is lower sensitivity of CA50 for optimized EGR than without EGR.

- The combustion efficiency often deteriorates under delayed CA50 behavior.

3.2.2. Global effect of intake temperature – equivalence ratio on engine performance

HCCI operating range map based on IMEP has been suggested by Masurier et al. [125,126], Contino [127] and Saxena [128] as a function of intake temperature and pressure, as shown in Figure 3.7, by using as criteria, maximum of acceptable RI and misfire limit.

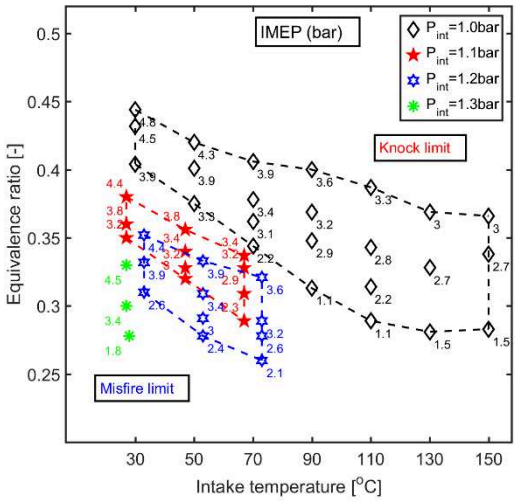

Figure 3.7. Example of IMEP map of PRF80 HCCI mode based on intake temperature – equivalence ratio for different intake pressure conditions

It can be seen that the shape of IMEP iso-contours, i.e. horizontally inclined, indicates how much the equivalence ratio controls the engine load and as the intake temperature changes mostly combustion timing and combustion phasing. At the naturally aspirated, the highest IMEP was approximately 4.8 bar, for the highest equivalence ratio (0.45) at the lowest intake temperature (30°C) and the lowest IMEP 1.1 bar, for a minimum equivalence ratio (around 0.3) with intermediate intake temperatures (90 - 110°C). But the increase of intake temperature increases this low limit value until 1.5 bar. Under slightly boosting conditions, globally the operating conditions map is reduced but as already discussed, for on intake temperature the IMEP range is increased, as for example, from 1 bar to 1.3 bar of intake pressure at a constant intake temperature of 30°C, the IMEP range becomes from 1.8 - 4.5 bar instead of 3.9 - 4.8 bar.

3.2.3. 'Limit' conditions

To allow efficient and subsequent comparison of Alcohols blends, many parameters as well as possible should be held constant. However, spanning wide ranges of equivalence ratio in stable combustion region as a function of different fuel auto-ignition properties, especially high-octane fuels, it becomes impossible to work with predetermined equivalence ratio or combustion phasing. The "Limit conditions" is proposed to evaluate the high-octane fuels used in HCCI mode. This part considers the Limit conditions from to start burning to maximum

ringing intensity, for 1 bar intake pressure and 30 to 150ºC intake temperature and for 1.2 bar and 30 to 70ºC intake temperature, as listed in Table 3.10.

Table 3.10. Experiment conditions of PRF80-fuel HCCI mode for Limitation conditions

No. Case	**Intake pressure [bar]**	**Intake temperature [ºC]**	**Equivalence ratio**	
			ER_{min}	**ER_{max}**
1	1.0 bar	30	0.40	0.45
2		50	0.38	0.42
3		70	0.35	0.41
4		90	0.31	0.40
5		110	0.29	0.39
6		130	0.28	0.37
7		150	0.28	0.36
8	1.2 bar	30	0.31	0.35
9		50	0.28	0.33
10		70	0.26	0.32

Figure 3.8 shows in-cylinder pressure and HRR under 'limit' equivalence ratio for maximum ringing intensity (left) and start burning (right).

For both 'limit' conditions and also both intake pressures, the HRR exhibits the first-stage of low temperature heat release decreases by increasing the intake temperature from 30ºC to 150ºC. Under intake temperature of 130ºC and 150ºC, this first stage is very low. The main combustion stage for all cases is generally advanced with higher intake temperature and/or higher intake pressure despite of lower equivalence ratio. The variation of performances, combustion and emissions versus intake temperature is given at Figure 3.9, on the left above (a), left below (c) for limit ringing intensity without and with boosting, respectively, and right above (b), right below (d) for start burning without and with boosting, respectively.

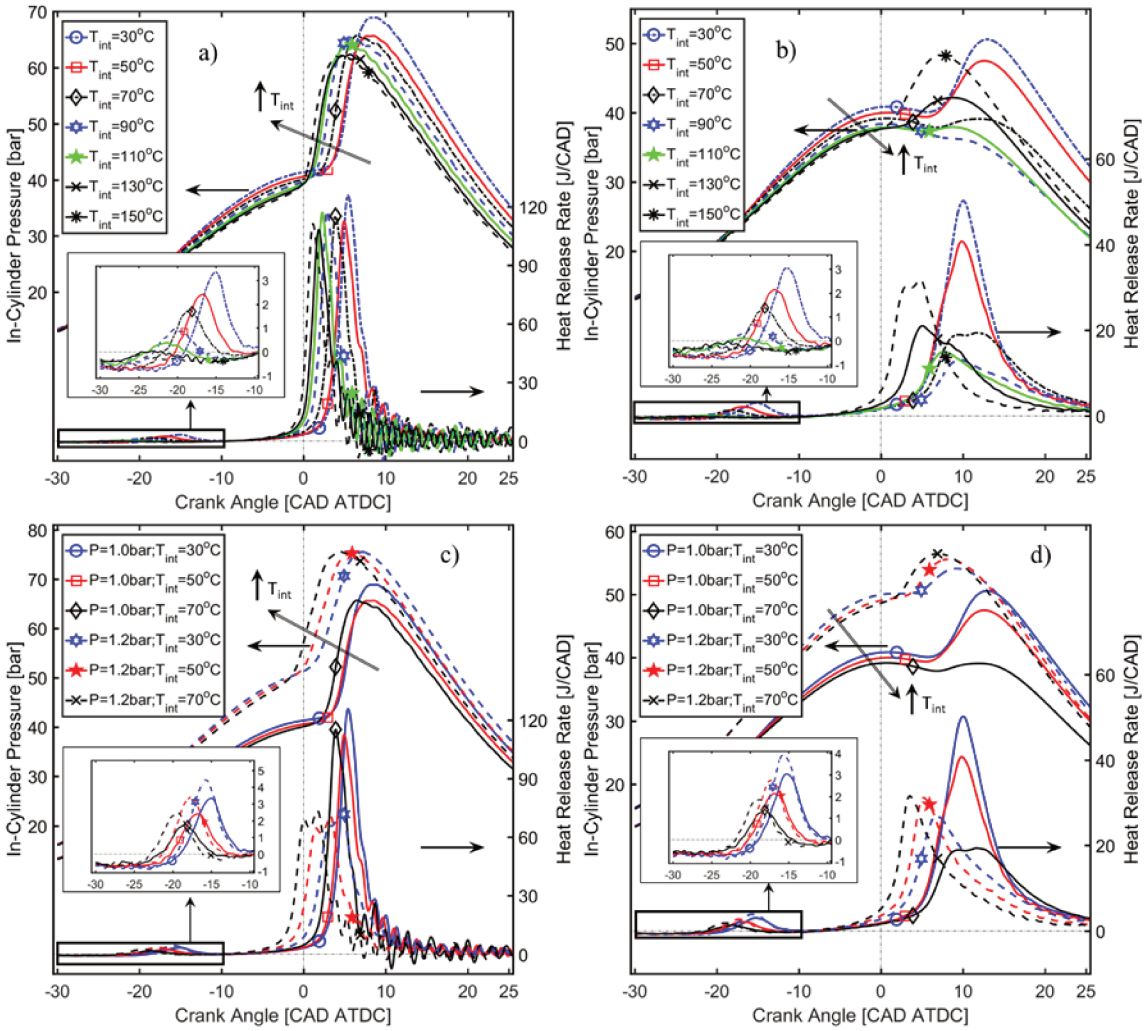

Figure 3.8. In-cylinder pressure and Heat release rate under limited Ringing intensity (left) and start burning (right)

In the Figure 3.9 a) shows the possibility to reach higher IMEP value at low intake temperature under same the level of ringing intensity (around 2 MW/m^2), by controlling the combustion phasing from 1.69 to 5.87 CAD ATDC from 150 and 30°C intake temperature respectively. The intake temperature has no significant impact on the combustion efficiency, but strongly on indicated efficiency, highest intake temperature with lowest indicated efficiency. This is certainly due to the negative work during compression stroke (see the CA02 and CA10, which occur before TDC). The intake temperature increases, the combustion phasing is advanced and the combustion duration is shortened. The ignition delay for main combustion phase (CA10) is advanced, but CA02, which indicates ignition delay for the cool flame has not the same trend. The emissions of HC, CO are slightly increased with the increase of the intake temperature, because the equivalence ratio is lower for higher intake temperature.

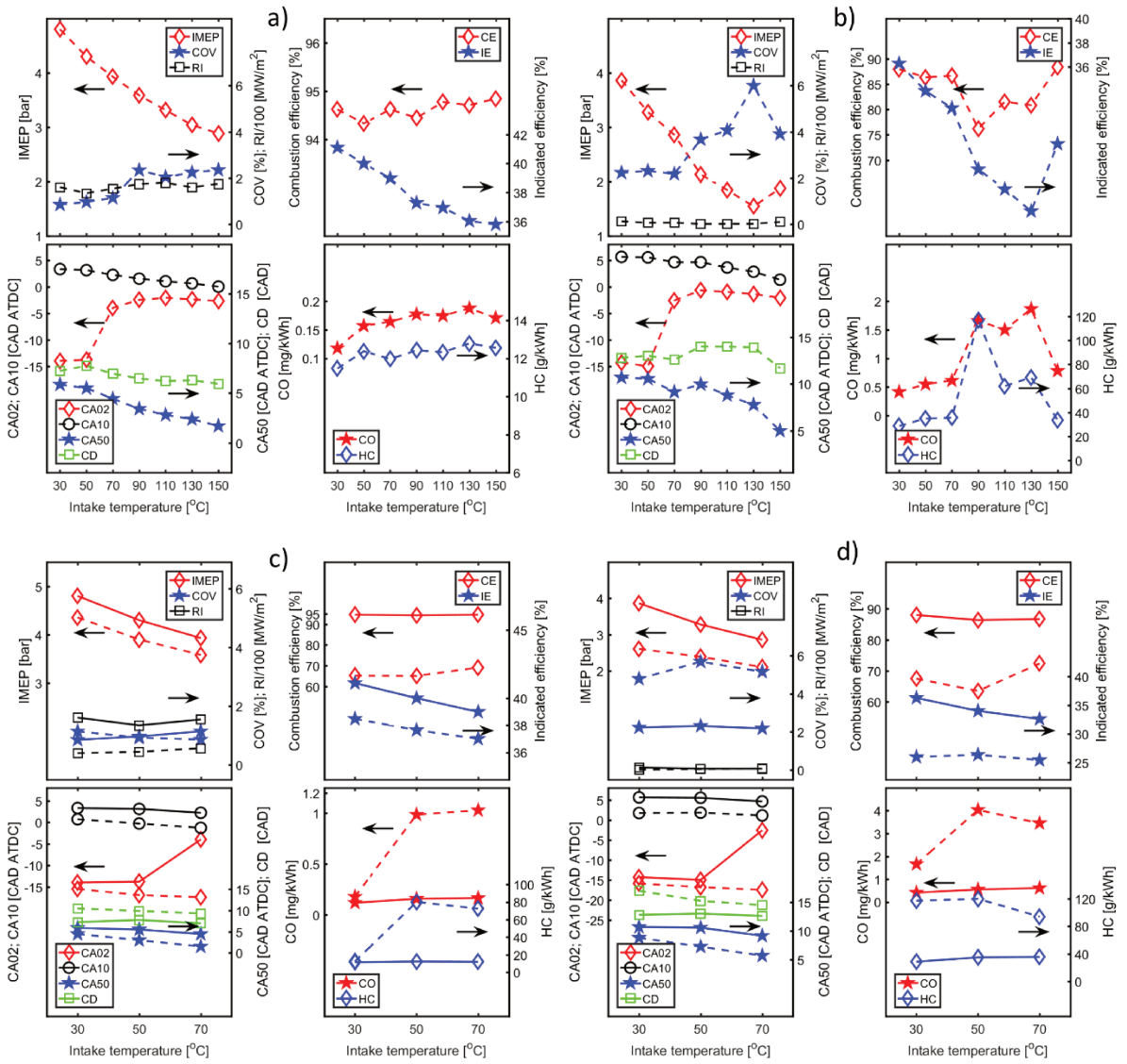

Figure 3.9. Performance, combustion and emissions characteristics under limit ringing intensity (left: (a) and (c)) and start burning (right: (b) and (d)) for each condition. For (c) and (d): Solid line and Dashed line for without boosting and with boosting, respectively.

In Figure 3.9 b) the limit condition as the start burning is as a function of intake temperature: the acceptable lower IMEP is around 2 bar for higher intake temperature (more than 90°C) and the highest IMEP around 3.8 bar. The cool flame is also exhibited under lower intake temperature range (less than 90°C) despite the lowest equivalence ratio. Due to this low IMEP limit, the COV level is increased with a decrease of the indicated efficiency in spite of stable combustion efficiency. By increasing the intake temperature, the combustion phasing is advanced but without significant change on combustion duration.

Normally the influence of intake temperature on performance, combustion and emissions is similar for boosting and naturally aspirated conditions and both maximum RI and start burning

limits. It is shown in the Figure 3.9 c) when the comparison between boosting and naturally aspirated conditions under maximum RI is presented. The maximum IMEP capable of the boosting is generally lower than without boosting, also for the lower ringing intensity. The combustion efficiency and indicated efficiency are lower for boosting conditions at all intake temperature conditions. The boosting conditions induce more cool flame stage than without boosting. The intake pressure also advances the combustion phasing but also a longer combustion duration. The HC and CO emissions are higher for boosting than naturally aspirated condition, the reason may be than the equivalence ratio is lower and combustion duration longer. In the Figure 3.9 d), the boosting condition promotes the auto-ignition, and advances the combustion phasing.

The influence of equivalence ratio on the performances, combustion process and emissions is represented by a linear regression in Eq. 3.10, with the coefficients for each intake temperature at 1 bar intake pressure and 1.2 bar in Table 3.11 and Table 3.12, respectively.

$$Y=a*ER+b \qquad \textbf{Eq. 3.9}$$

Table 3.11. Coefficients for Eq. 3.9, at 1 bar intake pressure conditions

	Coef.	**Intake temperature variation**						
		30ºC	**50ºC**	**70ºC**	**90ºC**	**110ºC**	**130ºC**	**150ºC**
CA10	a	-55.64	-42.17	-44.76	-47.13	-32.56	-24.31	-15.64
	b	28.06	22.22	21.54	20.47	13.30	9.41	5.70
	R^2	0.992	0.886	0.827	0.718	0.961	0.935	0.990
CA50	a	-115.87	-106.83	-106.40	-100.43	-76.49	-60.60	-40.40
	b	57.28	51.87	48.25	42.71	31.49	24.22	16.27
	R^2	0.982	0.628	0.770	0.912	0.941	0.935	0.986
CD	a	-132.82	-111.68	-116.97	-101.94	-96.60	-84.96	-68.92
	b	66.50	55.46	54.56	46.43	43.07	37.37	31.23
	R^2	0.986	0.883	0.923	0.909	0.979	0.974	0.998
IMEP	a	22.41	22.26	23.98	22.97	21.24	16.84	12.80
	b	-5.14	-5.12	-5.69	-5.25	-4.63	-3.05	-1.73
	R^2	0.975	0.921	0.910	0.786	0.898	0.953	0.986
CE	a	208.86	227.21	280.73	317.76	311.47	204.19	106.15
	b	-7.90	-13.68	-28.47	-36.24	-28.72	13.12	49.07
	R^2	0.930	0.717	0.761	0.595	0.752	0.799	0.813
IE	a	114.3	134.5	166.5	188.2	188.8	131.9	81.4
	b	-9.4	-17.4	-27.5	-33.5	-32.2	-10.9	6.8

	Coef.	Intake temperature variation						
		30ºC	**50ºC**	**70ºC**	**90ºC**	**110ºC**	**130ºC**	**150ºC**
	R^2	0.925	0.783	0.799	0.594	0.759	0.841	0.938
RI	a	3462.9	2250.0	2225.0	1886.0	1853.7	178.8	1984.2
	b	-1397.2	-852.3	-789.1	-613.1	-563.3	-513.7	-561.7
	R^2	0.895	0.740	0.807	0.881	0.893	0.950	0.979
CO	a	-0.007	-0.008	-0.011	-0.045	-0.031	-0.017	-0.008
	b	0.003	0.004	0.005	0.017	0.011	0.006	0.003
	R^2	0.935	0.866	0.752	0.314	0.421	0.786	0.978
HC	a	-410.2	-222.9	-524.8	-427.8	-1002.1	-595.3	-268.8
	b	192.3	165.2	262.2	220.8	376.7	224.3	108.8
	R^2	0.913	0.522	0.851	0.723	0.632	0.821	0.971

Table 3.12. Coefficients for Eq. 3.10, at 1.2 bar intake pressure

	Coef.	Intake temperature variation				Coef.	Intake temperature variation		
		30ºC	**50ºC**	**70ºC**			**30ºC**	**50ºC**	**70ºC**
CA10	a	-25.52	-40.42	-39.11	IE	a	270.7	241.3	199.4
	b	9.82	13.17	11.11		b	-54.9	-40.6	-25.1
	R^2	0.874	0.940	0.959		R^2	0.779	0.842	0.861
CA50	a	-102.30	-87.35	-72.90	RI	a	887.3	774.2	895.3
	b	40.25	31.70	24.49		b	-274.4	-212.7	-227.8
	R^2	0.974	0.963	0.949		R^2	0.969	0.924	0.835
CD	a	-149.12	-112.65	-97.99	CO	a	-0.072	-0.064	-0.039
	b	62.32	46.56	39.90		b	0.026	0.022	0.013
	R^2	0.913	0.886	0.836		R^2	0.756	0.769	0.793
IMEP	a	39.09	31.37	25.92	HC	a	-660.8	-782.7	-477.46
	b	-9.21	-6.33	-4.55		b	308.5	339.5	223.93
	R^2	0.874	0.900	0.905		R^2	0.945	0.735	0.617
CE	a	451.42	339.97	328.95					
	b	-75.28	-48.08	-19.39					
	R^2	0.786	0.833	0.863					

The following observations on the impact of equivalence ratio can be drawn:

- For any intake temperature, CA10 advances as the mixture becomes richer, hence advanced CA50 and shorter CD. The reasons can be the strongly of pre-ignition chemistry of richer fuel and air mixture, as specially of lowest intake temperature condition.

- For constant intake temperature, the CA10 is more sensitive to ER at lower intake temperature as compared to higher intake temperature, and at lower intake pressure as compared to higher intake pressure.

**) Controlling combustion phasing*

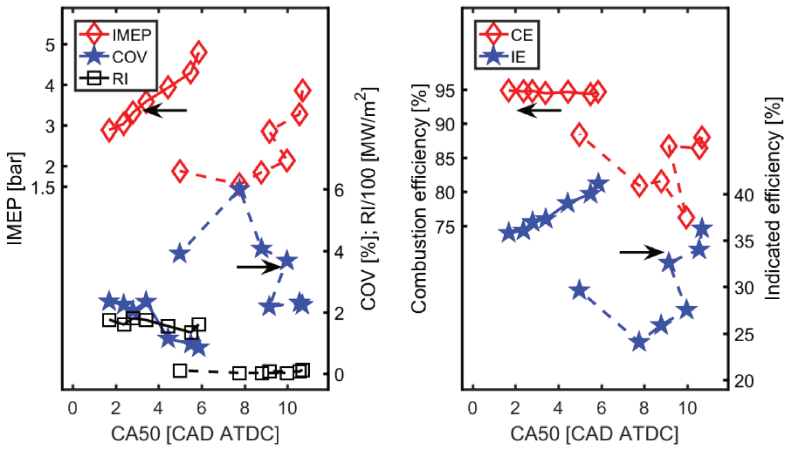

Figure 3.10. Performance parameters as a function of combustion phasing under 2 stable combustion limits (Solid line: maximum ER, Dashed line: minimum ER) with the intake temperature and equivalence ratio variation.

Based on Figure 3.10, retarding the combustion phasing can induce higher IMEP under maximum ER limit, as well as maximum Ringing intensity, furthermore indicated efficiency increases. High IMEP can be obtained also with a delay of the combustion phasing for the minimum ER. In contrary, under start burning behavior, to reach lower IMEP with lower equivalence ratio requires to advance the combustion phasing, which is benefit for the combustion efficiency.

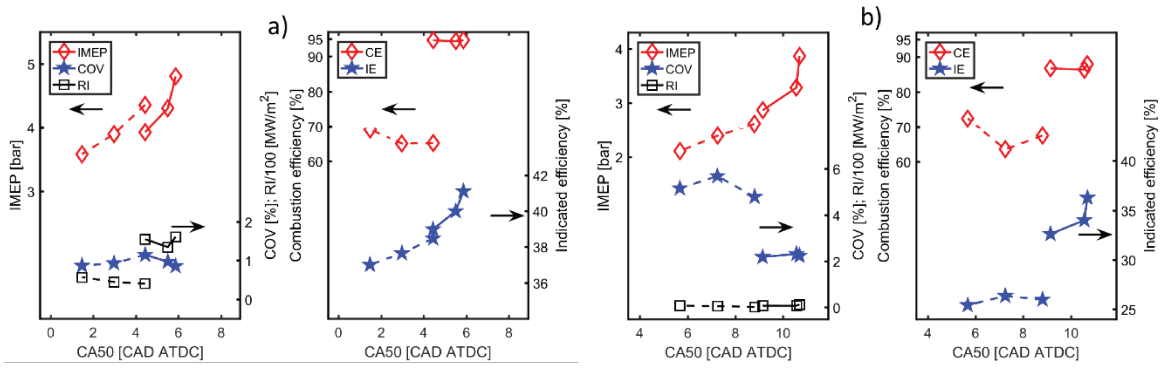

Figure 3.11. Performances as a function of combustion phasing under 2 stable combustion limits ((a) for maximum ER, (b) for minimum ER) for two intake pressures (Solid line and Dashed line for without boosting and boosting, respectively)

Boosting has the benefit of advanced combustion phasing to decrease the IMEP range but the combustion and indicated efficiencies are strongly affected and reduced. Example, to reach 4 bar IMEP, CA50 is advanced from 4.5 to 3 CAD ATDC for intake pressure of 1.0 bar and 1.2 bar respectively. The Ringing intensity of boosting is lower under maximum equivalence ratio limit.

**) Low temperature reaction*

This part is focused on the low temperature reaction (LTR), as known as the cool flame of HCCI mode. The period of LTR is defined as the time from the first-ignition timing to the second-ignition timing, as the minimum value between of two peaks of HRR curves (cool flame and main flame of HCCI mode). The first-ignition timing was approximately from -26 to -18 CAD ATDC, as in Figure 3.12. The peak of LTR decreases by increasing the intake temperature and decreasing the intake pressure, but at different equivalence ratio as a function of the stable operating conditions range, for intake temperatures from 30 to 110°C and of 30, 50 and 70°C at 1.2 and 1.0 bar, respectively with minimum and maximum equivalence ratio. The main reason is the decomposition of the precursors of the chain branching on LTR back to the reactants at higher temperature [129], and that the intake pressure increases the O_2 addition reactions to chain branching on LTR to OH radical [130,131].

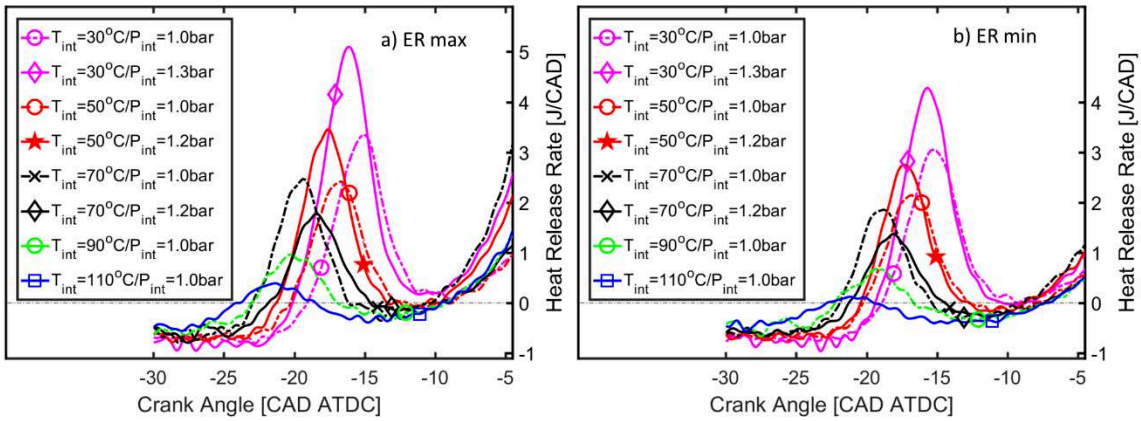

Figure 3.12. The influence of intake temperature and intake pressure at limited condition on first stage ignition of PRF80 fuel: a) Maximum Equivalence ratio, b) Minimum Equivalence ratio

The percentage of the LTHR is illustrated versus the difference equivalence ratio, intakes temperature and pressure conditions, as seen in Figure 3.13. The low intake temperature and high intake pressure conditions lead to higher amounts of LTHR, which similar results in gasoline fuel for HCCI mode [132]. The influence of equivalence ratio on amount of LTHR

under each intake pressure and temperature conditions is indicated the increasing the value LTHR maximum, but decreasing the ratio of LTHR and LHV while increase the equivalence ratio.

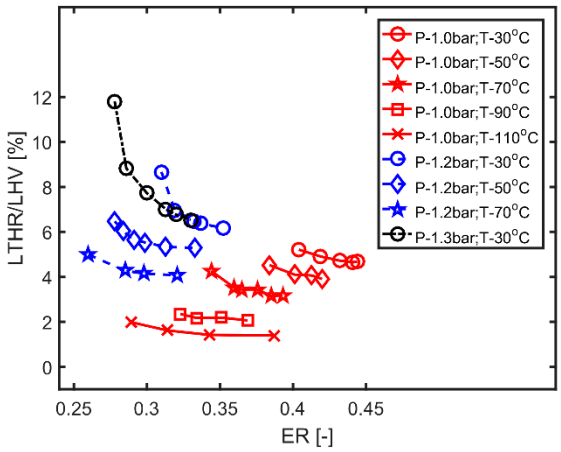

Figure 3.13. Amount of the LTHR as a function of equivalence ratio for difference intake temperature and pressure conditions.

The linear model for LTHR and the ratio of LTHR and LHV, based on Equivalence ratio is presented in Eq. 3.10 and Eq. 3.11, with the coefficient for each intake temperature at 1 bar intake pressure and boosted pressure is listed in Table 3.13 and Table 3.14, respectively.

$$LTHR=a*ER+b \qquad \textbf{Eq. 3.10}$$

$$LTHR/LHV(\%)=a'*ER+b' \qquad \textbf{Eq. 3.11}$$

Table 3.13. Coefficient for Eq. 3.10, at 1.0 bar intake pressure conditions. LTHR in Joule and LTHR/LHV in %

	Coef.	**Intake pressure and temperature conditions**					
		1 bar					
		30°C	**50°C**	**70°C**	**90°C**	**110°C**	**All**
LTHR	A	446.8	438.4	294.4	268.6	179.6	1371.4
	B	29.4	-9.5	10.9	-23.1	-15.3	-38939
	R^2	0.900	0.909	0.784	0.942	0.924	0.780
LTHR/LHV	a'	-13.76	-16.103	-20.72	-5.25	-5.70	
	b'	10.73	10.66	11.17	4.00	3.51	
	R^2	0.944	0.927	0.824	0.802	0.795	

Table 3.14. Coefficient for Eq. 3.10, at 1.2 and 1.3 bar intake pressure conditions. LTHR in Joule and LTHR/LHV in %

	Coef.	Intake pressure and temperature conditions				
		1.3 bar	1.2 bar			
		30°C	30°C	50°C	70°C	All
LTHR	A	677.9	523.4	767.4	544.1	1580.2
	B	82.5	96.0	-31.8	-9.7	-280.5
	R^2	0.873	0.891	0.775	0.972	0.638
LTHR/LHV	a'	-88.48	-53.48	-21.23	-18.61	
	b'	35.05	24.58	12.09	9.82	
	R^2	0.804	0.759	0.745	0.800	

The constants are shown in Table 3.13 and Table 3.14 indicate that the impact of equivalence ratio on LTHR and LTHR/LHV is more sensitivity at low intake temperature and high intake pressure. The constants of equivalence ratio for LTHR and LTHR/LHV are positive and negative, respectively, for all test cases.

The effect of intakes temperature and pressure conditions on LTHR is presented in Eq. 3.12 and Eq. 3.13, the coefficients in Table 3.15

$$LTHR=a*ER+b*T+c*P+d \quad \textbf{Eq. 3.12}$$

$$LTHR/LHV(\%)=a'*ER+b'*T+c'*P+d' \quad \textbf{Eq. 3.13}$$

Table 3.15. Coefficient for Eq. 3.12 and Eq. 3.13. LTHR in Joule and LTHR/LHV in %, T in °C, P in bar

	Coef.				
	a	b	c	d	R^2
LTHR	867.4	-1.05	600	-728.7	0.879
	a’	b’	c’	d’	R^2
LTHR/LHV	-32.8	-0.075	-7.5	28.5	0.764

The constants for the effect of intake temperature are negative for both LTHR and LTHR/LHV, those of ER and intake pressure are positive for LTHR, but negative for LTHR/LHV. The tendency of effect of intake temperature on LTHR/LHV is similar observed in [133], with RCM experimental and simulation results for FACE-F gasoline fuel, equivalence ratio of 0.3, ambient pressure of 23 and 43 bar, range ambient temperature from 800 to 1000 K. The influence of intake temperature on amount LTHR is found in [134], under CFR engine experiments, for PRF80 fuel, Equivalence ratio of 0.33, engine speed of 600 rpm, range intake temperature from 50 to 150°C.

Under higher intake temperature conditions from 110 to 150ºC, the auto-ignition timing (CA02) of single combustion phase of HCCI mode, where the LTHR does not exist, is also modeled as a linear function of equivalence ratio and intake temperature, shown in Eq. 3.14, with coefficients in Table 3.16 to give some perspectives under the range low intake temperature, this was not true linear function (R^2=0.463), where two combustion phases of HCCI mode.

$$CA02=a*ER+b*T+c \qquad \textbf{Eq. 3.14}$$

Table 3.16. Coefficient for Eq. 3.14. CA02 in CAD ATDC, T in ºC

	Intake Temperature [ºC]	Coef.			
		A	B	C	R^2
CA02	30-150	-27.91	-0.025	10.64	0.463
	110-150	-10.44	-0.025	4.731	0.923

Conclusions that can be drawn by this model are the intake temperature and equivalence ratio increase lead to auto-ignition timing advanced.

The overall ignition characteristics of PRF80 fuel as a function of wide range of ambient temperature and pressure conditions and equivalence ratio (0.3, 0.4, 0.5 and 0.6) are shown in Figure 3.14 to understand the effect of equivalence ratio variation on auto-ignition. The history of the in-cylinder pressure and temperature of motoring condition of 1 bar intake pressure and 40, 100 and 150ºC intake temperature is overlapped on the iso-contour of ignition delay. The instantaneous chemical reactivity (as the value inverse of ignition delay time) of PRF80-air mixture, integrated during the continuous in-cylinder thermodynamics cycle until auto-ignition occurs (indicated by the beginning of the heat release) highlights if one combustion or two combustion phases occur. As it can be seen in Figure 3.14, at a 150ºC intake temperature, the high temperature chemistry dominates for all equivalence ratio but for a 40ºC intake temperature, both high and low temperature chemistries are involved.

The NTC behavior is more and more pronounced with the equivalence ratio increase, as for example the ignition delay iso-contour lines for values 6, 5, 4 and 3 ms are almost vertical for initial temperature and pressure from 750 to 900 K and from 30 to 40 bar respectively. Consequently, the ignition delay in the NTC zone is more sensible to the initial temperature for the richest mixture (i.e. 0.60 E.R.) or to both initial temperature and pressure for the leanest one (0.30 ER).

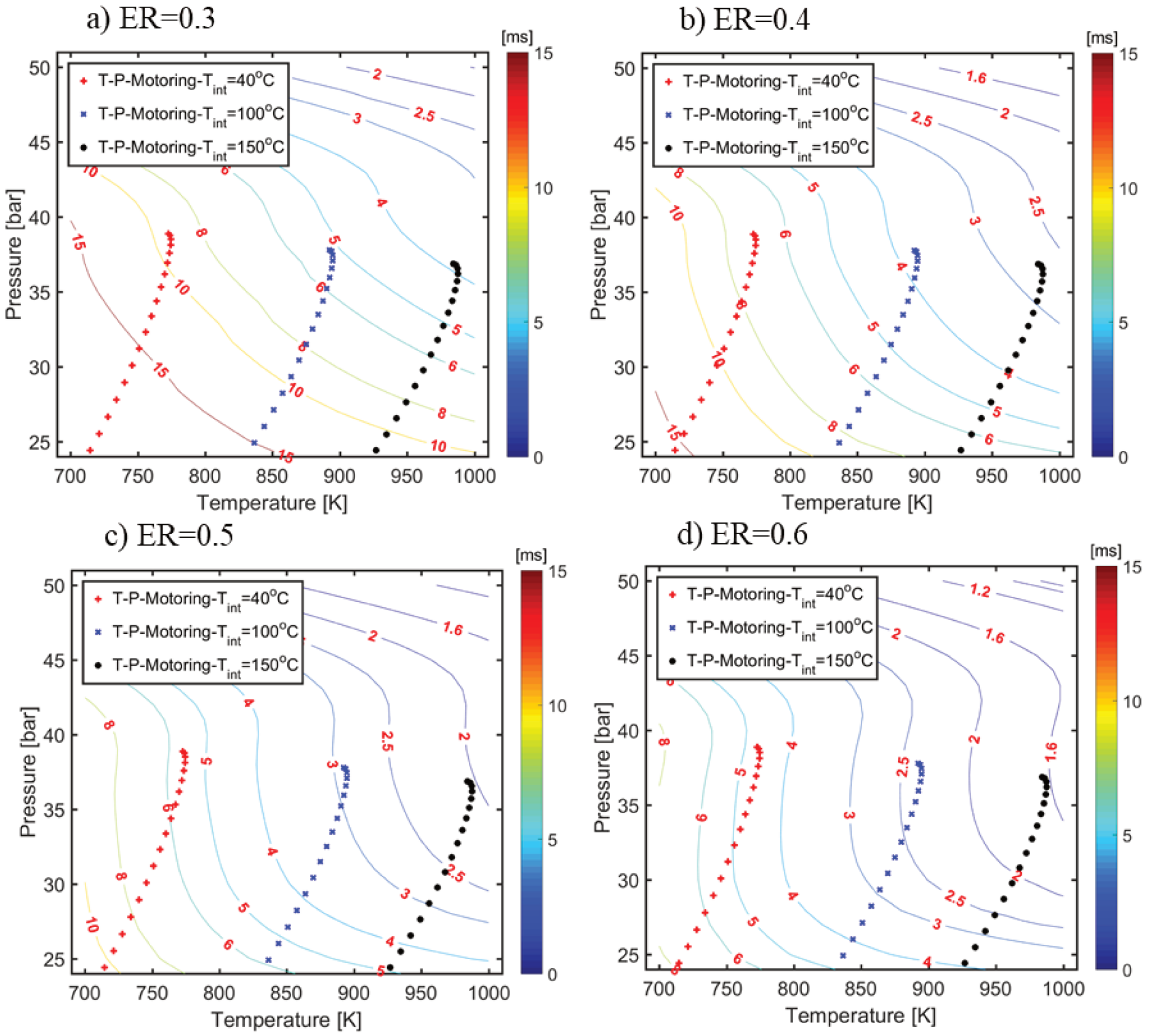

Figure 3.14. Iso-contours of ignition delay for PRF80 fuel and air mixture under wide-range temperature and pressure with equivalence ratio of a) 0.3, b) 0.4, c) 0.5 and d) 0.6

3.2.4. Effect of intake pressure – EGR ratio on engine performance

The simultaneous effect of intake pressure and EGR ratio is investigated to extend the engine the operating conditions range, to avoid the ringing phenomenon under high load in the HCCI mode and to promote the auto-ignition under low-load. Figure 3.15 shows the IMEP range of PRF80 fuel with variation of intake pressure and EGR ratio under intake temperature of 100°C and 0.35 equivalence ratio.

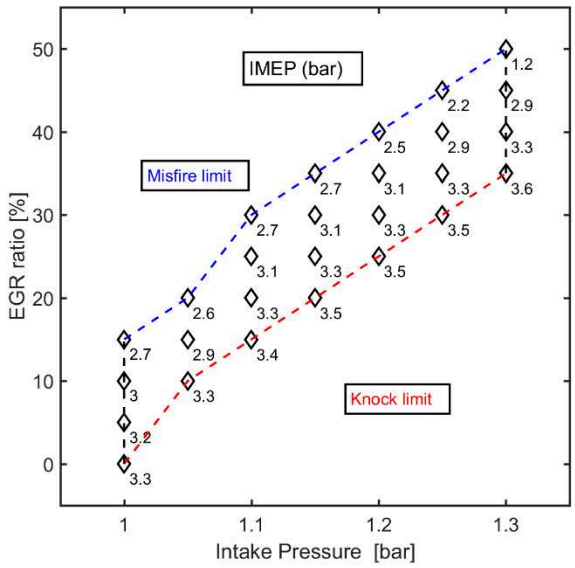

Figure 3.15. Example of IMEP range of HCCI mode based on intake pressure – EGR ratio for PRF80 under intake temperature of 100°C and equivalence ratio of 0.35

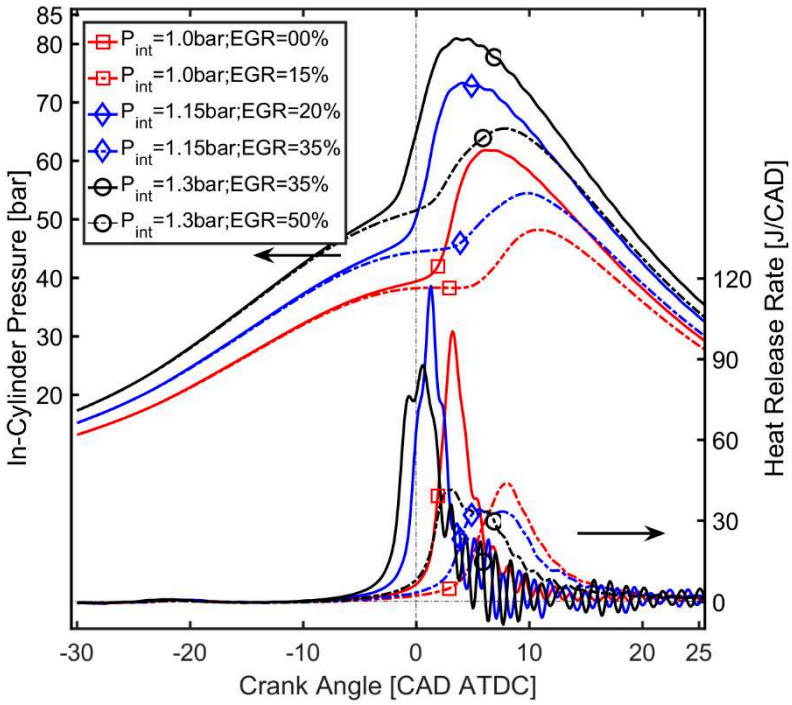

Figure 3.16. In-cylinder pressure and Heat release rate for 3 cases of intake pressure with minimum (Solid line) and maximum (Dashed line) EGR

While adjusted simultaneous EGR ratio and boosted conditions, one can observe the extension of the IMEP range. With an intake pressure of 1 bar, the IMEP limit range is from 2.7 bar to 3.3 bar with 15% EGR and without EGR, respectively, and with an increase of intake pressure to 1.3 bar, from 1.2 to 3.6 bar with 30% to 50%, respectively. The in-cylinder pressure and the HRR for 6 experimental conditions (minimum and maximum amount of EGR with intake

pressure of 1.0 bar, 1.15 bar and 1.3 bar) are plotted in Figure 3.16. The HRR curves indicate that the intake pressure has a strong impact on the combustion phasing despite the different EGR ratio.

Performance, combustion and emissions characteristics for these conditions are plotted in Figure 3.17. The ignition timing occurs before TDC, delayed with the increase of EGR. With maximum of EGR, the influence of EGR on IMEP is more sensible than intake pressure, as seen in Figure 3.17, as example, an increment of 10% EGR from 35% to 45%, with intake pressure increment of 0.15 bar from 1.15 to 1.3 bar, induces an IMEP decrease of 1.5 bar. The combustion phasing is delayed and the combustion duration is longer, thus, the combustion efficiency and indicated efficiency significantly decreased, inducing higher CO and HC emissions.

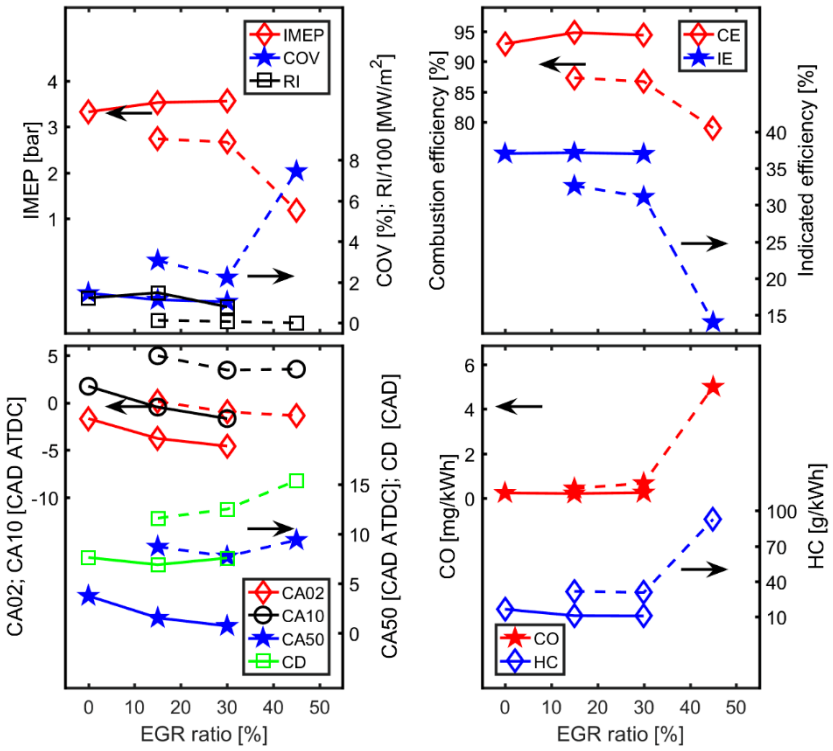

Figure 3.17. Performance, combustion and emissions characteristics of 3 case of intake pressure with lower (Solid line) and higher (Dashed line) EGR

At the highest EGR (50%), the IMEP can reach 1.0 bar, but with a COV increase (7.5%), the combustion phasing is also slightly delayed, with a combustion duration of 15 CAD. Hence, the combustion and indicated efficiency become very low (80% and 14%). With minimum of EGR, at a given ringing intensity of 1 MW/m^2, the influence of the intake pressure to IMEP is more sensible than EGR, which is promote auto-ignition timing and combustion phasing also.

Hence, the combustion and indicated efficiencies significantly increased then, the CO, HC emissions slightly reduced.

At 35% EGR, which corresponds to the highest intake pressure (1.3 bar), the IMEP reaches 3.8 bar, the highest value, with an advanced combustion timing and phasing (- 2 and 0.5 CAD ATDC), respectively, while combustion duration has no significantly change (around 7.5 CAD).

Correlation between performance, combustion characteristics and emission parameters (Y) and EGR, intake pressure is presented in Eq. 3.15, with coefficients in Table 3.17.

$$Y=a*EGR+b*P+c \qquad \textbf{Eq. 3.15}$$

Table 3.17. Coefficients for Eq. 3.15. EGR in %, P in bar

	Coef.					**Coef.**			
	a	b	c	R^2		A	B	c	R^2
CA10	0.41	-55.0	55.9	0.956	IE	-0.70	58.6	-0.185	0.862
CA50	0.64	-78.2	80.59	0.956	RI	-13.27	1429.0	-1293.0	0.939
IMEP	-0.09	9.09	-5.43	0.916	CO	$60*10^{-6}$	-0.03	0.027	0.829
CE	-0.87	93.13	2.62	0.937	HC	2.46	-243.4	248.5	0.846

Several features impact of EGR and intake pressure for PRF80 HCCI mode:

-Simultaneous of EGR and intake pressure can be used to control the auto-ignition timing (CA10), combustion phasing (CA50), with high confidence correlation.

- EGR addition reduces CE and IE and has no significant benefit for extending the high-load limit.

Adjusted coefficients for impact of EGR and P to the Eq. 3.6, the correlation is shown in Eq. 3.16, with coefficients in Table 3.18.

$$IMEP=a*LHV+b*EGR+c*P+d \qquad \textbf{Eq. 3.16}$$

Table 3.18. Coefficients for Eq. 3.16. LHV in Joule, EGR in %, P in bar

	Coef.				
	a	b	c	d	R^2
IMEP	0.033	-0.024	5.45	-5.96	0.923

The influence of energy content on IMEP in this case, at fixed equivalence ratio, with higher R^2, cannot explain EGR impact on IMEP of HCCI mode.

*) Controlling combustion phasing

The performance and combustion characteristics are plotted as a function of the combustion phasing in Figure 3.18. Under lower EGR ratio, the IMEP, combustion and indicated efficiencies are well optimized with the optimized combustion phasing. But, under higher EGR, the combustion phasing is too retarded from 8 to 10 CAD ATDC.

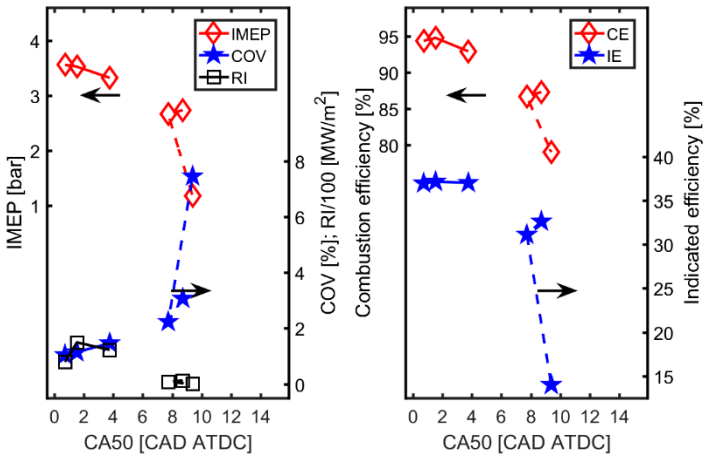

Figure 3.18. The performance and combustion parameters as a function of combustion phasing under the various intake pressure with lower (Solid line) and higher (Dashed line) EGR

The performance and combustion characteristics are directly correlated to the combustion phasing, in Eq. 3.8 with the coefficients in Table 3.19.

Table 3.19. Coefficients for Eq. 3.8. CA50 in CAD ATDC

	Coef.		
	A	b	R^2
IMEP	-0.161	3.80	0.735
RI	-14.40	125.8	0.637
CE	-1.336	96.83	0.826
IE	-1.299	39.97	0.534

The influence of EGR and intake pressure on performance and efficiencies of HCCI mode through combustion phasing (CA50) is related to the combustion phasing advanced which leads the higher IMEP, CE and IE, but higher RI level.

3.2.5. Conclusions

HCCI combustion experiments of PRF80 fuel were performed under wide range of intake temperature and equivalence ratio, some cases of intake pressure sweep and wide range of

EGR, in order to remind the sensitivity of these different input parameters to optimize and to control HCCI combustion. The main tendencies are summarized as follows:

- The pre-heated intake temperature strongly impacts the Low Temperature Reaction stage of HCCI combustion mode for gasoline-like (PRF80) fuel and the intake pressure enhances it.

- Reducing the intake temperature, or more correctly the in-cylinder temperature before TDC can able to improve the combustion efficiency and the EGR ratio and intake pressure could control combustion phasing and extend the IMEP range.

- Increasing the equivalence ratio increases the combustion efficiency mainly because more complete combustion is done with higher combustion temperature. The retarded combustion phasing is one of most important factors affecting indicated efficiency.

- The optimization combustion phasing is about 4 to 6 CAD ATDC to reach 4 to 5 bar IMEP with acceptable Ringing intensity, which can be able to be controlled by equivalence ratio, intake pressure and EGR ratio while intake temperature was given 30 to 50^{o}C, as a little pre-heater.

3.3. Effect of Ethanol, Butanol and ABE blend on combustion characteristics

In this section, the different blends: ethanol, butanol and ABE mixture with PRF80, as the base fuel, are evaluated in HCCI mode under 1500 rpm engine speed condition. Each bio-fuel has different oxidation paths. This section is separated to two main parts: (1) ethanol blend with various equivalence ratio and intake temperature to reach stable combustion; (2) the comparison between Butanol and ABE blend with Ethanol blend.

3.3.1. Ethanol blend fuel

3.3.1.1. HCCI combustion characteristics for Ethanol/PRF80 blend

With a RON of 98, HCCI ethanol combustion is difficult to achieve without intake heating and/or boosting, therefore the maximum content of ethanol in the blend has been limited to 60% in volume. HCCI mode experiments were conducted at an intake temperature of 150^{o}C with various fuel mass per cycle. In Table 3.20, the range of equivalence ratio conditions which guarantees stable combustion, i.e. between the misfire and the ringing limits, is given.

Table 3.20. Experimental conditions - 1500 rpm

N₀ Case	Fuel	ER Variation
1	PRF80	0.28, 0.30, 0.33, 0.35, 0.36
2	Et20	0.52, 0.54, 0.56, 0.57
3	Et40	0.46, 0.49, 0.51, 0.53
4	Et60	0.44, 0.45, 0.47, 0.48, 0.49

Figure 3.19 presents the evolution of the in-cylinder pressure and the heat release rate for all fuel blends under an intake temperature of 150°C and atmospheric intake pressure. The equivalence ratio is varied to guarantee the combustion and acceptable Ringing intensity.

As expected, the increase of Ethanol ratio on PRF80 fuel delays the combustion phasing, with ignition timing after TDC for all blends which content ethanol, in contrast to pure PRF80, even while the mixture is rich.

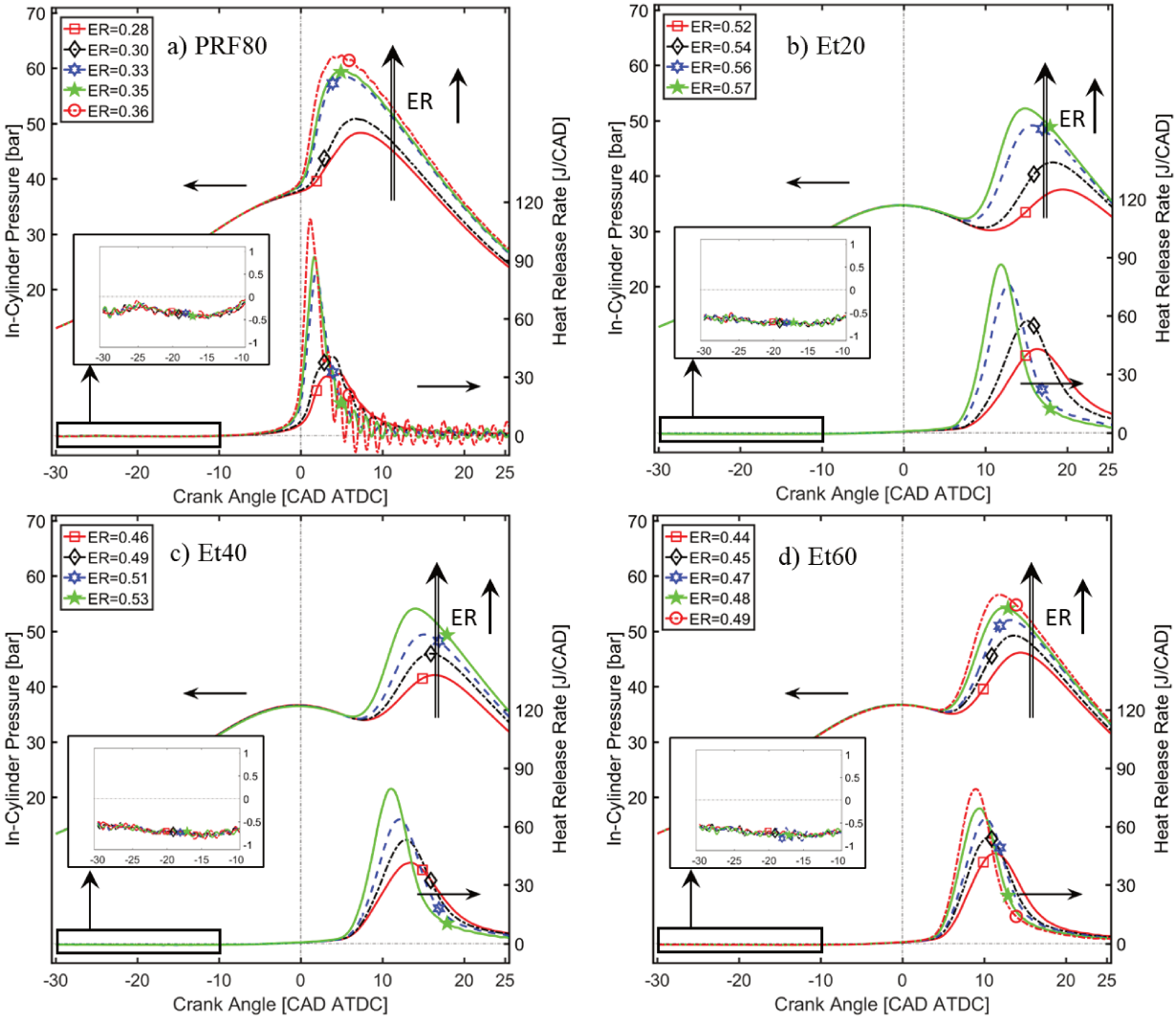

Figure 3.19. In-cylinder pressure and Heat release rate presented as a functions of equivalence ratio for PRF80 and Et20/Et40/Et60 blend fuel

For all fuels, the HRR curves show a single-stage heat release, as previously observed for PRF80 under high intake temperature of 150ºC, accentuated by the addition of ethanol, which is an inhibitor of low temperature reactions [134–136] for all equivalence ratio. The comparison for all blends is highlighted in Figure 3.20 where only the in-cylinder pressure trace and HRR are plotted for the minimum and maximum equivalence ratio. Due to the combustion phasing for PRF80 fuel, at maximum ER, the pressure waves are distinguishable due to the ringing limit. It is interesting to notice that the ignition timing is advanced for Et60, which is the lowest reactive blend, to reach maximum ringing intensity limit despite the lowest equivalence ratio (about 0.49). Under maximum equivalence ratio, the peak of HRR for PRF80 is the highest (110 J/CAD) and similar for the blend fuels (around 70-75 J/CAD). Under minimum equivalence ratio, all HRR peaks are about 30-40 J/CAD.

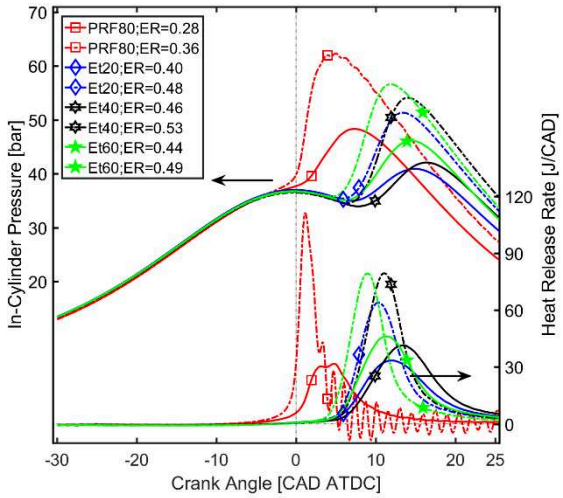

Figure 3.20. In-cylinder pressure and Heat release rate for PRF80 and Et20/Et40/Et60 blends with maximum and minimum equivalence ratio

Figure 3.21 illustrates the performance, combustion process and emissions for all ethanol blends as a function of the equivalence ratio. As it can be seen in Figure 3.20 and Figure 3.21, the low reactivity gasoline-like blends with high ethanol fraction affects significantly the combustion and the performance. The IMEP increases linearly with the equivalence ratio, as the fuel mass per cycle, for each fuel, with a continuity as a function of ethanol content. The IMEP for all ethanol blend fuels (PRF80, Et20, Et40 and Et60) were modeled as a linear function of energy content, as low heat value per cycle (LHV, in Joule/cycle), in Eq. 3.6, with the coefficients in Table 3.22. But the trend of COV or RI depends on the blend fuel. The RI increases with the equivalence ratio increase, hence RI of PRF80 fuel seems increase faster than for ethanol blends. The combustion efficiency is better for PRF80 fuel than ethanol blend

but as due to the important heat loss due to the combustion near TDC, as discussed previously, the indicated efficiency is not lower than other ethanol blends. At the maximum possible IMEP (about 4.8 bar), the indicated thermal efficiency for ethanol blend is nearly 38% versus 36% for PRF80. Because of lower reactivity of ethanol, hence the later combustion timing and combustion phasing, no less than 3 bar of IMEP can be reached with the lowest possible equivalence ratio for stable combustion. The indicated thermal efficiency is deteriorated with increase of ethanol fraction in the blend fuels in this case. The delay of the combustion can explain the higher CO and HC emissions of ethanol blends compared to PRF80 fuel. It has to be noted that even if the maximum equivalence ratio for Et60 is lower than the maximum for Et40, inducing as shown in Figure 3.20 and Figure 3.21, advanced auto-ignition timing and combustion phasing (approximately 7.5 and 9.5 CAD ATDC, respectively). The reason can be from fuel chemical kinetics of ethanol has consistently higher reactivity than Iso-octane under some engine-relevant conditions [137,138], which provides the Et60 blend to promote auto-ignition behavior.

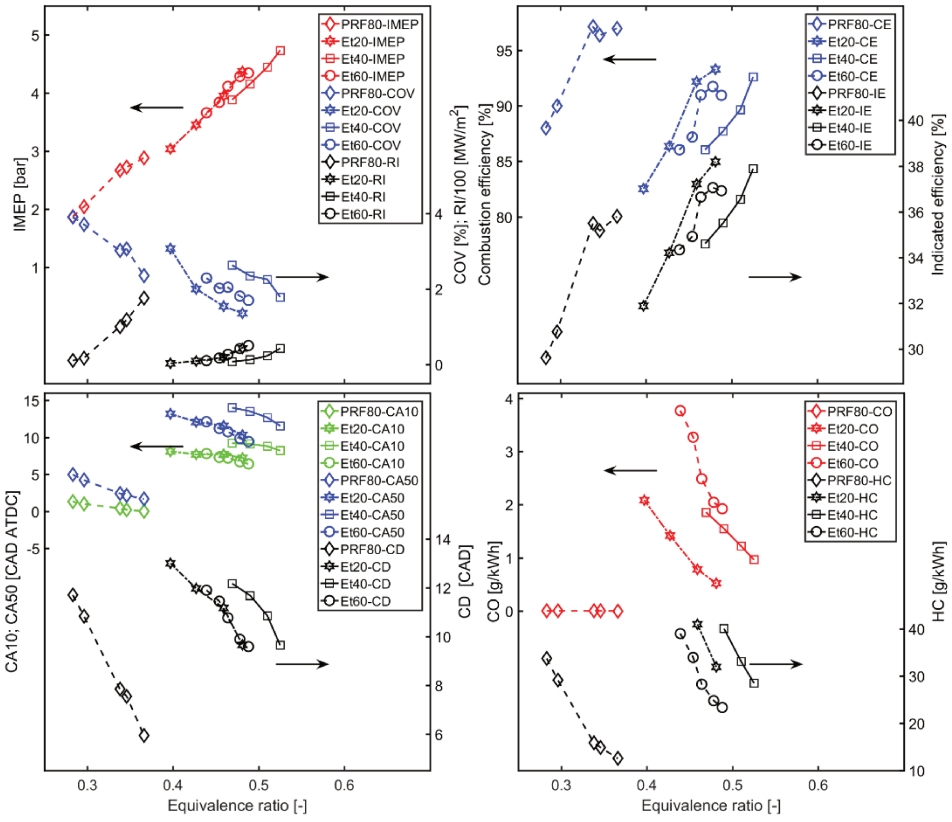

Figure 3.21. Performance, combustion process and emission as a function of equivalence ratio of PRF80 and Ethanol blend

Correlation between performance, combustion characteristics and emissions parameters (Y)

and equivalence ratio (X) are shown in Eq. 3.9, the coefficients in Table 3.21.

Table 3.21. Coefficients for Eq. 3.9, Ethanol blends

	Coef.	Fuel			
		PRF80	**Et20**	**Et40**	**Et60**
CA10	a	-15.64	-70.69	-12.52	-34.84
	b	5.70	49.17	15.05	23.35
	R^2	0.991	0.778	0.768	0.876
CA50	a	-40.40	-134.5	-37.30	-65.18
	b	16.27	88.38	31.50	41.09
	R^2	0.986	0.826	0.937	0.904
CD	a	-68.92	-93.00	-39.46	-52.62
	b	31.23	61.49	30.76	35.25
	R^2	0.998	0.905	0.940	0.961
IMEP	a	12.80	16.94	14.56	14.40
	b	-1.73	-4.66	-2.95	-2.65
	R^2	0.986	0.957	0.984	0.905
CE	a	106.15	163.19	94.65	95.30
	b	49.07	-8.30	32.24	35.27
	R^2	0.913	0.926	0.904	0.565
IE	a	81.4	70.4	54.0	56.6
	b	6.8	-0.9	9.2	9.6
	R^2	0.938	0.956	0.933	0.636
RI	a	1984.2	1279.0	497.6	857.7
	b	-561.7	-674.1	-226.2	-370.2
	R^2	0.979	0.862	0.863	0.967
CO	a	-0.008	-7.62	-21.14	-39.66
	b	0.003	4.68	11.97	21.18
	R^2	0.978	0.794	0.909	0.862
HC	a	-268.8	-273.3	-314.7	-332.9
	b	108.8	180.5	193.7	184.9
	R^2	0.971	0.860	0.991	0.861

Several features can be attributed HCCI mode were identified for Ethanol blends, under 150^{o}C intake temperature, 1 bar pressure and without EGR conditions:

- The ignition timing (CA10) and combustion phasing (CA50) are strongly controlled by the equivalence ratio for all test blend fuels, the most sensitivity for Et20 blend fuel.

- The IMEP, RI are increase at rich mixture conditions. RI of Et40 and Et60 is less sensitivity

of equivalence ratio.

- The combustion efficiency and indicated efficiency are increasing at rich mixture conditions for all test fuel. The Et20 has combustion efficiency most sensitivity on equivalence ratio.

- The HC and CO emissions are increasing at rich mixture for all fuel test. The CO emission for ethanol blends (Et20, Et40 and Et60) is strongly sensitivity with equivalence ratio.

The correlation between IMEP and energy content is presented in Eq. 3.6, the coefficients for Ethanol blends is shown in Table 3.33. The Et20 has most sensitivity of IMEP as a function of energy content.

Table 3.22. Coefficients for Eq. 3.6, Ethanol blends

	Coef.	**Fuel**			
		PRF80	**Et20**	**Et40**	**Et60**
IMEP	a	0.012	0.015	0.013	0.013
	b	-1.942	-4.33	-3.24	-3.09
	R^2	0.991	0.978	0.984	0.912

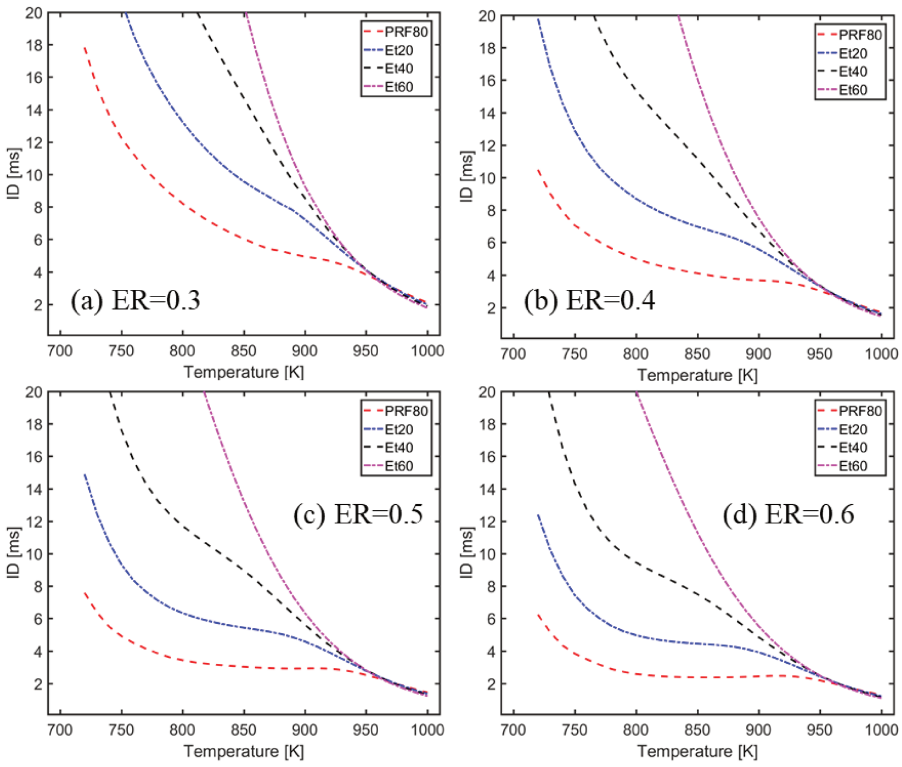

Figure 3.22. Ignition delays of Ethanol blends-air mixture homogeneous under variation of ambient temperature with ambient pressure of 40 bar and four equivalence ratio of a) 0.3, b) 0.4, c) 0.5 and d) 0.6

Figure 3.22 shows a comparison of calculated ignition delays versus the initial temperature for

ethanol blends and PRF80 under homogeneous condition for four equivalence ratios (0.3, 0.4, 0.5 and 0.6) at 40 bar initial pressure. As in engine experiments, the ethanol addition significantly increases the ignition delays and decreases the blends reactivity at this initial pressure of 40 bar. The NTC exists for PRF80 fuel at all equivalence ratio but longer as a function of the equivalence ratio increase. It can be seen also for some ethanol blends, especially for lower contents of ethanol but it does not occur for Et60 even at the highest equivalence ratio. Therefore, for Et60 there is no plateau zone: the ignition delay continuously decreases with the temperature increase for all equivalence ratio.

Figure 3.23 highlights this behavior for higher initial temperature, from 950 to 1000 K. In this range of temperature, for all equivalence ratio, the addition of ethanol fraction promotes the ignition with shorter ignition delay time, as previously assuming from HCCI results.

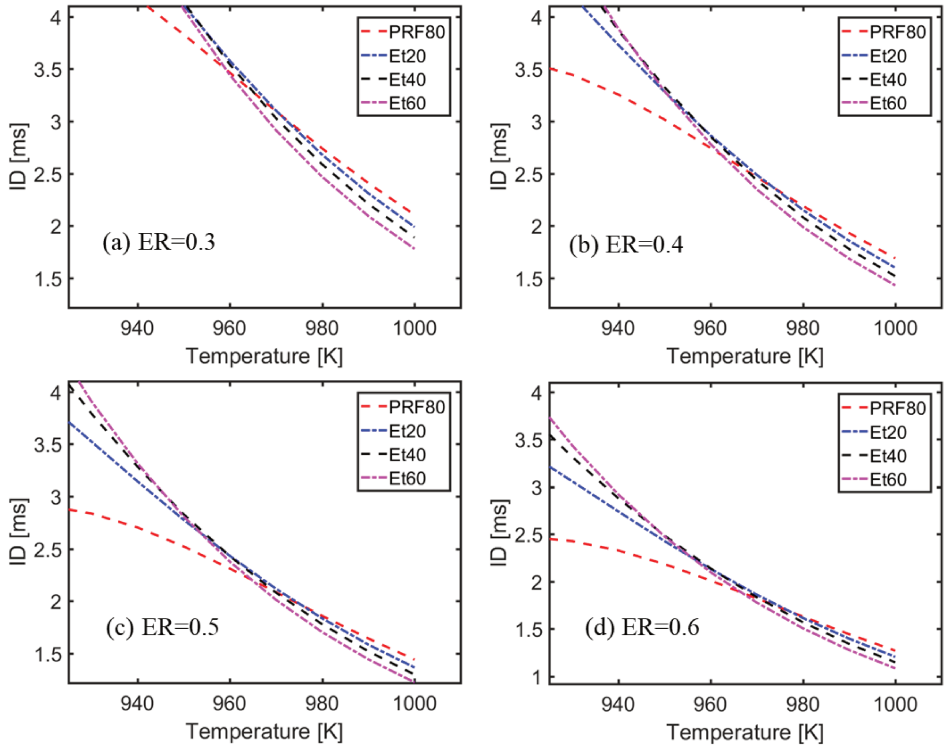

Figure 3.23. Scaled Ignition delays of Ethanol blends-air mixture homogeneous

**) Controlling combustion phasing*

The relationship between the engine performance and the combustion phasing is presented in Figure 3.24. Under operating conditions, IMEP decreases linearly with the combustion phasing, delayed with ethanol content. Et40 allows higher load than both Et20 and Et60, which have similar IMEP range. This is also observable by considering the combustion and indicated

efficiencies.

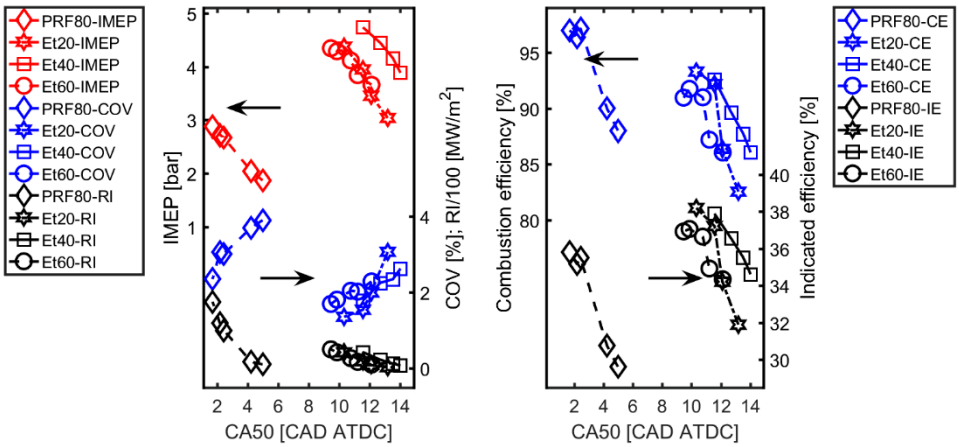

Figure 3.24. The operating and combustion parameters as a function of combustion phasing under the various equivalence ratio. (reproduction of data from Figure 3.21)

The correlation between operating, combustion parameters and combustion phasing is shown in Eq. 3.8, with coefficients in Table 3.23.

Table 3.23. Coefficient for Eq. 3.8. CA50 in CAD ATDC.

	Coef.	Fuel			
		PRF80	**Et20**	**Et40**	**Et60**
IMEP	a	-0.316	-0.111	-0.371	-0.211
	b	3.42	6.24	9.09	6.32
	R^2	0.997	0.894	0.948	0.914
RI	a	-47.60	-9.15	-13.66	-12.34
	b	232.5	160.9	198.1	161.5
	R^2	0.932	0.965	0.965	0.940
CE	a	-2.676	-1.087	-2.455	-1.533
	b	91.96	97.07	111.1	96.12
	R^2	0.960	0.900	0.903	0.886
IE	a	-2.039	-0.455	-1.391	-0.897
	b	39.70	44.29	54.06	45.57
	R^2	0.975	0.873	0.918	0.859

As expected, the performances of HCCI mode is strongly correlated with the CA50. For Et40 blend, higher ethanol fraction compared to Et20 but CA50 are more strongly impact on the performances and efficiencies, which is similar to PRF80 fuel.

3.3.1.2. Global operating range for PRF80 and Ethanol blend

The effect of ethanol fraction of IMEP map as a function of the intake temperature and

equivalence ratio from atmospheric to slightly boosted intake pressures can be seen in Figure 3.25. The lower reactivity of ethanol induces the need of higher intake temperature to guarantee stable HCCI combustion mode. Therefore, the range of possible operating conditions is strongly reduced and the intake pressure has to be increased until 1.2 and 1.55 bar, to reach stable combustion to run with lower intake temperatures than 150°C and 130°C respectively for more than 20% in the blend.

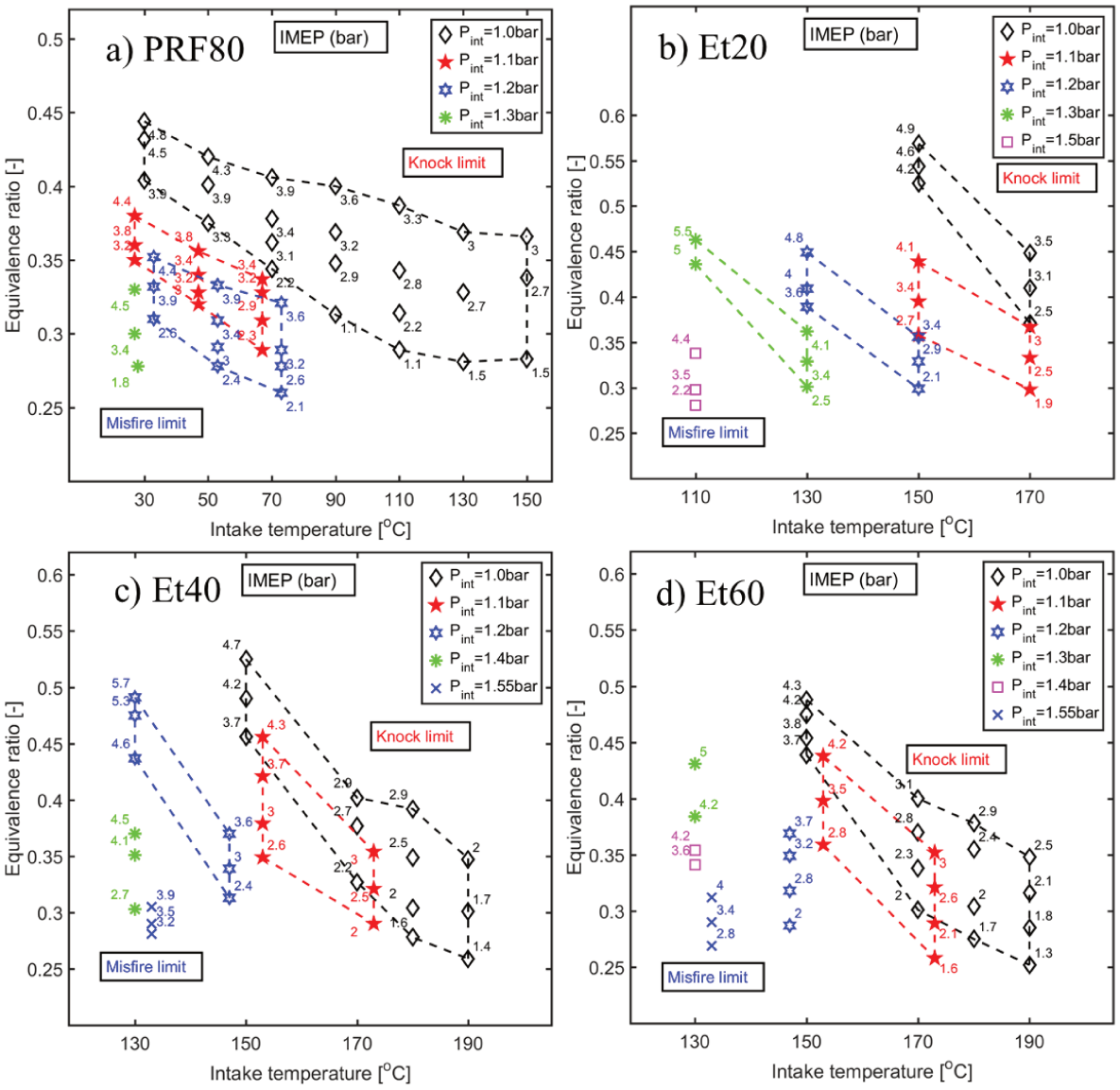

Figure 3.25. IMEP range of HCCI mode based on intake temperature – equivalence ratio for a) PRF80, b) Et20, c) Et40 and d) Et60

To emphasize the role of ethanol addition in the auto-ignition behavior, the iso-contour of computed ignition delays with the engine thermodynamic trajectories are plotted in Figure 3.26 at the equivalence ratio of 0.4. As a function of the increase of ethanol, the ignition delay

contours are less and less vertical in the pressure-temperature domain of LTC, but the auto-ignition iso-contours become a linear line, with a negative slope indicating how the ethanol content affects the ignition delay dependency on temperature and pressure. It is clear that the influence of ethanol fraction significantly inhibits the LTC region but also prevents the ignition for low initial temperature: for high ethanol contents, the p-T trace never meets auto-ignition contours corresponding to ignition delays below 8 ms.

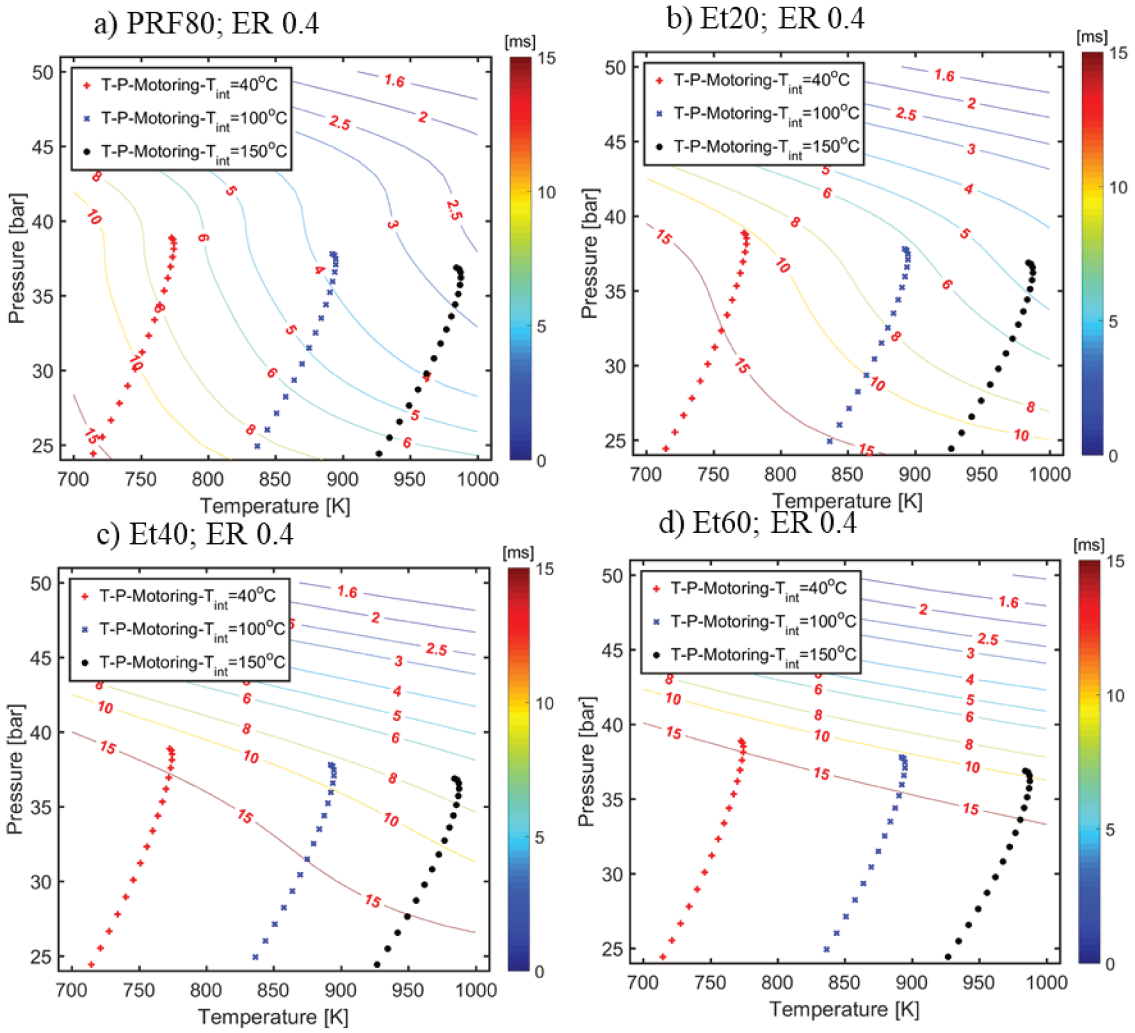

Figure 3.26. Iso-contours of ignition delay for PRF80 and Ethanol blends under wide-range temperature and pressure with equivalence ratio of 0.4

3.3.1.3. Evolution of intake temperature effect on combustion process

As the intake temperature is varied in order to achieve combustion process closer to the TDC, its effect is evaluated to reach HCCI acceptable conditions, it means between RI and misfire limits, represented as the equivalence ratio. These equivalence ratio limits are indicated as a

function of the temperature for an atmospheric intake pressure in Table 3.24.

Table 3.24. Experiment conditions for evolution of intake temperature effect on HCCI mode for Ethanol blend fuel

N_o Case	**Fuel**	**Intake temperature [^oC]**	**Equivalence ratio**	
			ER_{min}	**ER_{max}**
1	PRF80	30	0.40	0.45
2		150	0.28	0.36
3	Et20	150	0.52	0.57
4		170	0.37	0.45
5	Et40	150	0.46	0.53
6		170	0.33	0.40
7		190	0.26	0.35
8	Et60	150	0.44	0.49
9		170	0.30	0.40
10		190	0.25	0.35

Figure 3.27 presents the in-cylinder pressure and HRR obtained for ethanol blend on comparison with PRF80 fuel, under the limit conditions. As already discussed, as ethanol blends require higher intake temperature, the ethanol blend exhibits single-stage heat release, without any LTC, as also PRF80 at 150°C. For all ethanol blending with base fuel (PRF80), increase intake temperature condition, the HRR peaks advanced to close the TDC in spite of decreasing the equivalence ratio to avoid the excessive Ringing intensity. The HRR peaks of Et40 and Et60 blends under both limitations are closer TDC than Et20 at higher intake temperature (170°C). It can again confirm the role of the Ethanol fraction on the blend with PRF80, to promote auto-ignition behavior for large contents of ethanol when the intake temperature is adjusted and therefore increased.

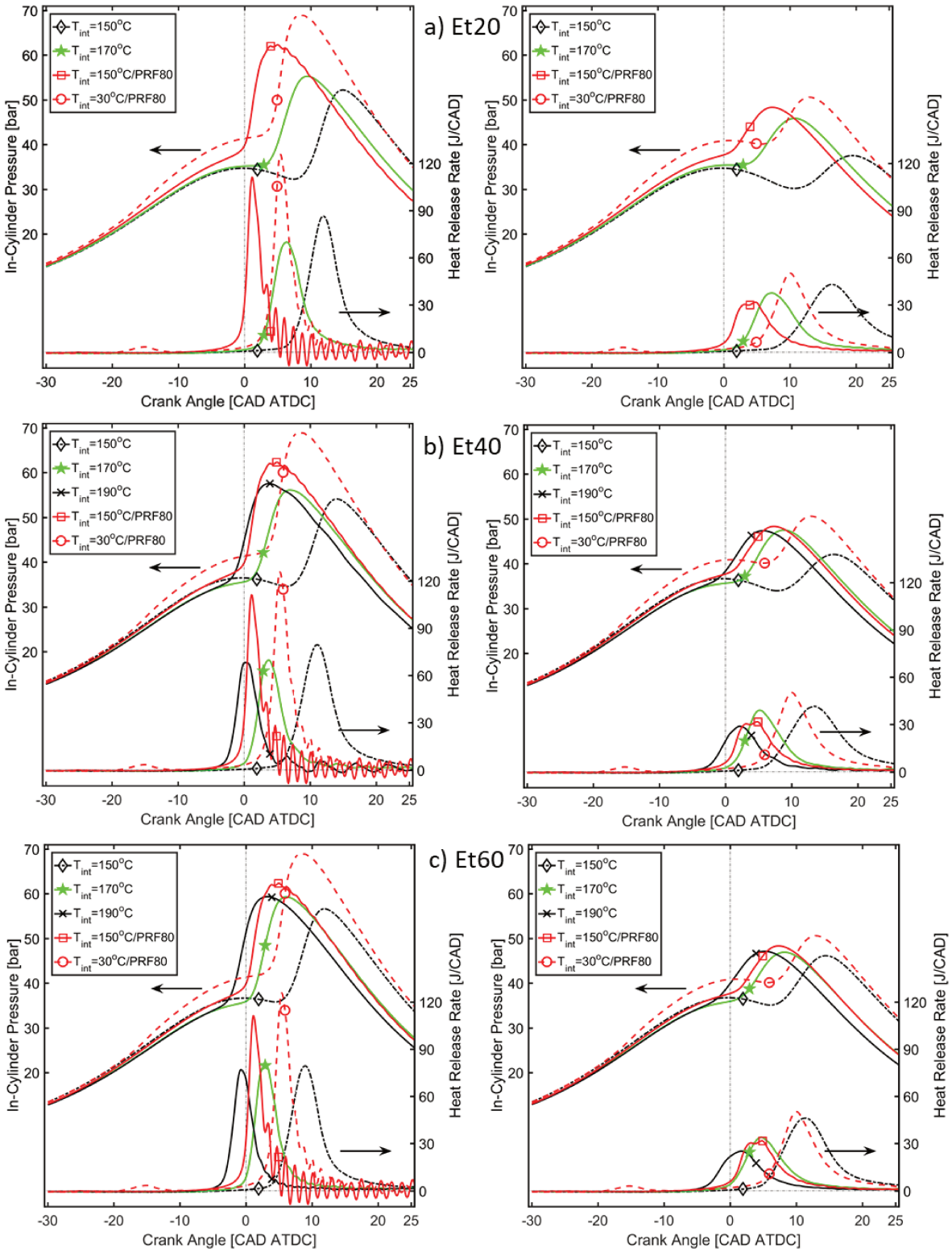

Figure 3.27. In-cylinder pressure and Heat release rate of Ethanol blend on base comparison of PRF80 under Ringing intensity limit (left) and misfire limit (left)

Performance, combustion process and emissions of ethanol blend as a function of temperature

are included in Figure 3.28 a) and b) for maximum and minimum, respectively, equivalence ratio. Under both behaviors, the time period between CA02 and CA10 demonstrates that the single-stage of HRR of Ethanol blend towards the IMEP and auto-ignition timing and combustion phasing are strongly sensitive with intake temperature, more than for PRF80.

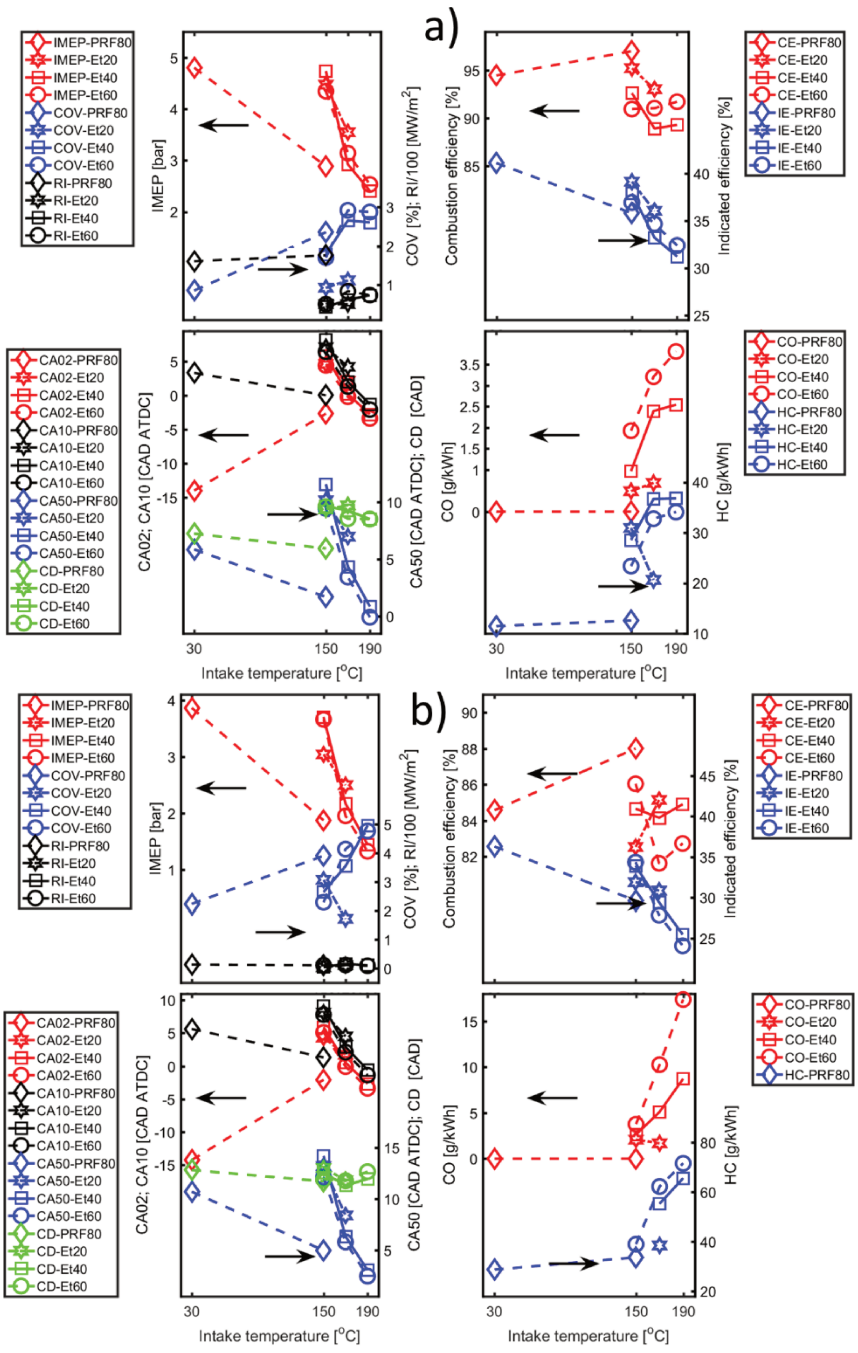

Figure 3.28. Performance, combustion process and emission for Ethanol blend with (a) Maximum ER and (b) Minimum ER limits

The auto-ignition timing and the combustion timing under both limitations tend to advance and

the IMEP tends to decrease with hotter intake temperature. The PRF80 fuel has an IMEP range, from 2.8 to 4.8 bar, more than Ethanol blend. Ethanol blends with more than 20% ethanol volume, provide similar IMEP maximum values. Combustion efficiency of PRF80 fuel is higher than all of Ethanol blends but no significant difference for indicated efficiency. The HC and CO emissions of Et40 and Et60 are higher than PRF80 and tend to increase with higher intake temperature. The reason can be explained from the lower equivalence ratio required to avoid the ringing plays more impact on complete combustion than hotter initial in-cylinder temperature. Especially, the trend of emissions and combustion efficiency is inverse for Et20 blend fuels, the combustion process is the more sensitive to initial temperature.

**) Controlling combustion phasing*

Performance and combustion parameters are plotted as a function of combustion phasing in Figure 3.29 a) and b) for maximum and minimum equivalence ratio limits, respectively.

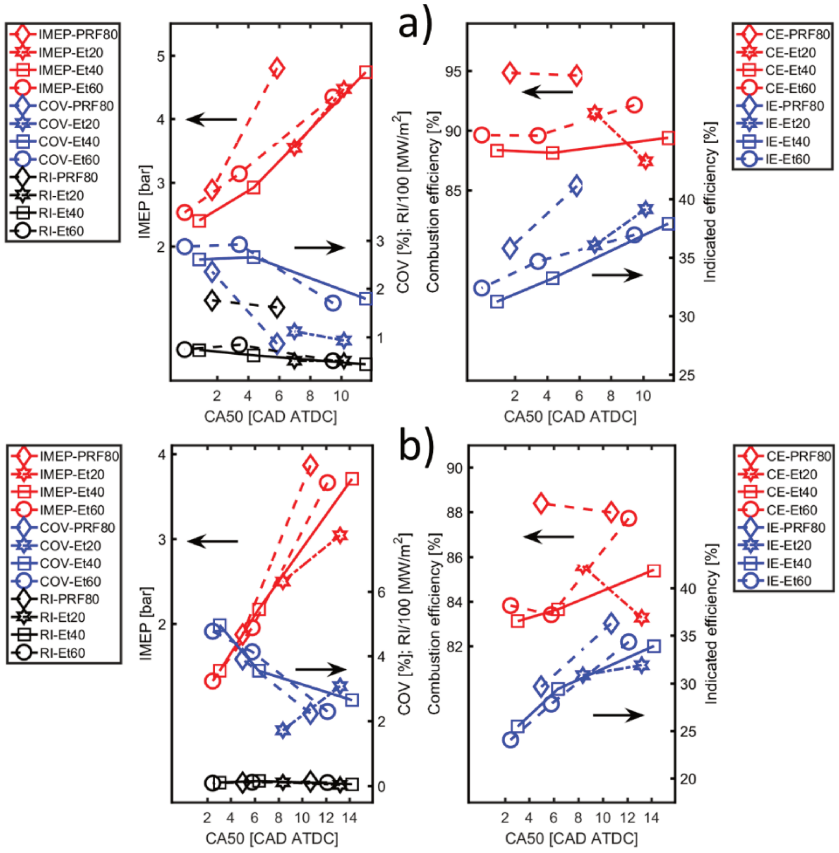

Figure 3.29. Performance and combustion parameters as a function of combustion phasing under (a) Maximum ER to avoid RI and (b) Minimum ER before misfire

A linearly increase of IMEP is obtained when the combustion phasing is delayed from 2 to 10 CAD ATDC, under maximum and minimum equivalence ratio limits for all fuels. Even if the

equivalence ratio value is higher before reach the ringing limit, the combustion efficiency is no significantly changed with the combustion, unless the point of Et20 blend fuel at later combustion phasing. This induces a higher indicated efficiency at later combustion phasing, with a maximum around 38% and 37%, for Et40 and Et60 respectively, while combustion phasing is about of 10 CAD ATDC, but around 35%, in the minimum limit, with a combustion phasing around 12 CAD ATDC.

The performance, combustion process and emissions parameters (Y) were modeled as a linear function of the equivalence ratio (ER) and the intake temperature (T, in ^{o}C). The applicability of Eq. 3.17 was used, the coefficients are listed in Table 3.25. The intake temperature of PRF80 fuel cases is separated from lower temperature (from 50 to 90^{o}C) and higher temperature (from 110 to 150^{o}C), as the coefficients of the empirical correlations differ significantly in Eq. 3.17. The coefficients for intake temperature (b-value) is set with coefficient from results in Table 3.6, and adjustment to each fuel to improve the linear fit.

$$Y=a*ER+b*T+c \qquad \textbf{Eq. 3.17}$$

Table 3.25. Coefficients for Eq. 3.15. T in ^{o}C

	Coef.	Fuel				
		PRF80 - Low T	**PRF80 - High T**	**Et20**	**Et40**	**Et60**
CA10	a	-47.41	-25.48	-15.89	-29.25	-37.33
	b	-0.05	-0.05	-0.40	-0.40	-0.40
	c	26.03	16.44	79.20	82.88	84.35
	R^2	0.781	0.872	0.757	0.741	0.807
CA50	a	-81.46	-60.99	-32.33	-53.00	-66.88
	b	-0.074	-0.074	-0.56	-0.56	-0.56
	c	44.31	34.32	115.72	121.78	124.83
	R^2	0.855	0.865	0.814	0.800	0.855
CD	a	-84.56	-84.81	-89.77	-116.94	-132.88
	b	-0.063	-0.063	-0.63	-0.63	-0.63
	c	47.13	46.00	154.53	163.37	167.26
	R^2	0.892	0.958	0.966	0.889	0.892
IMEP	a	17.32	17.05	8.81	8.72	8.91
	b	-0.01	-0.01	-0.02	-0.02	-0.02
	c	-2.55	-1.92	2.82	2.92	2.90
	R^2	0.905	0.714	0.962	0.962	0.950

CE	a	182.30	216.51	110.63	144.67	165.33
	b	0.071	0.071	0.71	0.71	0.71
	c	2.71	-1.94	-86.10	-98.81	-103.95
	R^2	0.785	0.520	0.990	0.914	0.937
IE	a	108.1	139.1	30.5	41.7	48.3
	b	$2.3*10^{-3}$	$2.3*10^{-3}$	$0.14*10^{-3}$	$0.14*10^{-3}$	$0.14*10^{-3}$
	c	-5.88	-13.9	21.1	15.8	13.9
	R^2	0.809	0.592	0.873	0.919	0.926
RI	a	2351.8	1955.9	1408.5	1874.1	2117.3
	b	2.03	2.03	10.16	10.16	10.16
	c	-919.8	-835.8	-2272.8	-2425.7	-2480.8
	R^2	0.922	0.863	0.970	0.892	0.899
CO	a	-0.012	-0.020	-5.122	-22.018	-45.819
	b	$9.8*10^{-6}$	$9.8*10^{-6}$	$14*10^{-6}$	$14*10^{-6}$	$14*10^{-6}$
	c	0.005	0.008	3.27	11.94	23.13
	R^2	0.629	0.773	0.850	0.763	0.744
HC	a	-780.4	-662.7	-248.3	-413.9	-507.5
	b	-0.082	-0.082	-1.64	-1.64	-1.64
	c	358.0	255.5	409.0	482.1	509.5
	R^2	0.408	0.602	0.820	0.866	0.958

The analyses of the results indicate the following:

- Under various intake temperature condition, the higher ethanol blends are more sensitivity of auto-ignition timing (CA10), combustion phasing (CA50) and combustion duration (CD) as a function of equivalence ratio.

- IE of Ethanol blends is less sensitive to the intake temperature than PRF80.

- HC and CO emissions are more sensitive with higher ethanol ratio on blends.

The linear model for IMEP, based on energy content and intake temperature is presented in Eq. 3.18, with the coefficients in Table 3.26.

$$IMEP=a*LHV+b*T+c \qquad \textbf{Eq. 3.18}$$

Table 3.26. Coefficients for Eq. 3.18, Ethanol blends. IMEP in bar, LHV in Joule/cycle, T in ^oC

	Coef.	Fuel				
		PRF80 - Low T	**PRF80 - High T**	**Et20**	**Et40**	**Et60**
IMEP	a	0.017	0.016	0.011	0.011	0.011
	b	0.01	0.01	0.01	0.01	0.01
	c	-5.53	-4.96	-3.58	-3.50	-3.57
	R^2	0.982	0.900	0.997	0.996	0.996

The ethanol blend fuels have similar trends of effect from energy content and intake temperature.

3.3.1.4. Investigation of influence of EGR and intake pressure for HCCI mode of Ethanol blend

The intake conditions, including the intake temperature and equivalence ratio, are presented in Table 3.27. The intake temperature of 170ºC was used because this condition allows a combustion phasing closer to TDC, about 5 CAD ATDC, and consequently, the influence of EGR ratio and intake pressure can be obviously demonstrated. Based on the considering stable combustion, for each intake pressure, the effect of EGR sweeps were conducted from without EGR until to acceptable COV level.

Table 3.27. Intake conditions

No. Case	**Fuel**	**Intake temperature [ºC]**	**Intake pressure [bar]**	**Equivalence ratio**
1	PRF80	100	1:1.3; with increment of 0.05	0.35
2	Et20	170		0.45
3	Et40	170		0.45
4	Et60	170		0.42

The investigation of EGR and intake pressure effect is presented in Figure 3.30. With an intake pressure of 1 bar, higher EGR can be used for higher ethanol fraction on blend, providing lower IMEP. While increase both intake pressure and EGR, the IMEP map is extended for low IMEP.

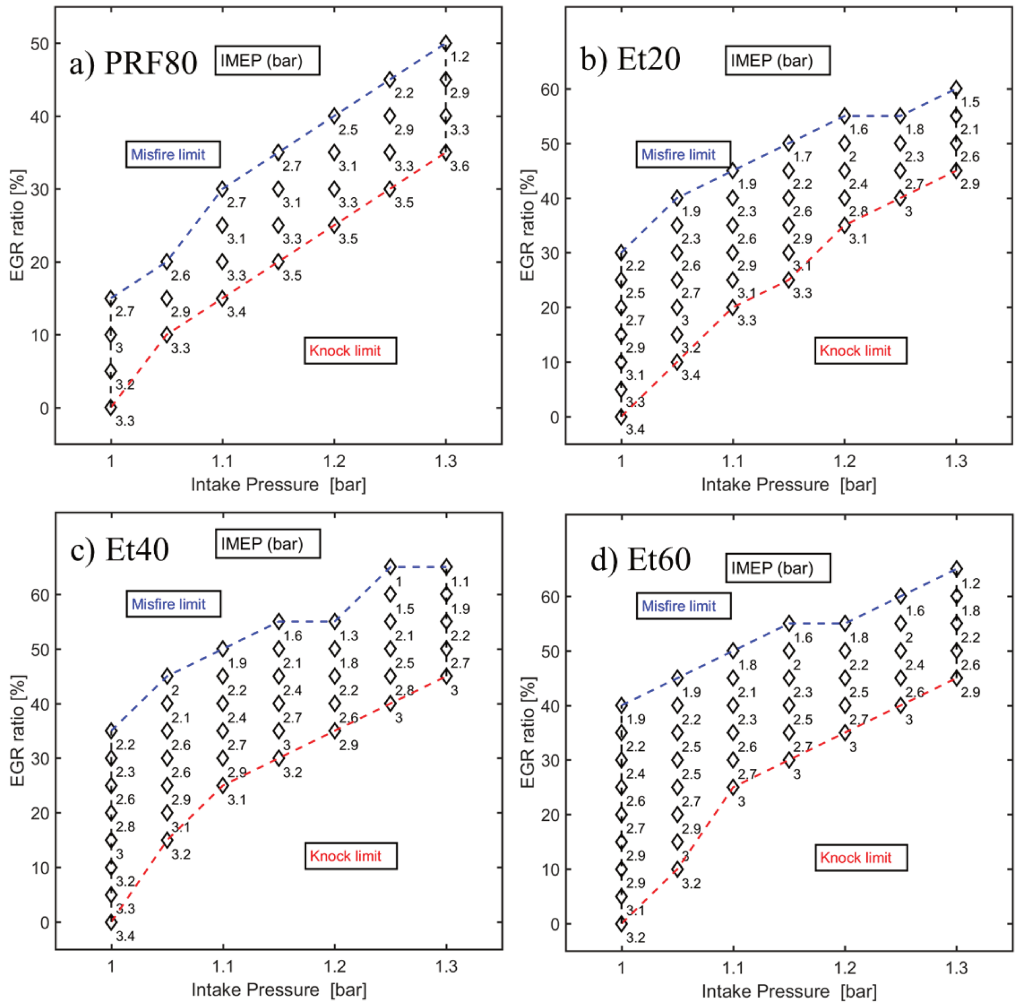

Figure 3.30. IMEP range of HCCI mode based on intake pressure – EGR ratio for a) PRF80 and Ethanol blends: b) Et20, c) Et40 and d) Et60

Figure 3.31 shows the in-cylinder pressure and HRR for PRF80 and Ethanol blends under limitation of EGR, and three intake pressure level of 1.0, 1.15 and 1.3 bar.

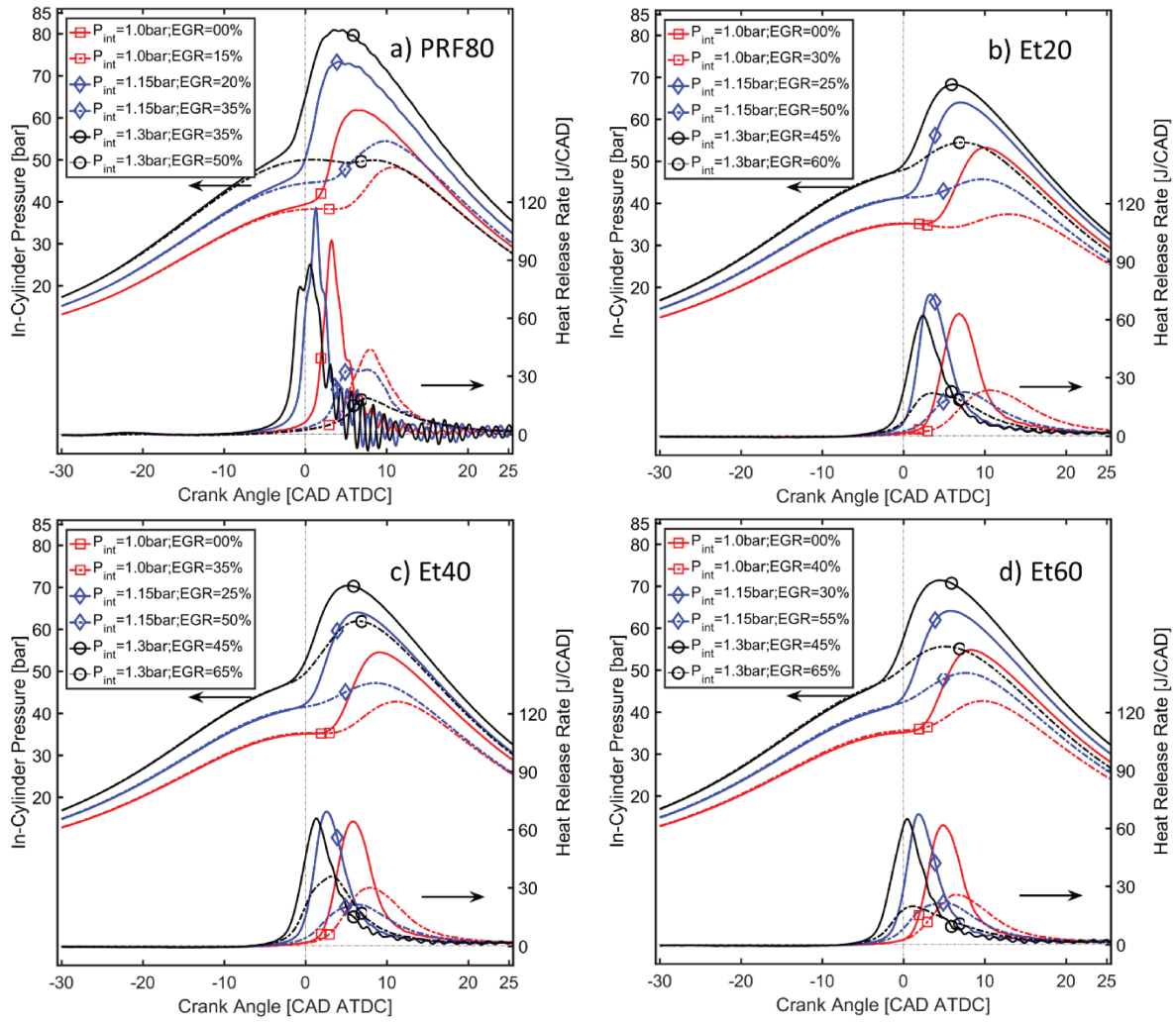

Figure 3.31. In-cylinder pressure and HRR for PRF80 and Ethanol blends under limitation of EGR, and three intake pressure level of 1.0, 1.15 and 1.3 bar

Under naturally aspirated condition and without EGR, the HRR is closer to TDC for PRF80. The increase of intake pressure contributes to advance HRR peak nearer to TDC, and as more as the ethanol content increases. It is clear here that ethanol can extend the operating limits of HCCI combustion if EGR is used with higher intake temperature, as it can observed in Figure 3.32.

The IMEP of Ethanol blend tends to decrease while both EGR ratio and intake pressure are increased, contrary to PRF80. For maximum acceptable EGR before misfire, for each intake pressure, as expected IMEP decreases as EGR increases for all fuels.

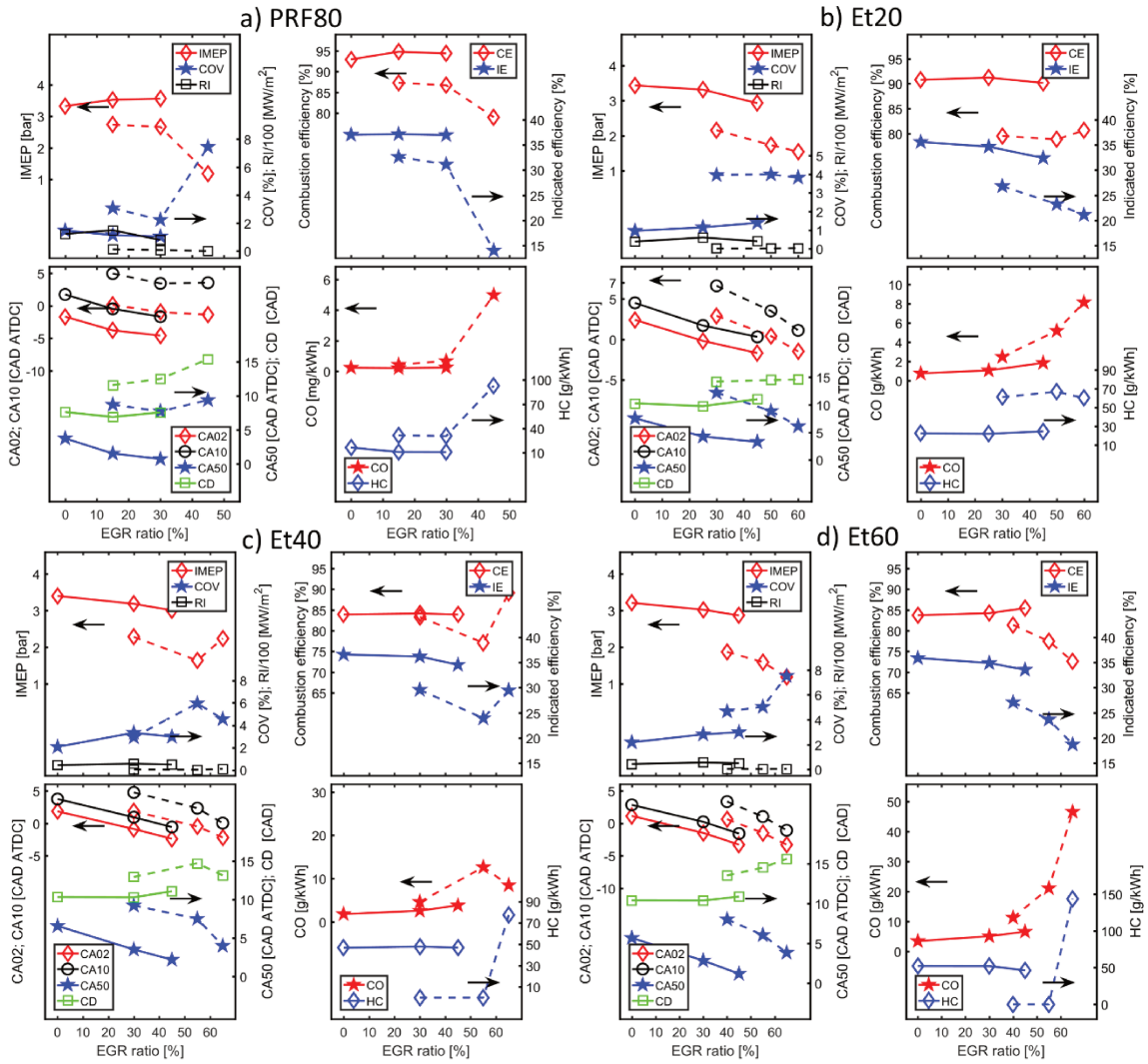

Figure 3.32. Performance, combustion and emission characteristics of of a) PRF80 and Ethanol blends: b) Et20, c) Et40 and d) Et60. Solid line and Dashed line for lower and higher EGR level, respectively

The performance, combustion process and emissions parameters (Y) were modeled as a linear function of the EGR ratio (in %) and the intake pressure (P, in bar). The coefficient (b) for intake pressure is referred in Table 3.17, and adjusted to improve the linear fit.

$$Y=a*EGR+b*P+c \qquad \textbf{Eq. 3.19}$$

Table 3.28. Coefficients for Eq. 3.15, for Ethanol blend fuels

	Coef.	Fuel			
		PRF80	**Et20**	**Et40**	**Et60**
CA10	a	0.408	0.238	0.227	0.216
	b	-55.0	-55.0	-55.0	-55.0
	c	55.90	57.22	55.85	55.00

	Coef.	Fuel			
		PRF80	**Et20**	**Et40**	**Et60**
	R^2	0.956	0.793	0.703	0.618
CA50	a	0.608	0.353	0.361	0.340
	b	-78.2	-78.2	-78.2	-78.2
	c	80.41	82.53	80.14	79.37
	R^2	0.863	0.739	0.723	0.632
IMEP	a	-0.09	-0.077	-0.077	-0.071
	b	9.09	9.09	9.09	9.09
	c	-5.43	-5.04	-4.92	-5.17
	R^2	0.916	0.938	0.875	0.870
RI	a	-13.27	-8.19	-7.98	-7.84
	b	1429.0	1429.0	1429.0	1429.0
	c	-1293.0	-1314.9	-1297.6	-1296.9
	R^2	0.939	0.758	0.715	0.677
CE	a	-0.873	-0.657	-4.72	-4.75
	b	93.13	93.13	931.3	931.3
	c	2.62	3.10	-788.2	790.9
	R^2	0.937	0.933	0.563	0.552
IE	a	-0.684	-0.519	-0.54	0.49
	b	58.6	58.6	58.6	58.6
	c	-18.5	-18.2	-15.5	-17.1
	R^2	0.862	0.930	0.833	0.849
CO	a	0.027	0.090	0.266	0.362
	b	-0.03	-0.03	-0.03	-0.03
	c	0.029	-0.58	-3.41	3.35
	R^2	0.829	0.604	0.463	0.534
HC	a	1.496	12.46	12.34	11.44
	b	-243.4	-2434.0	-2434.0	-2434.0
	c	250.7	2332.5	2325.8	2330.0
	R^2	0.745	0.661	0.550	0.546

Some general trends, with regard to Ethanol HCCI mode, were identified for impact of EGR and intake pressure:

- The three ethanol blends induce less sensitivity of the auto-ignition timing (CA10) and the combustion timing (CA50) to EGR ratio.

- The combustion efficiency and HC emission for Et40 and Et60 fuel are more affected by the

intake temperature than PRF80 and Et20. However, the CO emission of Et40 and Et60 is more sensitive to EGR.

- The CE of Et40 and Et60 is more affected by the intake pressure.

**) Controlling combustion phasing*

The performance and combustion parameters as a function of combustion phasing are shown in Figure 3.33.

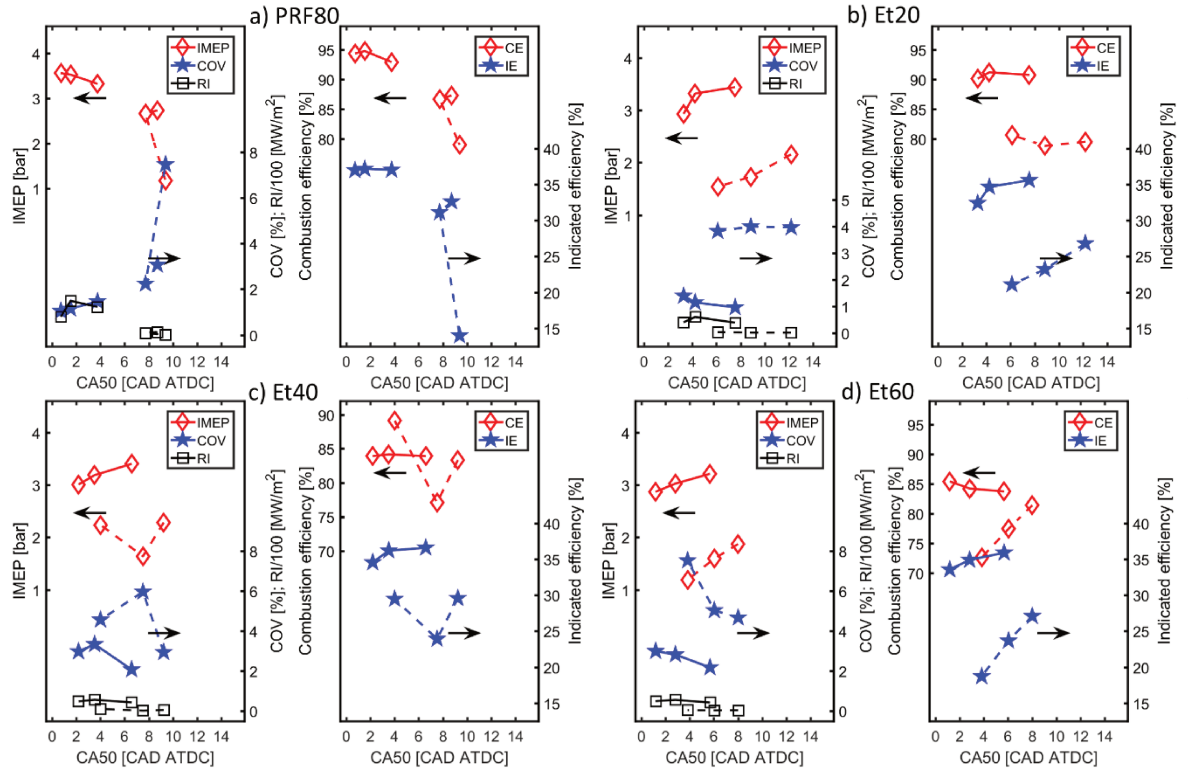

Figure 3.33. The performance and combution parameters as a function of combustion phasing of a) PRF80 and Ethanol blends: b) Et20, c) Et40 and d) Et60. Solid line and Dashed line for lower and higher EGR level, respectively. (reproduction of data from Figure 3.32)

Under both lower and higher EGR level to reach stable combustion, the retarded combustion phasing actually allows the higher IMEP and higher indicated efficiency. The higher EGR can be able to decrease the engine load to about 1.5 bar of IMEP.

Under lower EGR and adjusted intake pressure to reach maximum RI, the PRF80 fuel have more complete combustion than Ethanol blends, despite the initial temperature lowest. Besides for ethanol blend fuel, the large proportions of ethanol addition actually accelerate the progress of the advanced combustion phasing, although the Et20 fuel has highest combustion efficiency.

3.3.1.5. Conclusions

The addition of ethanol in gasoline type fuel requires higher intake temperature and/or pressure to establish the stable combustion in HCCI mode. No LTC phase was found when ethanol is added as suggested by the auto-ignition delay estimated by kinetics model as a function of the temperature and pressure. Hence, the combustion phasing of ethanol blend has the higher sensitivity to the changes of intake temperature. Under high intake temperature (more than 150°C) and naturally aspirated condition, the ethanol fraction can promote the auto-ignition behavior, as found in simulation and experiment results: a small quantity of ethanol, with increasing the ethanol fraction from 0 to 20% in volume, leads to a significant rise in the auto-ignition timing, but from 20 to 60%, the auto-ignition timing is slightly advanced. The combustion efficiency decreases with the amount of ethanol in the blend, inducing higher CO and HC emissions. The addition of ethanol allows the use of higher EGR to extend the IMEP range in low load.

3.3.2. Butanol and ABE blends

3.3.2.1. Comparison between Ethanol, Butanol and ABE blend in HCCI mode

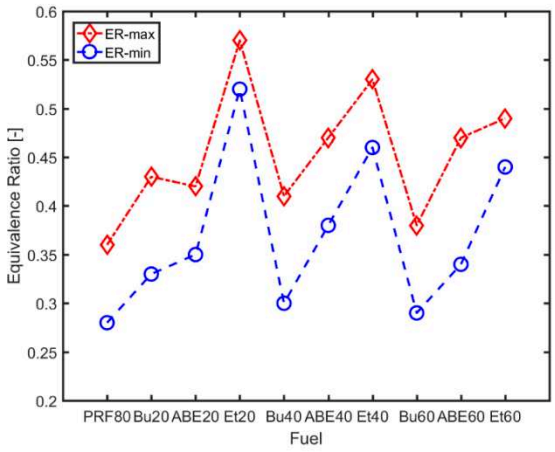

Figure 3.34. Equivalence ratio limits for all blends

In this section, in order to compare the reactivity between Ethanol, Butanol and ABE blend in PRF80 in the case of HCCI combustion mode, under stable operating conditions at ringing and misfire limits, different amounts of these fuels, 0, 20, 40 and 60% in volume were considered, under 1 bar and 150°C of intake conditions. The two equivalence ratio limits obtained for each blend are listed in Figure 3.34. First it can be noted that for Ethanol and Butanol blend, the

minimum and maximum equivalence ratios decrease as a function of the volume fraction in the blend, but for ABE the effect is not monotone (first an increase then a decrease). Only Bu60 reaches similar values than PRF80.

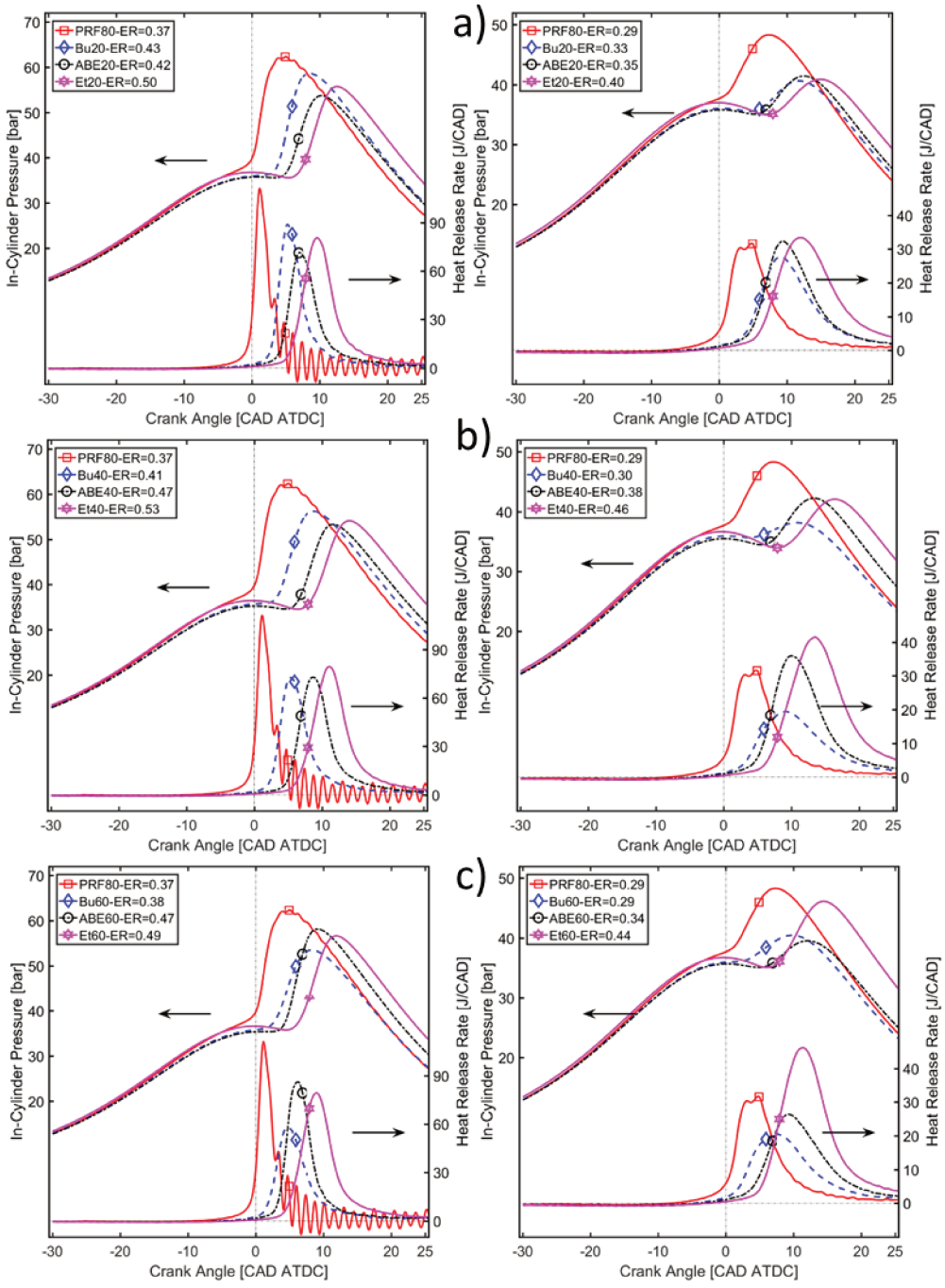

Figure 3.35. In-cylinder pressure and Heat release rate of (a) Bu/ABE/Et20; (b) Bu/ABE/Et40; (c) Bu/ABE/Et60 with maximum equivalence ratio (left) and minimum equivalence ratio (right) limits. Results without blend are added. P_{in}=1bar, T_{in}=150°C

Figure 3.35 a), b) and c) presents the comparison of the in-cylinder pressures and heat release

rate obtained for Ethanol, Butanol and ABE blend with volume fraction of 20%, 40% and 60%, respectively for the equivalence ratio limit to reach ringing (left column) or misfire (right column). As shown Figure 3.35 a), for both equivalence ratio limits to guarantee stable HCCI combustion mode, the combustion phasing for the blends with 20% alcohols is delayed in comparison to PRF80 and ranked as PRF80 < Bu20 < ABE20 < Et20, inversely to the equivalence ratios limits rank. For the misfire limit, the HRR curves of Bu20 and ABE20 are quite similar, the HRR curves for all Butanol blends have lower peak than other fuels and ethanol the most delayed combustion process.

The comparisons of start of combustion and combustion phasing as a function of PFR80 content in the blends under minimum/maximum equivalence ratio limits are presented in Figure 3.36 (left) and (right), respectively.

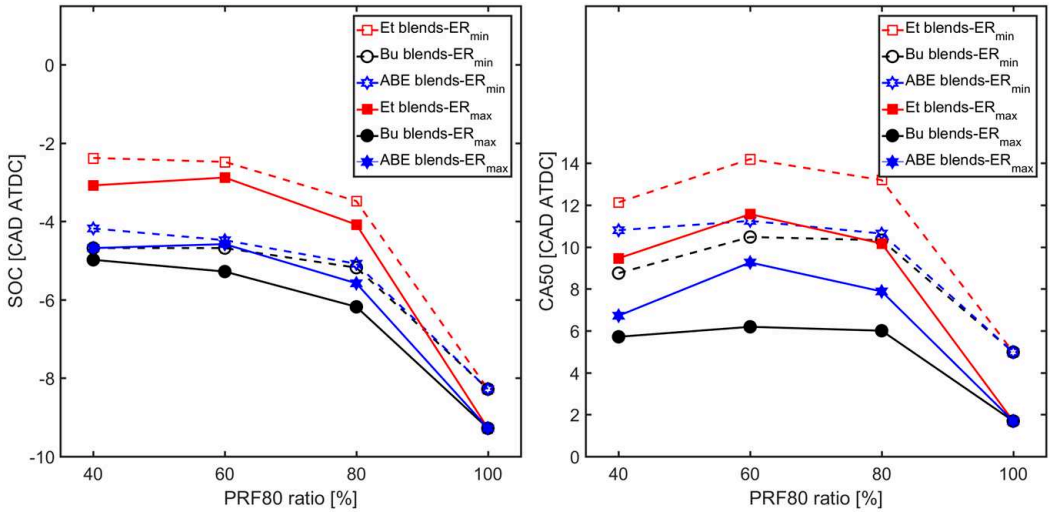

Figure 3.36. Comparisons of Start of Combustion (SOC) and combustion phasing (CA50) for all blends as a function of the PRF80 content

Under both maximum and minimum equivalence ratio limits, the auto-ignition timing is more and more delayed with the increase of ethanol, butanol and ABE contents in the blend. This dependence is monotone but not linear: the effect is more important for low content additions (until 20%) than for high content. Moreover, it can be noted that when 60% of ABE is added in PRF80, the auto-ignition is promoted for maximum ER limit as already concluded for ethanol blends. As similar trend, the combustion phasing is strongly delayed from 0% alcohol to 20% alcohol blends, with lower effect for 20% to 40% alcohol contents and a change in the slope when 60% alcohol is added for both ER limits. It indicates that 60% of alcohol contents in blends favors the auto-ignition and then the combustion development. It can be concluded

also that the rank as a function of the alcohol or ABE mixture is as: Butanol blends > ABE blends > Ethanol blends.

IMEP and combustion efficiency as a function of PRF80 fraction are shown in Figure 3.37. Due to the lowest reactivity of ethanol, the combustion for ethanol blends is the most delayed one with as consequence an increase of the IMEP with better combustion efficiency. Globally the combustion efficiency is higher than 90%, for maximum ER limit (only Bu60 around 83%). But for the minimum ER limit, the combustion efficiency is more around 80%.

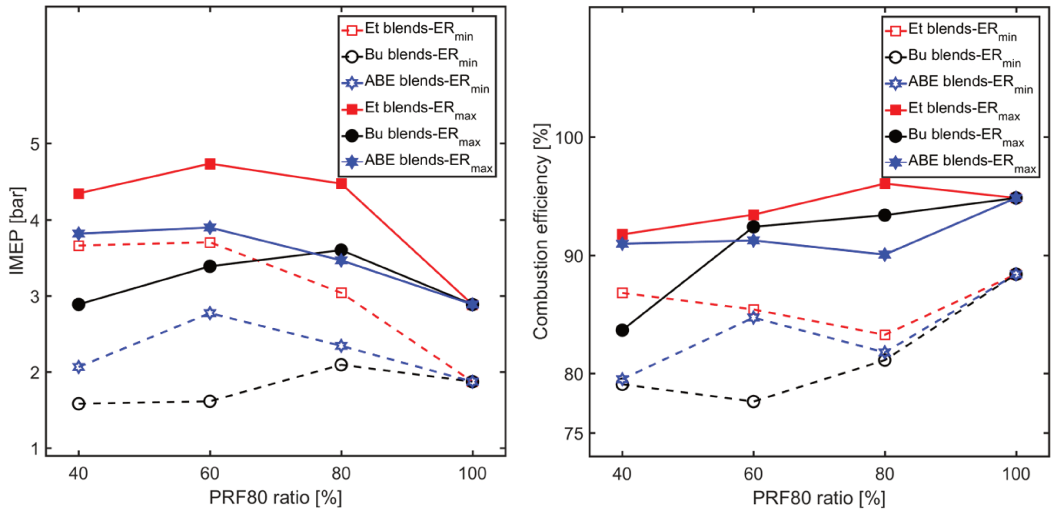

Figure 3.37. The The IMEP (left) and Combustion efficiency (right) at ER limits for all blends

*) Correlation between performance, combustion process and emissions as linear model of equivalence ratio for 20%, 40% and 60% of Ethanol, Butanol and ABE blends under 1 bar pressure and 150^{o}C temperature of intake conditions is shown in Eq. 3.9, with the coefficients for Ethanol blend in Table 3.21 and for Butanol, ABE blend in Table 3.29.

Table 3.29. Coefficients for Eq. 3.9, for Butanol and ABE blend fuels under 1bar pressure and 150^{o}C Temperature of intake conditions

	Coef.	**Fuel**					
		Bu20	**Bu40**	**Bu60**	**ABE20**	**ABE40**	**ABE60**
CA10	a	-18.77	-13.35	-7.41	-15.09	-12.93	-12.78
	b	11.87	9.18	5.97	11.56	9.05	10.58
	R^2	0.981	0.934	0.672	0.971	0.740	0.860
CA50	a	-43.49	-41.50	-31.60	-40.16	-23.5	-32.02
	b	24.51	22.98	17.79	24.61	20.79	21.76
	R^2	0.980	0.990	0.962	0.994	0.730	0.962
CD	a	-51.49	-47.78	-38.87	-42.27	-33.28	-35.00

	Coef.	Fuel					
		Bu20	**Bu40**	**Bu60**	**ABE20**	**ABE40**	**ABE60**
	b	29.96	28.71	24.98	26.95	25.41	24.92
	R^2	0.990	0.986	0.946	0.985	0.934	0.966
IMEP	a	14.88	16.83	13.74	16.06	14.11	13.41
	b	-2.71	-3.40	-2.25	-3.23	-2.68	-2.36
	R^2	0.972	0.992	0.960	0.991	0.992	0.984
CE	a	136.70	193.12	122.75	160.33	97.71	103.36
	b	29.18	10.19	36.93	19.11	37.81	35.88
	R^2	0.892	0.954	0.720	0.971	0.924	0.914
IE	a	90.8	127.8	96.0	104.8	66.7	74.8
	b	-0.1	-13.1	-0.8	-6.0	6.3	3.2
	R^2	0.910	0.962	0.823	0.975	0.951	0.938
RI	a	879.6	542.4	395.3	670.8	436.3	598.3
	b	-294.1	-171.1	-115.5	-223.5	-166.4	-209.5
	R^2	0.952	0.909	0.923	0.948	0.864	0.907
CO	a	-19.05	-48.97	-69.73	-18.51	-23.20	-44.74
	b	8.78	20.47	30.45	8.26	11.71	21.89
	R^2	0.933	0.896	0.880	0.963	0.989	0.921
HC	a	-426.4	-491.9	-273.0	-445.7	-282.6	-367.1
	b	195.2	212.8	144.1	207.7	154.2	191.6
	R^2	0.930	0.940	0.923	0.949	0.989	0.926

Several features can be identified for Ethanol, Butanol and ABE blends in HCCI combustion mode, under 150^{o}C intake temperature, 1 bar pressure and without EGR conditions:

- The sensitivity of equivalence ratio on both auto-ignition timing (CA10) and combustion phasing (CA50) is decreased while Bu/ABE ratio increase.

- A much higher sensitivity of equivalence ratio on CO emission is observed while Bu/ABE ratio increases, and more strongly for Butanol blends.

- The Bu20 and ABE20 have lower sensitivity of equivalence ratio on both auto-ignition timing (CA10) and combustion phasing (CA50) than Et20.

- The sensitivity of equivalence ratio on combustion efficiency (CE) of Bu20 and PRF80 is less than that of ABE20 and Et20.

- The sensitivity of equivalence ratio on CO emission of Bu20 and ABE20 is more than that of Et20, that of HC emission of Bu20 and ABE20 is less.

- The sensitivity of equivalence ratio on both auto-ignition timing (CA10) and combustion phasing (CA50) of Et40, Bu40 and ABE40 are similar.

- The sensitivity of equivalence ratio on both for CE and IE of Bu40 is highest.

- The sensitivity of equivalence ratio on auto-ignition timing (CA10), combustion phasing (CA50) and RI are in order: Bu60 < ABE60 < Et60.

- The sensitivity of equivalence ratio on CE, IE and CO emission are in order: Bu60 > ABE60 > Et60.

The correlation of IMEP as a function of energy content for Ethanol, Butanol and ABE blend is shown in Eq. 3.6, with coefficients for Ethanol blend in Table 3.22 and for Butanol, ABE blends in Table 3.30. The constants for Bu40 and ABE20 are higher.

Table 3.30. Coefficients for Eq. 3.6. LHV in Joule/cycle

	Coef.	**Fuel**					
		Bu20	**Bu40**	**Bu60**	**ABE20**	**ABE40**	**ABE60**
IMEP	a	0.014	0.016	0.013	0.015	0.013	0.013
	b	-2.94	-3.60	-2.30	-3.60	-2.65	-2.92
	R^2	0.989	0.992	0.958	0.995	0.986	0.987

The correlation between performance and efficiencies and combustion phasing is presented in Eq. 3.8, the coefficients for Ethanol blend in Table 3.23 and for Butanol, ABE blend in Table 3.31.

Table 3.31. Coefficients for Eq. 3.8. CA50 in CAD ATDC

	Coef.	**Fuel**					
		Bu20	**Bu40**	**Bu60**	**ABE20**	**ABE40**	**ABE60**
IMEP	a	-0.343	-0.404	-0.429	-0.399	-0.451	-0.406
	b	5.68	5.91	5.44	6.61	8.18	6.64
	R^2	0.997	0.996	0.974	0.993	0.966	0.961
RI	a	-19.61	-12.88	-12.50	-16.68	-16.66	-18.94
	b	197.0	127.6	106.9	177.4	198.9	199.3
	R^2	0.912	0.891	0.957	0.950	0.954	0.969
CE	a	-3.21	-4.68	-4.04	-3.99	-3.08	-3.09
	b	106.7	117.3	107.1	117.3	112.5	104.8
	R^2	0.948	0.975	0.810	0.973	0.893	0.868
IE	a	-2.12	-3.09	-3.08	-2.61	-2.08	-2.23
	b	51.28	57.80	53.58	58.22	57.05	53.10
	R^2	0.961	0.979	0.879	0.979	0.902	0.892

The analyses of the results indicate the following:

- For the same ratio of alcohols/ABE, the sensitivity of combustion phasing on IMEP is in order: Ethanol < Butanol < ABE, the sensitivity of combustion phasing on combustion efficiency and indicated efficiency is a function of % of alcohols/blend as Et20 < Bu20 < ABE20 but Et40 < ABE40 < Bu40 and Et60 < ABE60 < Bu60.

- For Butanol blends, the increase of the Butanol ratio on blends increases the sensitivity of combustion phasing on IMEP, but on RI decreases. For ABE blends, the ABE40 fuel has higher sensitivity on combustion phasing than ABE20 and ABE60. The impact of combustion phasing on CE and IE of Bu40 fuel is highest between Butanol blends, and that of ABE20 fuel between ABE blends.

The auto-ignition timing (CA10) is modeled linear of equivalence ratio and components of ethanol, butanol and acetone, based on PRF80, Et20, Bu20 and ABE20 fuels, as shown in Eq. 3.20, the coefficients in Table 3.32.

$$CA02=a*ER+b*x_{PRF80}+c*x_{Ethanol}+d*x_{Butanol}+e*x_{Acetone}+f \qquad \textbf{Eq. 3.20}$$

Table 3.32. Coefficients for Eq. 3.20. Where x is volume percentage of component

	Coef.						
	a	b	C	d	e	f	R^2
CA10	-22.67	-0.04	0.70	0.240	0.162	8.799	0.922

The constants shown in Table 3.32 indicate that the ethanol, butanol and acetone are higher resistance to auto-ignition than PRF80, as expected. In comparison between these components, the impact on auto-ignition of blends is in order: Ethanol > Butanol > Acetone. As estimated the constant from these component of ABE (3:6:1) mixture, the constant for ABE is 0.263. Hence, the impact of ABE on auto-ignition of blends is more resistant than Butanol, and less than Ethanol.

Figure 3.38 shows the simulated ignition delays of Ethanol, Butanol and ABE mixtures as a function of PRF80 content at 850 K and 40 bar, condition very close to the in-cylinder condition at TDC for 1 bar and 150°C of intake pressure and temperature conditions in the HCCI operating mode, for four level of equivalence ratio: 0.3, 0.4, 0.5 and 0.6. This underlines the stronger reactivity of butanol blend than ABE and ethanol blends. But in comparison to ethanol, ABE ID are in the same order of magnitude than butanol. This also explains that higher

equivalence ratio is required to reach stable combustion for ethanol blends than for butanol or ABE ones.

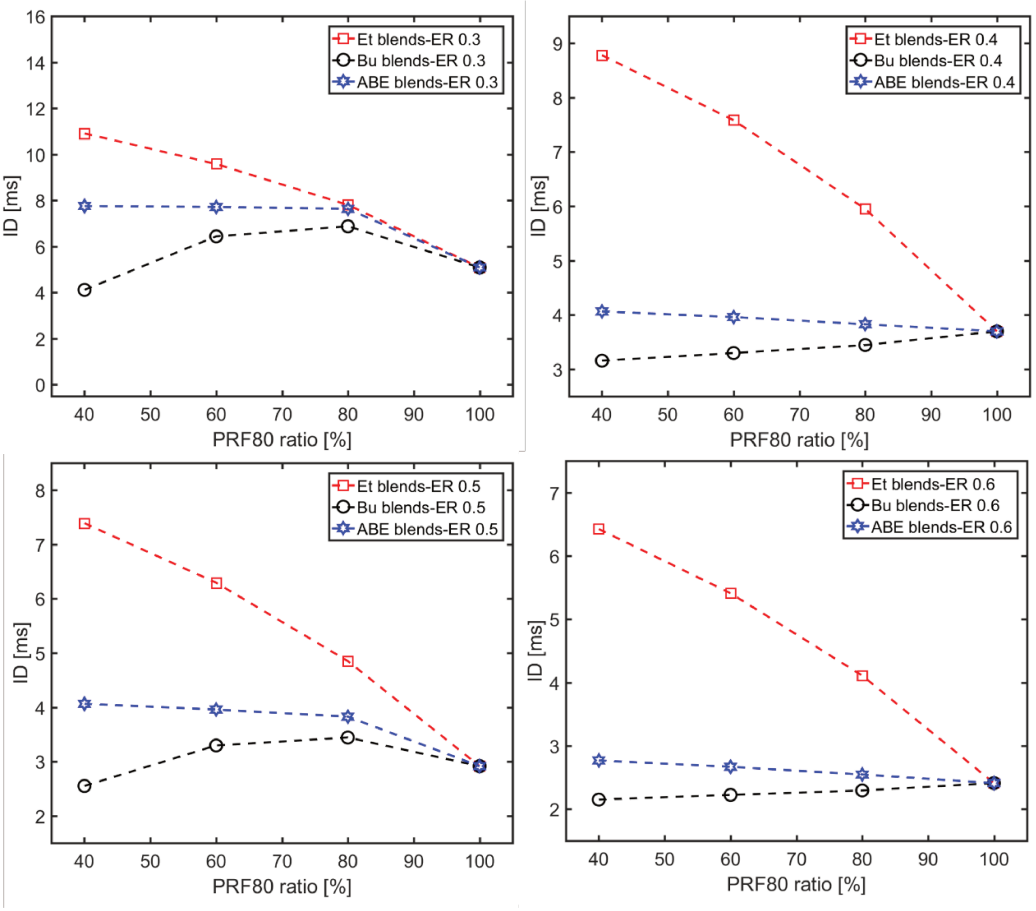

Figure 3.38. Simulated ignition delay as a function of PRF80 content for ER 0.3, 0.4, 0.5 and 0.6 under the condition 850 K, 40 bar

3.3.2.2. Global operating range

As previously done for ethanol blend fuel, the IMEP maps are plotted as a function of intake temperature and equivalence ratio for different intake pressures, for different alcohol/ABE contents (20%, 40% and 60%) in Figure 3.39, Figure 3.40 and Figure 3.41, respectively. First, it is evident that the addition of alcohol or ABE in gasoline type fuel reduces strongly the acceptable operating conditions to maintain stable HCCI combustion, especially for the lowest conditions, inducing lowest IMEP. As already shown with ethanol blending, higher intake temperature is needed due to the auto-ignition resistance of alcohols. Moreover, these maps highlight the difference between ethanol and butanol to achieve stable combustion: lower intake temperature can be sufficient for butanol and ABE. This is also more important with the increase of alcohol/ABE content in fuel blend. It has to be noted also that with ABE the

operating conditions limits are more similar to butanol blend that ethanol one but not exactly the same.

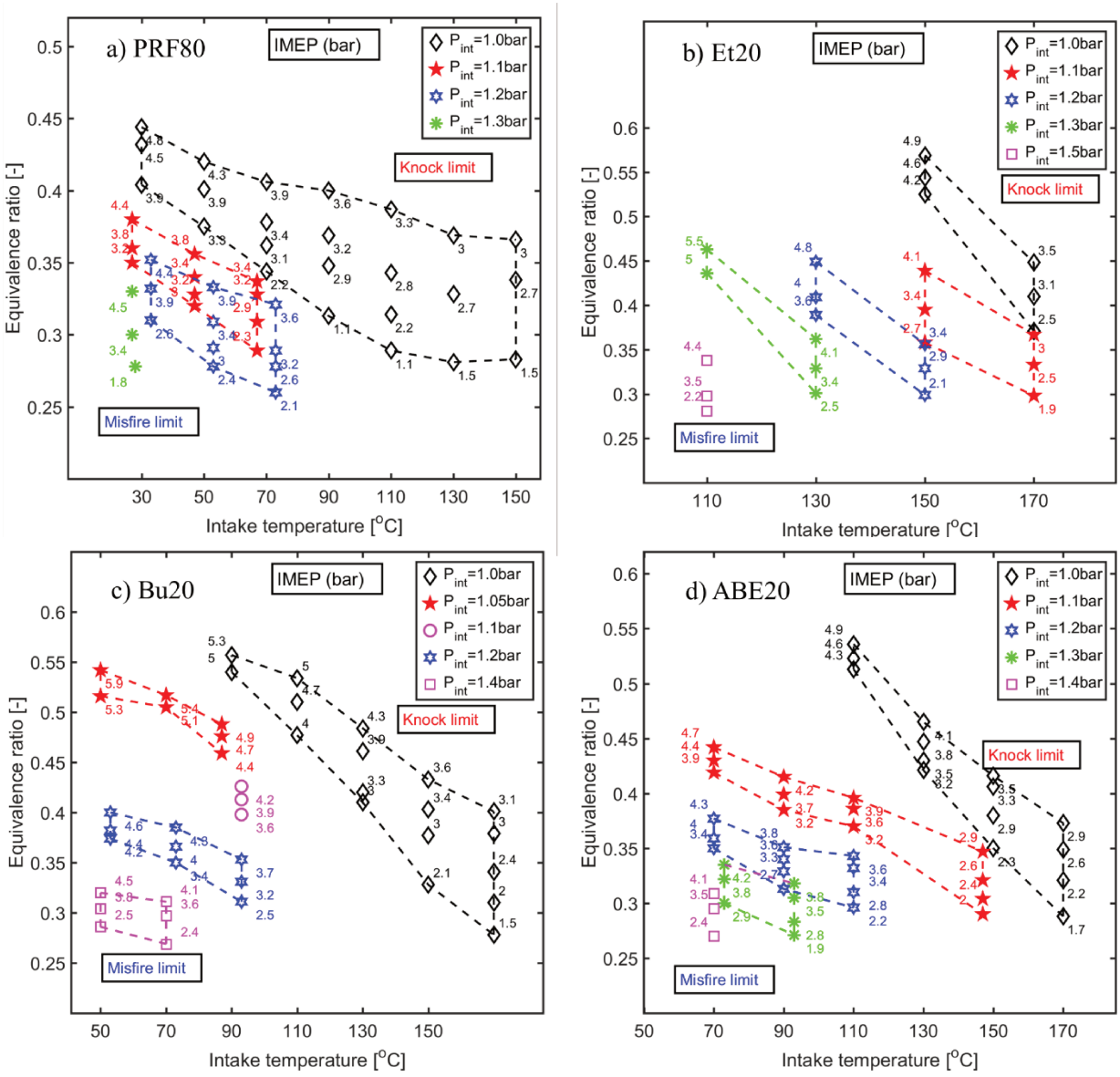

Figure 3.39. IMEP Map as a function of intake temperature and ER for a)PRF80, b)Et20, c)Bu20 and d)ABE20

It can be seen from Figure 3.39, the intake temperature range to achieve stable operating HCCI mode is strongly affected by type of alcohol or ABE: lower reactive blend fuel requires higher intake temperature.

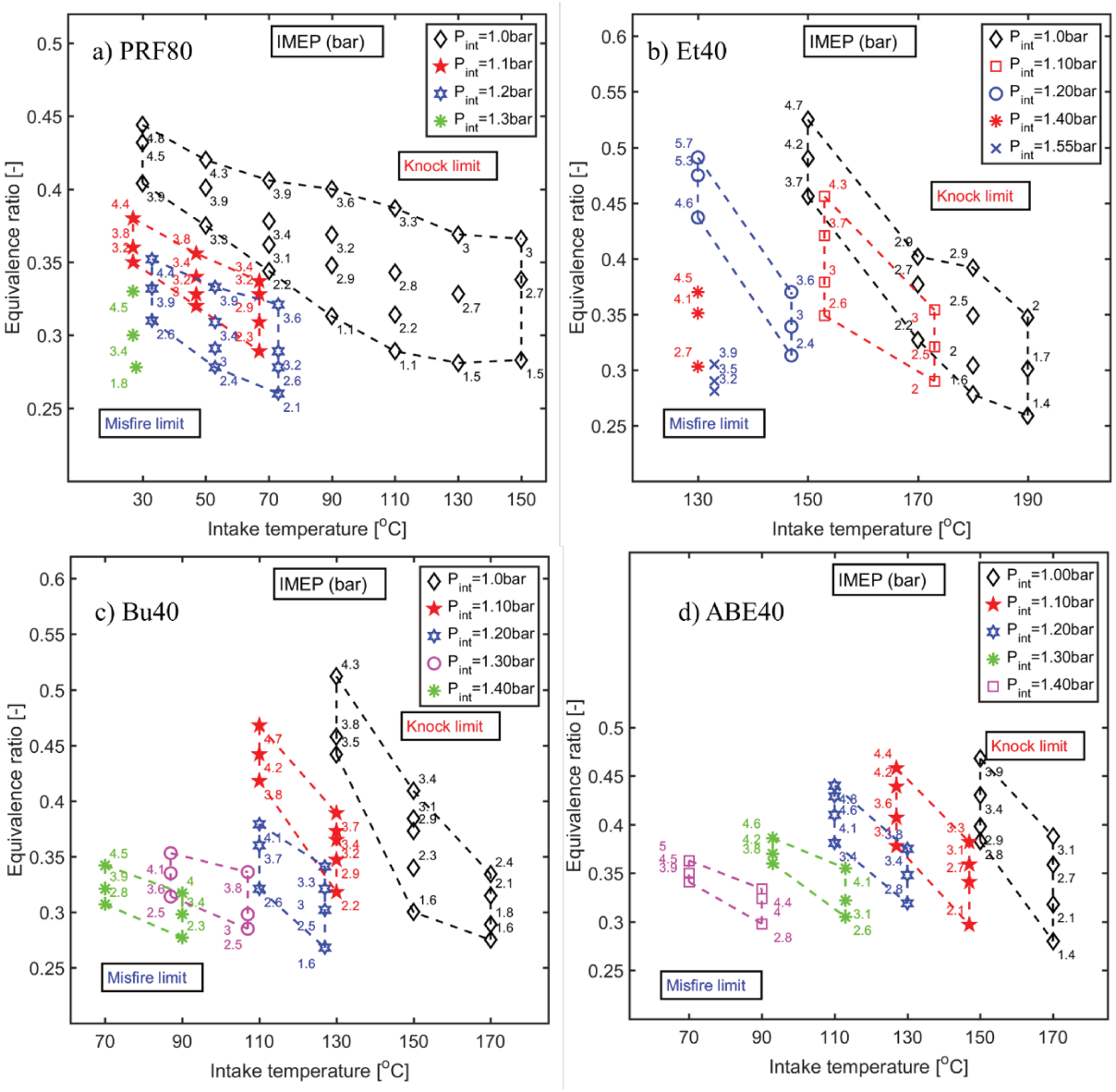

Figure 3.40. IMEP Map as a function of intake temperature and ER for a)PRF80, b)Et40, c)Bu40 and d)ABE40

Under naturally aspired condition, the temperature requirement to stable combustion of alcohols blends 40% is increased, as example 150°C for Et40, ABE40 and 130°C for Bu40.

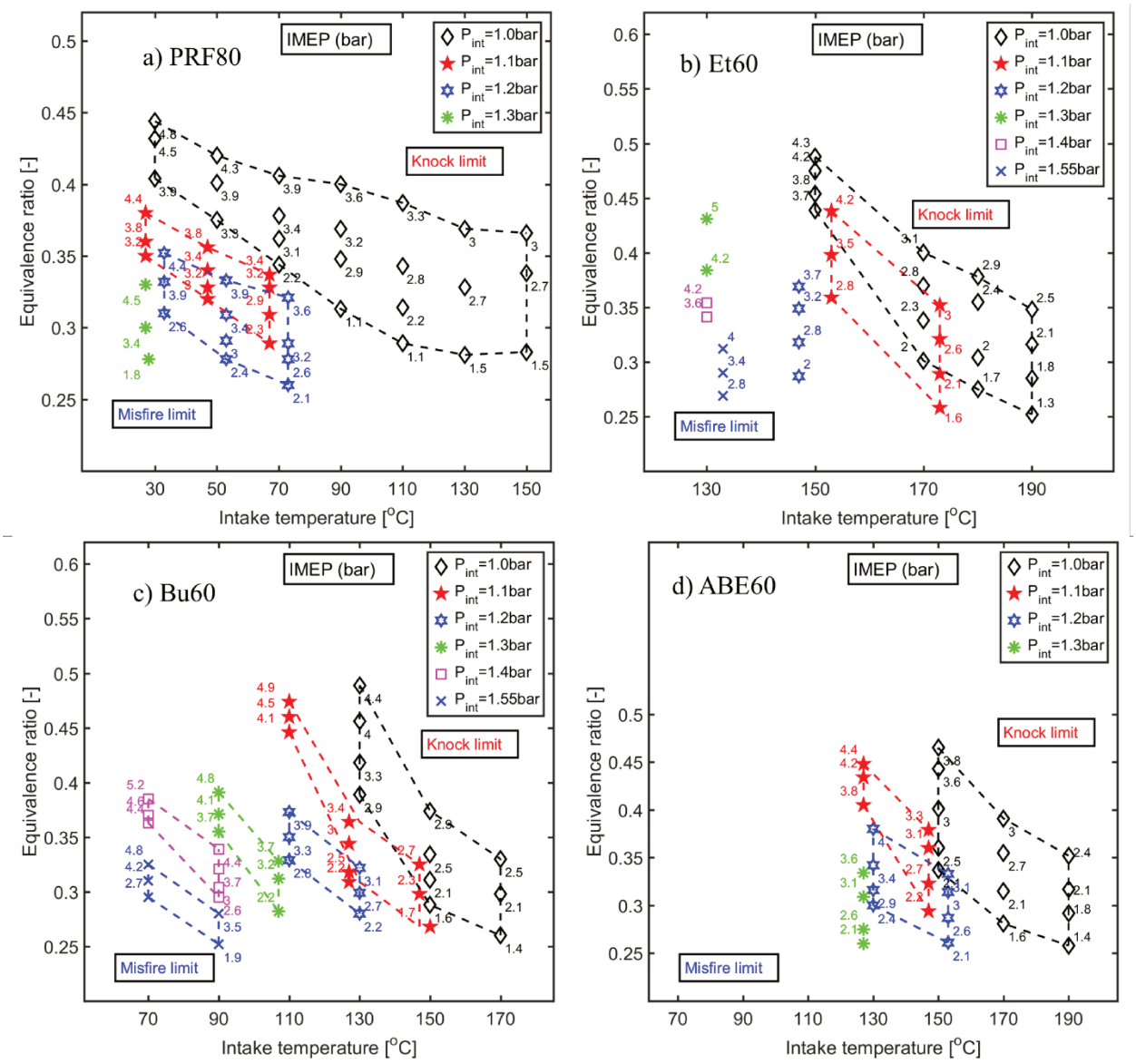

Figure 3.41. IMEP Map as a function of intake temperature and ER for a)PRF80, b)Et60, c)Bu60 and d)ABE60

**) Simulated auto-ignition delay*

The comparison between Ethanol, Butanol, ABE and pure PRF80 auto-ignition delay is presented in Figure 3.42, Figure 3.43 and Figure 3.44 for blends of 20%, 40% and 60%, respectively. The computed ignition delays from chemical kinetic simulation are presented in a temperature – pressure space, with also three engine thermodynamics compression trajectories. As it can be seen, the Butanol blends have the highest reactivity under these wide-range of initial temperature – pressure at the equivalence ratio of 0.4, even when 60% of butanol is in the blend. Moreover, ABE blends have similar iso-contours than Bu ones, only small

differences can be noted in LTR region, inducing by the presence of ethanol in ABE mixture.

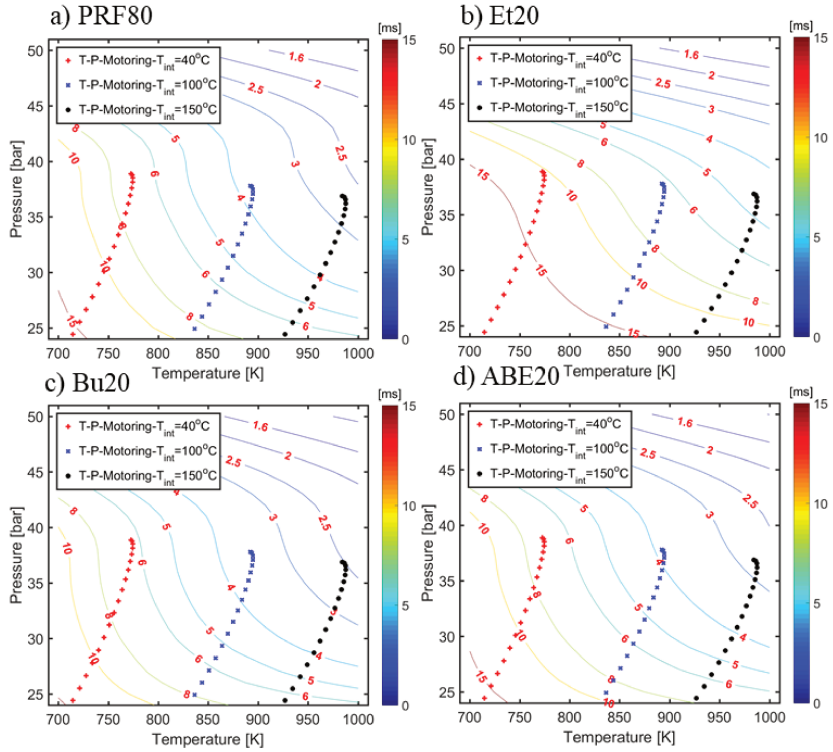

Figure 3.42. Iso-contours of ignition delay for a)PRF80 b)Et20 c)Bu20 and d)ABE20 under wide-range temperature and pressure at 0.4 ER

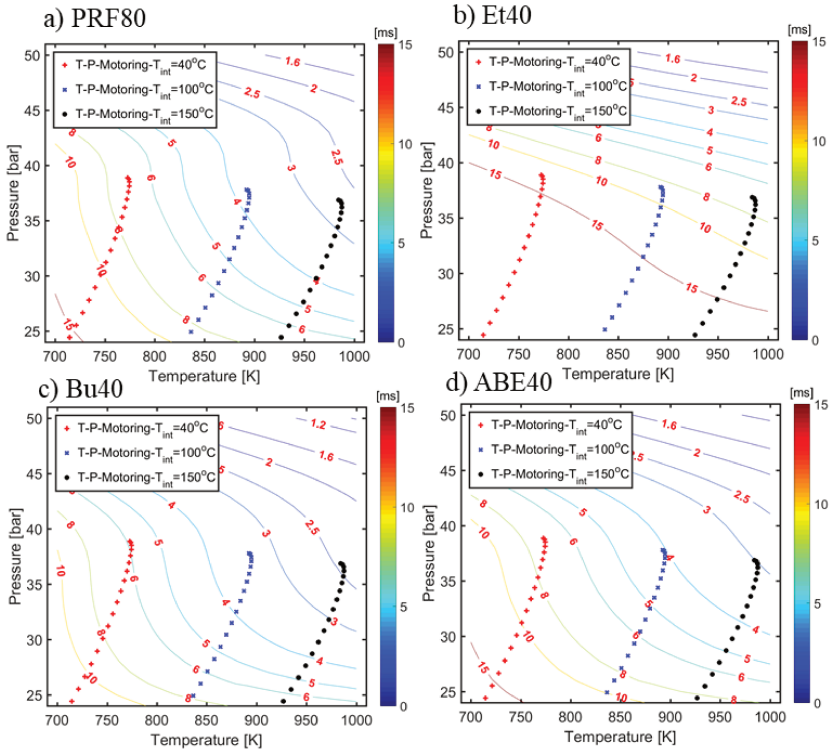

Figure 3.43. Iso-contours of ignition delay for a)PRF80 b)Et40 c)Bu40 and d)ABE40 under wide-range temperature and pressure at 0.4 ER

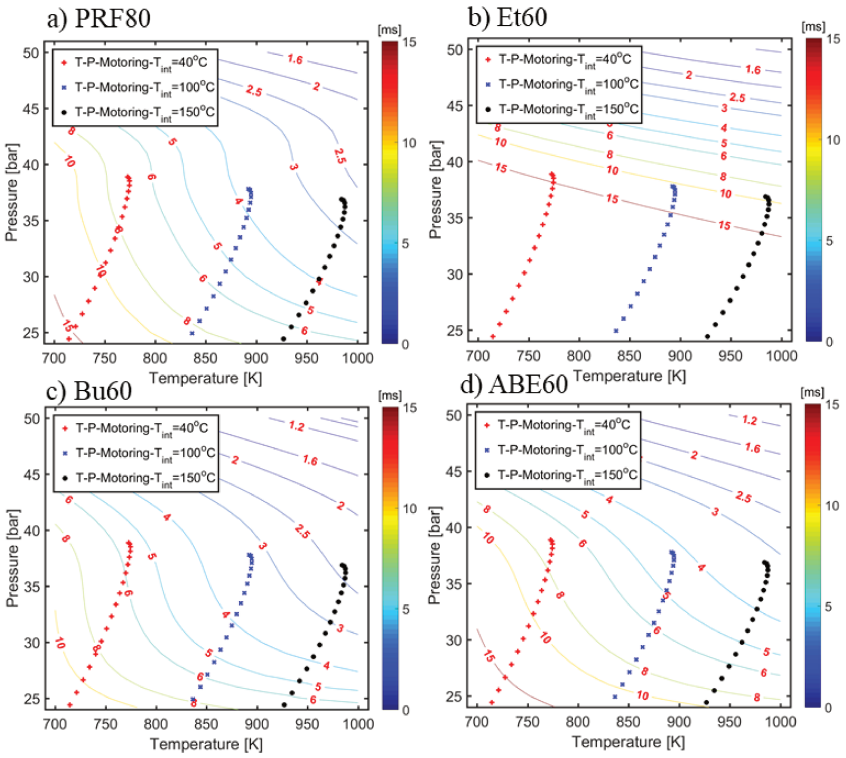

Figure 3.44. Iso-contours of ignition delay for a)PRF80 b)Et60 c)Bu60 and d)ABE60 under wide-range temperature and pressure at 0.4 ER

3.3.2.3. Comparison ethanol, butanol and ABE blend fuel under operating limit as a function of intake temperature

As similar previous section about ethanol, the operating limits for ethanol, butanol and ABE blends is discussed under fully-HCCI mode for naturally aspired operating conditions at 1500 rpm.

a) For 20% alcohol/ ABE blend

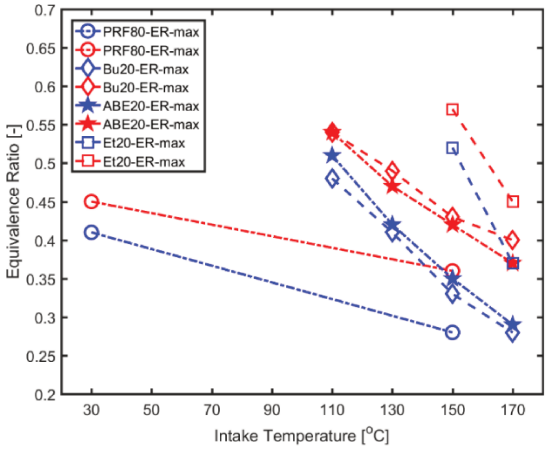

Figure 3.45. Equivalence ratio - Intake temperature limits of blends of Ethanol, Butanol, ABE (20%) and PRF80

The various intake temperature and equivalence ratio limits for of different blends are summarized in Figure 3.45. Figure 3.46 a) and b) illustrate the change of trend on performance, combustion process and emissions as a function of the intake temperature for the maximum and minimum equivalence ratio limits, respectively.

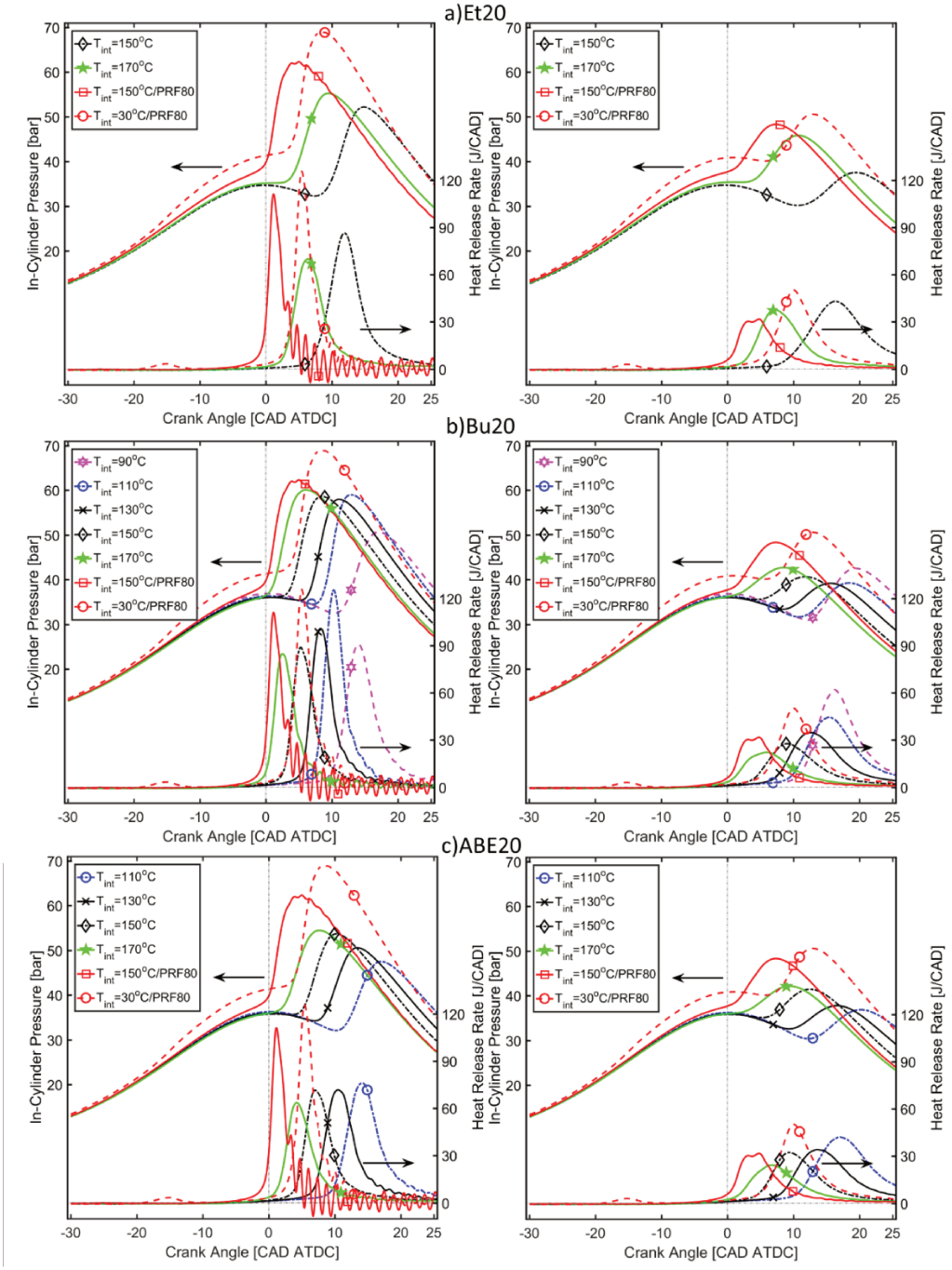

Figure 3.46. In-cylinder pressure and Heat release rate of a) Et20, b) Bu20 and c) ABE20 blend fuel on base comparison of PRF80 under limited Ringing intensity (left) and start

burning (left)

As it can be seen in Figure 3.46 a), at same intake temperature, the blend with higher octane number, i.e. ethanol, induces higher IMEP, as example, at 150°C of intake temperature, the IMEP is ranked as 3 bar for PRF80 (RON=80), 3.5 bar for Bu20 (RON=83.2) and for ABE20 (RON=84.2) and 4.4 bar for Et20 (RON=86.5). This also proves than ABE can be used instead of butanol and guarantees similar performance in HCCI combustion mode when 20% is added to gasoline type fuel. However, when the intake temperature is lower, only Bu20 is able to guarantee stable combustion (at 90ºC) with an IMEP of 5.8 bar. For the same intake temperature, the indicated efficiency of all blends is higher than pure PRF80 even if the combustion efficiency is worse, inducing higher unburnt HC and CO emissions.

Figure 3.47 a) and b) illustrate the trend of performance, combustion process and emissions for 20% Ethanol, Butanol and ABE blends versus the intake temperature with maximum and minimum equivalence ratio limits, respectively. Under both equivalence ratio levels, Et20 blends auto-ignites later at the same intake temperature of 150 and 170ºC, despites a higher equivalence ratio. Bu20 and ABE20 provide similar combustion development.

As seen Figure 3.47 a), for the same intake temperature, higher octane number of bio-fuel induces higher IMEP, as example, at the intake temperature of 150ºC, the IMEP obtained are 3 bar (PRF80/RON=80), 3.5 bar (Bu20/RON=83.2; ABE20/RON=84.2) and 4.4 bar (Et20/RON=86.5). However, for an intake temperature lower than 150ºC, the Bu20 is able to reach intake temperature of 90ºC to establish the stable combustion, until an IMEP of 5.8 bar, which is the highest for all 20% alcohols blends. The indicated blends of PRF80 with an intake temperature of 30ºC is the highest under this operating condition range.

Under the minimum equivalence ratio limit to start stable HCCI mode, the trend of IMEP as a function of intake temperature shows a sensitivity to the intake temperature for alcohols blends (see Figure 3.47 b), more than for the maximum equivalence ratio limit. The similar impact of intake temperature on combustion and indicated efficiencies, auto-ignition timing and combustion phasing for all blends.

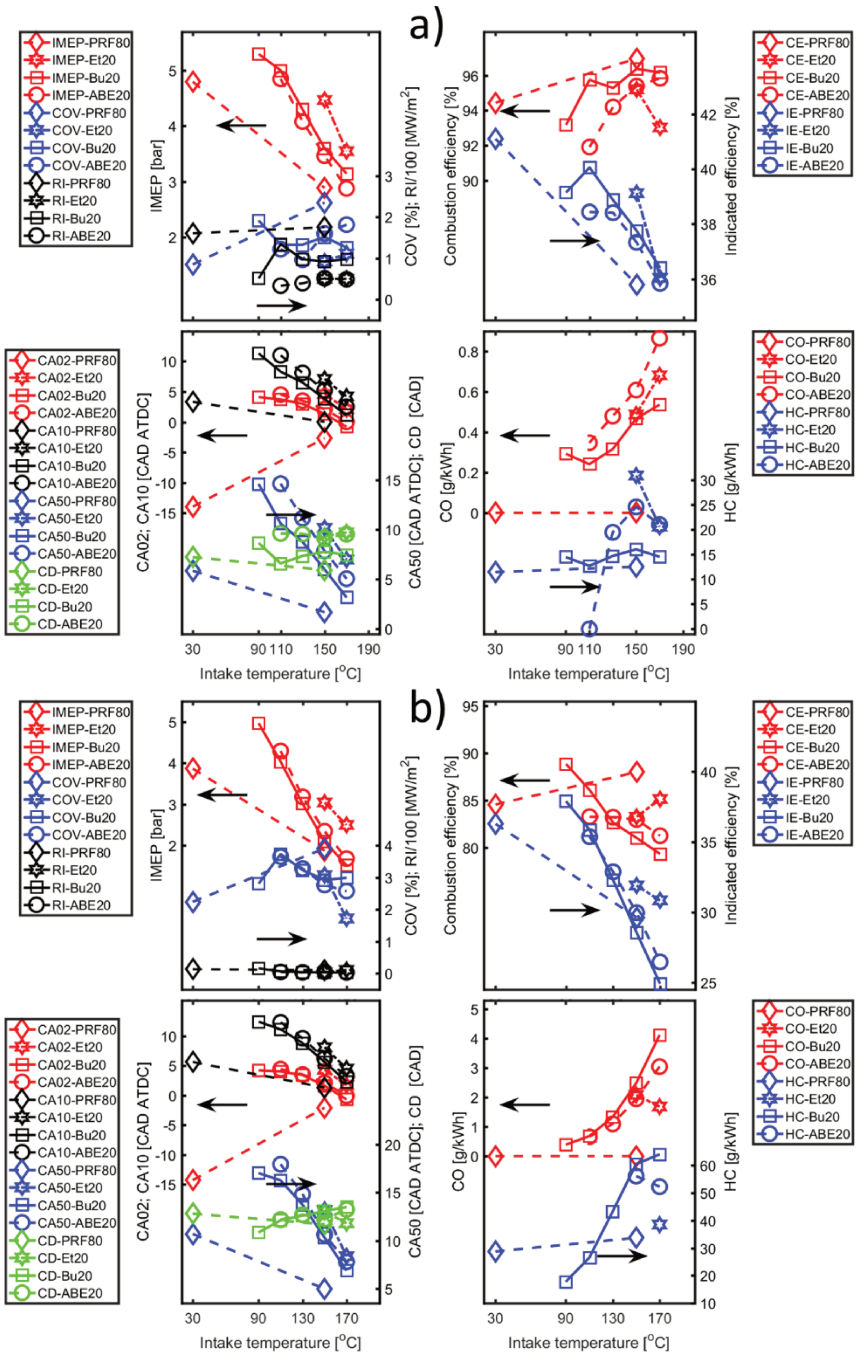

Figure 3.47. Performance, combustion process and emission for Blend 20% Ethanol, Butanol and ABE and 80% PRF80 with (a)maximum and (b) minimum equivalence ratio limits

The performance, combustion process and emissions parameters were modelled as a linear function of the equivalence ratio and intake temperature, for Eq. 3.17 for PRF80, Et20, Bu20 and ABE20 with the coefficients shown in Table 3.33.

Table 3.33. Coefficients for Eq. 3.17, for Et20, Bu20 and ABE20 fuels. T in °C

	Coef.	Fuel			
		PRF80-High T	**Et20**	**Bu20**	**ABE20**
CA10	a	-25.48	-15.89	-39.98	-35.71
	b	-0.05	-0.40	-0.27	-0.27
	c	16.44	79.20	60.12	59.59
	R^2	0.872	0.757	0.907	0.952
CA50	a	-60.99	-32.33	-72.56	-63.14
	b	-0.074	-0.56	-0.37	-0.37
	c	34.32	115.72	91.55	89.33
	R^2	0.865	0.814	0.942	0.963
CD	a	-84.81	-89.77	-86.96	-78.57
	b	-0.063	-0.63	-0.25	-0.25
	c	46.00	154.53	81.92	79.20
	R^2	0.958	0.966	0.960	0.970
IMEP	a	17.05	8.81	10.40	9.35
	b	-0.01	-0.02	-0.01	-0.01
	c	-1.92	2.82	0.475	0.868
	R^2	0.714	0.962	0.950	0.949
CE	a	216.51	110.63	232.28	213.68
	b	0.071	0.71	0.71	0.71
	c	-1.94	-86.10	-115.89	-108.95
	R^2	0.520	0.990	0.942	0.973
IE	a	139.1	30.5	48.3	36.0
	b	$-2.3*10^{-3}$	$-0.14*10^{-3}$	$-0.28*10^{-3}$	$-0.28*10^{-3}$
	c	-13.9	21.1	15.2	20.0
	R^2	0.592	0.873	0.801	0.670
RI	a	1955.9	1408.5	1685.6	1500.3
	b	2.03	10.16	5.08	5.08
	c	-835.8	-2272.8	-1375.1	-1319.9
	R^2	0.863	0.970	0.941	0.958
CO	a	-0.020	-5.122	-10.890	-7.557
	b	$14*10^{-6}$	$14*10^{-6}$	$14*10^{-6}$	$14*10^{-6}$
	c	0.008	3.27	5.562	4.14
	R^2	0.773	0.850	0.718	0.715
HC	a	-662.7	-248.3	-599.6	-692.6
	b	-0.082	-1.64	-1.64	-1.64
	c	255.5	409.0	508.95	538.20
	R^2	0.602	0.820	0.955	0.910

The analyses of the results indicate the following:

- In comparison with alcohols/ABE blends, PRF80 fuel at high intake temperature condition

(from 110 to 150ºC) provides less sensitivity of auto-ignition timing and combustion phasing e to the intake temperature than Bu20 and ABE20 fuels, but more than Et20 fuel.

- In comparison with 20% alcohols/ABE blends, the auto-ignition timing and combustion phasing is less sensitive on equivalence ratio for Et20 but more on intake temperature.

- The combustion efficiency of 20% alcohols/ABE blends is more affected by the intake temperature than for PRF80 fuel. The combustion efficiency of Et20 is less sensitive to the equivalence ratio, as ranked as Et20 (110.63) < ABE20 (213.68) < Bu20 (232.28).

- The indicated efficiency of 20% alcohols/ABE blends is less sensitive to the equivalence ratio and intake temperature than PRF80 fuel, ranked as Et20 (30.5) < ABE20 (36.0) < Bu20 (48.2).

- The CO and HC emissions of these blends are more related to the equivalence ratio in the following rank Et20 < ABE20 < Bu20.

The IMEP as a function of energy content and intake temperature is presented in Eq. 3.14, the coefficients for Et20, Bu20 and ABE20 are shown in Table 3.34. The sensitivity to the energy content is more important for PRF80 and less for Et20.

Table 3.34. Coefficients for Eq. 3.14. for Et20, Bu20 and ABE20 fuels.

	Coef.	**Fuel**			
		PRF80-High T	**Et20**	**Bu20**	**ABE20**
IMEP	a	0.016	0.011	0.012	0.012
	b	0.01	0.01	0.01	0.01
	c	-4.96	-3.58	-3.87	-3.51
	R^2	0.900	0.997	0.996	0.988

**) Combustion characteristics: first ignition stage*

The Heat Release rate for Bu20 and ABE20 is plotted for both ER limits and different intake temperature and pressure conditions, but only along the CAD zone where the first ignition stage zone can occur. It is clear the butanol and ABE additions strongly reduce the LTR as it can be seen in Figure 3.48, as ethanol (Figure 3.19) [123,134,136].

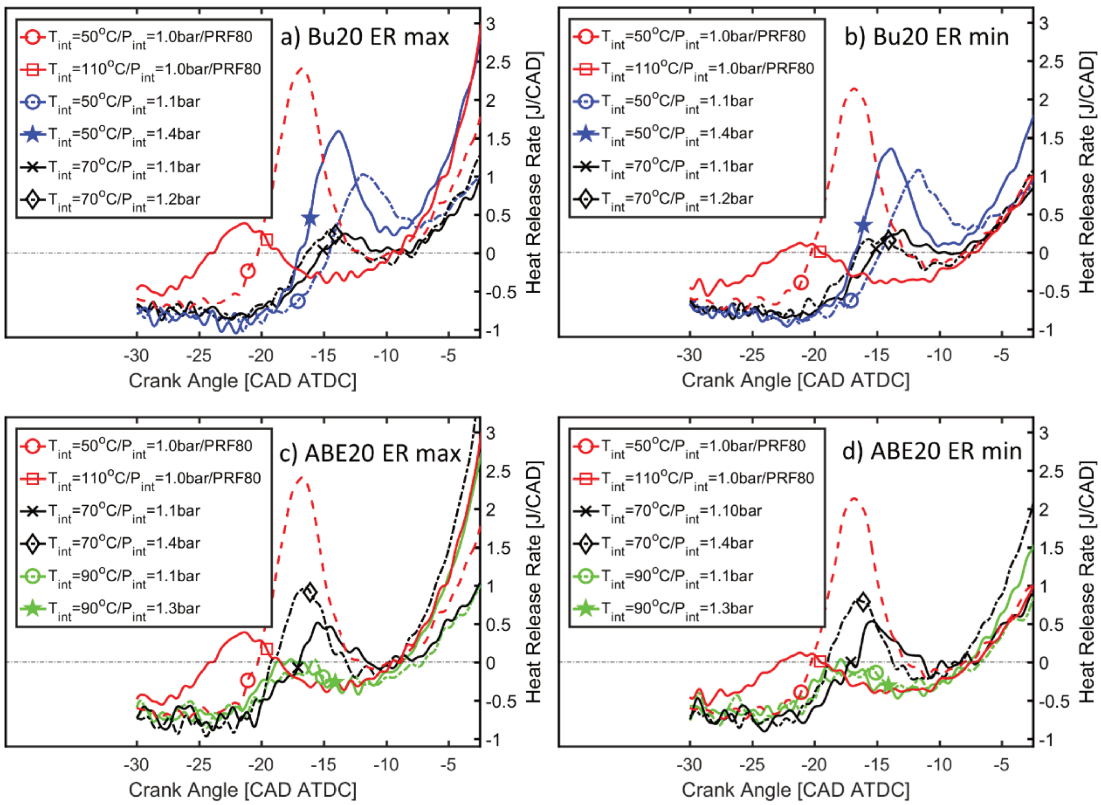

Figure 3.48. The influence of 20% Butanol and ABE on the first stage ignition at ER limits

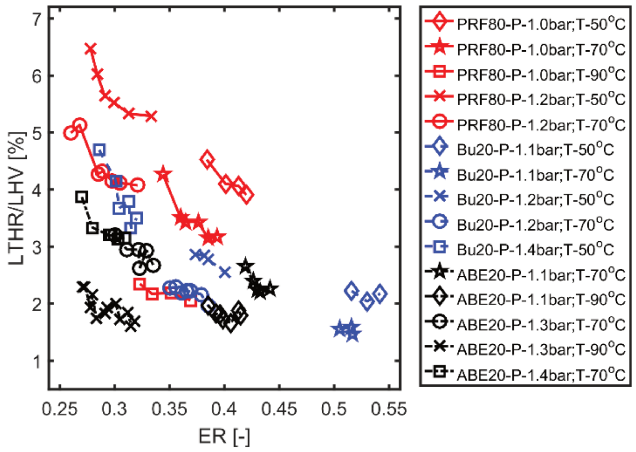

Figure 3.49. The amount of LTHR as a function of the equivalence ratio for PRF80, Bu20 and ABE20 under various intake temperature and pressure conditions

The amount of LTHR as a function of equivalence ratio for PRF80, Bu20 and ABE20 under low intake temperature and without/with boosted conditions is given at Figure 3.49. The Bu20 and ABE20 fuels show significant decrease of LTHR amount compared with PRF80 fuel, even if the trends of amount LTHR as a function of equivalence ratio, temperature and pressure is similar as for PRF80.

ABE20 has the stronger effect on pre-reactions than Bu20, as example, ER=0.3, P_{int}=1.4 bar, T_{int}=70°C, the amount of Bu20 and ABE20 is 4.2% and 3.3%, respectively.

*) *Controlling combustion phasing*

The performance and combustion parameters are presented as a function of CA50 in Figure 3.50 a) and b) for maximum and minimum equivalence ratio limits, respectively. The highest IMEP is achieved with retarded combustion phasing for all 20% fuel blends, under both ER limits. For Bu20 blend fuel, the load was increased by 3.1 bar to 5.2 bar IMEP for combustion phasing change from 3 to 15 CAD ATDC, at the maximum equivalence ratio. The maximum load of these blends is 5.2 bar IMEP, for Bu20 blends. As seen same combustion phasing of 15 CAD ATDC, Bu20 provides higher IMEP (about 10% more) than ABE20. In comparison at combustion phasing of 11 CAD ATDC for maximum equivalence ratio, the IMEP of these blends is in order: ABE20 < Et20 < Bu20.

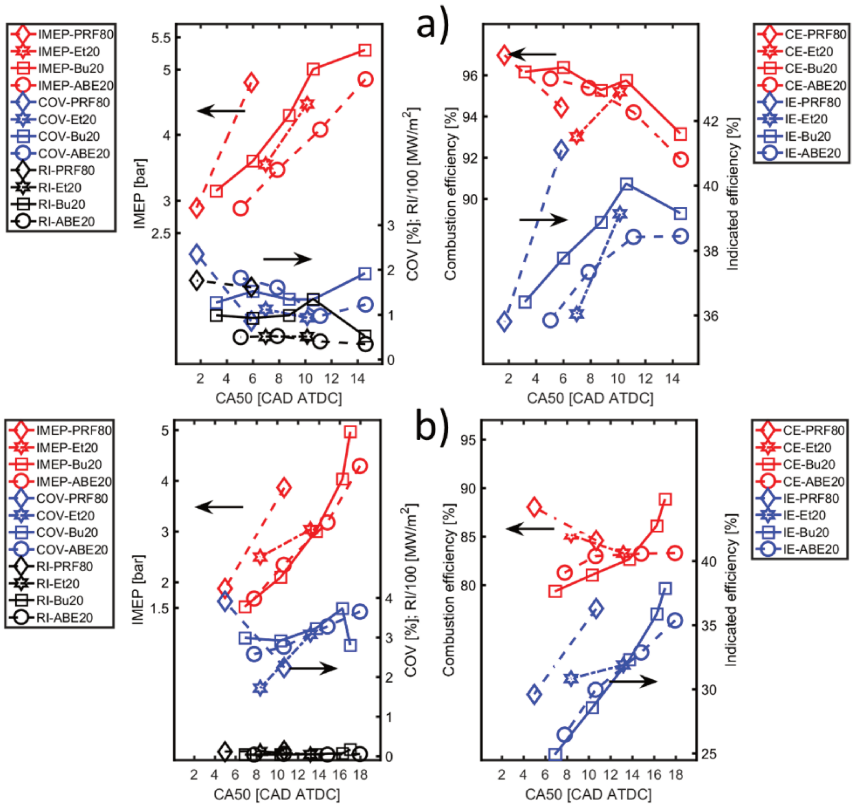

Figure 3.50. The performance and efficiencies as a function of combustion phasing under (a) maximum and (b) minimum equivalence ratio limits

The combustion efficiency and indicated efficiency are generally reduced as the combustion phasing is retarded. The indicated efficiency of PRF80 at combustion phasing of 5 CAD ATDC

is highest, and for these blends, the combustion phasing of 11 CAD ATDC reaches the highest value.

The performance and efficiencies are modelled as a function of combustion phasing and intake temperature, in Eq. 3.21, with coefficients in Table 3.35.

$$Y=a*CA50+b*T+c \qquad \textbf{Eq. 3.21}$$

Table 3.35. Coefficients for Eq. 3.21. for Et20, Bu20 and ABE20 fuels

	Coef.	Fuel			
		PRF80-High T	**Et20**	**Bu20**	**ABE20**
IMEP	a	-0.262	-0.205	-0.416	-0.374
	b	-0.015	-0.150	-0.100	-0.100
	c	5.59	30.18	21.25	21.51
	R^2	0.968	0.913	0.963	0.981
RI	a	-30.29	-27.22	-60.28	-58.20
	b	-2.44	-10.16	-10.16	-10.16
	c	521.0	1962.9	2021.5	2087.0
	R^2	0.793	0.936	0.902	0.948
CE	a	-3.469	-1.122	-2.755	-2.771
	b	0.053	-0.426	-0.426	-0.426
	c	88.41	161.4	166.4	170.3
	R^2	0.868	0.890	0.966	0.986
IE	a	-2.686	-1.391	-3.686	-3.564
	b	-0.176	-0.702	-0.702	-0.702
	c	66.95	163.97	167.5	172.68
	R^2	0.929	0.910	0.915	0.979

The constants shown in Table 3.35 indicate that the impact of intake temperature on performance and efficiencies for Et20, Bu20 and ABE20 is similar with more sensitivity for Et20 than Bu20 and ABE20. But the combustion phasing affects more the performance and efficiencies for Bu20 than Et20 and ABE20.

The auto-ignition timing (CA10) is modeled as a linear dependency of equivalence ratio as shown in Eq. 3.22, by adjusting the impact of intake temperature to Eq. 3.20, the coefficients in Table 3.37. Although this is not true linear function (R^2=0.507), Eq. 3.22 gives some ideas about auto-ignition characteristics.

$$CA10=a*ER+b*x_{PRF80}+c*x_{Ethanol}+d*x_{Butanol}+e*x_{Acetone}+f*T+g \qquad \textbf{Eq. 3.22}$$

Table 3.36. Coefficients for Eq. 3.22. Where x is volume percentage of component, T in °C

	Coef.							
	A	b	c	d	e	f	g	R^2
CA10	-25.37	-0.04	0.70	0.240	0.162	-0.19	38.49	0.507
CA10*	-25.37	-0.04	0.70	0.240	0.162	-0.19	38.49	0.715
* without case of Et20 fuel, T170°C								

The impact of intake temperature on auto-ignition properties is to promote reaction for all blends, but differently for each biofuel on the blends.

b) Blend of 40% Ethanol, Butanol, ABE and 60% PRF80

The equivalence ratio limits are summarized for various intake temperature in Figure 3.51. If one considers the same intake temperature, at 150°C for example, both ER limits are higher for alcohol and ABE 40% blends in comparison to pure PRF80 and the range of these limits is also extended.

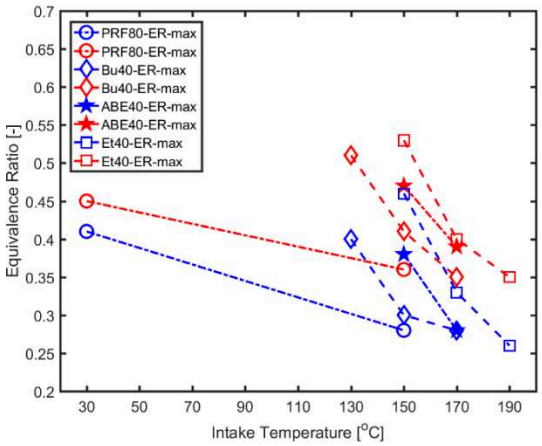

Figure 3.51. Equivalence ratio-Intake temperature limits of blends of Ethanol, Butanol, ABE (40%) and PRF80

Figure 3.52 illustrates the comparison of the in-cylinder pressure and HRR for 40% alcohol/ABE blends. The auto-ignition of blends is significantly different as: Bu40 auto-ignites the earliest even if the minimum equivalence ratio limit is the lowest one, Et40 is the latest for auto-ignition even if the ER is the highest one and ABE40 is between both alcohols blends at the same intake temperature for both limits conditions. It has to be also noted that no first stage of ignition is obtained with any blends with 40% of alcohol or ABE. The peak of HRR is decreased as the intake temperature increases, where the combustion phasing is advanced closer to TDC.

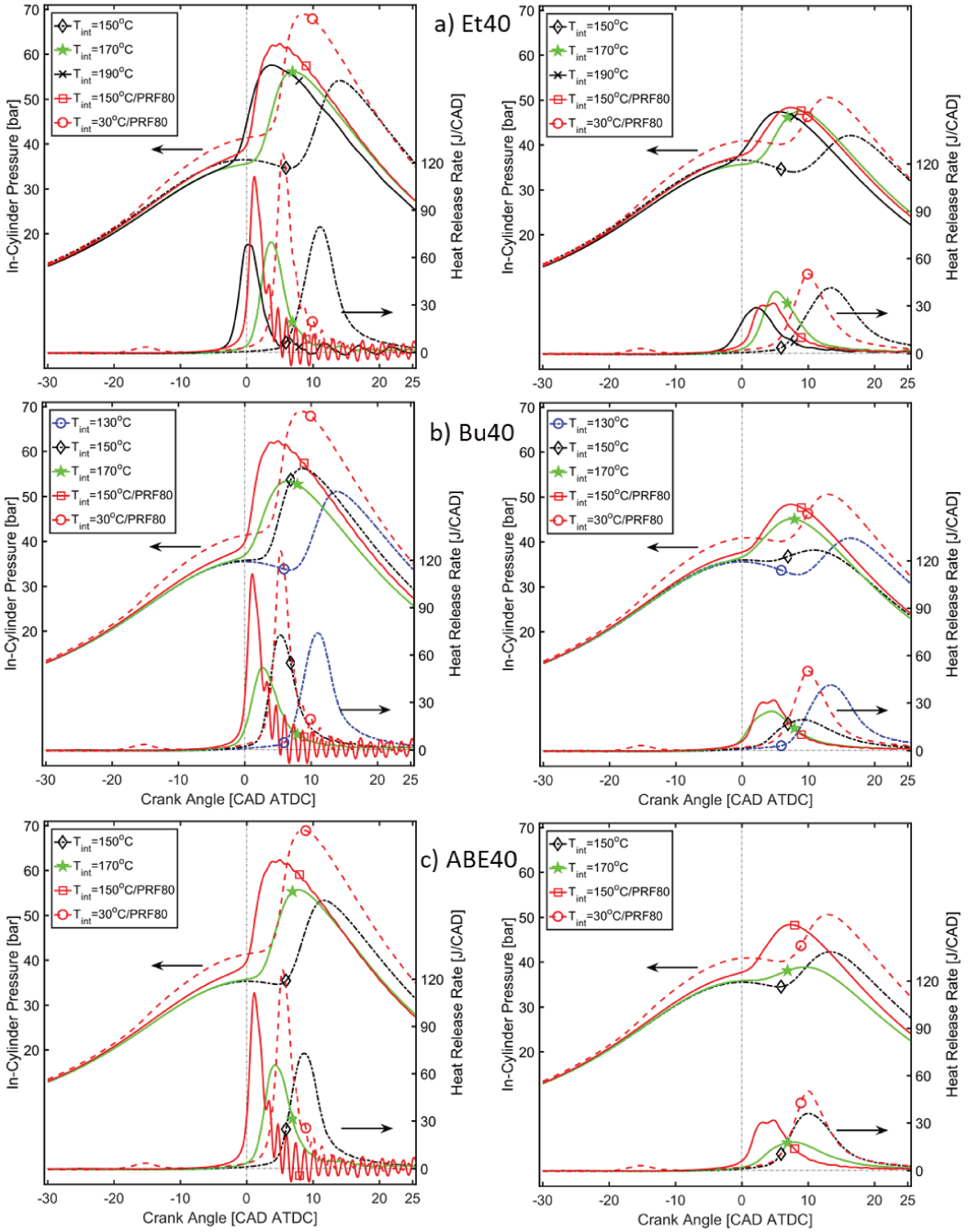

Figure 3.52. In-cylinder pressure and Heat release rate of a) Et40, b) Bu40 and c) ABE40 blend fuel on base comparison of PRF80 under limited Ringing intensity (left) and start burning (left)

Figure 3.53 a) and b) illustrate the change of trend for the performance, efficiencies and exhaust emissions. The IMEP decreases with the intake temperature for all fuels but more strongly for blends, as example for Bu40 blend fuel, the load was decreased by 4.5 bar to 2.3 bar IMEP (about 50%) while the intake temperature increases from 150 to 170°C, for maximum equivalence ratio behavior. At the intake temperature of 150°C, the maximum load is in the

following rank: PRF80 (2.8 bar) < Bu40 (3.5 bar) < ABE40 (3.9 bar) < Et40 (4.8 bar).

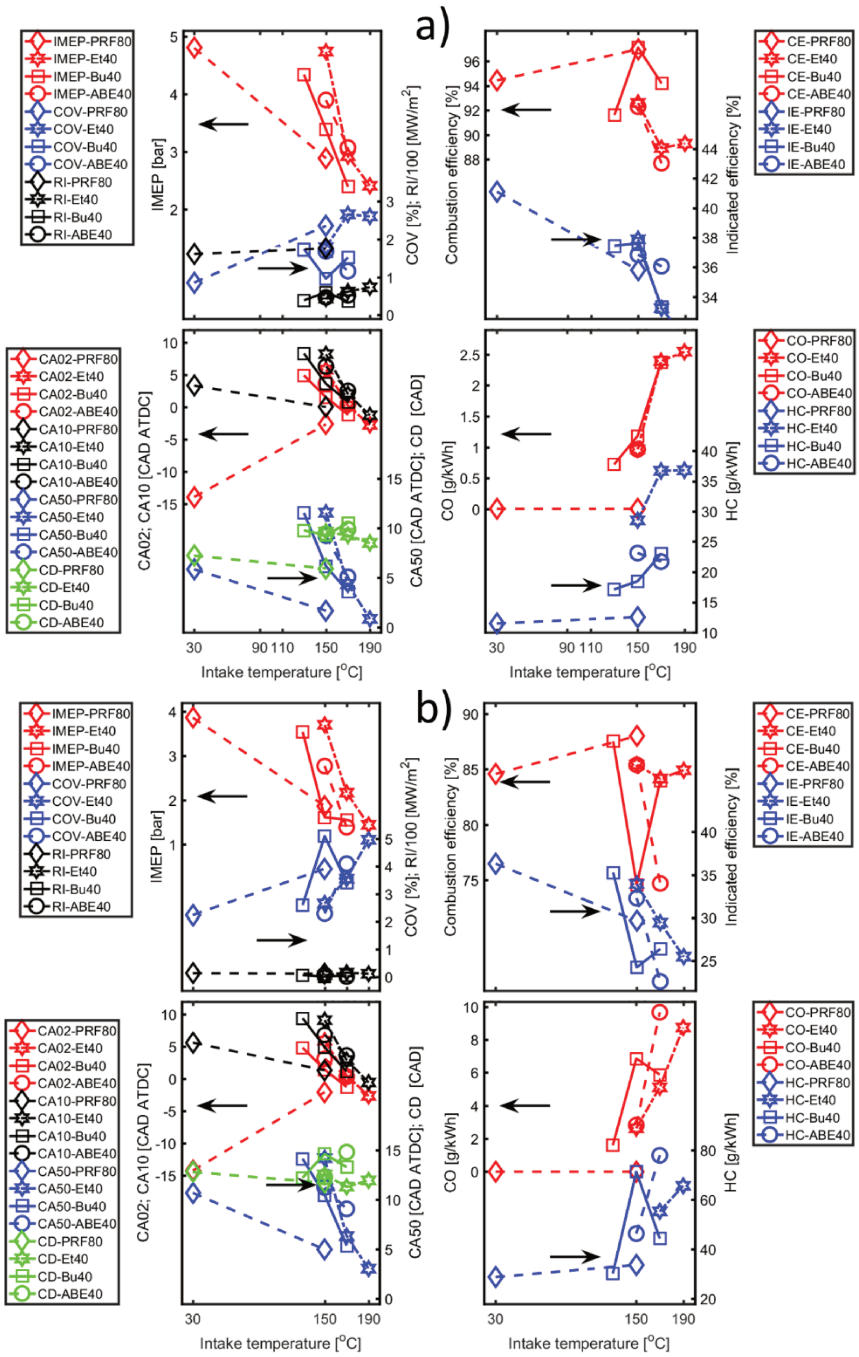

Figure 3.53. Performance, combustion process and emission for Blend 40% Ethanol, Butanol and ABE and 60% PRF80 with (a) maximum and (b) minimum equivalence ratio

As it can be seen, the maximum value of the combustion efficiency is observed at the intake temperature of 150°C condition, 97% for PRF80 and Bu40, 92% for Et40 and ABE40. The Et40, Bu40 and ABE40 have a maximum indicated efficiency at the intake temperature of 150°C, about 37-38%, while PRF80 observed minimum value of 36%.

The performance, combustion process and emissions parameters were modeled as linear function of the equivalence ratio and intake temperature, for Eq. 3.17 for PRF80, Et40, Bu40 and ABE40 with the coefficients shown in Table 3.37.

Table 3.37. Coefficients for Eq. 3.17, for Et40/60, Bu40/60 and ABE40/60. T in ^{o}C

	Coef.	**Fuel**					
		Et40	**Bu40**	**ABE40**	**Et60**	**Bu60**	**ABE60**
CA10	a	-29.25	-14.77	-13.33	-37.33	-17.09	-24.93
	b	-0.40	-0.27	-0.27	-0.40	-0.27	-0.27
	c	82.88	50.33	52.74	84.35	50.15	55.78
	R^2	0.741	0.746	0.868	0.807	0.667	0.675
CA50	a	-53.00	-36.03	-35.06	-66.88	-40.55	-51.03
	b	-0.56	-0.37	-0.37	-0.56	-0.37	-0.37
	c	121.78	77.56	81.28	124.83	77.70	85.38
	R^2	0.800	0.878	0.959	0.855	0.846	0.783
CD	a	-116.94	-59.55	-54.92	-132.88	-65.88	-66.77
	b	-0.63	-0.25	-0.25	-0.63	-0.25	-0.25
	c	163.37	71.72	72.78	167.26	72.85	76.39
	R^2	0.889	0.942	0.948	0.892	0.935	0.804
IMEP	a	8.72	10.23	10.61	8.91	10.34	9.83
	b	-0.02	-0.01	-0.01	-0.02	-0.01	-0.01
	c	2.92	0.50	0.40	2.90	0.48	0.70
	R^2	0.962	0.934	0.921	0.950	0.938	0.911
CE	a	144.67	168.67	154.91	165.33	176.15	179.83
	b	0.71	0.71	0.71	0.71	0.71	0.71
	c	-98.81	-89.55	-93.3	-103.95	-89.60	-103.75
	R^2	0.914	0.954	0.948	0.937	0.945	0.804
IE	a	41.7	48.6	56.5	48.3	43.7	50.7
	b	$-0.14*10^{-3}$	$-0.14*10^{-3}$	$-0.28*10^{-3}$	$0.14*10^{-3}$	$0.14*10^{-3}$	$0.14*10^{-3}$
	c	15.8	15.2	11.7	13.9	21.4	18.2
	R^2	0.919	0.645	0.692	0.926	0.696	0.742
RI	a	1874.1	1076.3	894.9	2117.3	1185.0	1311.3
	b	10.16	5.08	5.08	10.16	5.08	5.08
	c	-2425.7	-1145.4	-1133.1	-2480.8	-1162.8	-1275.4
	R^2	0.892	0.885	0.890	0.899	0.881	0.794
CO	a	-22.018	-20.345	-29.675	-45.819	-8.516	-35.33
	b	$14*10^{-6}$	$14*10^{-6}$	$14*10^{-6}$	$14*10^{-6}$	$14*10^{-6}$	$14*10^{-6}$
	c	11.94	10.25	14.03	23.13	10.71	17.25
	R^2	0.763	0.686	0.654	0.744	0.565	0.650
HC	a	-413.9	-444.5	-414.4	-507.5	-359.8	-528.4

	Coef.	Fuel					
		Et40	**Bu40**	**ABE40**	**Et60**	**Bu60**	**ABE60**
	b	-1.64	-1.64	-1.64	-1.64	-1.64	-1.64
	c	482.1	444.4	456.4	509.5	422.2	507.4
	R^2	0.866	0.975	0.947	0.958	0.958	0.875

The analyses of the results indicate the following:

- Under high alcohol/ABE ratio on blends, the correlation for auto-ignition timing and combustion phasing is not a true linear function of the intake temperature ($R^2 < 0.80$).

- The auto-ignition timing and combustion phasing are more sensitive to the intake temperature than PRF80 fuel.

- In comparison between 40% alcohol/ABE blends, a strong impact of equivalence ratio and intake temperature on auto-ignition timing and combustion phasing was observed for Et40.

- The CO and HC emissions are more sensitive to the equivalence ratio for ABE40 and Bu40 respectively.

The correlation between IMEP and energy content and intake temperature is presented in Eq. 3.18, the coefficients for Et40, Bu40 and ABE40 are shown in Table 3.38.

Table 3.38. Coefficients for Eq. 3.18. for Et40/60, Bu40/60 and ABE40/60 fuels

	Coef.	Fuel					
		Et40	**Bu40**	**ABE40**	**Et60**	**Bu60**	**ABE60**
IMEP	a	0.011	0.012	0.012	0.011	0.012	0.012
	b	0.01	0.01	0.01	0.01	0.01	0.01
	c	-3.49	-3.51	-3.63	-3.57	-3.51	-3.89
	R^2	0.996	0.985	0.981	0.996	0.993	0.991

In comparison between 40% alcohol/ABE blends, the sensitivity of IMEP to the energy content is the lowest for Et40.

**) Controlling combustion phasing*

As it can be seen in Figure 3.54 a), the impact of combustion phasing on IMEP is similar for Et40, Bu40 and ABE40 under maximum equivalence ratio behavior, with an increase of the IMEP as the combustion phasing is retarded, this trend is similar for 20% alcohol/ABE blends. At combustion phasing of 11 CAD ATDC, the most delayed combustion, the maximum load observed for Bu40 and Et40 are 4.3 and 4.6 bar IMEP, respectively. At combustion phasing

about 5 CAD ATDC, the load for maximum equivalence ratio is ranked as Bu40 (2.4 bar) < Et40 (2.9 bar) < ABE40 (3.1 bar) < PRF80 (4.9 bar).

The combustion efficiency is increased as the combustion phasing is the more delayed, for Et40, ABE40. The maximum combustion efficiency is obtained for Bu40 at combustion phasing of 6 CAD ATDC. The indicated efficiency is generally increased as the combustion phasing is more delayed for all fuels and both maximum and minimum equivalence ratio limits.

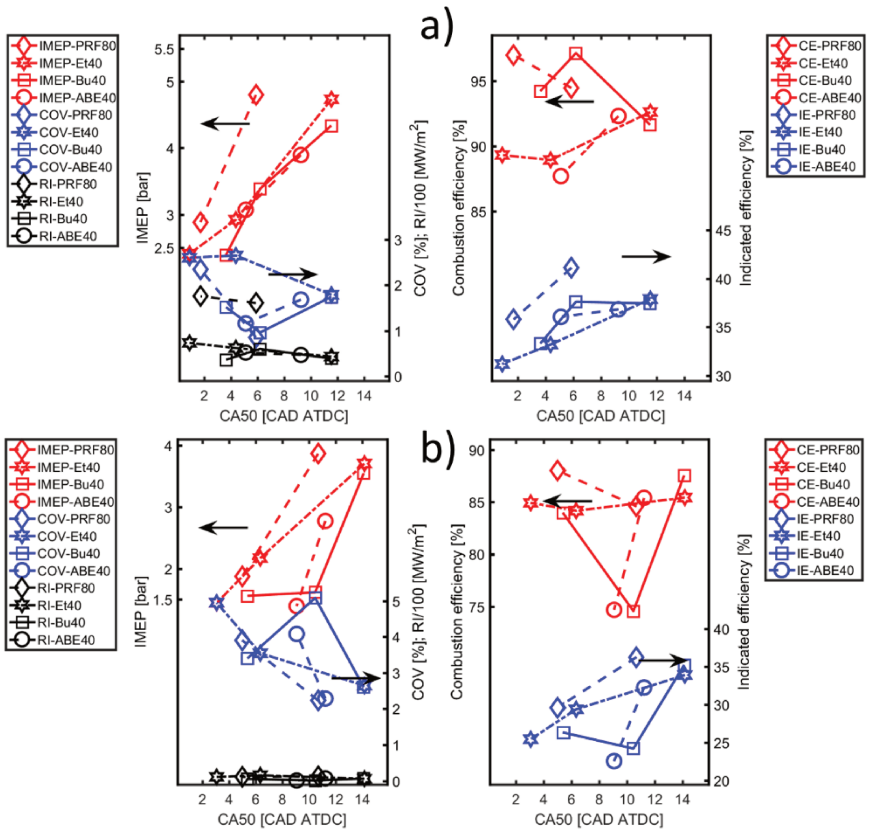

Figure 3.54. The performanceand combution parameters as a function of combustion phasing under (a) maximum and (b) minimum equivalence ratio behavior. (reproduction of data from Figure 3.53)

As shown in Figure 3.54 b), the trend of IMEP of Et40, Bu40 and ABE40 is different for all blends. The combustion efficiency is increased as combustion phasing more delayed for Et40 and ABE40. Minimum combustion efficiency of Bu40 blend fuel is obtained at the combustion phasing of 10 CAD ATDC.

The performance and efficiencies are modelled as a function of combustion phasing and intake temperature, in Eq. 3.21, with coefficients in Table 3.39. In comparison between these blends, the sensitivity of intake temperature on IMEP is the highest for Et40, but the sensitivity of combustion phasing on RI, CE and IE is the lowest for Et40 and the highest for ABE40.

Table 3.39. Coefficients for Eq. 3.21. for Et40/60, Bu40/60 and ABE40/60 fuels

	Coef.	Fuel					
		Et40	**Bu40**	**ABE40**	**Et60**	**Bu60**	**ABE60**
IMEP	a	-0.476	-0.258	-0.290	-0.571	-0.286	-0.381
	b	-0.200	-0.100	-0.100	-0.200	-0.100	-0.100
	c	40.15	20.03	21.36	39.99	19.90	21.32
	R^2	0.890	0.893	0.908	0.917	0.867	0.963
RI	a	-36.21	-43.33	-42.57	-41.00	-46.49	-51.09
	b	-10.16	-10.16	-10.16	-10.16	-10.16	-10.16
	c	2003.3	1915.4	2019.47	1988.79	1903.69	2013.47
	R^2	0.949	0.939	0.888	0.957	0.941	0.941
CE	a	-1.379	-2.203	-2.497	-1.567	-2.229	-2.660
	b	-0.426	-0.426	-0.426	-0.426	-0.426	-0.426
	c	160.03	162.85	169.06	159.50	160.87	164.35
	R^2	0.920	0.848	0.820	0.908	0.868	0.961
IE	a	-1.761	-2.561	-2.751	-2.058	-2.705	-3.098
	b	-0.702	-0.702	-0.702	-0.702	-0.702	-0.702
	c	163.26	160.51	169.42	162.67	159.07	165.82
	R^2	0.935	0.957	0.972	0.940	0.935	0.970

c) Blend of 60% Ethanol, Butanol, ABE and 40% PRF80

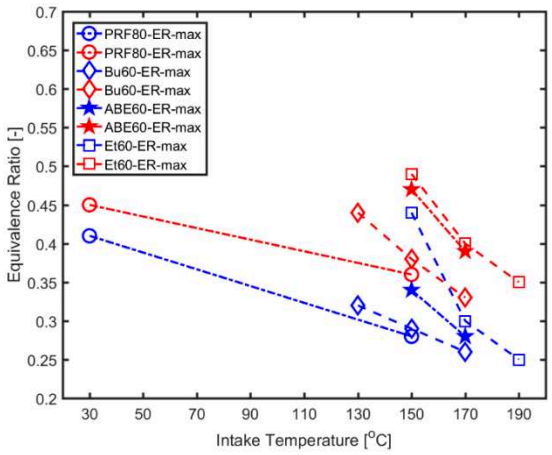

Figure 3.55. Equivalence ratio-Intake temperature limits of blends of Ethanol, Butanol, ABE (60%) and PRF80

The various intake temperature and equivalence ratio limitations for all 60% blends are summarized in Figure 3.55 with the plot, in Figure 3.56, of the in-cylinder pressure and HRR of Et60 (a), Bu60 (b) and ABE60 (c).

By more pre-heating the fuel-air charge up to 170ºC for Bu60, and 190ºC for ABE60, Et60, these blends can reach a start of combustion before TDC with combustion phasing close to

TDC under both of minimum and maximum equivalence ratio limits, as shown in Figure 3.56. The maximum peak of HRR of the blends is lower than that of PRF80, and is decreased as increasing the intake temperature, under maximum equivalence ratio conditions.

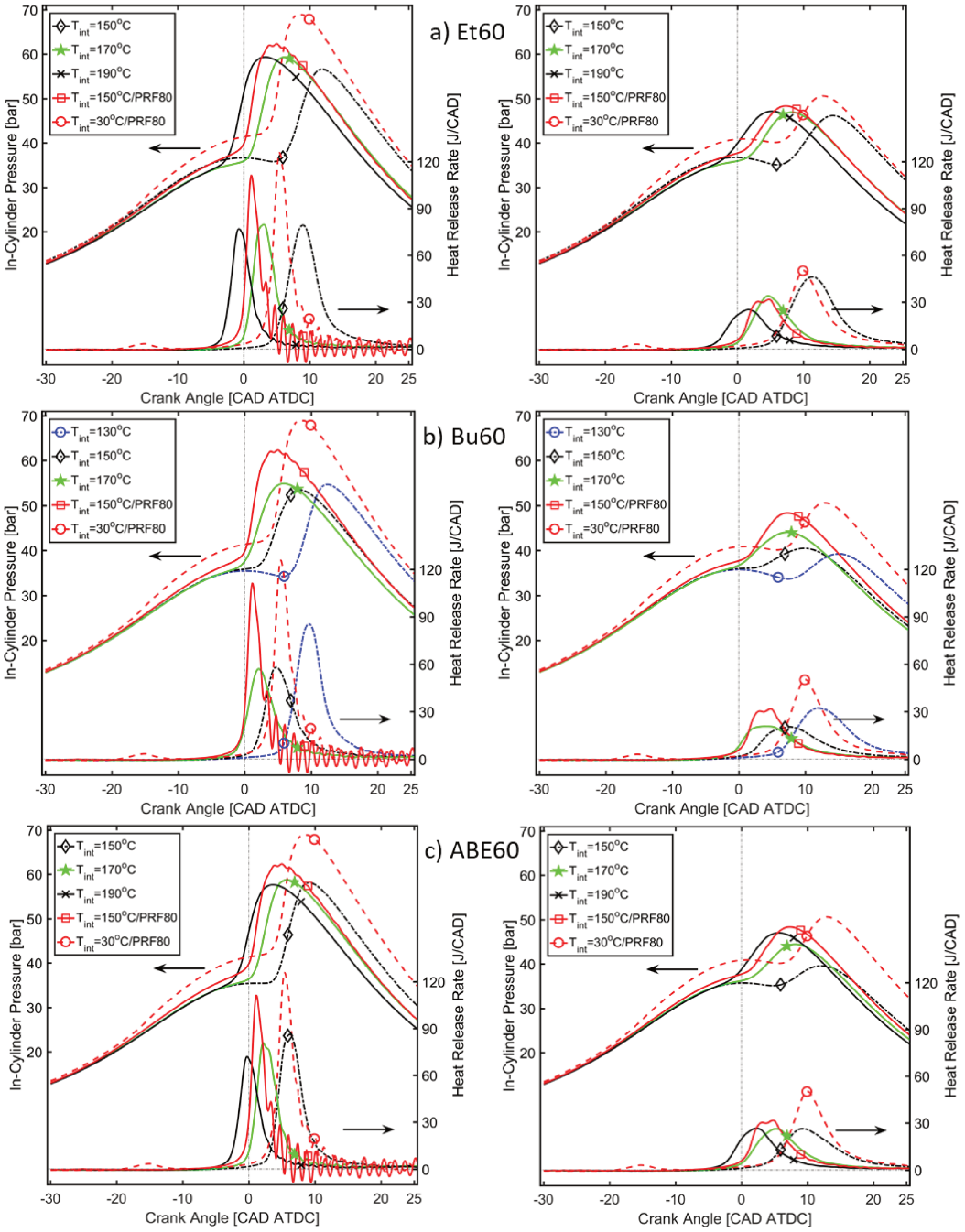

Figure 3.56. In-cylinder pressure and Heat release rate of a) Et60, b) Bu60 and c) ABE60 blend comparison of PRF80 under limited Ringing intensity (left) and start burning (left)

The Et60 and ABE60 blends, at 190°C intake temperature condition, have combustion phase occurs earlier than PRF80 fuel at 150°C intake temperature condition for both maximum and

minimum equivalence ratio conditions.

Under maximum equivalence ratio condition, the combustion phase for these blends are more delayed than PRF80 fuel at 30°C intake temperature, as example Et60 fuel at 150°C and ABE60 at 130°C. However, under minimum equivalence ratio condition, the combustion phase of PRF80 occurred at 30°C is the most delayed.

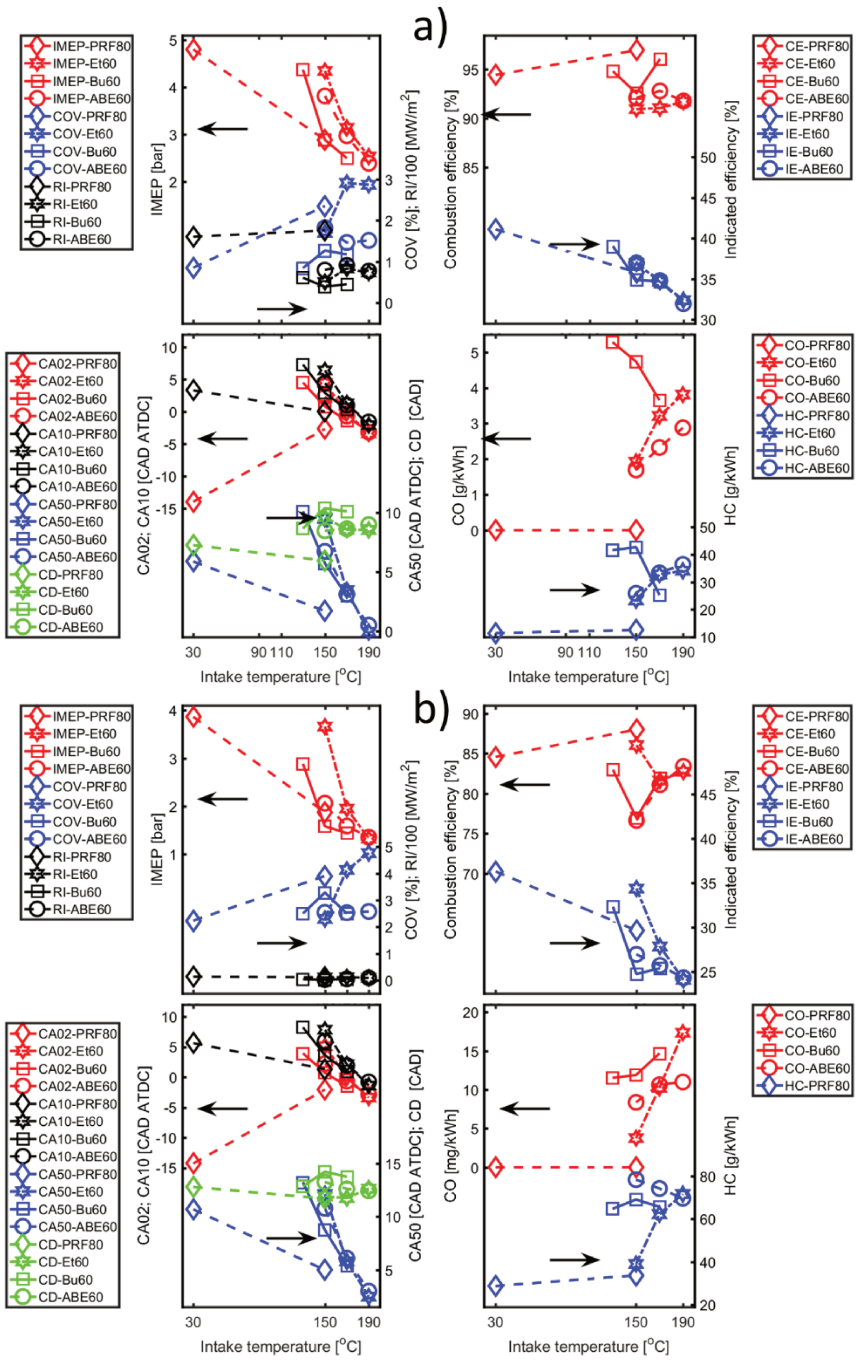

Figure 3.57. Performance, combustion process and emission for Blend 60% Ethanol, Butanol and ABE and 40% PRF80 with (a) maximum and (b) minimum equivalence ratio

Figure 3.57 a) and b) highlight the trend of performance, combustion process and emissions for blend of 60% alcohols or ABE as a function of the intake temperature with maximum and minimum equivalence ratio limits, respectively. The trend for IMEP is similar than ones for blends of 20% and 40%, which strongly decreases as the intake temperature increases. As example, the maximum load at 150ºC ranked as: PRF80 (2.9 bar) = Bu60 (2.9 bar) < ABE60 (3.9 bar) < Et60 (4.5 bar) and the minimum load at 150ºC: Bu60 (1.5 bar) = PRF80 (1.8 bar) < ABE60 (2.1 bar) < Et60 (3.6 bar).

Under higher intake temperature (i.e. 170 and 190ºC), small difference is observed for auto-ignition timing and combustion timing for all blends but at 150ºC, Et60 has the most delayed combustion development. The auto-ignition timing and combustion phasing of all blends test fuels (Et60, Bu60 and ABE60) are strongly advanced as intake temperature increasing from 150 to 190ºC for both maximum and minimum equivalence ratio, as comparison with PRF80 fuel.

The combustion efficiency for all blends has no significant difference at both minimum and maximum equivalence ratio limitations. The indicated efficiency is reduced as the intake temperature increases at both minimum and maximum equivalence ratio for all test fuels.

The HC and CO emissions observed for ABE60 and Et60 increase as a function of the intake temperature increase but decrease for Bu60.

The performance, combustion process and emissions parameters were modeled as a linear function of the equivalence ratio and intake temperature, for Eq. 3.17 for Et60, Bu60 and ABE60 with the coefficients shown in Table 3.37. The analyses of the results indicate the following:

- For auto-ignition timing (CA10) and combustion phasing (CA50), the R^2 observed is less than 0.85, as similar with 40% alcohol/ABE blends. The auto-ignition timing, combustion phasing and combustion duration of Et60 are more sensitive to the intake temperature and equivalence ratio than Bu60 and ABE60, as Et60 > ABE60 > Bu60.

- The combustion efficiency and indicated efficiency of ABE60 is most sensitivity of equivalence ratio.

- CO and HC emissions of Bu60 are the lowest sensitivity to the equivalence ratio, ranked as Et60 > ABE60 > Bu60 for CO and ABE60 > Et60 > Bu60 for HC.

The correlation between IMEP and energy content and intake temperature is presented in Eq. 3.18, the coefficients for Et60, Bu40 and ABE60 are shown in Table 3.38. In comparison between 60% alcohol/ABE blends, the sensitivity of energy content of Et60 is the lowest, as similar with 40% alcohol/ABE blends.

**) Controlling combustion phasing*

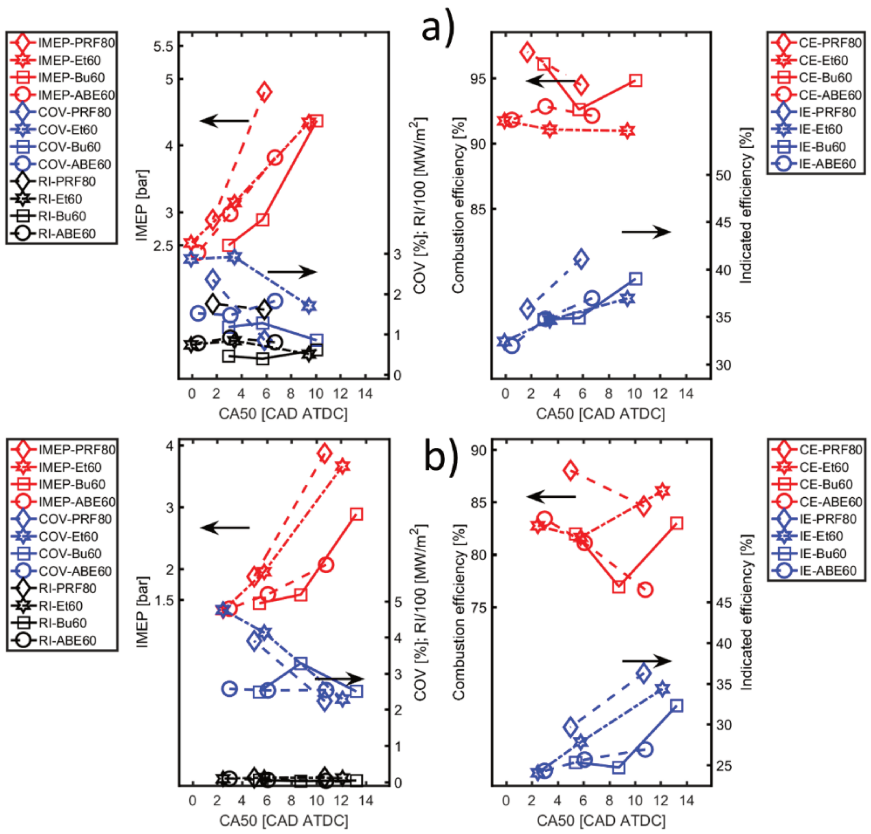

Figure 3.58. The performance and combution parameters as a function of combustion phasing under (a) maximum and (b) minimum equivalence ratio behavior. (reproduction of data from Figure 3.57)

As shown in Figure 3.58 a), the evolution of the IMEP as a function of the combustion phasing is identical for ABE60 and Et60 and not for Bu60, which provides lower values of IMEP. On the contrary, under leaner mixture limit, before misfire, in Figure 3.58 b), the evolution of the IMEP and the level of IMEP values are identical for ABE60 and Bu60 while ET60 is upper and closer to the PRF80 one.

The performance and efficiencies are modeled as a function of combustion phasing and intake temperature, in Eq. 3.20, with coefficients in Table 3.37. The analyses of the results indicate the following:

- The combustion phasing and intake temperature strongly influence the IMEP for Et60.

- The RI, CE and IE are more sensitive to the combustion phasing as: ABE60 > Bu60 > Et60.

d) Conclusions

The trend decreasing of LTR phase of Bu20 and ABE20, as compared with PRF80 fuel, under lower intake temperature and boosting behavior.

The comparison of n-butanol, ABE et ethanol blend with gasoline-like PRF80 showed that the butanol blend auto-ignites earliest for the lowest possible equivalence ratio, following by ABE blend, and the Ethanol one with the highest minimum equivalence ratio limit for all alcohols volume fraction (20%, 40% and 60%). This trend is similar to that already observed by He et al. [139] in HCCI combustion or by Dagaut and Togbe [140] in Jet-Stirred Reactor. This confirms that Butanol blend is more reactive at low initial temperature conditions than Ethanol blend. As ABE is composed of three components (acetone, butanol and ethanol), the combustion development speed is also intermediate due to the intermediate reactivity properties of ethanol and butanol.

3.3.2.4. Influence of EGR on HCCI mode of Alcohols blends

The influence of EGR ratio and intake pressure on combustion process for all blends is compared in Figure 3.59, Figure 3.62 and Figure 3.65, respectively, with intake conditions summarized in Table 3.40.

Table 3.40. Intake conditions

N₀ Case	**Fuel**	**Intake temperature [°C]**	**Equivalence ratio**
1	PRF80	100	0.30
2	Et20	170	0.45
3	Bu20	150	0.42
4	ABE20	150	0.36
5	Et40	170	0.45
6	Bu40	150	0.32
7	ABE40	150	0.41
8	Et60	170	0.42
9	Bu60	150	0.32
10	ABE60	170	0.40

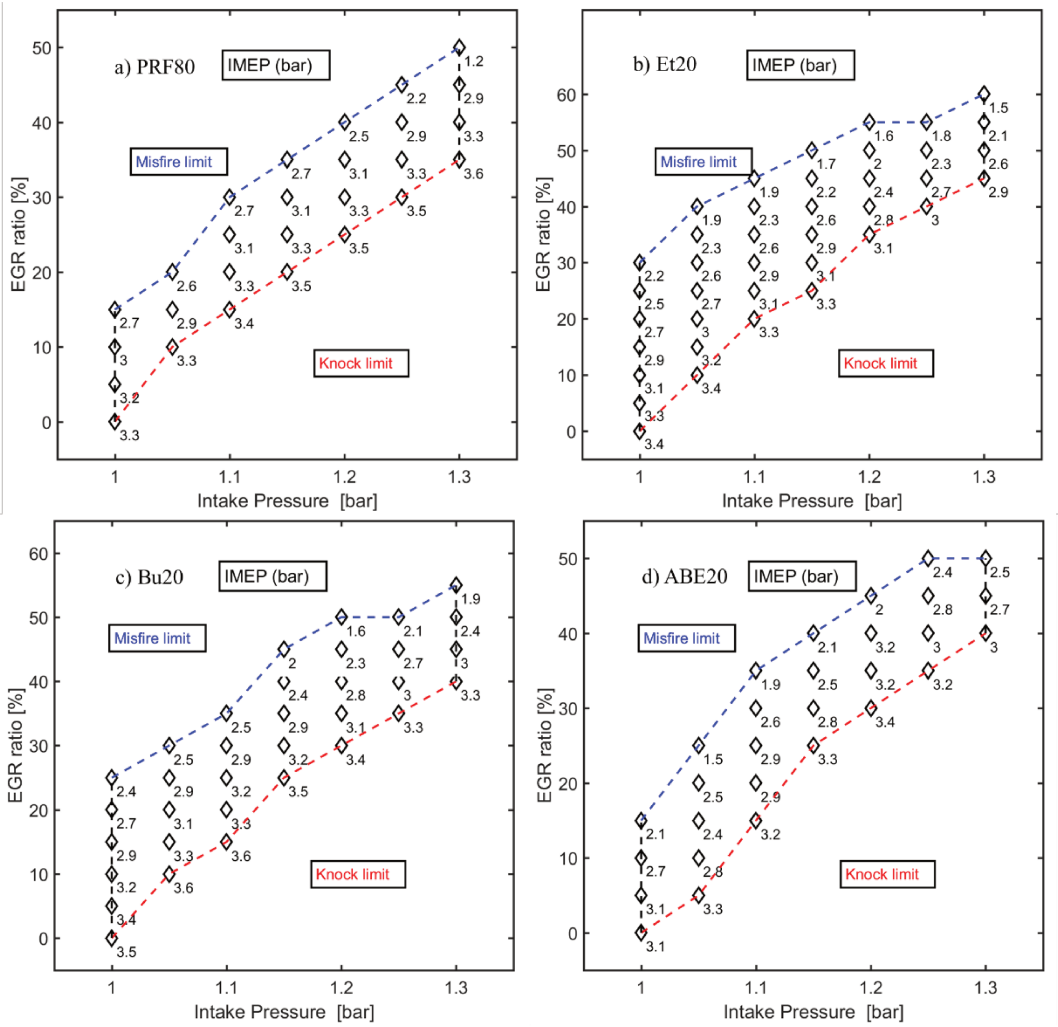

Figure 3.59. IMEP range of HCCI mode based on intake pressure – EGR ratio for a) PRF80 and blend of 80% PRF80 and 20% alcohols/ABE: b) Et20, c) Bu20 and d) ABE20

As seen at the intake pressure of 1 bar condition, the Et20 can accept high level of EGR, up to 30%, then Bu20 is 25% and PRF80 and ABE20 is 15%. Under highest intake pressure of 1.3 bar condition, the maximum load is reduced for Et20 (from 3.4 to 3 bar), Bu20 (3.5 to 3.3 bar) and ABE20 (3.1 to 3.0 bar), while that of PRF80 is increased from 3.5 to 3.5 bar. The minimum load observed for these fuels in order: PRF80 (1.2 bar) < Et20 (1.5 bar) = ABE20 (1.5 bar) < Bu20 (1.6 bar). The conditions to achieve minimum load are different for each fuel: PRF80 and Et20 at the highest intake pressure and EGR ratio, ABE20 at 1.05 bar intake pressure and 25% EGR, Bu20 at 1.2 bar intake pressure and 50% EGR.

Figure 3.60 highlights the comparison of the in-cylinder pressure and HRR for Et20 (b), Bu20 (c), ABE20 (d) with PRF80 (a) for 3 intake pressures and 2 EGR limits.

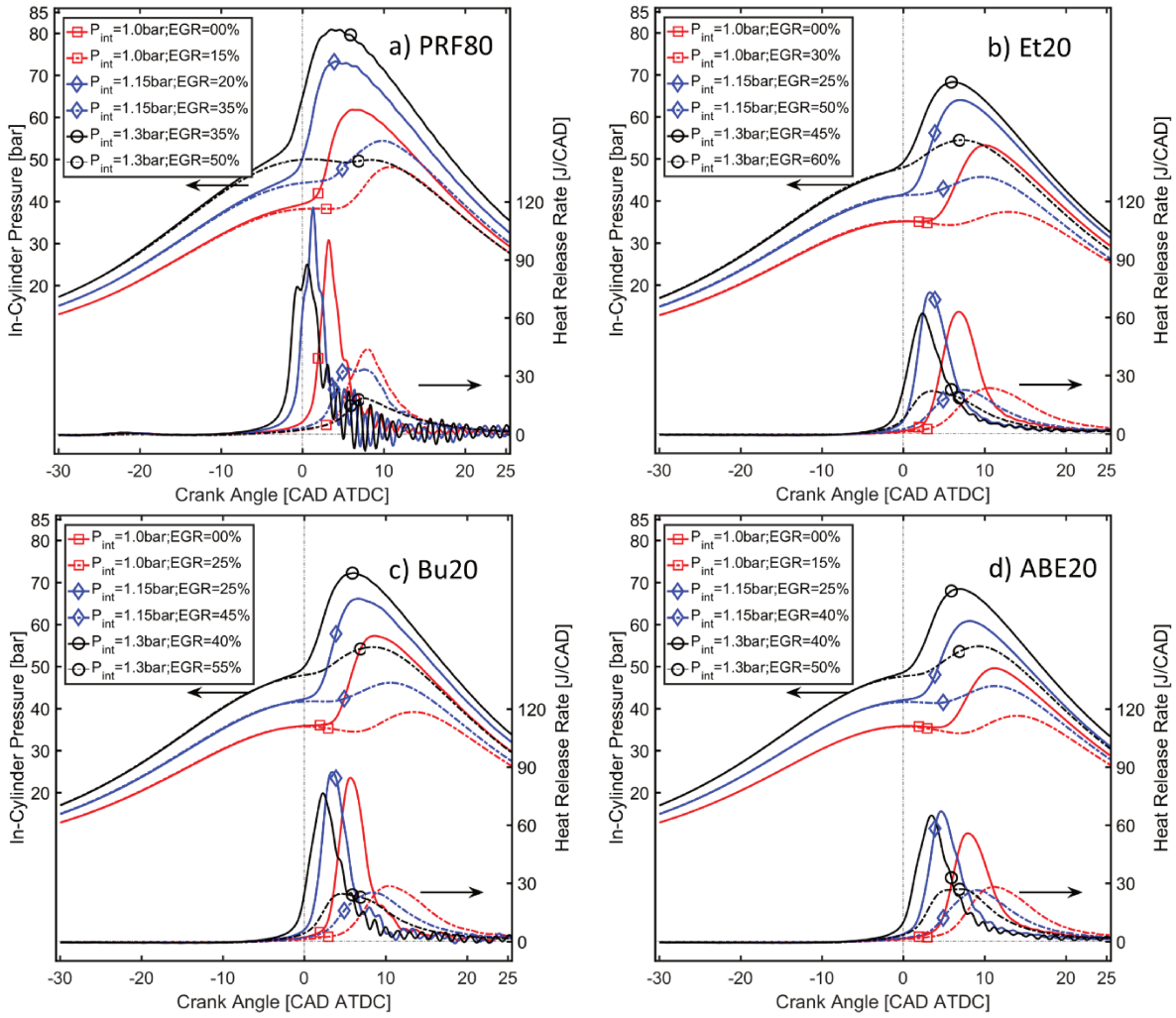

Figure 3.60. In-cylinder pressure and HRR for pure PRF80 and Ethanol/Butanol/ABE of 20% and PRF80 of 80% in volume blends under limitation of EGR, and three intake pressure levels of 1.0, 1.15 and 1.3 bar

The peak levels of HRR of the blends are significantly lower than PRF80, while the same IMEP obtained about 3 - 3.4 bar. As seen HRR curves of these test fuels, the intake pressure of 1.3 bar under minimum EGR ratio achieve the peak of HRR closest TDC.

The impact of butanol and ABE on the EGR limit is similar than previously observed with ethanol, for 20%, 40% and 60% alcohols/ABE blends. Performance, combustion and emissions characteristics of 20%, 40% and 60% alcohols/ABE are illustrated in Figure 3.61, Figure 3.64 and Figure 3.67, respectively. To well compare between these blends, the sensitivity analysis of impact of ethanol, butanol and ABE blends on operating, combustion and emissions characteristics is used in this section.

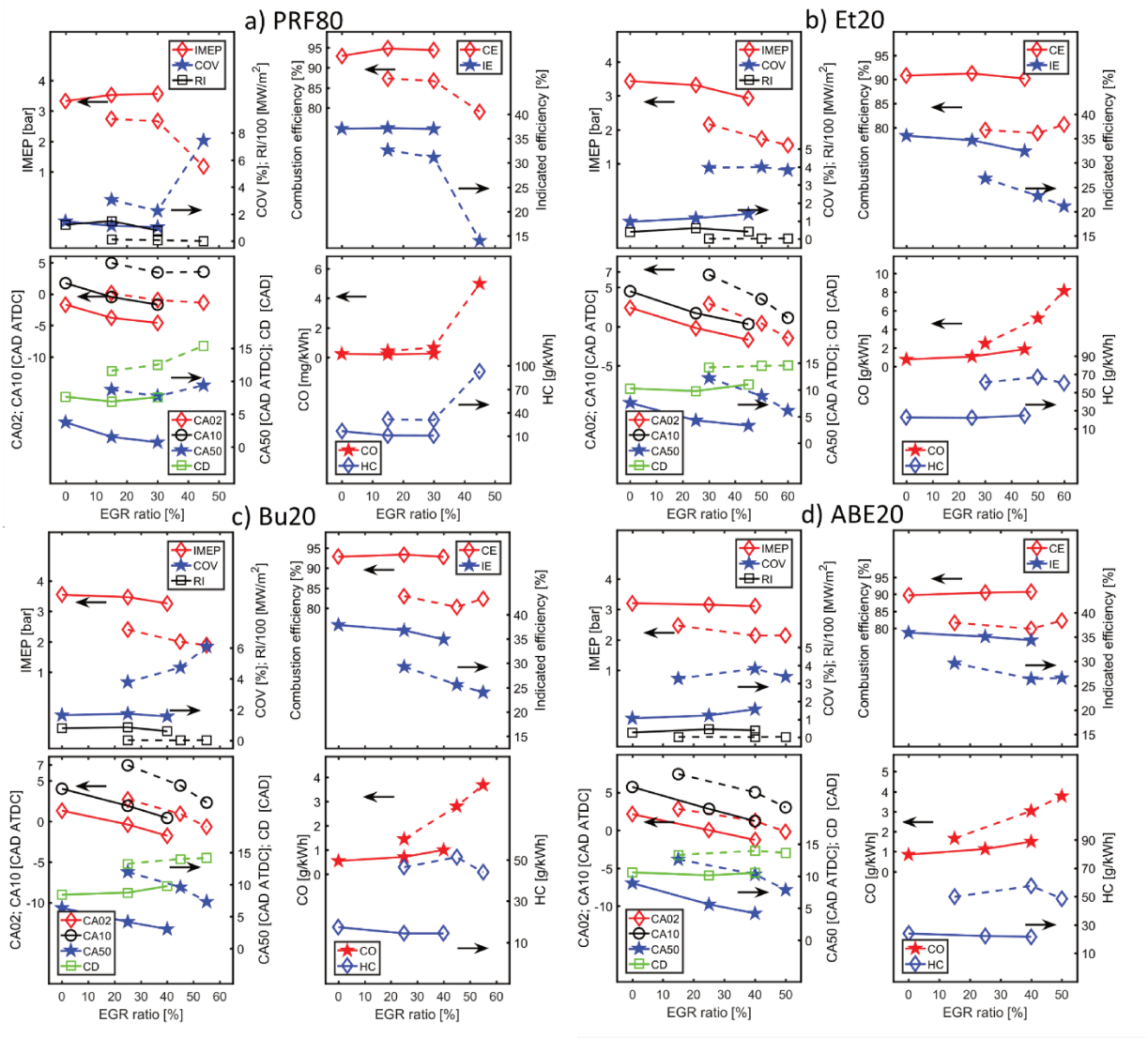

Figure 3.61. Performance, combustion and emissions characteristics of a) PRF80 and alcohols/ABE of 20% in volume and PRF80 of 80%: b) Et20, c) Bu20 and d) ABE20. Solid line and Dashed line for lower and higher EGR level, respectively

The performance, combustion process and emissions parameters were modeled as a linear function of the EGR and intake pressure, for Eq. 3.15 for Et20, Bu20 and ABE20 with the coefficients shown in Table 3.28 and Table 3.41.

Table 3.41. Coefficient for Eq. 3.15. EGR in % and intake pressure in bar

	Coef.	**Fuel**					
		Bu20	**ABE20**	**Bu40**	**ABE40**	**Bu60**	**ABE60**
CA10	a	0.289	0.276	0.261	0.243	0.231	0.243
	b	-55.0	-55.0	-55.0	-55.0	-55.0	-55.0
	c	57.03	59.08	57.59	60.49	56.16	54.86
	R^2	0.872	0.911	0.816	0.922	0.751	0.659

	Coef.	Fuel					
		Bu20	**ABE20**	**Bu40**	**ABE40**	**Bu60**	**ABE60**
CA50	a	0.427	0.407	0.396	0.368	0.349	0.362
	b	-78.2	-78.2	-78.2	-78.2	-78.2	-78.2
	c	81.72	84.86	82.52	86.45	81.41	79.64
	R^2	0.790	0.815	0.764	0.931	0.716	0.629
IMEP	a	-0.081	-0.075	-0.081	-0.079	-0.072	-0.068
	b	9.09	9.09	9.09	9.09	9.09	9.09
	c	-4.98	-5.50	-5.39	-4.87	-5.59	-4.58
	R^2	0.954	0.957	0.936	0.968	0.909	0.877
RI	a	-9.92	-9.17	-8.83	-8.65	-7.87	-8.38
	b	1429.0	1429.0	1429.0	1429.0	1429.0	1429.0
	c	-1288.5	-1350.2	-1335.5	-1347.3	-1331.2	-1309.4
	R^2	0.865	0.871	0.794	0.894	0.746	0.686
CE	a	-0.740	-0.717	-0.72	-0.70	-0.481	-5.11
	b	93.13	93.13	93.13	93.13	93.13	931.3
	c	5.43	0.18	2.57	1.41	-8.79	-798.4
	R^2	0.939	0.956	0.933	0.971	0.900	0.554
EI	a	-0.576	-0.541	-0.60	0.52	-0.56	-0.48
	b	58.6	58.6	58.6	58.6	58.6	58.6
	c	-16.4	-19.8	-17.3	-18.5	-17.4	-18.9
	R^2	0.945	0.937	0.911	0.956	0.888	0.878
CO	a	0.047	0.065	0.184	0.096	0.301	0.187
	b	-0.03	-0.03	-0.03	-0.03	-0.03	-0.03
	c	-0.032	0.157	-1.19	0.201	0.880	-0.120
	R^2	0.552	0.472	0.407	0.635	0.618	0.623
HC	a	14.41	14.27	13.30	13.54	11.59	12.35
	b	-2434.0	-2434.0	-2434.0	-2434.0	-2434.0	-2434.0
	c	2337.0	2378.1	2367.6	2365.7	2369.0	2346.9
	R^2	0.730	0.788	0.710	0.833	0.663	0.548

Some general trends, with regard to 20% Ethanol/Butanol/ABE blends were identified:

- The Et20, Bu20 and ABE20 fuels provide low sensitivity of CA10, CA50, CE and IE to the EGR ratio and ranked as Et20 < ABE20 < Bu20 < PRF80.

- The impact of EGR ratio on IMEP, RI is ranked as ABE20 < Et20 < Bu20 < PRF80.

- The CO and HC emissions have sensitivity of EGR as PRF80 < Bu20 < ABE20 < Et20, and sensitivity of intake pressure for Et20, Bu20 and ABE20, strongly more than for PRF80 fuel.

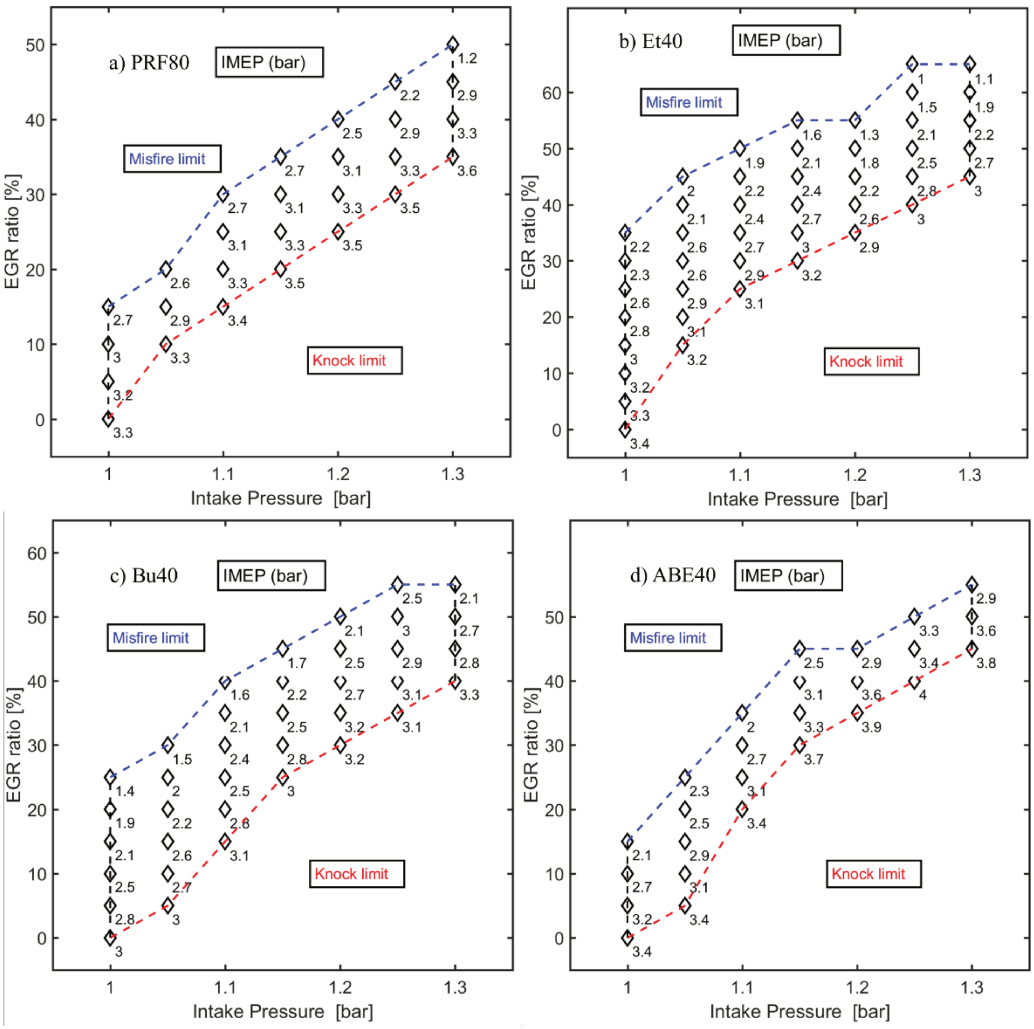

Figure 3.62. IMEP range of HCCI mode based on intake pressure – EGR ratio for a) PRF80 and blend of 60% PRF80 and 40% alcohols/ABE: b) Et40, c) Bu40 and d) ABE40

Under intake pressure of 1 bar, the maximum EGR ratio can be adjusted to these fuels in order: PRF80 (15%EGR) = ABE40 (15%EGR) < Bu40 (25%EGR) < Et40 (35%EGR). The Bu40 and ABE40 can reach higher maximum load under boosted conditions, as similar with PRF80. In contrary, the maximum load of Et40 is reduced from 3.4 to 3 bar while intake pressure increases from 1 to 1.3 bar.

The Et40 has a minimum load of 1 bar, under intake pressure of 1.25 bar and 65% EGR. The Bu40 and ABE40 fuels were difficult established low load by adjusted EGR at higher intake pressure conditions, as example the ABE40 reach minimum load of 2 bar, under intake pressure of 1.1 bar and 35% EGR, and Bu40 reaches minimum load of 1.4 bar, under intake pressure of 1 bar and 25% EGR.

Figure 3.63 illustrates a comparison of the in-cylinder pressure and HRR of Et40 blend (b),

Bu40 blend (c), ABE40 blend (d) and PRF80 (a), under three intake pressure levels and two limitation levels of EGR ratio.

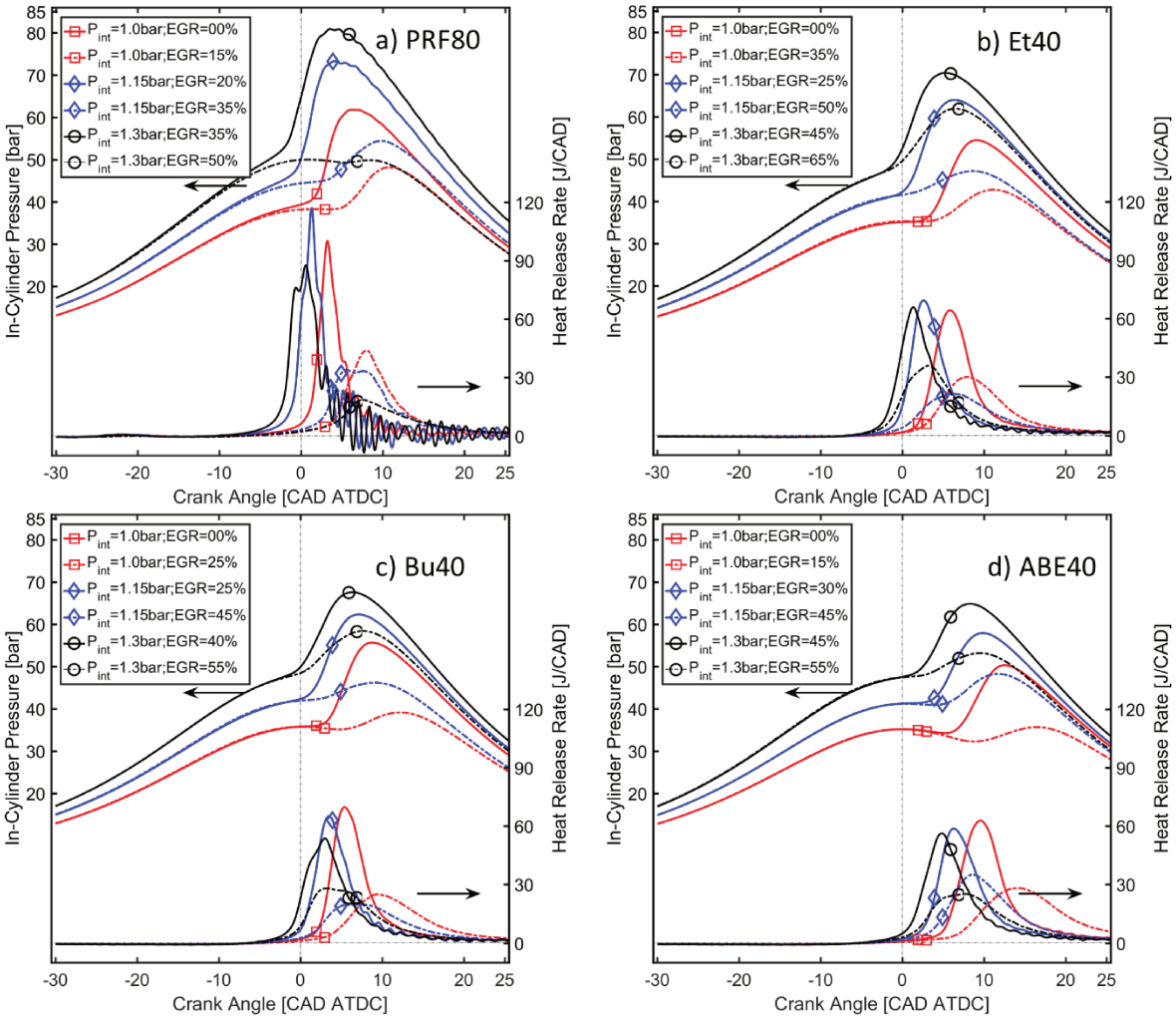

Figure 3.63. In-cylinder pressure and HRR for pure PRF80 and Ethanol/Butanol/ABE of 40% and PRF80 of 60% in volume blends under EGR limits, and three intake pressure levels of 1.0, 1.15 and 1.3 bar

The peak levels of HRR of the blends are around 60 J/CAD, significantly lower than PRF80, while the same IMEP obtained about 3 - 3.4 bar. For the ABE40 fuel, the combustion phasing of the maximum load is the most delayed.

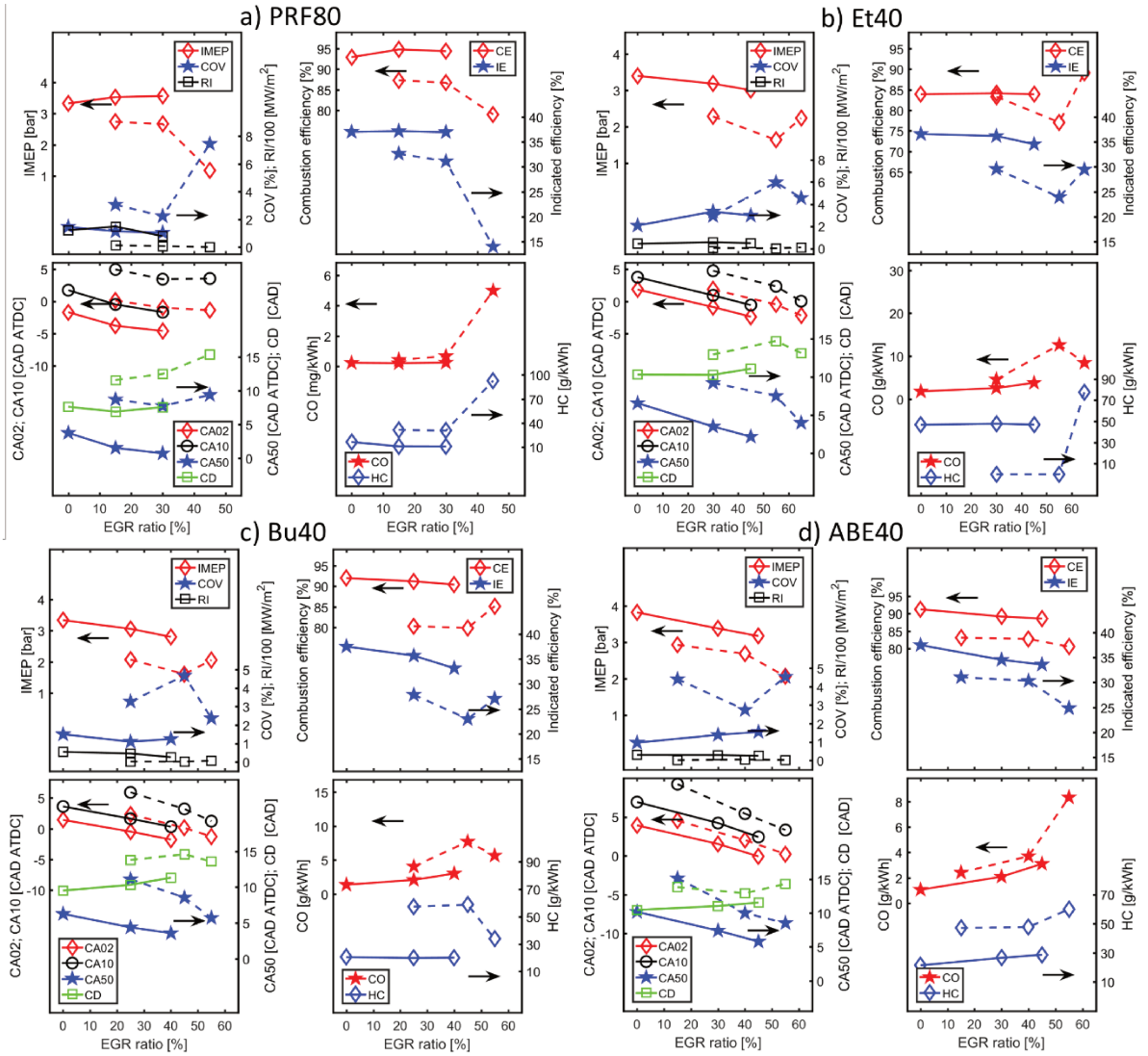

Figure 3.64. Performance, combustion and emissions characteristics of a) PRF80 and alcohols/ABE of 40% in volume and PRF80 of 60%: b) Et40, c) Bu40 and d) ABE40. Solid line and Dashed line for lower and higher EGR level, respectively.

The performance, combustion process and emissions parameters were modeled as a linear function of the EGR and intake pressure, for Eq. 3.15 for Et40, Bu40 and ABE40 with the coefficients shown in Table 3.28 and Table 3.41. Some general trends, with regard to 40% Ethanol/Butanol/ABE blends were identified for the impact of EGR and intake pressure:

- The sensitivity of auto-ignition timing and combustion phasing on EGR ratio of Bu40 is little bit more than Et40 and Et40.

- The EGR ratio and intake pressure strongly impact CE for Et40.

- RI is less sensitive to the EGR ratio and CO and HC emissions more sensitive for all 40% blends than PRF80.

- In comparison between these blends, the sensitivity of HC emission on EGR is similar, and of CO in this order: Et40 (0.266) > Bu40 (0.184) > ABE40 (0.096).

For 60% alcohols/ABE, the EGR range can be more extended as seen Figure 3.65. The maximum load of blends was generally reduced as increasing the intake pressure from 1 to 1.3 bar at maximum EGR limit. These blends can allow low load at high intake pressure condition of 1.3 bar.

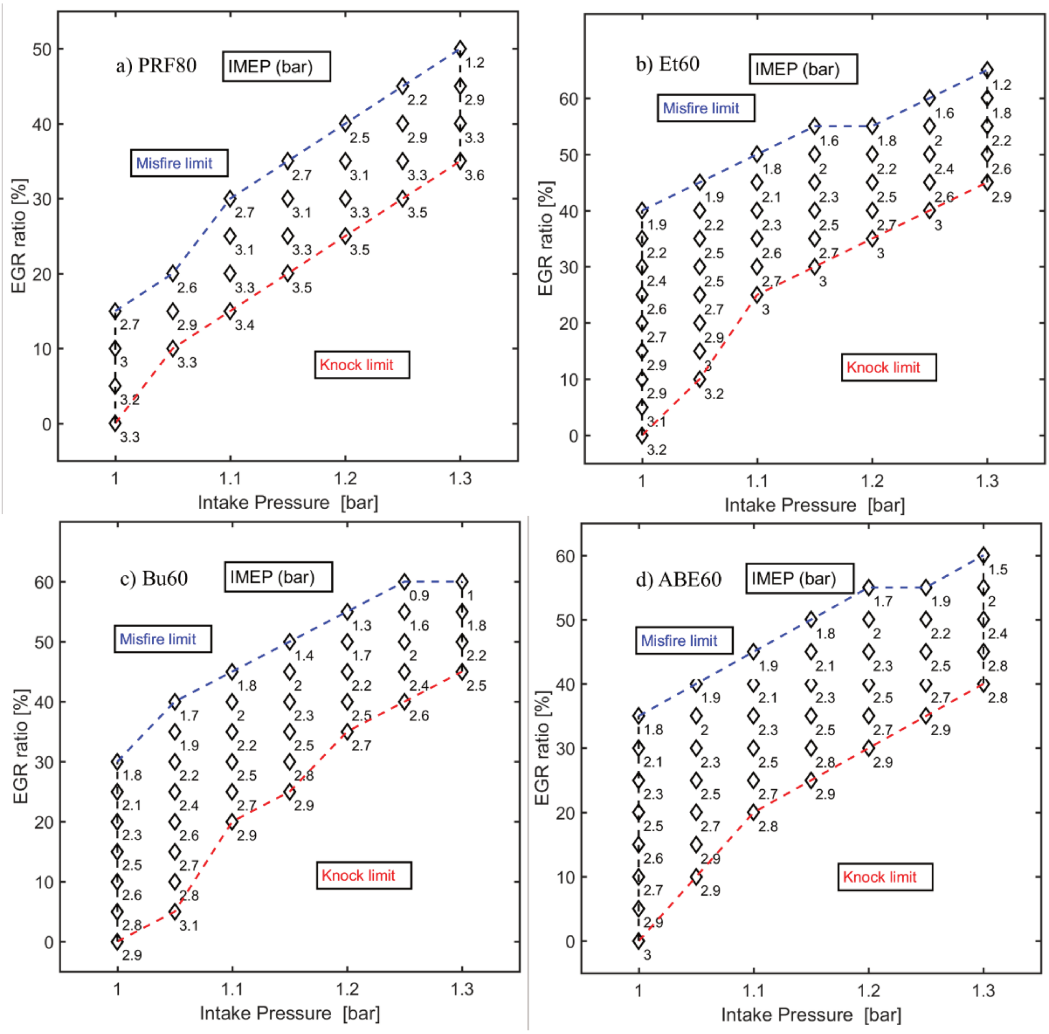

Figure 3.65. IMEP range of HCCI mode based on intake pressure – EGR ratio for a) PRF80 and blend of 40% PRF80 and 60% alcohols/ABE: b) Et60, c) Bu60 and d) ABE60

Figure 3.66 illustrates the comparison of the in-cylinder pressure and HRR of Et60 blend (b), Bu60 blend (c), ABE60 blend (d) and PRF80 (a), with three intake pressure level and two corresponding EGR ratio limits.

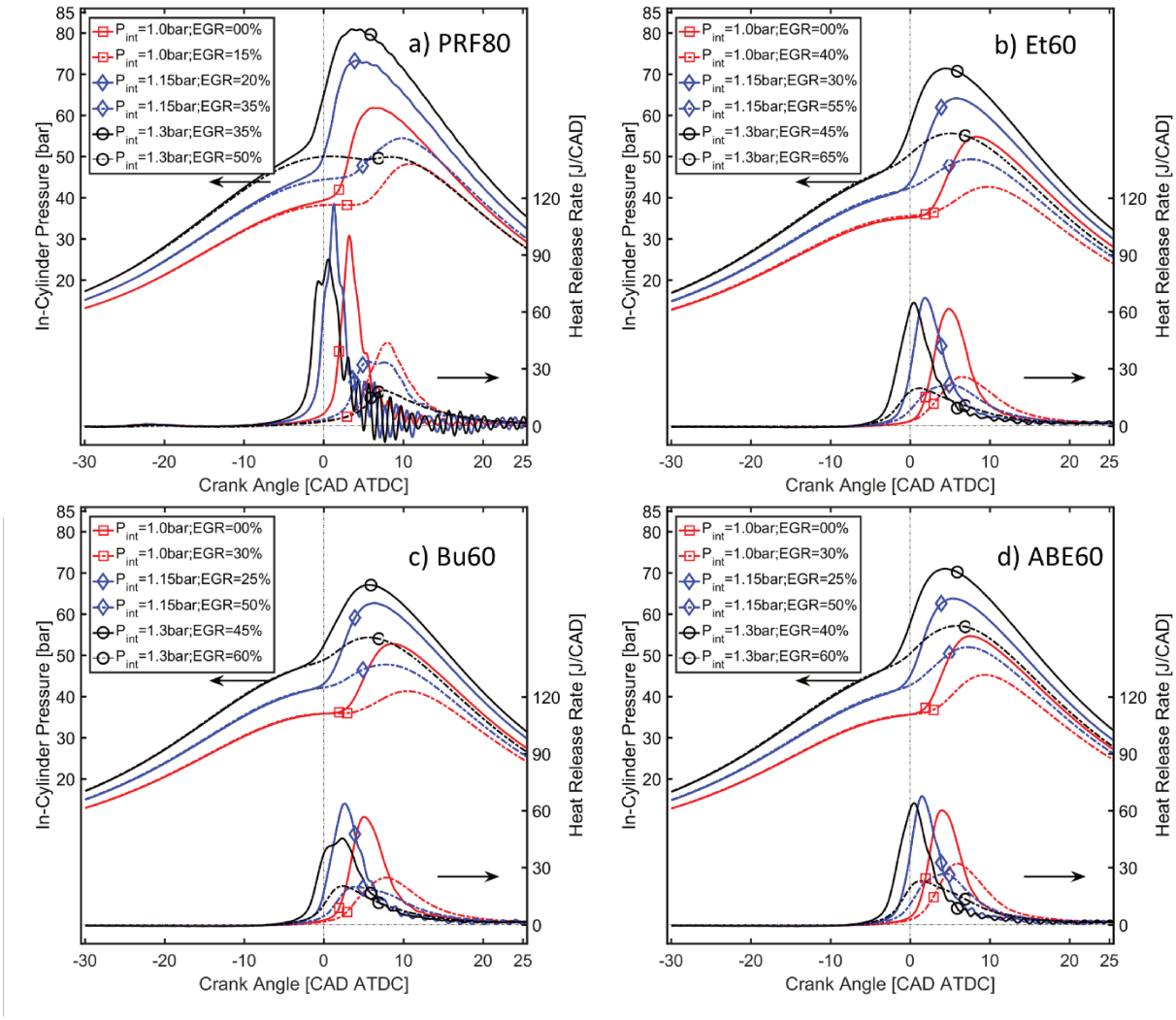

Figure 3.66. In-cylinder pressure and HRR for pure PRF80 and Ethanol/Butanol/ABE of 60% and PRF80 of 40% in volume blends under limitation of EGR, and three intake pressure level of 1.0, 1.15 and 1.3 bar

As similar with 20% and 40% alcohols/ABE blends, the peak levels of HRR for Et60, Bu60 and ABE60 are around 60 J/CAD, while IMEP obtained about 2.9 - 3.2 bar.

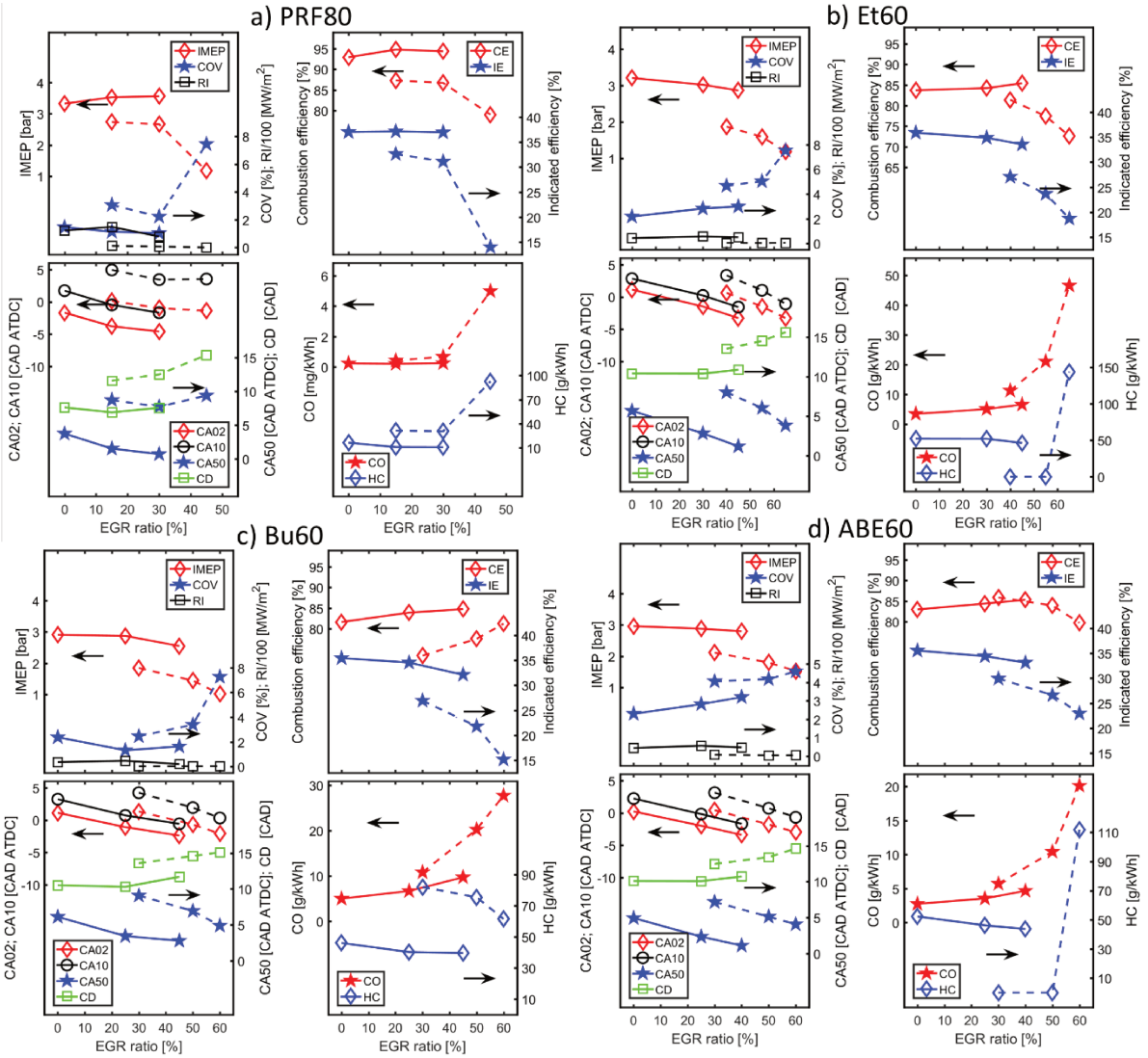

Figure 3.67. Performance, combustion and emissions characteristics of a) PRF80 and alcohols/ABE of 60% in volume and PRF80 of 40%: b) Et60, c) Bu60 and d) ABE60. Solid line and Dashed line for lower and higher EGR level limits, respectively.

The performance, combustion process and emissions parameters were modeled as a linear function of the EGR and intake pressure, for Eq. 3.15 for Et60, Bu60 and ABE60 with the coefficients shown in Table 3.28 and Table 3.41. Some general trends, with regard to 60% Ethanol/Butanol/ABE blends HCCI mode, were identified for impact of EGR and intake pressure:

- R^2 value of impact of EGR ratio and intake pressure for Et60, Bu60 and ABE60 are quite low (<0.80), this effect is not linear.

- The impact of EGR ratio on auto-ignition timing and combustion phasing is ranked as Et60 < Bu60 < ABE60.

- The impact of EGR and intake pressure on CE is more important for Et60 and ABE60 , and similar for Et40 fuel than for PRF80.

- The RI is less sensitive to the EGR ratio on and contrary to CO and HC emissions, for Et60, Bu60 and ABE60 than for 20% and 40% blends.

- The sensitivity of HC and CO emission on EGR is similar in order: Et60 (0.362) > Bu60 (0.301) > ABE60 (0.187).

**) Conclusions*

The comparisons of Ethanol, Butanol and ABE blends for HCCI combustion mode is evaluated, the conclusions of this section can be drawn as follows:

- Single phase HRR of HCCI combustion mode was observed with fuel blends more than 40% Butanol, ABE and all blends of ethanol under these engine conditions tested.

- Under naturally aspirated condition, the intake temperature range to establish HCCI mode of alcohols blend is ranked as: Butanol > ABE > Ethanol.

3.4. Conclusions

The new experiments for Ethanol, Butanol and ABE gasoline blends in HCCI combustion mode are provided across a range of intake conditions: temperature, pressure and equivalence ratio, including blending effects on LTR region, HRR, engine performance, combustion and emissions characteristics with also the evaluation of the EGR ratio effect. Several key experimental observations were made:

- LTR region was observed with fuel blends more than 20% Butanol, ABE and all blends of ethanol under these engine conditions tested, hence, that is impact on intake temperature range and the sensitivity of operating, combustion characteristics to the intake temperature for HCCI combustion of alcohols fuel.

- Under high intake temperature (more than 150^{o}C), by increasing the ethanol fraction from 0 to 20%, the auto-ignition delay increases, but from 20 to 60%, the auto-ignition timing slightly advances.

Chapter 4. SPRAY CHARACTERIZATION FOR ALCOHOLS BLEND

Chapter 3 conducted the experimental of HCCI mode for PRF80 fuel and blends with Ethanol, Butanol and ABE, as bio-fuel, to understand the chemical governing the combustion developed. The current chapter investigate the impact of some parameters and especially the properties of of alcohols fuel on the spray characteristics under inert and reactive conditions. This chapter begins with a description of the vessel chamber, injection system, then presents the optical equipment used and some results on spray single injection.

4.1. HPHT chamber and injection system

In 2014, the PRISME laboratory will integrate the engine combustion network (ECN). This network, co-founded by Sandia National Laboratory (USA) and IFPEN in 2008, contributes to this research through the production and sharing of new knowledge for the development of experimental and modelling activities to increase the efficiency of internal combustion engines. From 2014 to 2019, the laboratory PRISME has developed and validated an experimental device (named NOSE for New One Shot Engine) to study the sprays in hot and dense environment 900 K and 22.8 kg/m^3, respectively. These conditions, called spray A conditions are relevant to heavy duty Diesel engine with a moderate level of EGR with as a standard Bosh single-hole injector.

4.1.1. High-pressure and high-Temperature chamber vessel

NOSE is based on the concept of Rapid Cycling Machine [141]. A 4-stroke low-speed diesel engine was used and the original cylinder head was replaced with customized optical chamber equipped of four quarts windows (25 mm thick, 25 mm wide and 80 mm long). The piston head angle and the gap distance were optimized to eliminate squish and reduce gas velocity inside the chamber. A near-quiescent gas condition, less than 1 m/s, following the ECN Spray-A requirement is obtained. In addition, metal plates of different thicknesses are placed on the piston head to change the compression ratio in the chamber if necessary.

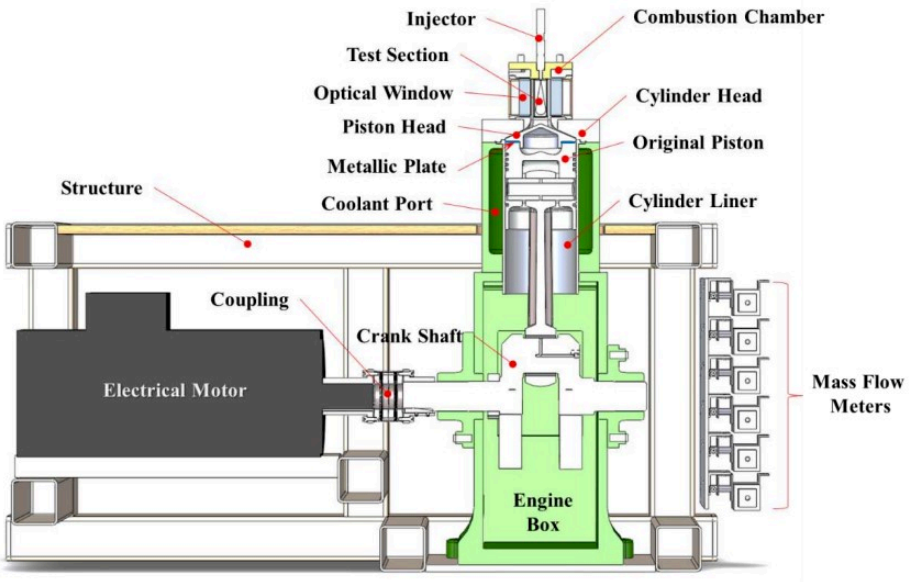

Figure 4.1. Schema of system NOSE with details of the engine, electrical motor and optical chamber

The general idea is to drive the engine with a high-power electric DC motor with a highly accurate velocity feedback controller. The piston stroke is perfectly controlled with a specific law to control the speed of piston movement during the compression phase and to stop the piston smoothly in the expansion phase in order to avoid noise and vibration. Thus, at top dead center high pressure and high temperature thermodynamic conditions are stabilized for 10 ms. This duration allows the study of the injection and combustion of a spray under stable pressure and temperature conditions. The entire system is described in the following figure and table.

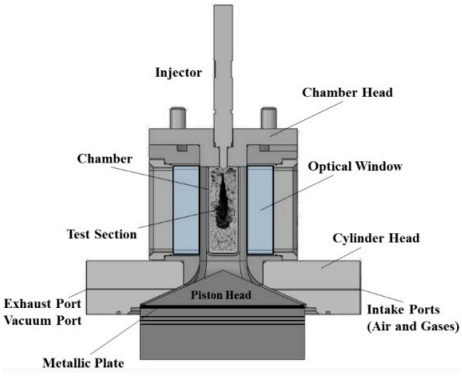

Figure 4.2. Cross-sectional view of the spray chamber (NOSE)

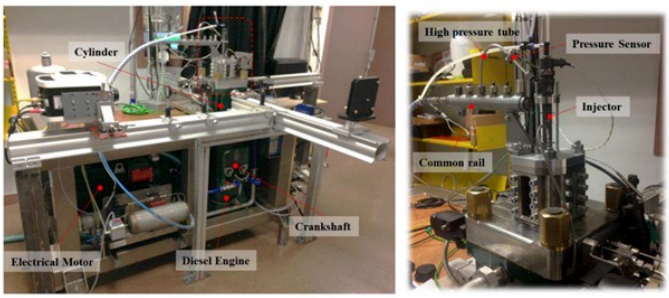

Figure 4.3. An experimental NOSE set-up used to study inerting/reacting jets with, the left with arrange globalement and the right with component of injection system

A schematic cut-through and the pictures of NOSE test facility are show in Figure 4.2.

Table 4.1. Specifications of system NOSE

Specifications Value	**Specifications Value**
Sweep volume V_s	3355 cm^3
Bore (B) x Stroke (S_p)	155 x 177.8 mm x mm
Dead Volume V_{dead}	240 cm^3
Rod lengh L_r	368 mm
Compression ratio	15 : 1
Number of optical windows	4
Window size	25 x 80 mm x mm
Intake gas (able to switch)	Gaseous species (N_2, O_2, Air, CO_2, …) and liquid species and fuel (H_2O, Silica oil)
Cooling system of Engine	Water
Engine speed (at TDC)	~ 100 rpm

The working mode of NOSE starts by setting the initial conditions as initial pressure, initial temperature and gas composition at BDC. After made the vacuum, different gas (N_2 or N_2 and O_2) were injected into the chamber by using mass flow controller (Brooks instruments). The initial temperature is specified by monitoring the water temperature around the liner and four heaters into the cylinder head, the injector temperature is assumed to be the same as the cylinder head temperature. Two thermocouples, type-K, are set-up inside the chamber and casing (near injector) to measure gas temperature inside chamber and casing, respectively. A high frequency piezo-electric pressure sensor (KISTLER 7001) is set-up at chamber head and works in combination with charge amplifier (KISTLER 5011). The initial pressure is checked. Moreover, the pressure development due to piston movement, injection or combustion is recorded.

The second step is the movement of the piston. In order to overcome the pressure forces the movement is decomposed into three phases: phase 1 backward movement of the piston at constant speed, phase 2 forward movement with a high acceleration of the piston from 100 CAD before bottom dead center (BDC) to 100 CAD before top dead center (TDC) and thus generate as adiabatic compression as possible, phase 3 the piston is braked to reach at TDC a speed lower than 100 rpm as described Figure 4.4.

In order to achieve the desired conditions 900 K and 22.8 kg/m^3, the conditions at bottom dead center are summarized in the table below:

Table 4.2. Conditions at the bottom dead center

Ambient gas	Initial temperature of water cooling	Initial temperature of cylinder head	Initial pressure
N_2 100%	356 K	363 K	0.182 MPa
N_2 85%; O_2 15%	356 K	363 K	0.181 MPa

The top dead centre conditions are thus stable for more than 5.0 ms and obtained with good repeatability as observed Figure 4.5.

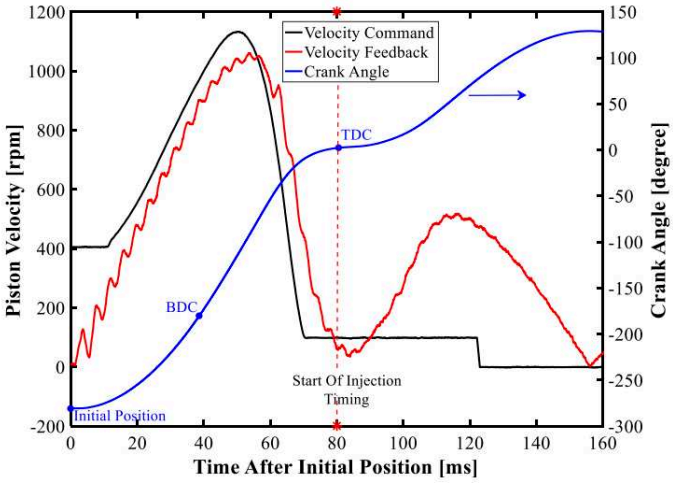

Figure 4.4. NOSE operating conditions: the feedback control command to control the piston movement as a function of time after the initial position (280 CAD BTDC) [142]

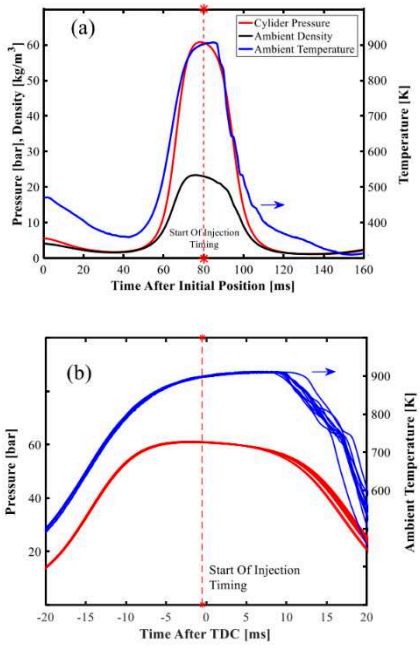

Figure 4.5. Thermodynamic conditions of NOSE: (a) an example of pressure, temperature and temporal density evolution (b) pressure and temperature evolutions from -20 to 20 ms ATDC for 10 repetitive tests [142]

4.1.2. Injection system overview

The fuel injector was mounted in the top window of the chamber and the fuel temperature is maintained at 90°C by heating the chamber to the same temperature. The selected injector

layout is based on modern advanced injector with common rail. The hole diameter of 88.5 µm and C_d of 0.86. The injection pressure is chosen from GCI mode around 400 bar (±20 bar). The Table 4.3 shows the main specifications of the fuel injection system.

Table 4.3. Specifications of Fuel injection system [143]

Specifications Details	**Specifications Details**
High pressure pump	MAXIMATOR M189 DVE-HD
Max. fuel pressure	2000 bar
Max. capacity	500 l/min
Injector body type	Bosch CR 2.16
Max. injection pressure	1500 (bar)
Nozzle type	Single hole, axially oriented
Nozzle outlet diameter Measured outlet diameter	90 µm (nominal) 88.5 µm
Nozzle shaping	Hydro-eroded
Nozzle k-factor	1.5
Mini-sac volume	0.2 mm^3
Discharge coefficient (C_d)	0.86
Injection pressure sensor	KISTLER Type 6533A11
Range	0-3000 (bar)
Linearity	<1.0 % FSO
Position	7 cm upstream of injector

4.2. Means of measurement and typical data

4.2.1. Pressure measurement

As indicated in the hardware description, two pressure sensors amplified via a Kistler 5019B charge amplifier are used to regulate the rail pressure and monitor the vessel pressure. These sensors coupled to the acquisition system allow the monitoring of the pressure values with a frequency of 400 kHz over 10 ms of recording.

It is possible to monitor the rail pressure (P_{inj}) and to record the pressure variations related to the dynamics of the moving parts of the injector (valve, needle) and on the other hand to follow the pressure inside the combustion chamber (P_{cyl}) associated with temperature variations due to fuel evaporation and combustion. The apparent heat release rate can thus be calculated for each combustion.

Appropriate signal processing based on the primary derivative of the rail pressure is used to

detect the opening and closing of the injector. The hydraulic delay (HD) can be measured with an accuracy of 7% (Figure 4.6).

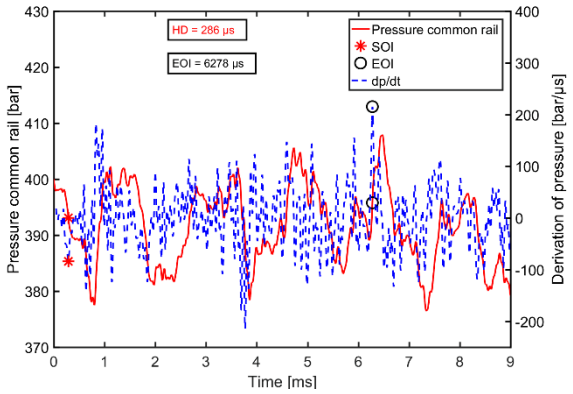

Figure 4.6. Common rail Pressure signal and detection of hydraulic delay open and close

This method was tested by simultaneously measuring the mass flow rate of fuel and pressure variations on 4 fuels (PRF80, Bu60, Et20 and ABE60) at room temperature, under 60 bar.

The same pressurization system is used to inject the fuel into injection rate IAV device as shown in Figure 4.7.

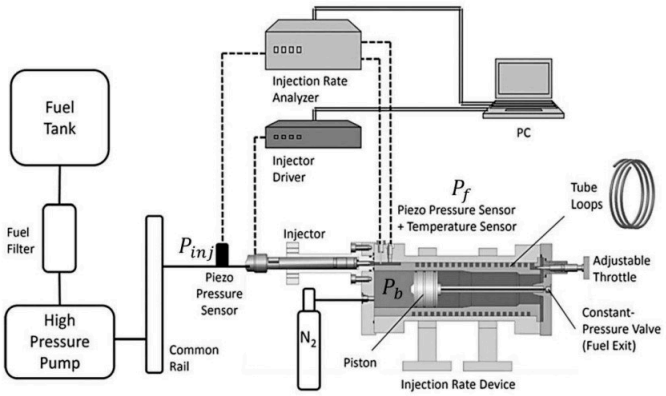

Figure 4.7. Mass Flow Rate experimental setup (from IAV GmbH® technical specification)

On hydraulic delay is very easily identified on the instantaneous flow signal. It corresponds to the passage from a negative to a positive value of the flow. It was thus possible to define a signature of the beginning of the injection on the derivative of the pressure signal. This is the moment when the first derivative reaches its minimum value on the first millisecond as shown in Figure 4.8 and Figure 4.9.

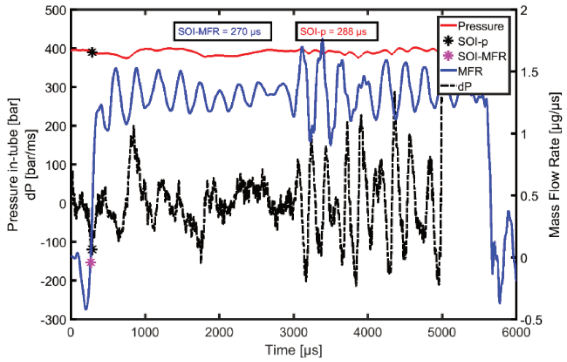

Figure 4.8. Detection of hydraulics delay on MFR (blue line) and also on the first derivation of common rail pressure signal, P_i=400 bar, P_b=60 bar

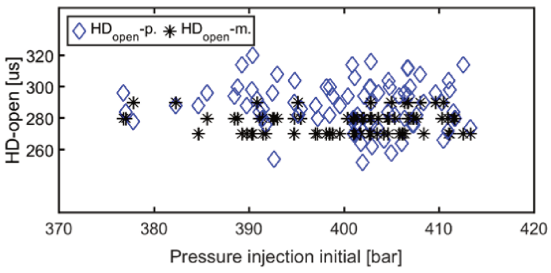

Figure 4.9. Hydraulics delay of nozzle injection on case of mass flow rate, P_i=400 bar, P_b=60 bar

The in-cylinder pressure signal (P_{cyl}) is used to determine the ignition delay and the rate of heat release after filtering and analysis. The following figures (Figure 4.10, Figure 4.11 and Figure 4.12) show a typical signal and its processing.

Figure 4.10 shows the typical steps in the processing of the pressure curve with the raw pressure signal (represented by the blue point) and the processing with the low bandpass filtered function (represented by the pink line).

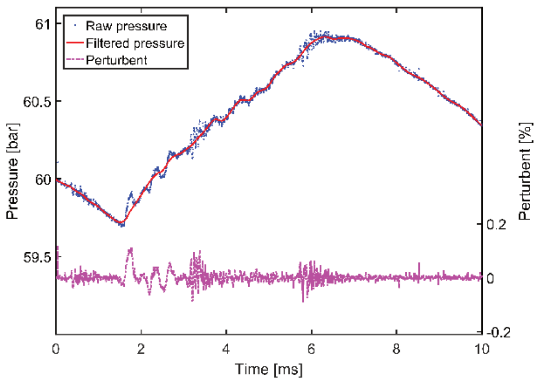

Figure 4.10. In-Cylinder Pressure signal raw and processed with low-pass filtered under reactive condition of PRF80 fuel, under ambient condition of 21% of oxygen concentration, 900 K of temperature and 60 bar of pressure

The smoothed in-cylinder pressure signal (P_{cyl_s}) and crank angle position (θ) are utilized to analysis heat release rate (*HRR*).

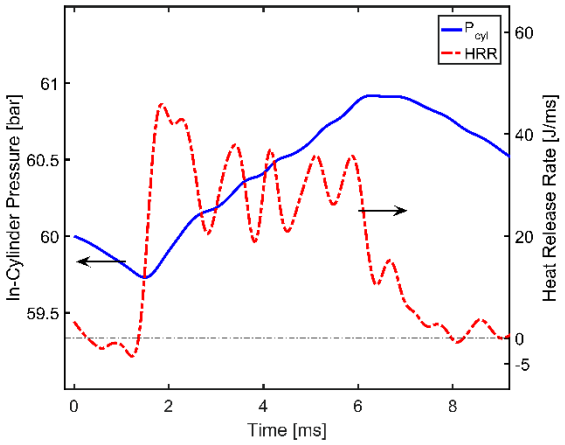

Figure 4.11. Typical In-Cylinder and Heat release rate event

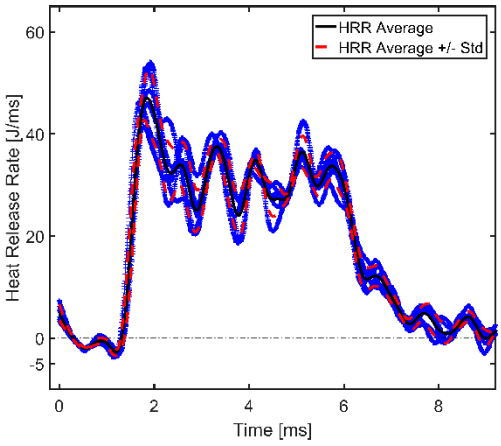

Figure 4.12. Heat release rate of 6 test (blue point) and average one (black line), average +/- standard deviation (red dashed)

4.2.2. Optical Set-Ups

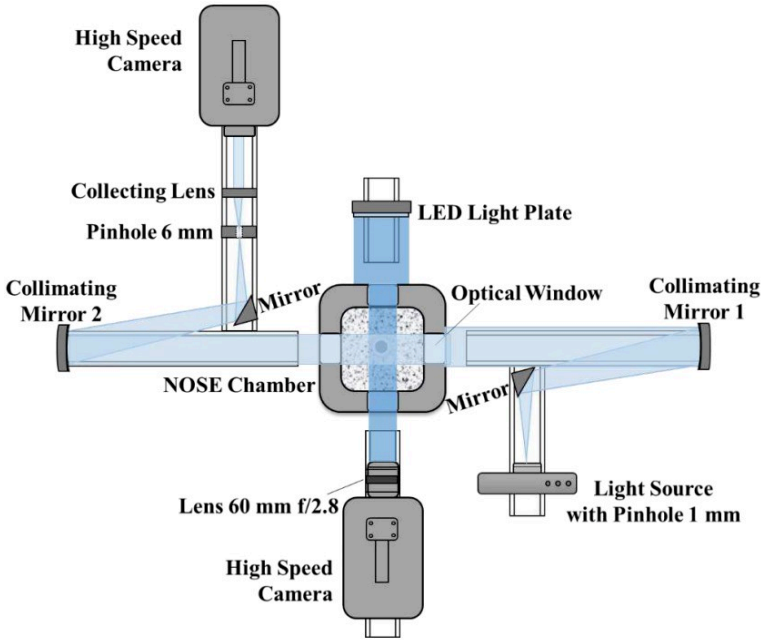

Figure 4.13. The optical techniques set-up scheme for the non-reactive atmosphere

Three optical set-ups were used, one for the non-reactive condition and two for reactive conditions. The two schemes are showed Figure 4.13 and Figure 4.14. Figure 4.13 shows the scheme of optical arrangement for non-reactive atmosphere to through the both direction by 4 windows to capture simultaneous data of liquid and vapor spray penetrations help to the Diffused Back-Illumination (DBI) and the Schlieren technique. Figure 4.14 shows the scheme

of optical arrangement for reactive atmosphere to track the propagation of spray during the combustion with Schlieren technique, the lift-off length and the ignition delay with the recording of natural OH* chemiluminescence of flame with an intensified camera and photomultiplier tube respectively.

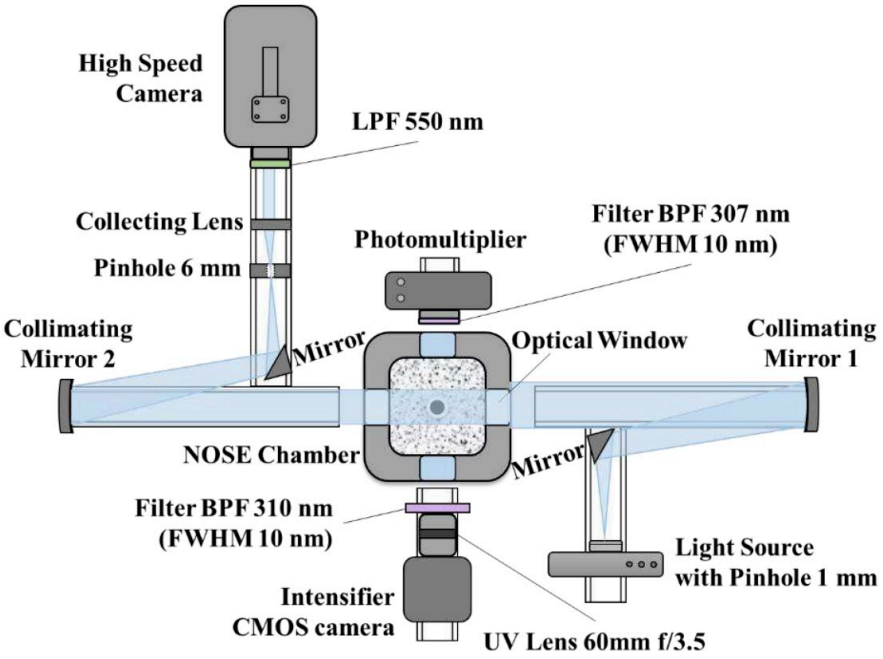

Figure 4.14. The schematic diagrams of physical arrangement for the reactive atmosphere

These optical setups used different diagnostics: (1) Diffused Back Illumination; (2) Schlieren and (3) Chemiluminescence OH*. Details of each optical elements given in Table 4.4.

Table 4.4 Technical details of different optical setups for non-reactive and reactive conditions

Optical Technique	**OH* Chemi.[1]**	**Schlieren**	**OH* Chemi.[1]**
Parameters	Lift-Off Length (LOL)	Ignition Delay (ID)	Ignition Delay (ID)
Light source		LED (white) 1 mm pinhole	
Mirrors		2 Parabolic Mirrors	
Detector	Photron - APX-I2	Phantom-V1611	PM[2] Newport PM 70680
Lens	UV 60 mm f/3.5	Collecting lens: 30 cm of focal length with 6 mm pinhole	
Filter	BPF 310 nm FWHM 10 nm	LPF ≤ 550 nm	BPF 307 nm FWHM 10 nm

Optical Technique	OH* Chemi.[1]	Schlieren	OH* Chemi.[1]
Frame speed / Data Recording	2 kHz	39 kHz	250 kHz
Exposure time	499 µs	5 µs	
Image size (pi²)	512 x 1024	1024 x 400	
Magnification	18.2 pix/mm	12.3 pix/mm	
Chemi.[1]: Chemiluminescence; PM[2]: Photomultiplier			

4.2.2.1. Diffused Back-illumination

Diffused back illumination technique is used to measure the liquid length and the soot mass with two specific arrangements.

The spray or flame is illuminated by a large light source. In the axis, at the image plane, a camera records the resulting images. The differences in contrast are due to the absorption of light by the liquid or by the soot according the Beer-Lambert law.

For the liquid measurement, a 100 x 100 mm² LED continuous light plate is used. The high-speed camera is a V1611 PHANTOM. The camera is equipped with a NIKON 60 mm f/2.8 lens, a frame rate of 49 kHz with an exposure time of 3 µs, and an image resolution of 512 x 512 pix² provide the most suitable values for capturing high-quality images at a high frequency.

Post-processing was performed using the code available on the ECN website [144]. The images acquired during the steady-state period of the spray are used to compute the time average intensity of the image I_{avg}, thus avoiding initial and final spray transients. I_{avg} is then normalized by the time averaged background image I_{bg}, obtained by averaging about fifteen images before the Start of Injection (SOI). Next, the light extinction factor along the spray core (τ) is calculated using the Beer-Lambert law as shown in Eq. 4.1 and Figure 4.15.

The Figure 4.16 shows an example of the liquid penetration length of PRF80 under Spray A conditions with time.

$$\tau(x,y) = -\log\left(\frac{I_{avg}(x,y)}{I_{bg}(x,y)}\right) \qquad \textbf{\textit{Eq. 4.1}}$$

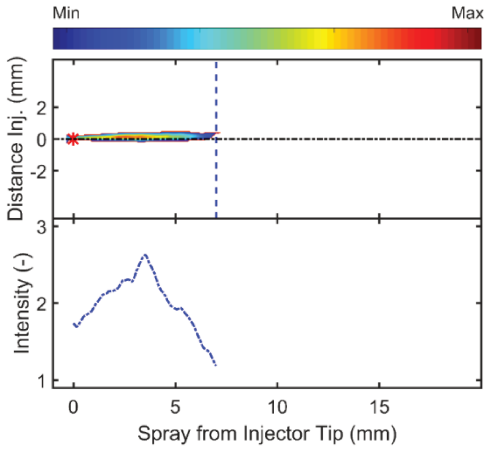

Figure 4.15. Image post-processing of DBI image: images for PRF80 at 900 K of temperature and 60 bar of pressure conditions and light extinction image

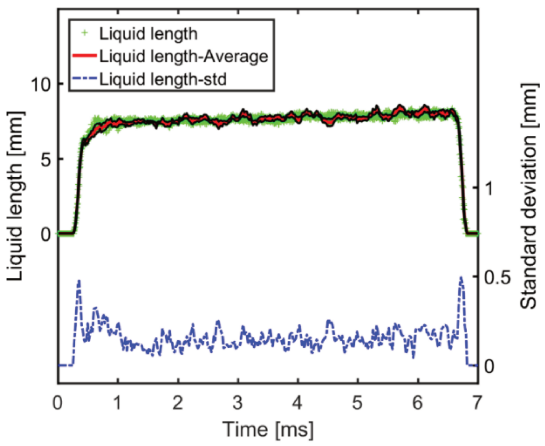

Figure 4.16. Liquid penetration versus time of PRF80 with - 6 measurement under ambient gas of 100% of nitrogen concentration, 900 K of temperature and 60 bar of pressure

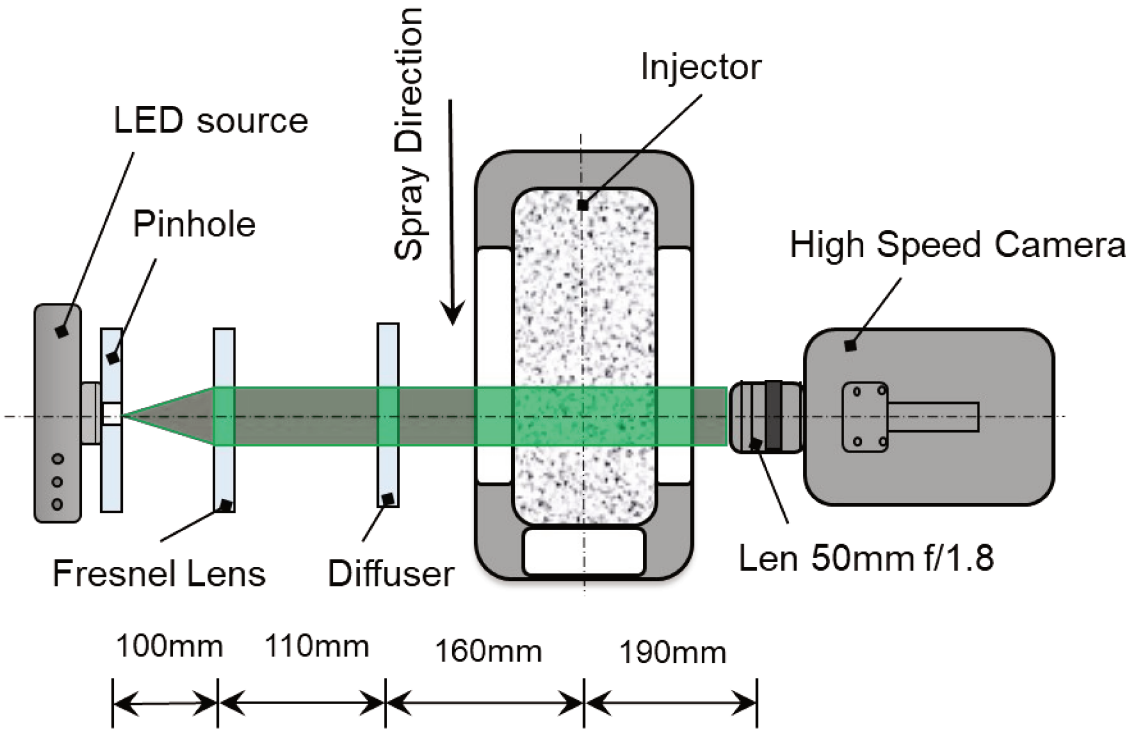

Figure 4.17. The schematic diagrams of physical arrangement for the reactive atmosphere of in-flame soot measurement

For the soot study a different configuration is used as it is necessary to correct the effect of natural luminosity of flame. The light source was generated by a green LED (CBT-120-GC11-JM200) at λ= 532 nm. The light rays from the LED were transferred to a Fresnel lens with an effective diameter of 63.5 mm and a focal length of 99 mm through a pinhole to generate

parallel light beam. Then this beam is transferred to an engineering diffuser to generate a homogeneous light distribution in the region of interest. Next, images of the transmitted light were captured by the Phantom V16 CMOS camera at a frame rate of 45 kHz with an exposure time of 3 µs while the LED frequency was kept 22500 pulse/sec. An AF Micro-Nikon 50 mm f/1.8 D lens with two filters, a BP filter centered at 520 nm and 75% a neutral density filter is used. The image resolution is 0.2 mm/pixel. Figure 4.17 is a scheme of optical arrangement.

A series of three images is recorded as shown in Figure 4.18: a) corresponds to the original light intensity I_o, b) to the natural luminosity of flame withou LED and c) to the image with natural luminosiy and absorption of soot. Finally d) is the resulting image of optical thickness (KL) cartography.

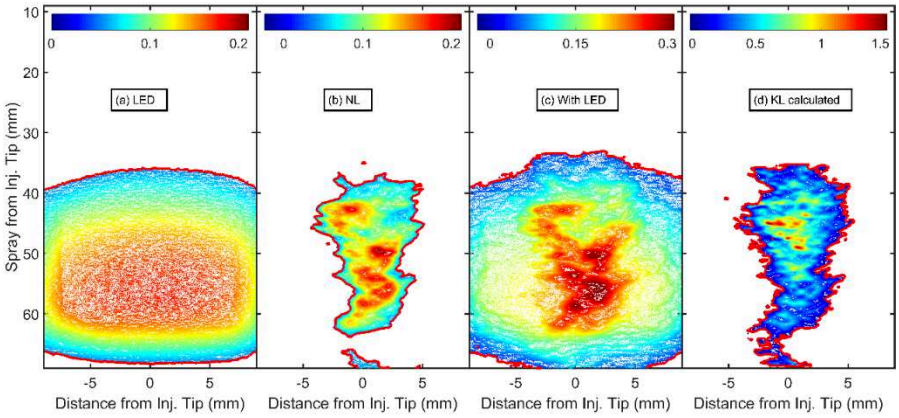

Figure 4.18. LED, Natural luminosity without LED, Natural Luminosity with LED and estimated KL

The optical thickness (*KL*) can be estimated by measuring the ratio between the transmitted light intensity I_t, and the original light intensity I_o, according the Beer-Lambert law [145]:

$$I_t / I_o = e^{-KL} \qquad \textit{Eq. 4.2}$$

KL is the product of the dimensional extinction coefficient *K* and the path length *L* through the particle cloud.

The extinction signal is corrected: $I_t = I - I_f$, with I_f the intensity of natural luminosity without LED, *I* the intensity of flame with LED. The obtained images of flame natural luminosity NL were processed by a median-filter to reduce impulse noise in the image, and the background was subtracted. A luminosity threshold is used to identify the flame boundary for next KL estimation step. Moreover, along the spray injection direction the intensity of each pixel of NL

image in the radial direction is summed. This vector is called SINL and can be show the location of flame and region of high soot fraction of the flame.

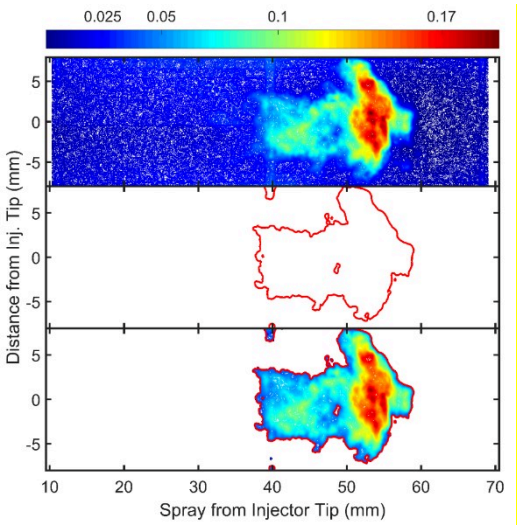

Figure 4.19. Sample image-set showing boundary detection procedure starting from natural luminosity (without LED) image

From the local particles, the soot volume fraction f_v can estimated by Mie theory [145]:

$$f_v = K\lambda / k_e \qquad \textit{Eq. 4.3}$$

With λ the wavelength of incident light and k_e the dimensionless extinction coefficient, which can be determined from Rayleigh-Debye-Gans theory, as presented in [72,79]:

$$k_e = \left(1+\alpha_{sa}\right).6\pi.E\left(m\right) \qquad \textit{Eq. 4.4}$$

With *E(m)* the refractive index function, as represented by: $E\left(m\right) = -\ln\left(\frac{m^2-1}{m^2+2}\right)$, with *m* the complex refractive index of the soot particles, α_{sa} the scattering absorption cross-sections ratio. It depends on the were length of the incident light, physicochemical structure of the soot particles, the primary particle size, the number of primary particles. In this study, following [79], $\left(1+\alpha_{sa}\right).E\left(m\right)$=0.26 is chosen to relationship between of *KL* and f_v, this value does not change with liquid fuel properties or ambient conditions.

The total soot mass is determined by integrating the soot volume fraction over the entire soot

area multiplied by the soot density, as shown in [146]. The total soot mass is calculated by integrating the soot volume fraction over the entire soot area multiplied by the soot density, as given by [146]:

$$m_{soot} = \rho_{soot} \int_{x_1}^{x_2} \int_{0}^{R} f_v . 2\pi r dr dx \qquad \textbf{Eq. 4.5}$$

with x_1, x_2 the certain axial limits over cross section of the jet flame, ρ_{soot} the soot density, assumed of 1.8 g/cm^3 [146] and *dr*, *dx* are equal at 0.089 mm.

Temporal and spatial features of the Natural Luminosity images and soot mass concentration estimated are plotted by integrating information at each axial location for two dimensions:

$$IXT(x,t) = \int_{-Y}^{Y} I(x,y,t)\,dy \qquad \textbf{Eq. 4.6}$$

With *x*: the axial direction, *y*: the radial direction and *Y*: intensity boundary width.

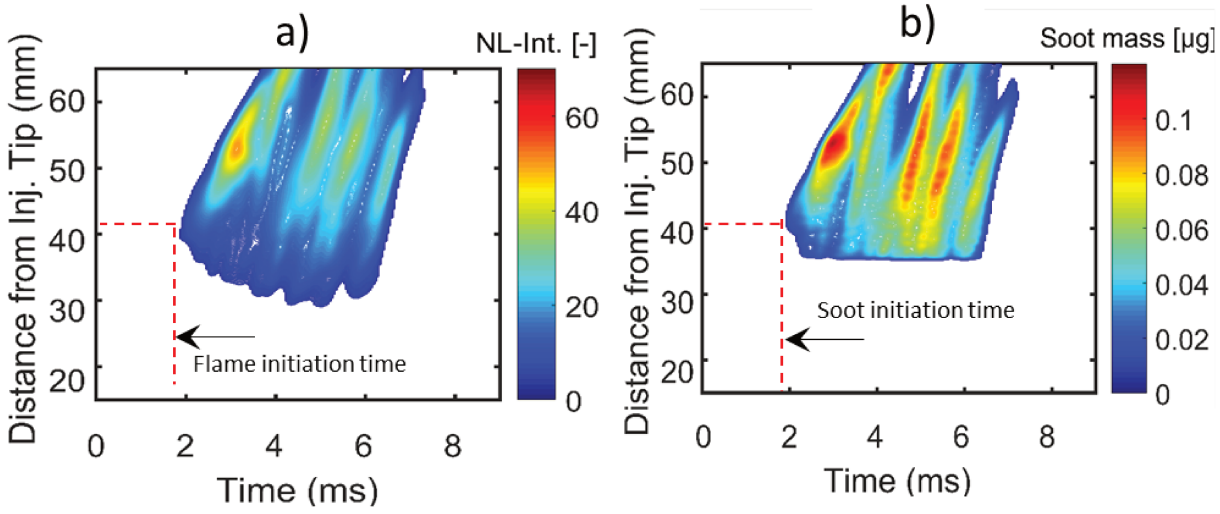

Figure 4.20. IXT plot of a) Natural Luminosity and b) Soot mass for PRF60 fuel under ambient gas of 18% of oxygen concentration, 900 K of temperature and 60 bar of pressure

From the temporal sequence of Natural Luminosity images, the intensity can be integrated along the radial direction of spray as shown Eq. 4.6, with x the spray axial direction, y the spray radial direction, and y_1, y_2 the spray boundary positions. The boundary of the Natural Luminosity map represents the location where the start of diffusion combustion is reached at the limit of detectability of the optical technique.

The IXT of soot mass concentration was estimated in a similar way, by replacing Natural Luminosity intensity to soot mass concentration. Note that the location of soot mass is limited by LED area.

Figure 4.20 (IXT) is the temporal sequence of vectors resulting from the integration of the natural luminosity along the direction of the spray at each instant for a) and the integration of the soot mass for b).

4.2.2.2. Schlieren technique

The Schlieren imaging is a well-known technique to visualize the refractive index gradients in transparent mediums [147]. In the case of vaporizing diesel sprays, this technique is able to capture the line-of-sight boundary between vaporized fuel and ambient gases [147].

In this study, the Schlieren setup is composed of the continuous white LED with a 1 mm pinhole, to represent the one point-light source and two parabolic mirrors with 108 mm diameter and 864 mm focal length. A 6 mm pinhole is used to record Schlieren light after the test section with the high-speed camera (Phantom V1611) and a collecting lens of 30 mm focal length. The image resolution was 1024 x 400 pix^2 for 39 kHz frame rate with 5 µs of exposure time and 0.083 mm/pix of magnification.

The images are post-processed using the same Matlab script shared thanks to ECN. The vapor phase edges are detected by comparing the projected density gradients from successive images. In Figure 4.21, examples of Schlieren image and of spray boundary (in red) determined from the processed image are given. The vapor penetration length, S is determined at the crossing point between the limit of the vertical spray front limit and the spray axis from injector tip.

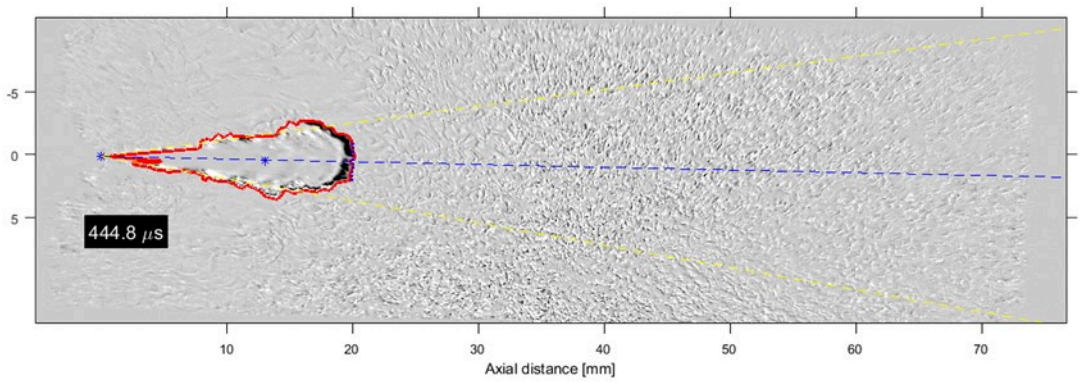

Figure 4.21. Example of Schlieren image processing with ECN code for inerting atmosphere condition

Thus at each time, the vapor penetration is known as shown in Figure 4.22.

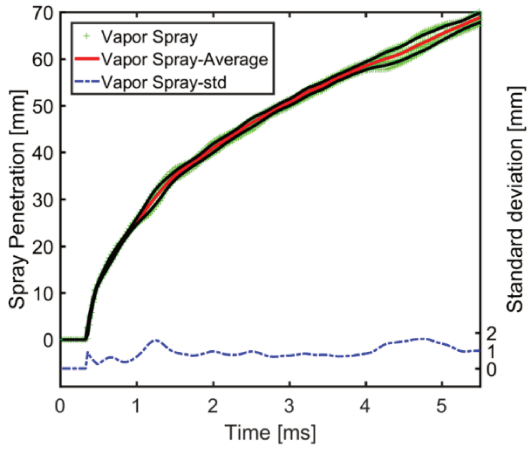

Figure 4.22. Vapor penetration versus time of PRF80 with 6 measurement under ambient gas of 100% of nitrogen concentration, 900 K of temperature and 60 bar of pressure

*4.2.2.3. Lift off length by *OH Chemiluminescence imaging*

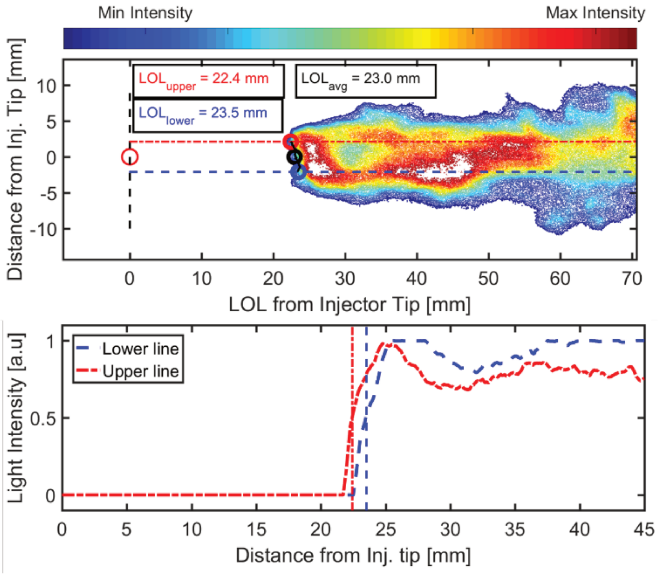

Figure 4.23. Flame Lift off length obtained by OH* chemiluminescence (ABE20) under ambient gas of 21% of oxygen concentration, 900 K of temperature and 60 bar of pressure

The determination of lift-off-length (LOL) and ignition delay or start of combustion (SOC) are also important to characterize and understand the combustion process in case of flame spray combustion. The LOL represents the distance the mixture (fuel sprayed on the entrained air) moves to the combustion zone, it is therefore the distance from the tip of the injector to the reaction zone where the flame is stabilized [55]. SOC is defined as the time between the Start Of Injection (SOI) and the start of 'high-temperature combustion phase'. LOL and SOC were measured by OH* chemiluminescence images or temporal signal (recorded by the

photomultiplier).

During the main combustion phase, OH* radicals produced can be detected from their UV chemiluminescence at 310 nm [59]. Intensity profiles around the spray axis are extracted from the recorded chemiluminescence images. The intensity is normalized to maximum values located at the flame lobes region: red and blue profiles around the spray centerline as shown in Figure 4.22.

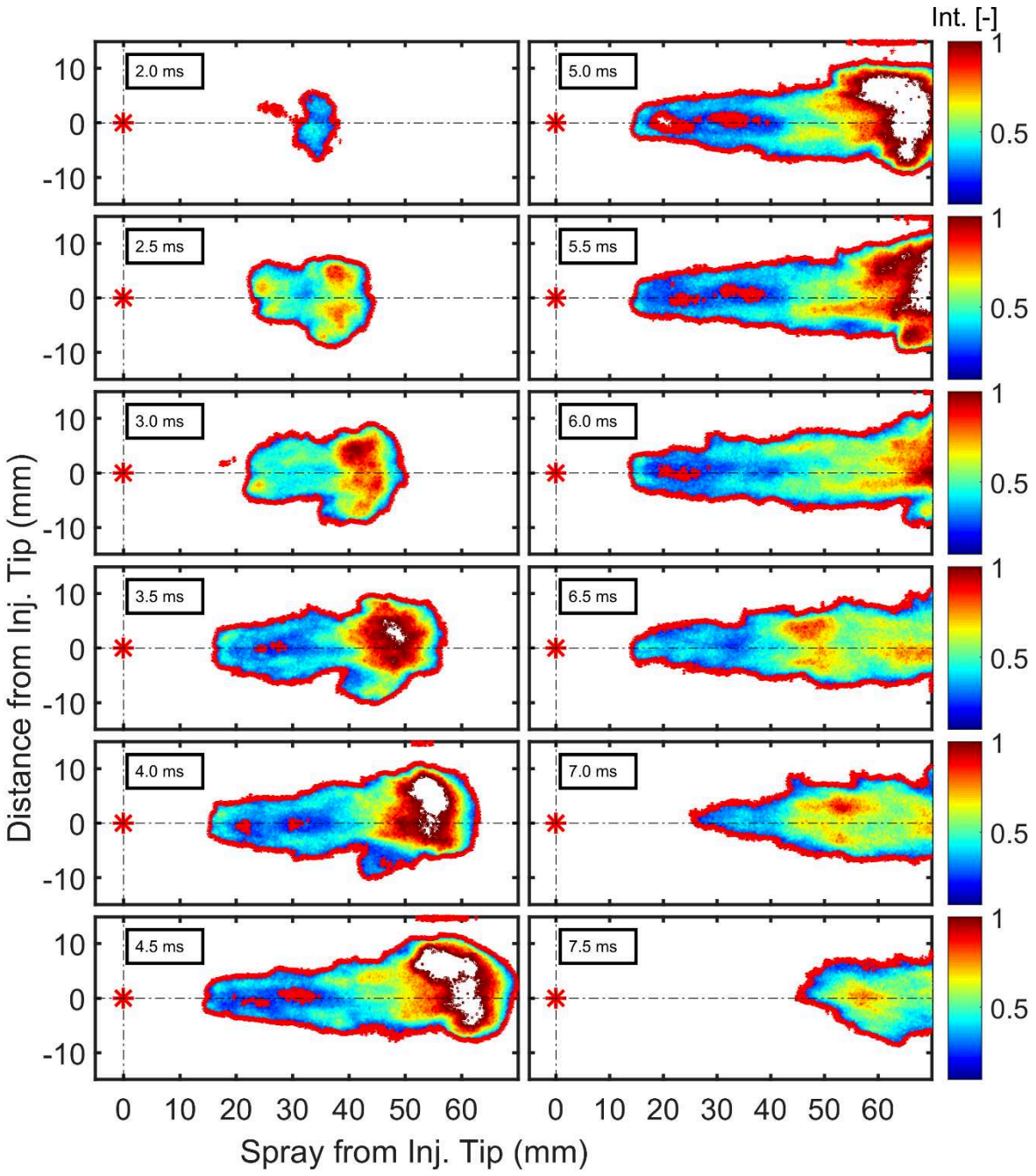

Figure 4.24. Continuous OH* chemiluminescence images of PRF80 under ambient gas of

21% of oxygen concentration, 900 K of temperature and 60 bar of pressure

LOL is defined as the average of the distances between the injector tip and the distance corresponding to 50% of the maximum intensity, according Siebers and Higgins approach [55] and the criteria of Benajes et al. in [148].

The intensified CMOS Photron Fastcam APX I2 camera was used with a 60 mm f/3.5 UV lens, equipped with a 310 nm (FWHM 10 nm) band-pass filter (BFP) with a long gating time of 449 µs. It is then possible to track the position of the flame over time as shown in the Figure 4.24. This time tracking of the OH* chemiluminescence is synchronized with the vapor penetration as visible on the Figure 4.25 and Figure 4.26.

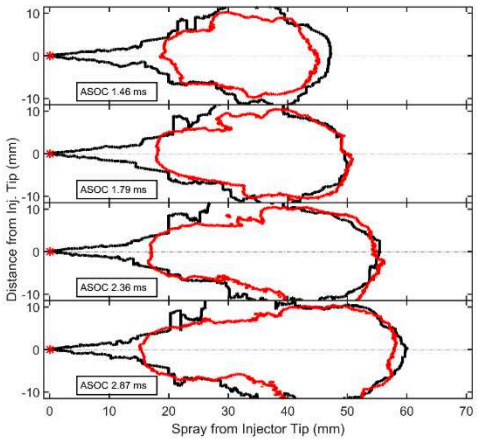

Figure 4.25. Combination temporal of Schlieren technique and OH* chemi. for PRF80 fuel

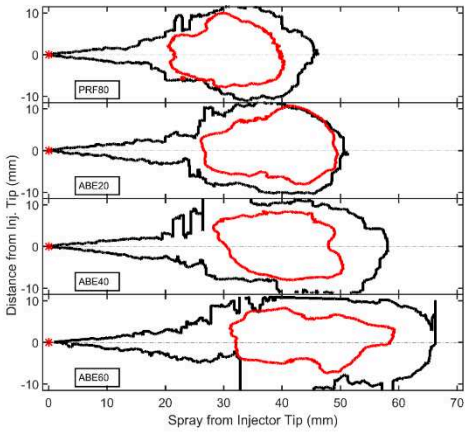

Figure 4.26. Combination temporal of Schlieren technique and OH* chemi. PRF80 and ABE blends at ASOC ≈ 2ms

Temporal and spatial features of the OH* chemiluminescence are plotted by integrating information at each axial location for two dimensions, as following Eq. 4.6.

From the temporal sequence of OH* images presented in Figure 4.27, the intensity can be integrated along the radial direction of spray according Eq. 4.6, with x the spray axial direction, y the spray radial direction, and y_1, y_2 the spray boundary positions. $I(x,t)$ map obtained from the images of Figure 4.27 is plotted in Figure 4.28. The boundary of the OH* map represents the location where the complete oxidation is reached with the limit of detectability the optical technique. The temporal evolution of the flame as region limitation by penetration flame is obtained.

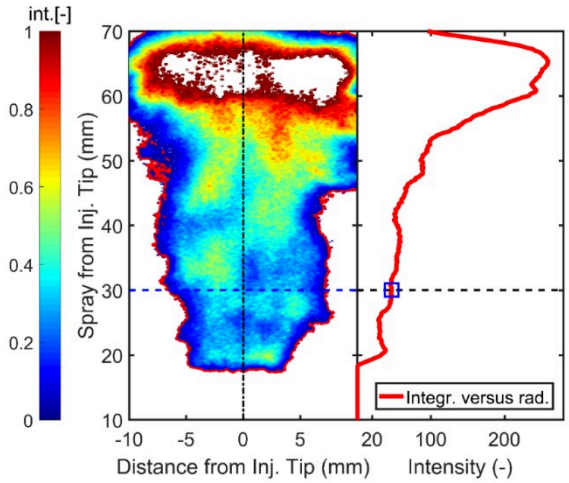

Figure 4.27. Integration of OH* chemi. image to obtain IXT plots for PRF80 fuel under ambient gas of 21% of oxygen concentration, 900 K of temperature and 60 bar of pressure

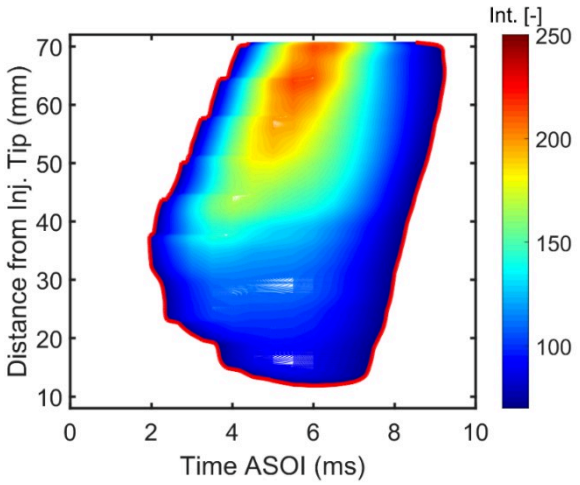

Figure 4.28. IXT plot of OH* chemiluminescence images for PRF80 fuel under ambient gas of 21% of oxygen concentration, 900 K of temperature and 60 bar of pressure

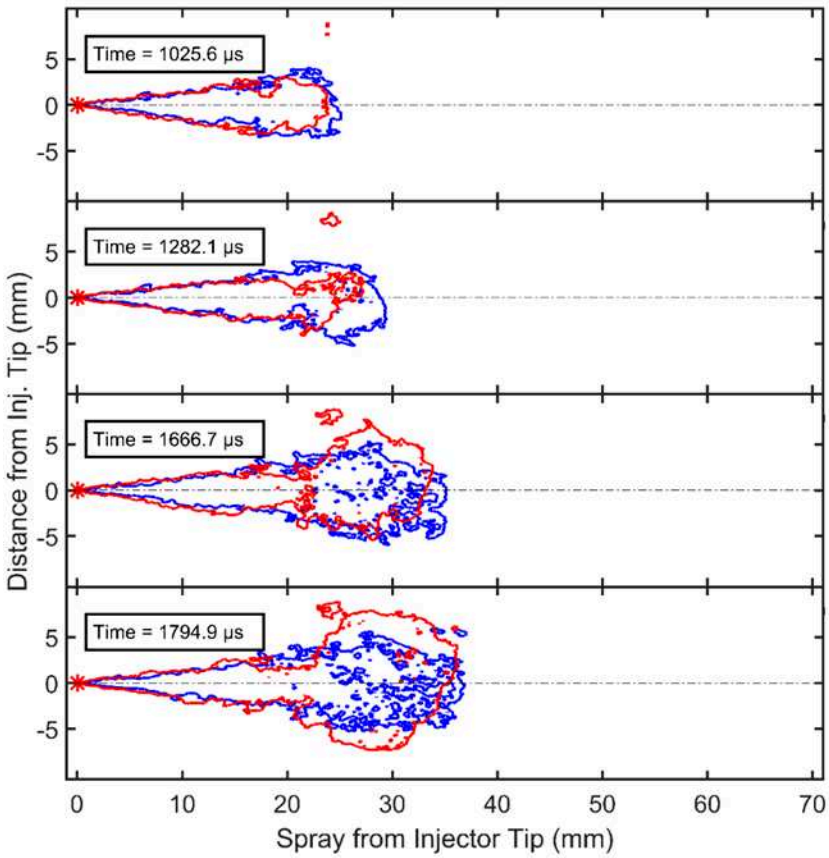

Figure 4.29. Contour of Schlieren images of PRF80 fuel under inerting (line blue) and reacting (line red) condition, 900 K of temperature and 60 bar of pressure

A Newport Oriel Photomultiplier, side-on with a PMT 70705 high voltage power supply and a

BPF of 307 nm (FWHM 10 nm) were used to record temporal OH* chemiluminescence signal every 4 µs in order to determine SOC as the moment where OH* intensity reaches its maximum value. In addition to this technique, the start of combustion is also shown in the Schlieren images. When the combustion is initiated, the spray shape is different from the case in inert condition as shown in Figure 4.29.

4.3. Results of inert conditions

4.3.1. Mass Flow rate (MFR)

The fuel injection pressure (P_{inj}) around 400 (±10) bar, the backpressure of 60 bar and the injection command duration of 3 ms are set for all experiments to measure MFR for PRF80, Bu60, ABE60 and Et20 fuels.

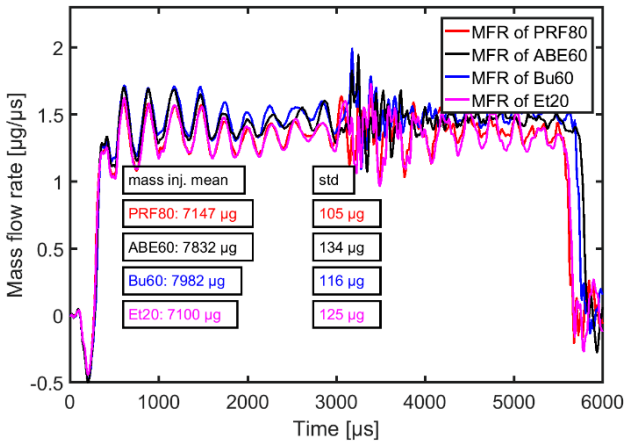

Figure 4.30. Mass flow rate of injection for PRF80, ABE60, Bu60 and Et20, P_i=400 bar, P_b=60 bar

The mass flow rate tested fuels are presented in Figure 4.30. Bu60 and ABE60 is higher mass injection about 7982 µg/cycle than its PRF80 of 7147 µg/cycle. The more detail results are given in Table 4.5.

In term of hydraulic delay, the initial hydraulic delay was no significantly different for four fuels, around 0.3 ms, however the end hydraulic delay of both ABE60 and Bu60 is longer than both PRF80 and Et20.

4.3.2. Liquid length

In this study, in order to evaluate the influence of fuel properties on liquid length under

injection pressure of 400 bar, ambient temperature of 900 K and ambient pressure of 60 bar conditions, the density, viscosity and volatility of fuel is considered. The liquid length results of Butanol blend of 20, 40 and 60 % with PRF80 is presented, on comparison with literature [20,26–28,30,149], as shown in Figure 4.31 and Figure 4.32.

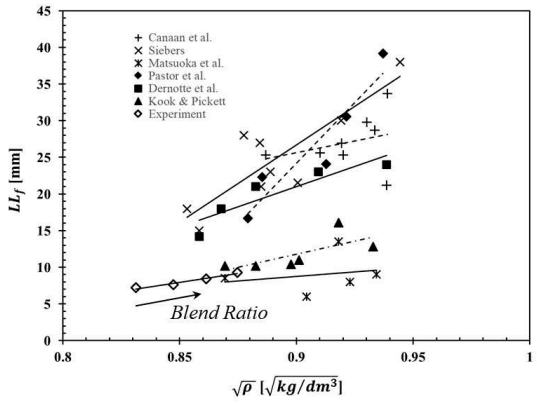

Figure 4.31. Liquid length in function of the square root of fuel density – Lines are linear regressions through the experiment and reference

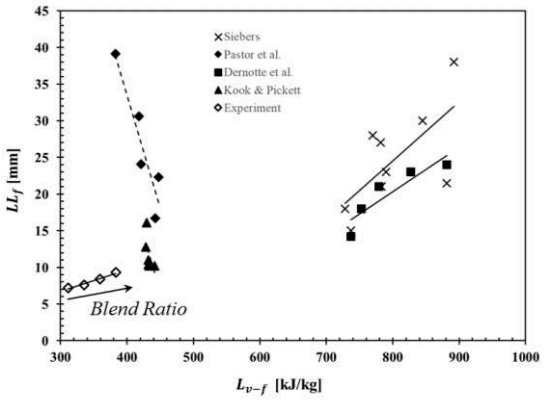

Figure 4.32. Liquid length in function of the lower heat vaporization - Lines are linear regressions through the experiment and reference

Figure 4.31 shows that the square root of density of fuel correlates well with the liquid length, while increase in fuel density from 0.830 to 0.875 $kg^{1/2}/dm^{3/2}$ (~5.4%), induces an increase in the liquid length by ~23%. For a liquid length of about 7 mm, it means an increase by 1.6 mm.

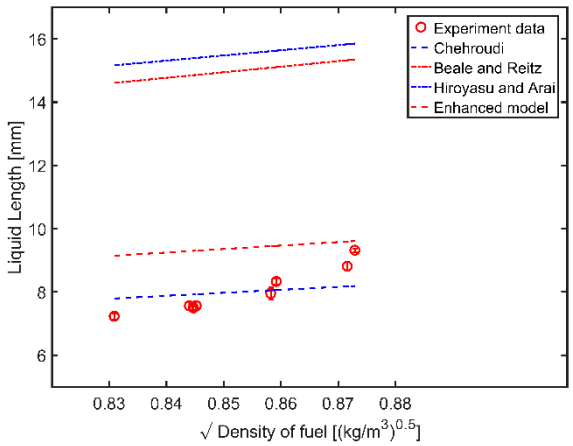

Figure 4.33. Liquid length in function of the square of fuel density – Lines are linear regressions through the experiment and some empirical equation

As the introduction in Chapter 2 of the fundamental physics governing the spray developed, experimental data shows a correlation between square root of density of fuel, as compare

previous models [20,32,33,35].

Table 4.5. Summary mass flow rate and liquid length

Fuel	Mass Injected (g)	Liquid length (mm)
PRF80	7.15 (±0.11 / 1.5%)	7.7 (±0.13 / 1.7%)
Bu20		8.0 (±0.08 / 1.0%)
Bu40		9.4 (±0.54 / 5.74%)
Bu60	7.98 (±0.12 / 1.5%)	10.1 (±0.42 / 4.16%)
ABE20		8.0 (±0.07 / 0.9%)
ABE40		8.5 (±0.57 / 6.7%)
ABE60	7.83 (±0.13 / 1.7%)	9.3 (±0.47 / 5.1%)
Et20	7.10 (±0.13 / 1.8%)	8.3 (±0.33 / 4.0%)

4.3.3. Vapor spray penetration

Figure 4.34 shows that the vapor penetration (dashed line), continues to develop beyond the liquid phase (dotted line). The vapor spray penetrations are not significantly different from one fuel to another.

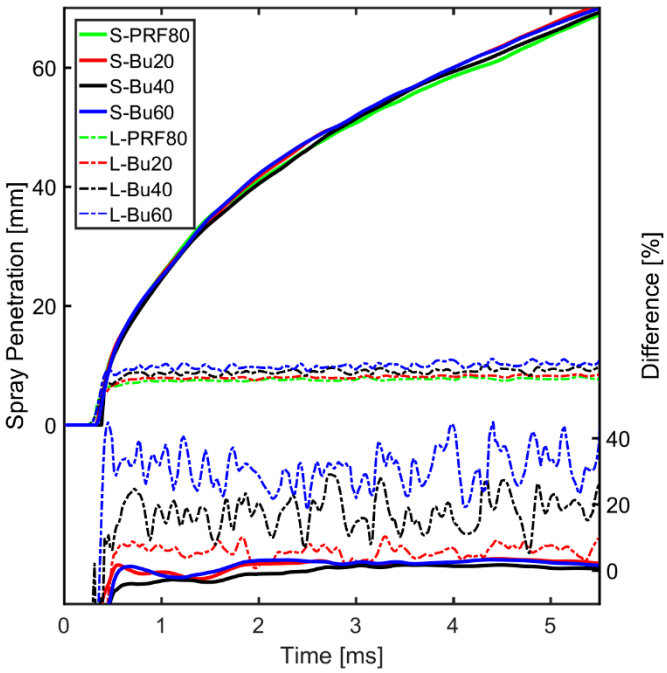

Figure 4.34. Spray vapor penetration and spray liquid penetration versus time

Figure 4.35 a) shows the predicted (with default coefficient proposed by the different authors) and measured spray penetration length for PRF80 fuel under ambient temperature and pressure of 900 K and 60 bar, respectively.

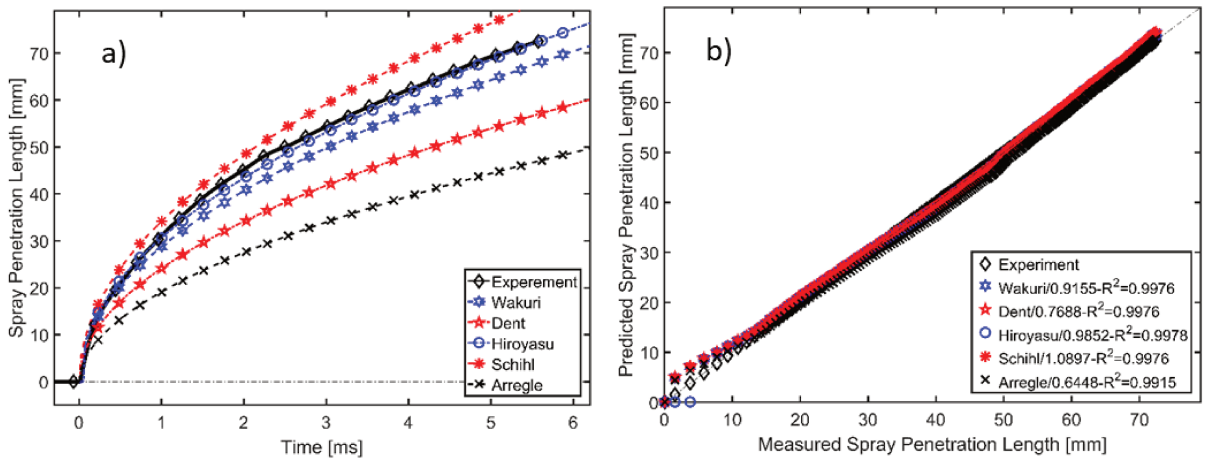

Figure 4.35. Comparison of experiment results and some model prediction spray vapor penetration length a) versus time and b) prediction with adding a constant value and measured spray penetration length

Figure 4.35 b) are presented the comparison between the measured and predicted spray penetration length with different angle coefficient specified in the legend. With adding the coefficient to models prediction, the results of experiment and prediction spray penetration length are similar, with high value of coefficient of determination.

In this case, Hiroyasu model gives a spray penetration length value closer to the measured results with high R-square of 0.9952, and also with adding coefficient of angle, R-square of 0.9978.

4.3.4. Conclusions

An experimental investigation into the behavior of common rail fuel injection equipment and subsequent characteristics of gasoline fuel spray was conducted.

The study under inert condition for measurement of liquid and vapor penetrations under high-temperature high-pressure behavior were performed. The mass flow rate is obtained with a small difference for all fuel blends, the vapor penetration profiles for all fuel blends under these conditions are similar and show that the air entrainment is identical for all fuels. Therefore, the local equivalence ratio of the mixture will depend on the stoichiometric ratio and not on the ratio of fuel flow to air flow. On the other hand, the liquid length penetration is most sensitive to the physical properties of fluids such as latent heat and density.

4.4. Results of reactive conditions

As observed in Chapter 3 the auto-ignition behavior is controlled by chemical kinetics of fuel-air mixture in the HCCI combustion mode. However, in terms of GCI (Gasoline Compression Ignition), as introduced in Chapter 2, the auto-ignition behavior is strongly influenced the mixture and thus the physicochemical properties of the fuel. Spray combustion will be studied this section experimentally. Simulation under OpenSMOKE++ will complete the analysis.

4.4.1. Ignition delays

4.4.1.1. Experiment results

To assess the impact of fuel blending or chemical properties, CMT data on different iso-octane-n-heptane mixture rates, oxygen and injection pressures are studied.

**) PRF Fuel, data from CMT*

Additional data to [65] collected at CMT concerning the measurement of ignition delay are presented in figure 4.37. These are measurements made under the conditions of spray A, 900 K 22.8 kg/m^3 under three injection pressure differences and three oxygen concentrations.

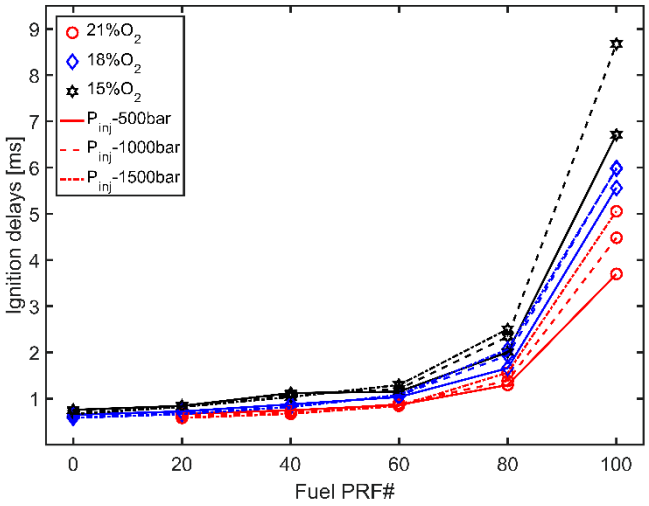

Figure 4.36. Ignition delay of spray for surrogate fuel with wide range iso-octane component with n-heptane, under ambient gas temperature of 900 K, difference of injection pressure and oxygen concentration

The results show the evolution of ignition delay as a function of oxygen concentration, injection pressure and fuel octane number. The evolution of the delay as a function of the octane number is not linear. For lower octane number (PRF00-PRF20-PRF40), the evolution of ignition delay increases with decreasing oxygen concentration, decreasing very slightly with increasing

injection pressure and increasing slightly with increasing octane number. But higher octane numbers (PRF60-PRF80-PRF100) is, the ignition sensitivity to these three parameters is higher: important increase of the delay for octane numbers higher than 60, increase of the delay also with the increase of the injection pressure significantly.

An empirical equation of the Arrhenius type is proposed, seen Eq. 4.7. The coefficients are adapted according to the octane number as shown in Table 4.6. The low ones between 0-50 and the high coefficients between 50-100.

This correlation was established over the following ranges: 800-900 K, 15-21% O_2, 500-1500 bar P_{inj}. The effects of back pressure are not studied. The ambient pressure was set at 60 bar.

$$ID = t_{mv}[ms] + A.P_{inj}^{a}[bar].ON^{b}.O_2^{c}[\%].e^{E_a/T_{amb}[K]} \qquad \textit{Eq. 4.7}$$

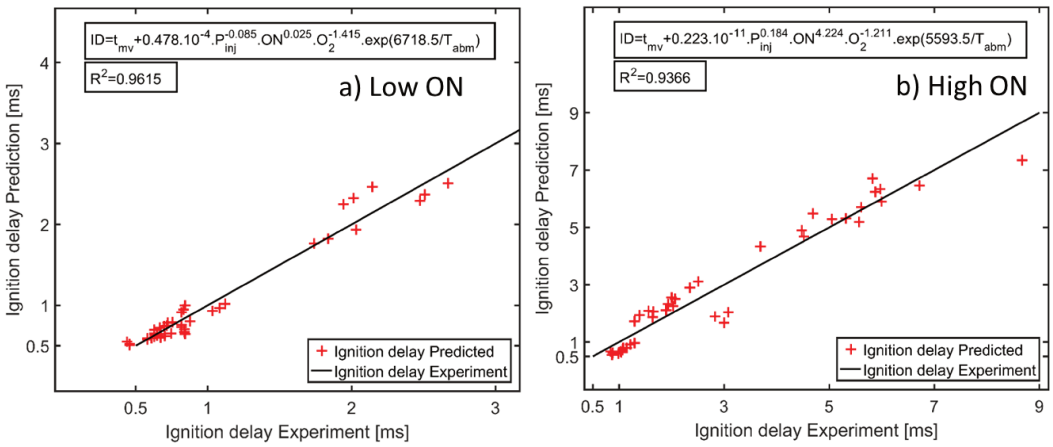

Figure 4.37. Ignition delays correlation for low octane number of fuel

Table 4.6. Coefficients for Eq. 4.7

Range Octane number	**T_{mv} (P_{inj} [bar]) [ms]**	**A**	**a**	**b**	**c**	**E_a**
0-50	$0.17 + 4.10^{-8}.P_{inj}^2 - 1.6.10^{-4}.P_{inj}$	$0.478.10^{-4}$	-0.085	0.025	-1.415	6718.5
50-100		$0.223.10^{-11}$	0.184	4.224	-1.211	5593,5

*) For low-octane number fuel used, the effect of the parameters on ignition delay similar with diesel-type fuel spray for this room temperature range (800-950 K): in physical terms increasing injection pressure reduces ignition delay time, the coefficient being negative -0.085;

in chemical terms, increasing oxygen concentration of ambient gas reduces the delay and finally, the octane number of fuels has an effect close to zero.

*) For high-octane number fuel used, the first major difference is in the physical aspect of the air/fuel mixing: increasing injection pressure increases the ignition delay. The coefficient is positive. In addition, on the chemical aspect, there is a greater sensitivity to the octane number of the fuel and less to the oxygen concentration of the ambient gas.

These 2 correlations established on a dataset provided by the CMT are also valid for slightly expanded conditions: back pressure of 55 bar, extended room temperature range up to 1100 K, other type of fuel. Adding results from Jain and Agarwal [70], the Figure 4.38 a) shows the well correlation between the prediction and the experiment with adjusted only the constant A.

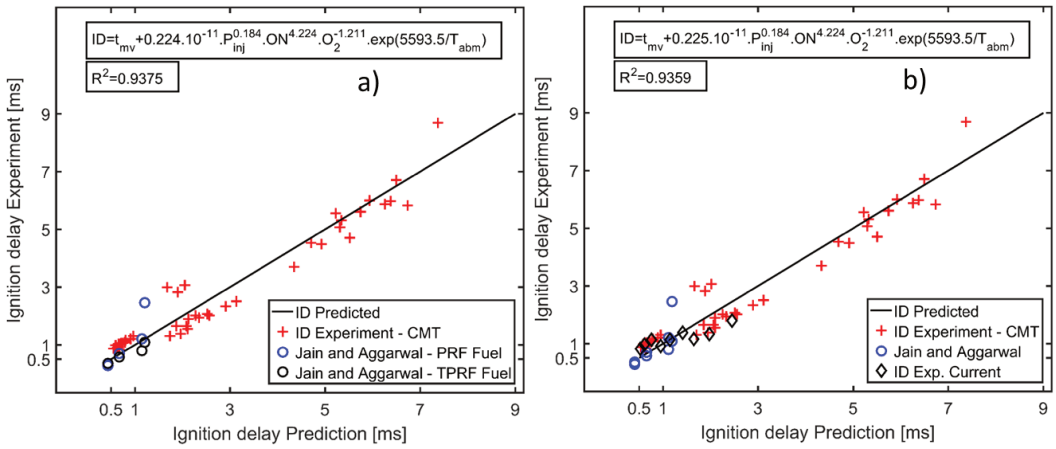

Figure 4.38. Results with a)Jain and Aggarwal for PRF, TPRF fuels with octane number RON of 70 and 80 under ambient gas pressure of 55 bar, injection pressure of 1500 bar, 21% of Oxygen concentration and ambient gas temperature 900, 1000, 1100 K; b) PRF60, PRF70, PRF80 under ambient gas temperature of 900 K, pressure 60 bar, 15/18/21% oxygen concentration and 400 bar of injection pressure

Similarly, in adding the current experiment on NOSE for PRF60, PRF70, PRF80 under ambient gas temperature of 900 K, pressure 60 bar, 15/18/21% oxygen concentration and 400 bar of injection pressure the constant A is adjusted, as show in Figure 4.38 b). This correlation remains valid when adding mixtures with alcohol (ABE, Butanol or ethanol) as shown in figure 4.40 with Bu20, ABE20 for matrix 1 and Bu20/40/60, ABE20/40/60 and Et20 for matrix 2.

Results in this section focus on influence of Alcohols on auto-ignition behavior is under high temperature and high pressure conditions.

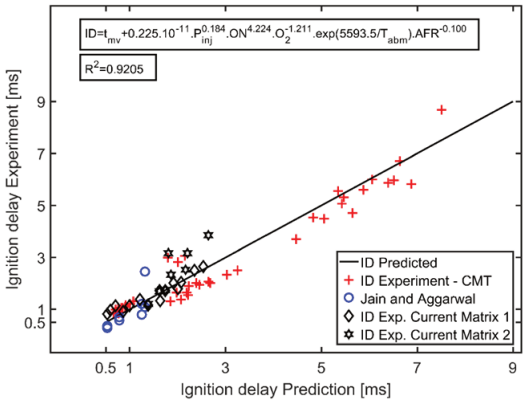

Figure 4.39. Adjusted results of Butanol and ABE blend with PRF80 (Bu20 and ABE20, as marked by matrix 1) and Butanol blends, ABE blends and Et blend with PRF80 (Bu20/40/60, ABE20/40/60 and Et20, as marked by matrix 2)

As expected, due to the higher latent heat of vaporization and oxygen content in fuel in ABE, Butanol and Ethanol, the ignition delay increases. To describe the effect of alcohols amounts, a power correlation can be established with a good correlation coefficient (0.96):

$$\frac{ID_{Bu}}{ID_{PRF80}} = 1.0886\left(1 - r_{V\%Bu}\right)^{-1.072}; \frac{ID_{ABE}}{ID_{PRF80}} = 1.0742\left(1 - r_{V\%ABE}\right)^{-1.289}; \frac{ID_{Et}}{ID_{PRF80}} = \left(1 - r_{V\%Et}\right)^{-4.53}$$

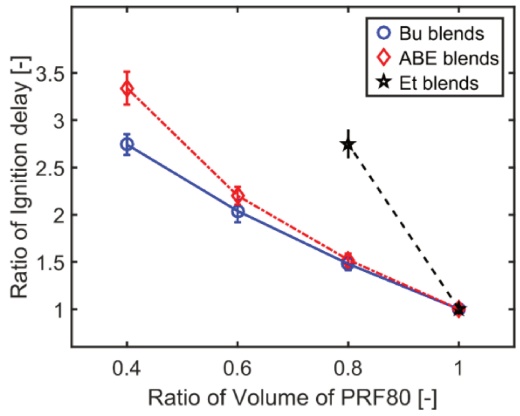

Figure 4.40. Ignition delays as a function of volume fraction of PRF80 on blends

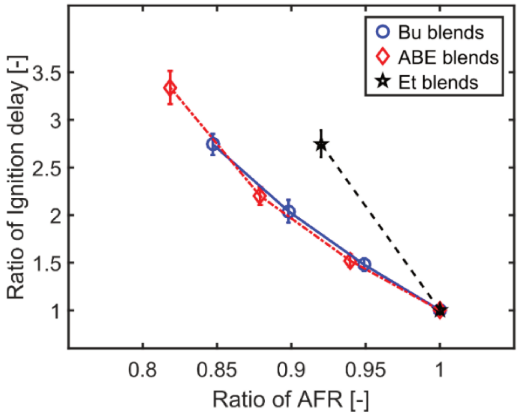

Figure 4.41. Ignition delays as a function of AFR stoichiometric of fuel

Another choice is establishing a power correlation in function of the air fuel ratio (AFR) stoichiometric for Butanol, ABE and Ethanol blends is presented in Figure 4.41:

$$\frac{ID_{Bu-blends}}{ID_{PRF80}} = 1.0193.r_{AFR-Bu-blends}^{8.856}; \qquad \frac{ID_{ABE-blends}}{ID_{PRF80}} = 0.998.r_{AFR-ABE-blends}^{10.938};$$

$$\frac{ID_{Et-blends}}{ID_{PRF80}} = r_{AFR-Et-blends}^{14.94}$$

As seen Figure 4.41, the influence of air fuel ratio for Butanol and ABE is similar and the trend is different with Ethanol blend fuel. In summary, the Ethanol has a significantly different effect on the behavior of ignition compared to mixtures of butanol and ABE.

Indeed, if we study the ignition of this fuel (Et20) during a homogeneous mixture under the following conditions 21% O_2 and 79% N_2, 800-900 K and an equivalence ratio between 0.3-3 with the OpenSMOKE++ simulations, the results show a greater resistance.

To compare the different effects of Butanol, ABE and Ethanol for different initial temperature and equivalence ratio, the iso-contours ignition delay of Bu60, ABE60 and Et20 is computed, as shown in Figure 4.42. With a higher fraction of alcohols on fuel blends, the NTC seems to be extinguished. The E20 fuel blend exhibits greatest ignition delay.

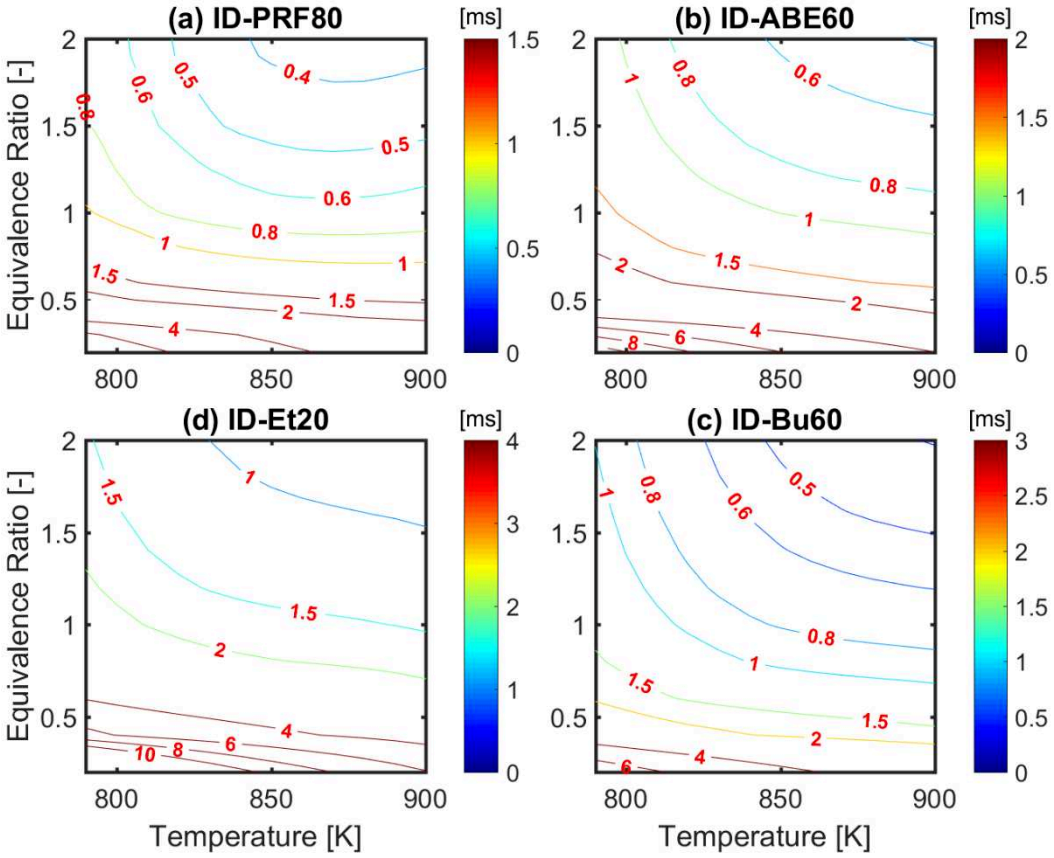

Figure 4.42. Iso-contours of ignition delay for PRF80 and ABE blends under wide-range temperature and equivalence ratio

4.4.2. OH Chemiluminescence imaging*

4.4.2.1. OH Chemiluminescence imaging for PRF80 fuel*

After the auto-ignition of fuel-air mixture, the flame is close to 30 mm downstream from injector nozzle, and the flame develops rapidly in both directions, upstream and downstream. At first, the lift-off length is close to the nose of the injector. This transition phase lasts about 1.5ms. Then the flame stabilizes and the Lift-Off Length oscillates around the 18 mm position downstream of the injector nozzle until the end of the injection, during the quasi-stationary phase of 3 ms. When the injection stops, the flame is convected.

As the time progresses from 2 to 7 ms after start of injection, the flame OH* chemiluminescence develops and continues to propagate downstream, as shown in Figure 4.43.

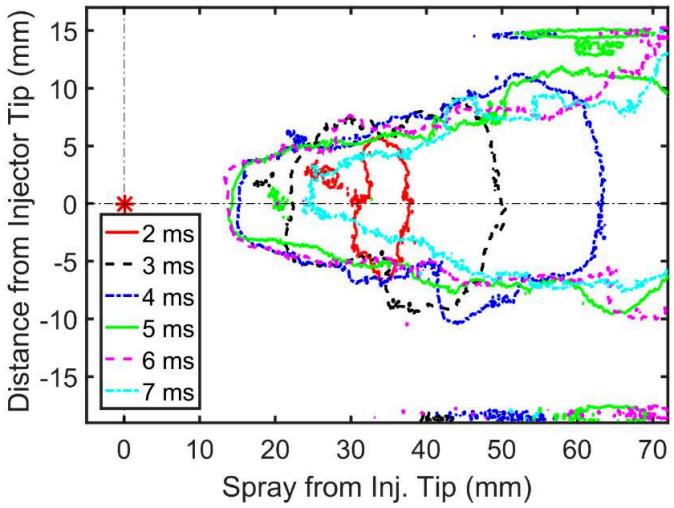

Figure 4.43. Boundary of OH* chemiluminescence evolution versus time of PRF80 fuel

4.4.2.2. OH Chemiluminescence imaging for Butanol blend fuel*

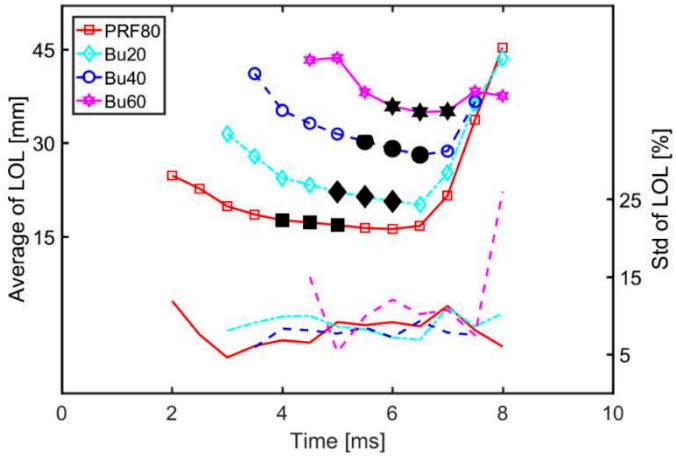

Figure 4.44. LOL time-resolved measurement from SOI until EOI for Butanol blends

In this section, the blends of butanol with PRF80 are selected to investigate the influence of alcohols on LOL. The time resolved LOL measurement of PRF80 and Butanol blends are

presented in Figure 4.44.

After a transient phase, the LOL stabilizes for PRF80, Bu20, Bu40 and Bu60 at 4 ms, 5 ms, 5.5 ms and 6 ms, respectively, after the start of injection. Increase the butanol ratio, the steady LOL period is shorter than PRF80 fuel. Three points of black marker are chosen to calculate the LOL for each fuel. Figure 4.45 shows the OH* chemiluminescence images at the beginning of the stabilization phase for four fuel blends.

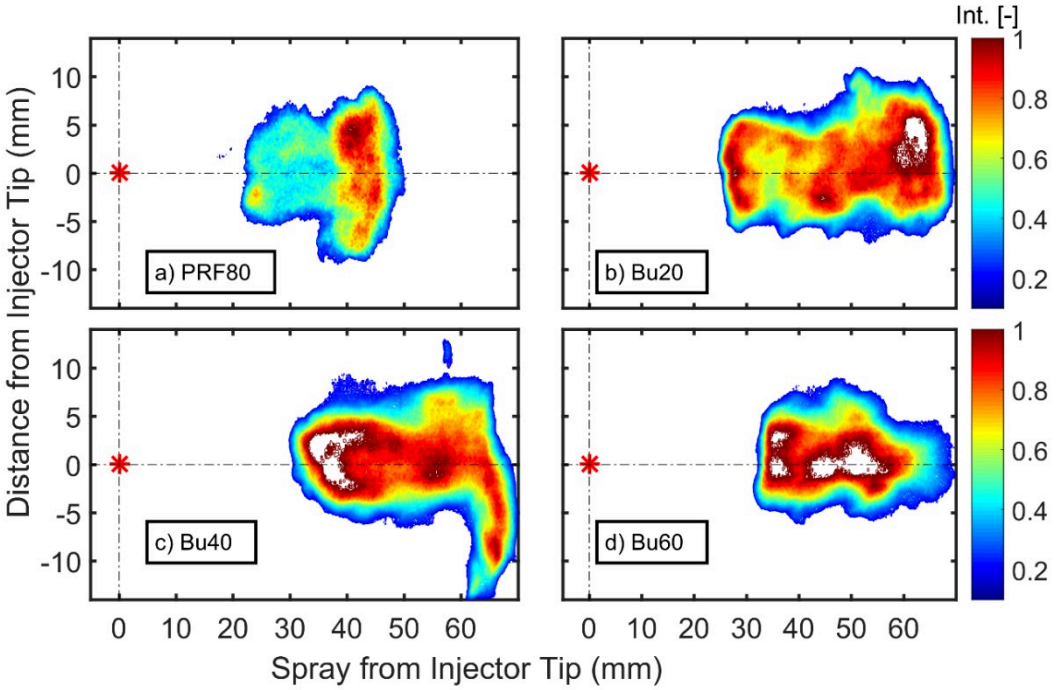

Figure 4.45. The images of OH* Chemiluminescence for Butanol fuel blends at start stabilize phase

The boundary of image of OH* Chemiluminescence from Figure 4.45 is replotted to overlapped in Figure 4.46. Among the Butanol blends, Bu60 shows longest Lift-Off length, as similar trend butanol blends ignition quality.

The flame front contours of IXT plots of Butanol fuel blends are calculated, as shown in Figure 4.47. This graph allows to see the position of the flame and its maximum development at any time. Thus, there is a delay in flame onset with the addition of butanol coupled with a smaller combustion zone.

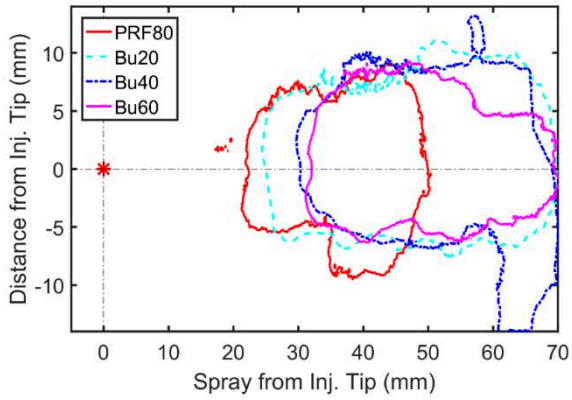

Figure 4.46. Overlapped OH* chemiluminescence boundary of Butanol blend fuel

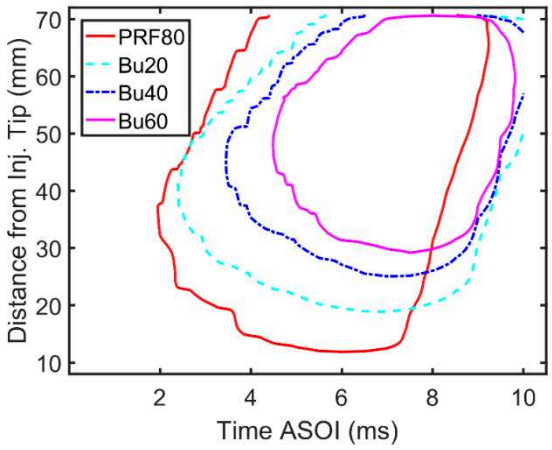

Figure 4.47. The flame front contours of IXT plots of OH* chemiluminescence for PRF80 and Butanol blends

4.4.2.3. Compare between Butanol, ABE and Ethanol blends

In current section, the blends with a highest ratio, Bu60, ABE60 and Et20 are evaluated. The boundary of PRF80, Bu60, ABE60 and Et20 fuel stabilized phase images is shown in Figure 4.48. Under the gas conditions examined in this study, the ordering in LOL as: PRF80 < Bu60 < Et20 < ABE60.

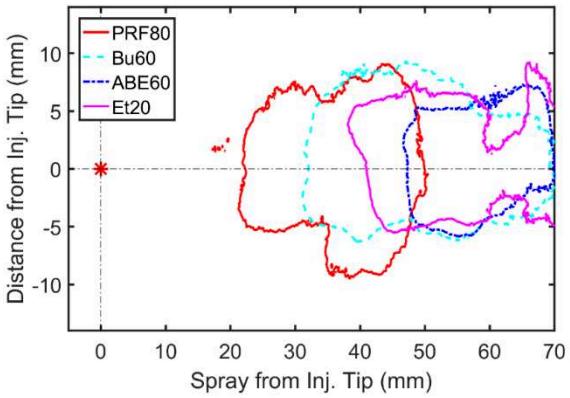

Figure 4.48. Overlapped of OH* Chemiluminescence of PRF80, Bu60, ABE60 and Et20 blends

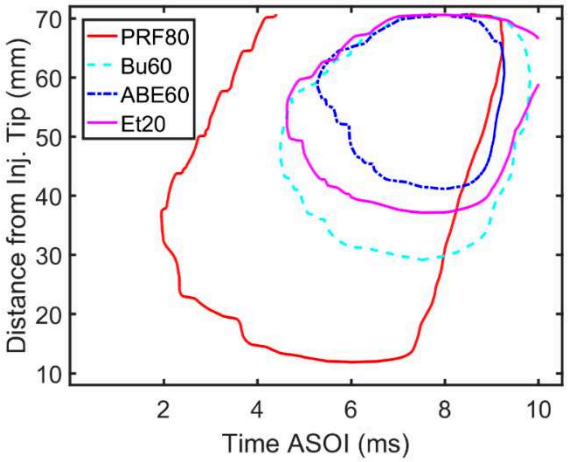

Figure 4.49. Flame front contours of OH* chemi. for PRF80, Bu60, ABE60 and Et20 blends

The flame front contours of IXT plots for the PRF80, Bu60, ABE60 and Et20 measurements are presented in Figure 4.49. The lift-off length according the correlation referenced by Manin et al. [69] depends on density and stoichiometric air-fuel ratio (AFR).

The fuel density influences the flame Lift-Off length through the fuel velocity at nozzle orifice, as presented in [64].

$$LOL = A.\sqrt{\rho_f}^{a_f}.AFR^{b_f} \qquad \textbf{Eq. 4.8}$$

Each coefficient is determined by biofuel family (PRF, Butanol, Ethanol and ABE), as shown in Table 4.7.

Table 4.7. Coefficients for Eq. 4.8

	Coefficients			
	A	a_f	b_f	R^2
Butanol	$3.66*10^{-8}$	-1.70	-5.418	0.970
ABE	9.7610^{-8}	-1.70	-5.056	0.991
Ethanol	$6.78*10^{18}$	-1.70	-11.366	0.999

We also observe on Figure 4.50 that the position of the lift-off is strongly correlated with the auto-ignition delay. The earlier the combustion starts, the more the flame is stabilized near the injector in a richer zone. The sensitivity is similar regardless of the type of blend.

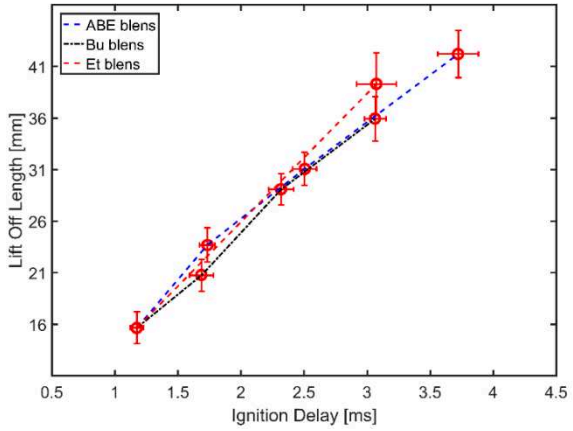

Figure 4.50. Lift off length and Ignition delay of PRF80, ABE20/40/60, Bu20/40/60 and Et20

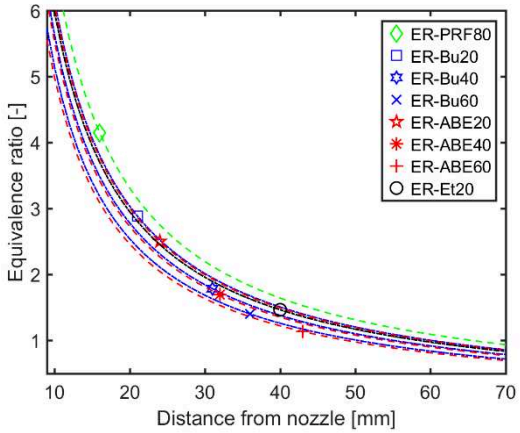

Figure 4.51. Cross-sectional average equivalence ratio at various distance from injector

According the Pickett and Siebers [79] the air entrainment and a cross-sectional average equivalence ratio at axial location can be estimated following the relationship developed by Naber and Siebers [44]. The mean equivalence ratio calculated across the jet for Butanol, ABE and Ethanol blends is shown in Figure 4.51. Here, the variation of cross-sectional average equivalence ratio is caused by both density and equivalence ratio stoichiometric of fuels.

Previous soot studies have observed that the diesel fuel jet soot decreases with increasing fuel-

air premixing upstream of the lift-off length, with the cross-sectional average equivalence ratio at the lift-off length ($\overline{\Phi}$) demonstrated to provide a useful estimate of the latter [79]. They reported observable soot luminosity when the $\overline{\Phi}$ value exceeds 2 [79].

The higher alcohols ratio in fuel blends lead to longer auto-ignition delays and longer lifted flames, hence reduction the fuel concentration in flame. The summary of ignition delays and Lift-Off Length is listed in Table 4.11.

Table 4.8. Summary of Ignition delays and Lift off length

Fuel	**Ignition delays (ms)**	**Lift off length (mm)**	$\overline{\Phi}$
PRF80	1.01 (±0.04/4.0%)	16.5 (±0.75/4.5%)	4.15 (±0.187/4.5%)
Bu20	1.50 (±0.09/6.0%)	20.7 (±0.75/3.6%)	2.89 (±0.104/3.6%)
Bu40	2.17 (±0.09/4.15%)	28.6 (±1.15/4.0%)	1.79 (±0.072/4.0%)
Bu60	3.16 (±0.12/3.8%)	35.1 (±1.75/5.0%)	1.47 (±0.074/5.0%)
ABE20	1.75 (±0.07/4.0%)	22.3 (±0.85/3.8%)	2.50 (±0.095/3.8%)
ABE40	2.53 (±0.10/4.0%)	31.8 (±1.10/3.5%)	1.70 (±0.060/3.5%)
ABE60	3.84 (±0.19/5.0%)	41.5 (±1.10/2.7%)	1.14 (±0.031/2.7%)
Et20	3.16 (±0.14/4.4%)	37.5 (±2.02/5.3%)	1.40 (±0.074/5.3%)

The observation of the increased luminosity within the fuel jet only at a lift-off length inferior to 25mm (i.e., ($\overline{\Phi}$) greater than a value of 2) appears consistent with the findings of previous studies. Thus, for the analysis of soot only the fuels PRF60, PRF70, PRF80, Bu20 and ABE20 will be studied.

4.4.3. Measurement on DBI extinction imaging setup

In this section, HRR, ignition delay, LOL, and soot are investigated for 5 fuels, allowing the influence of certain fuel properties on combustion and spray soot quality to be evaluated. Firstly, the PRF60 fuel is used to evaluate the DBI technique to quantify soot production. Then, PRF70, PRF80 and Bu20, ABE20 (PRF80 mixture with 20% Butanol, ABE) are investigated with various oxygen concentration in the ambient gas, as listed in Table 4.9.

Table 4.9. Fuel and condition test matrix

No.	**Fuel**	**Ambient gas**		
		O_2 [%]	**Temperature [K]**	**Pressure [bar]**
1	PRF60/PRF70/PRF80	15/18/21	900	60

No.	Fuel	Ambient gas		
		O_2 [%]	Temperature [K]	Pressure [bar]
2	Bu20/ABE20			

4.4.3.1. Cycle to cycle

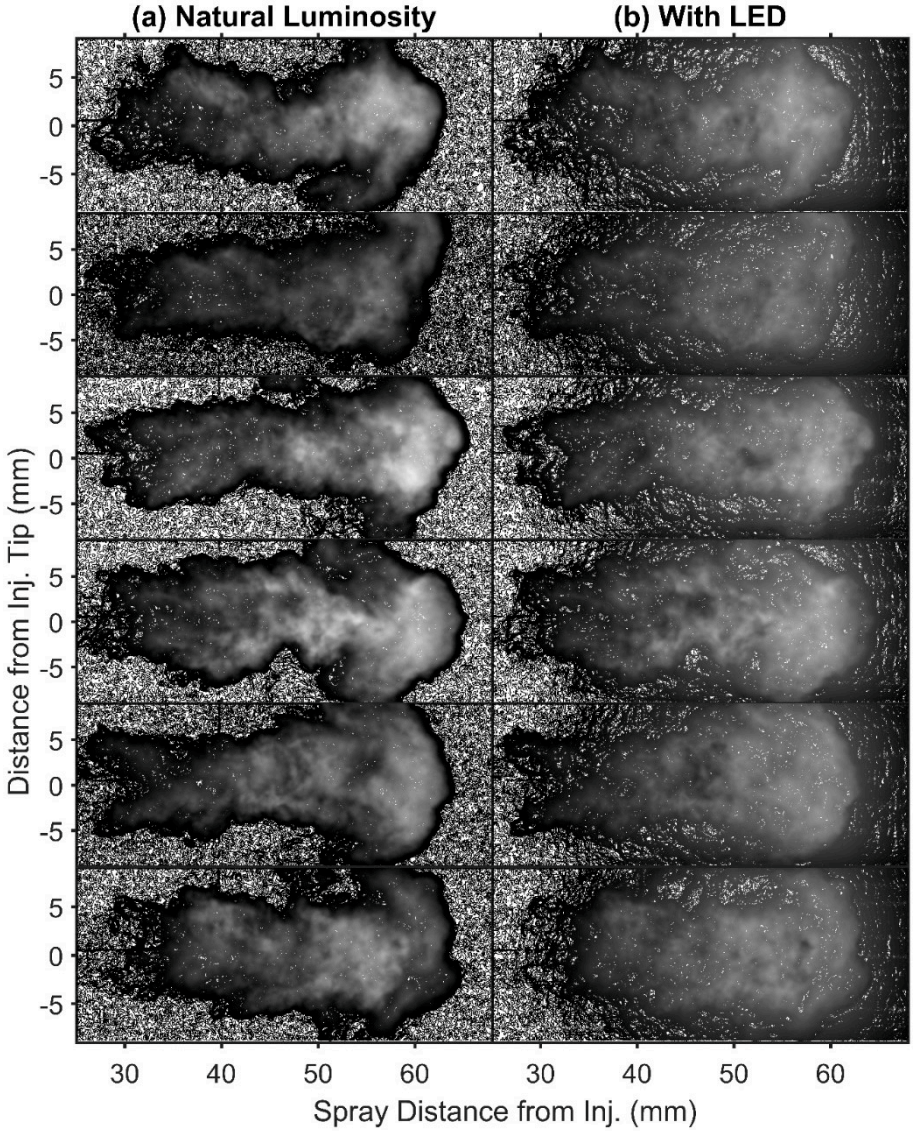

Figure 4.52. One of DBI set-up cycle-to-cycle variations of six tests at 3500 µs ASOI for PRF60 fuel under ambient gas conditions: 18% of Oxygen concentration, 900 K of temperature and 60 bar of pressure

The Figure 4.52 shows a sequence of 6 images of Natural Luminosity without LED and with LED images of PRF60 fuel at 3.5 ms ASOI under 18% Oxygen concentration in ambient gas, 900 K and 60 bar for the back pressure, which illustrates the cycle-to-cycle variations of soot

measurements.

The Natural Luminosity integral is calculated for 6 tests. The average, the standard deviation one over 6 tests, as shown in Figure 4.53. It could be observed that the Natural Luminosity integral evolution is quite repeatable.

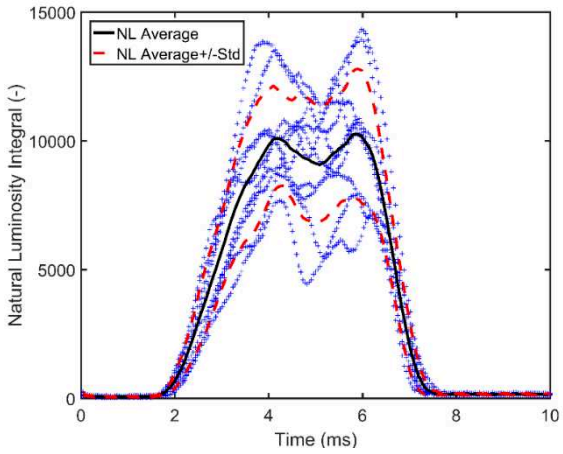

Figure 4.53. Integral of Natural Luminosity (Radial digital) values with time versus for 6 tests (blue point), the average one (black line) and average +/- standard deviation (red dashed)

The Natural Luminosity Intensity along spray axis (a) and cross-sectional at 50 mm of down-stream from nozzle (b) are illustrated in Figure 4.54.

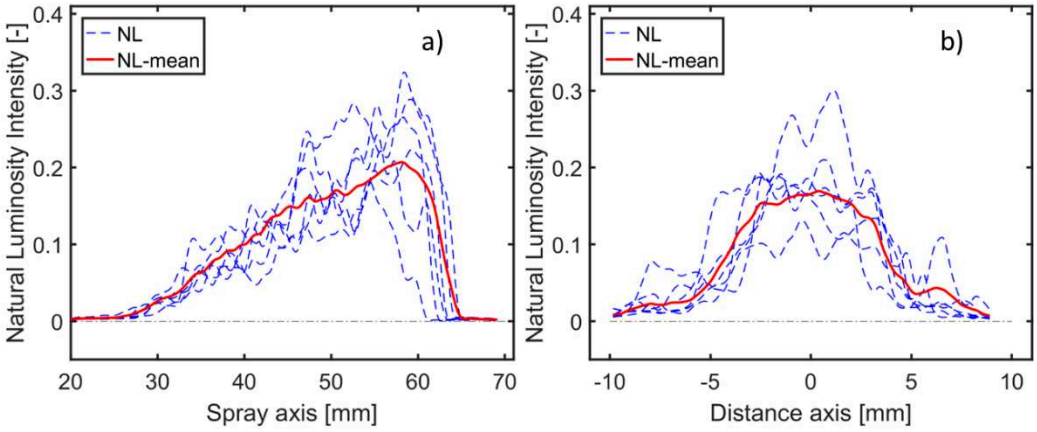

Figure 4.54. Natural Luminosity Intensity along spray axis and spray cross-sectional at 50 mm of downstream from nozzle

The 10 cylinder pressures and corresponding HRR and their average are shown in Figure 4.55. The evolution of HRR is similar from test to test, and the auto-ignition timing is also repeatable across all tests, as about of 0.9 ms ASOI with the standard deviation of 0.05 ms (5.5%).

The variations of HRR and auto-ignition behavior of spray under this condition tested do not

explain the cycle-to-cycle variations of soot.

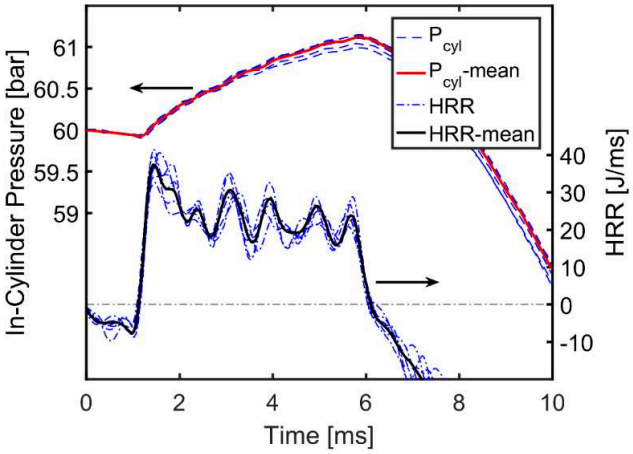

Figure 4.55. Corresponding in-cylinder pressure HRR to Figure 4.52 and Figure 4.53 and averaged one over 10 tests

4.4.3.2. Natural Luminosity and OH Chemiluminescence*

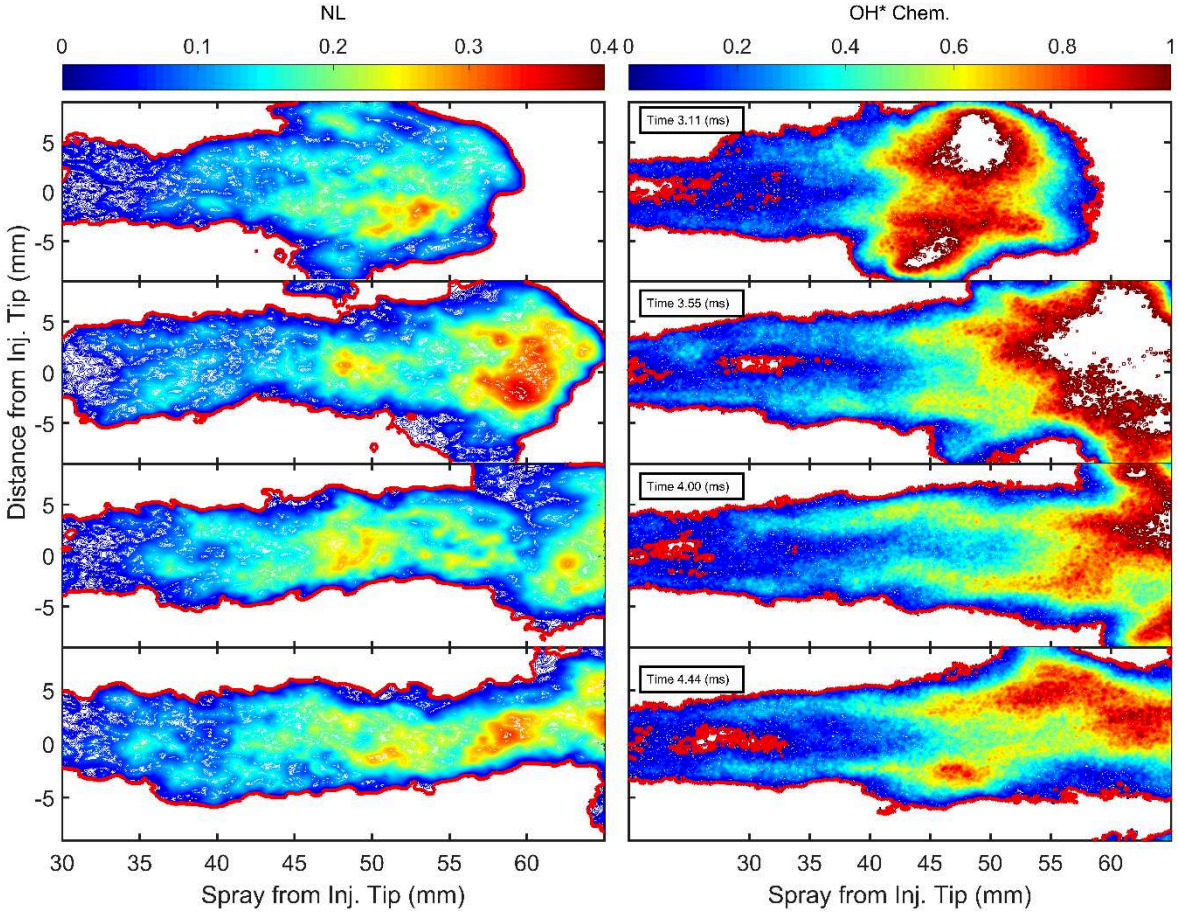

Figure 4.56. Natural Luminosity and OH* Chemi. at four times after SOI of PRF60 fuel under ambient gas of 18% Oxygen concentration, 900 K of temperature and 60bar of pressure

The Imaging of Natural Luminosity and OH* Chemiluminescence are presented in Figure 4.56.

The Natural Luminosity is replotted with boundary of OH* chemiluminescence in Figure 4.57, to check the relative location between OH radical and soot cloud in spray flame in the vessel.

IXT of Natural Luminosity, OH* Chemiluminescence and those's boundary for PRF60 fuel under 18% of oxygen in ambient gas are shown in Figure 4.58.

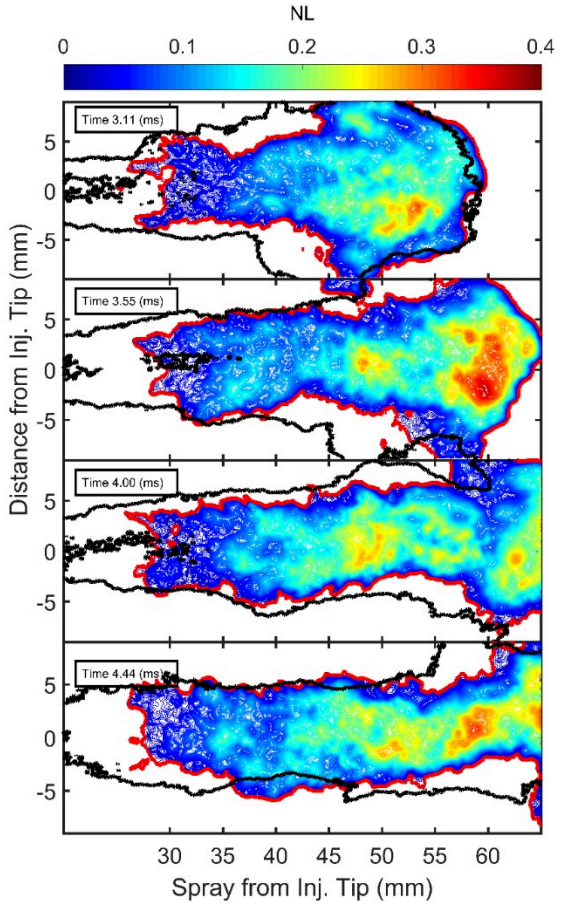

Figure 4.57. Simultaneous of Natural Luminosity and OH* Chemi. boundary (back line)

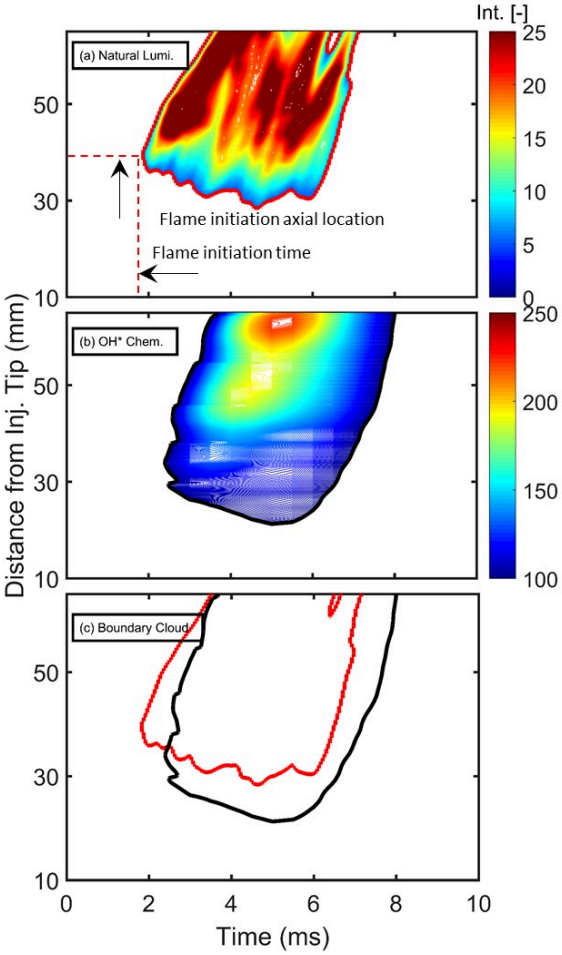

Figure 4.58. Cloud of Natural Luminosity, OH* Chem. and these boundary cloud (Natural Luminosity in red line and OH* Chem. in black line)

The Figure 4.58 shows that Natural luminosity begins at 1.9 ms ASOI (around at 0.9 ms ASOC), after auto-ignition behavior during the premixed combustion phase and the Natural Luminosity initially closer to the nozzle than initial lift off length. With IXT of Natural Luminosity, the soot initiation time and the soot initial axial location are defined 1.9 ms ASOI or 0.9 ms ASOC and 34 mm, respectively.

4.4.3.3. Natural Luminosity and KL estimated

A temporal sequence of images of Natural Luminosity and estimated KL are presented in Figure 4.59 left and right, respectively.

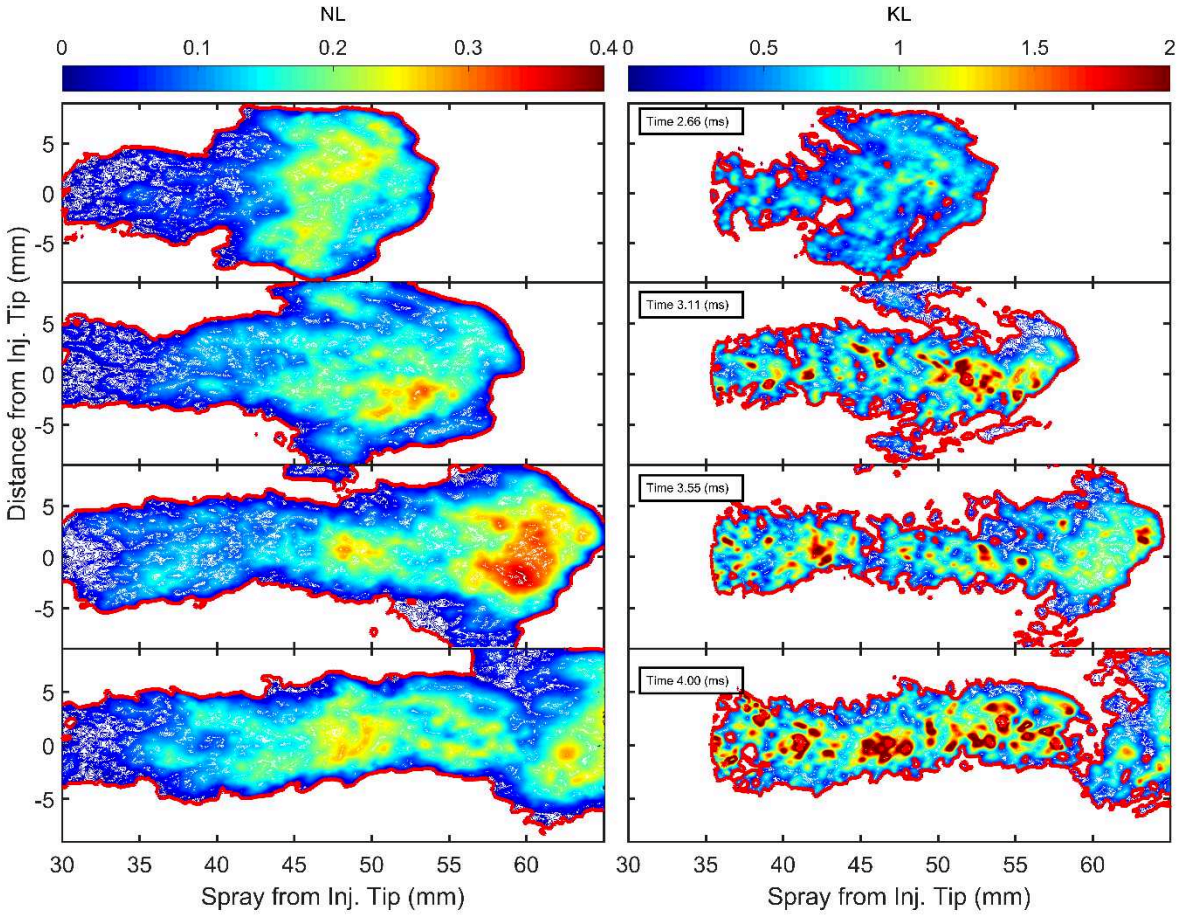

Figure 4.59. Imaging of Natural Luminosity and KL estimated at four times after SOI of PRF60 fuel under ambient gas conditions: 18% of Oxygen concentration, 900 K of temperature and 60 bar of pressure

The soot contour follows the area of highest luminosity (>0.15) as visible in the following image.

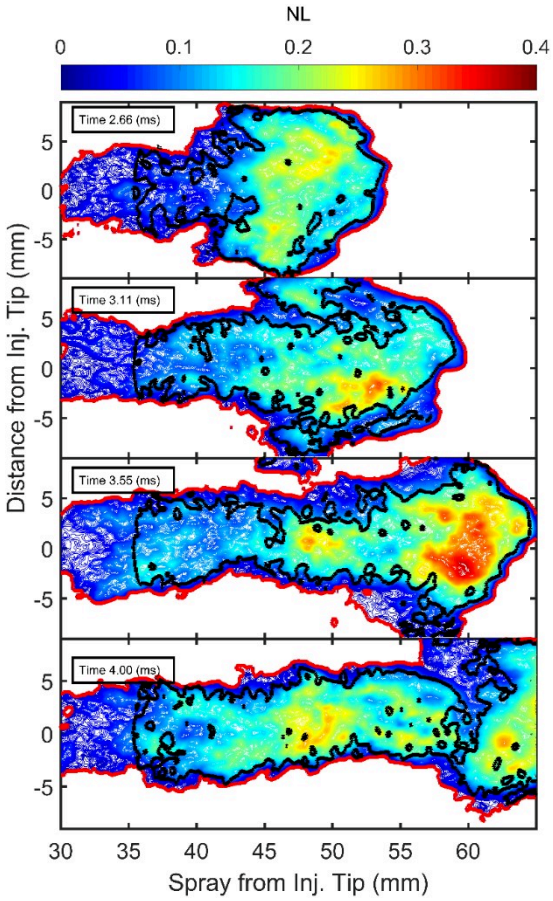

Figure 4.60. Simultaneous of Natural Luminosity and KL boundary (black line)

4.4.3.4. Effect of Oxygen concentration on Natural Luminosity signal

The IXT analysis for natural luminosity has been systematized for the three oxygen rates for the PRF60 and PRF70 fuels as shown in Figure 4.61 and in Figure 4.62, respectively.

It can be observed that as expected the flame starts is delayed and the flame region is far downstream nozzle for lower oxygen concentration. For the higher oxygen concentration conditions, the intensity measured intensity within the contour lines is higher due to contribution of soot illumination. The intensity level decreases with increasing the octane number. This aspect is studied in the next section.

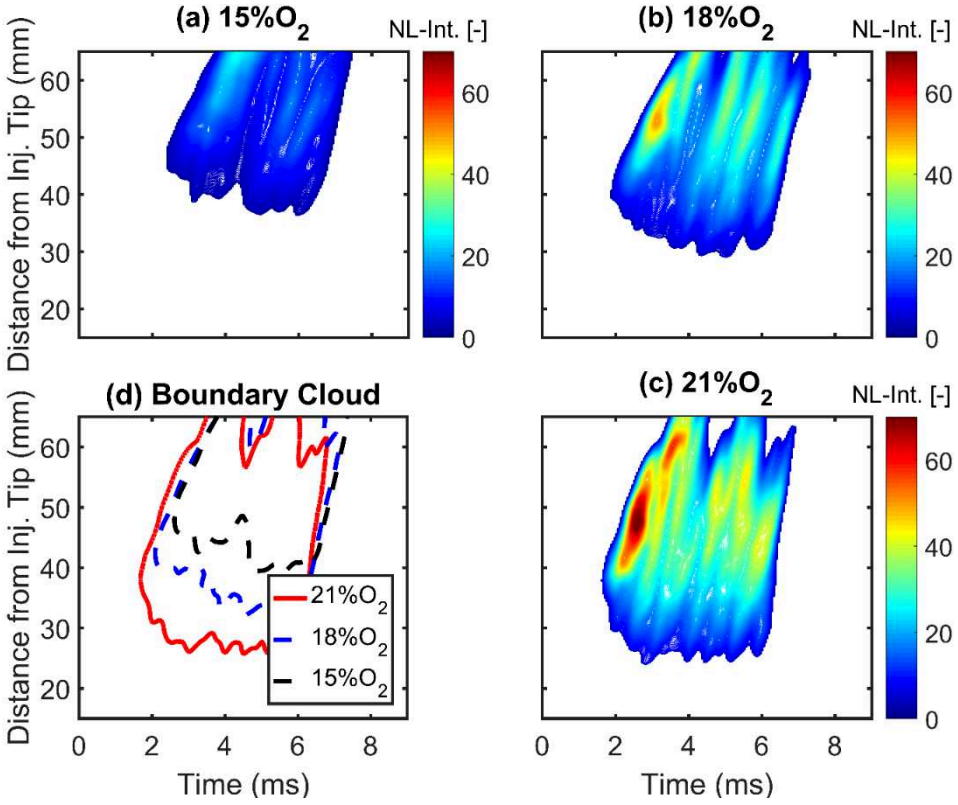

Figure 4.61. Cloud of Natural Luminosity of PRF60 fuel under ambient gas variation of 15/18/21% Oxygen concentration, 900 K of temperature and 60bar of pressure

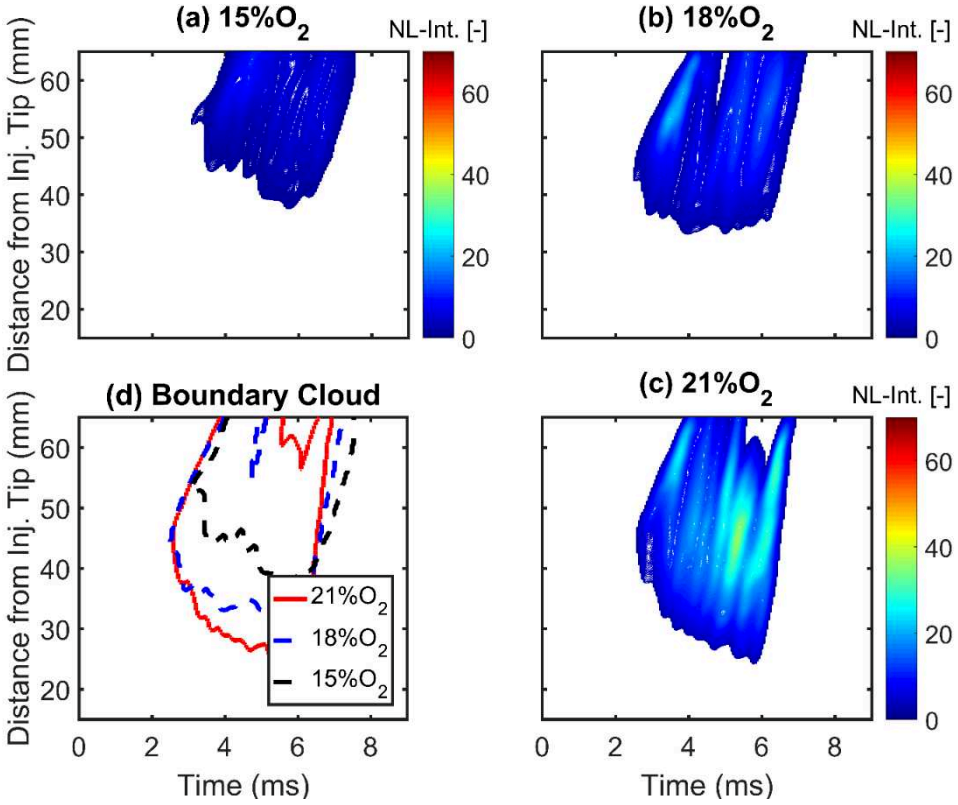

Figure 4.62. Cloud of Natural Luminosity of PRF70 fuel under ambient gas variation of 15/18/21% Oxygen concentration, 900 K of temperature and 60 bar of pressure

The soot initiation time and axial location for PRF60, PRF70 and PRF80 fuels under various ambient oxygen obtained by the analysis of IXT of natural luminosity are given in Table 4.10.

Table 4.10. Soot initiation time and axial location for PRF60, PRF70 and PRF80 fuels under various ambient oxygen

Fuel	Ambient oxygen [%]	Soot initiation time [ASOC ms]	Soot initiation axial location [mm]
PRF60	15	1.0	46
	18	0.9	40
	21	0.8	38
PRF70	15	1.5	50
	18	1.3	45
	21	1.2	42
PRF80	18	2.8	46
	21	1.7	33

4.3.3.5. Effect of octane number of fuels on flame under 21% oxygen in ambient gas

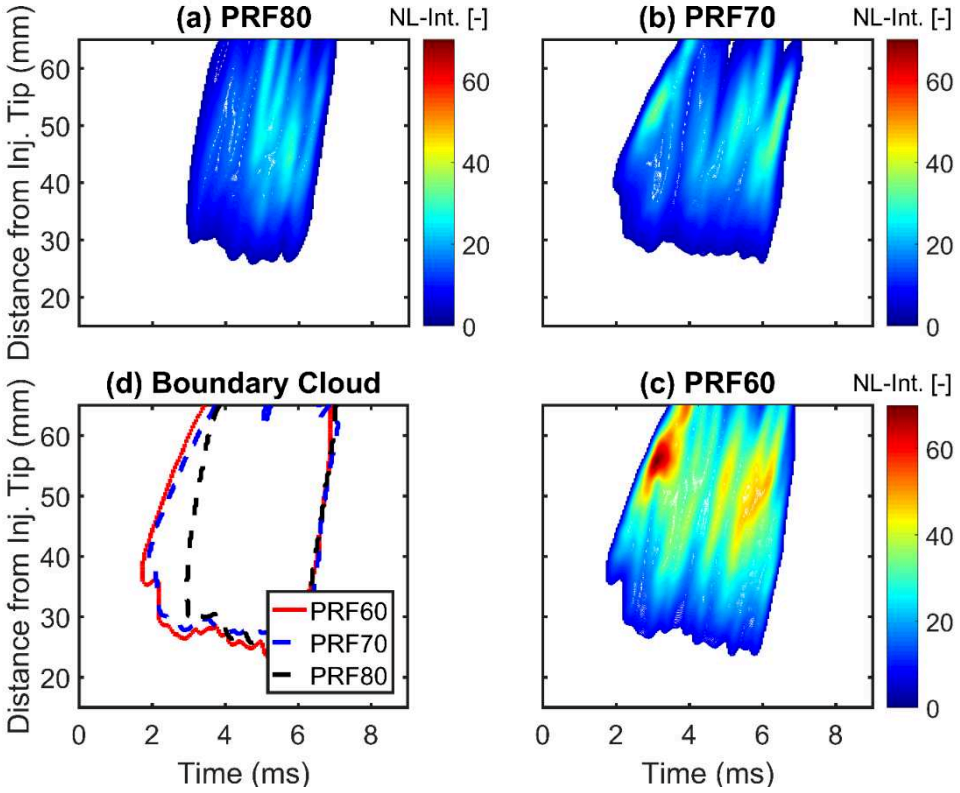

Figure 4.63. Cloud of Natural Luminosity of PRF60/ PRF70/ PRF/80 fuel under ambient gas conditions: 21% of Oxygen concentration, 900 K of temperature and 60 bar of pressure

The IXT plots, as shown in Figure 4.63, of different fuels are investigated under 21% oxygen: PRF60, PRF70 and PRF80.

The distance between the nozzle and the flame or soot region is slightly different depending on the octane number. The higher the octane number is, the more delayed the combustion. Conversely, the higher the octane number, the less luminous the flame. Thus, the intensity of contour lines is highest for PRF60 fuel.

The soot initiation time and axial location for PRF60, PRF70 and PRF80 fuels shown in Table 4.10, give the same sensitivity to octane number regardless of oxygen content.

4.4.4. Results of measurement soot

For fuels for which it is possible to record natural light, such as PRF60, PRF70 and PRF80, as well as ABE20, Bu20 (PRF80 and ABE/Butanol mixtures), we will evaluate the combustion characteristics under different oxygen levels.

4.4.4.1. Ignition delay and Lift off length

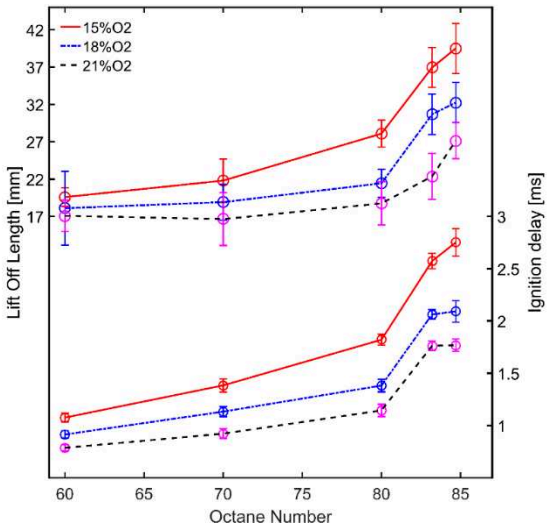

Figure 4.64. Ignition delay and Lift off length as a function of octane number under difference ambient gas oxygen concentration 15/18/21%

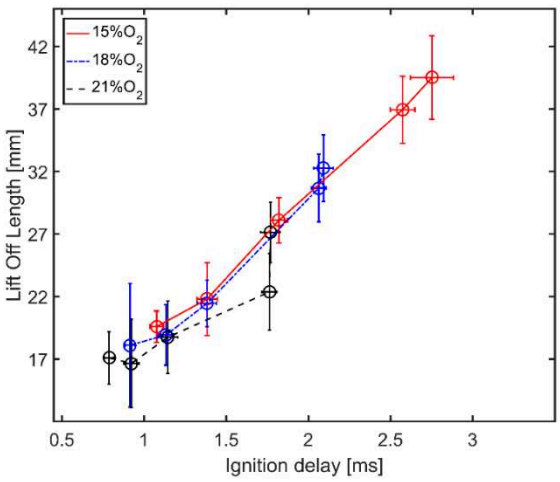

Figure 4.65. The trend of Lift off length versus ignition delay for PRF60, PRF70, PRF80, Bu20 and ABE20 fuels with 15, 18, 21% ambient gas oxygen concentration

The Lift off length and Ignition delay versus Octane number of fuels with three level of oxygen concentration (15%, 18% and 21%) are illustrated in Figure 4.64. Increasing the oxygen content does not have the same impact depending on the octane number of the fuel. The LOL

is reduced by 15% for PRF60 versus 32% for ABE20. Also, the ignition delay varies greatly for the highest octane number.

The trend of Lift off length versus auto-ignition delay for PRF60, PRF70, PRF80, Bu20 and ABE20 fuels with 15%, 18% and 21% Oxygen concentration in ambient gas is shown in Figure 4.65. The trend is similar to that in the previous section for the Alcohol blends with 21% oxygen concentration in ambient gas. The overall correlation between lift off length and auto-ignition delay is obtained in this section, further confirming the validity of this relation for lower octane number of fuel and lower oxygen content.

4.4.4.2. Effect of oxygen concentration on soot production

Soot distribution will be detailed for the PRF. The effect of oxygen content and octane number will be described.

a) PRF60 fuel

For different oxygen concentration in ambient gas, the IXT of soot mass of PRF60 fuel under 900 K temperature and 60 bar back-pressure is illustrated in Figure 4.66.

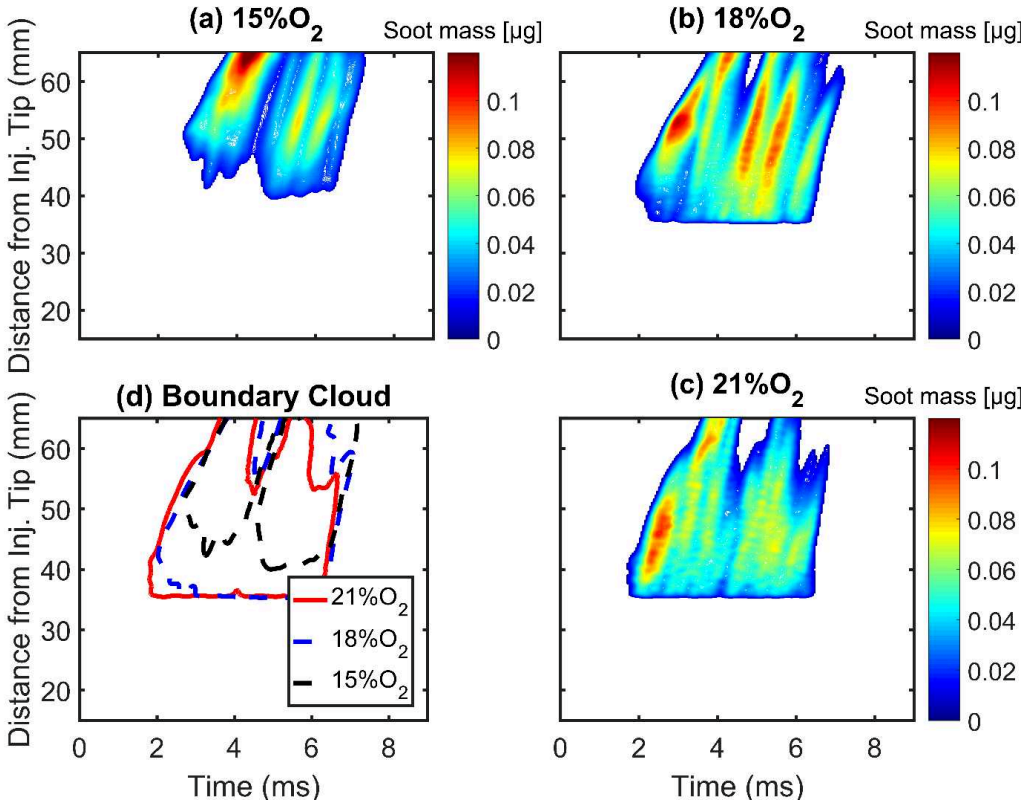

Figure 4.66. Cloud Soot mass of PRF60 under 3 different oxygen concentrations

The region of soot formation and oxidation tends to shift upstream with higher ambient oxygen. For example, at 15% oxygen the top of IXT is close to 40 mm. In contrast, at 21% oxygen, the soot formation process is earlier and pushed upstream, the top of IXT is close to 37 mm and the soot oxidation consumes almost all the soot at 60 mm.

The highest value of soot mass on IXT graph is closer to the upstream for a higher oxygen concentration. Figure 4.67 shows the soot mass versus time of six tests for the PRF60 fuel under 3 different oxygen concentrations.

The higher the oxygen level, the earlier soot appears due to the faster ignition. During the stationary phase for this fuel the average mass of soot is very close regardless of the oxygen level (about 20 µg).

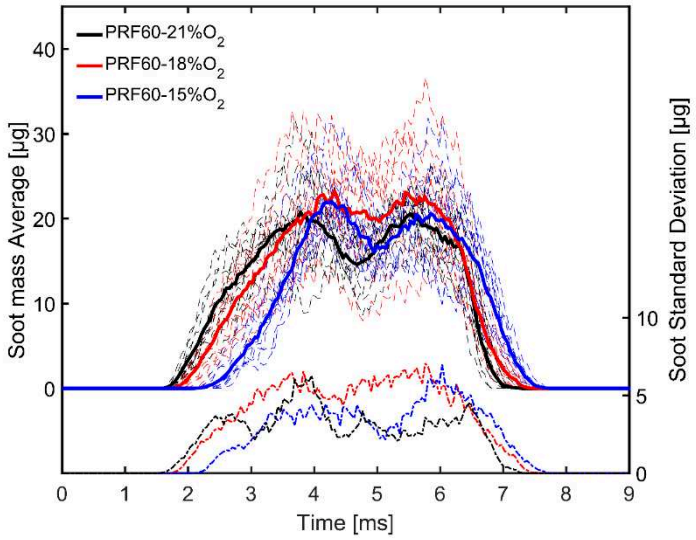

Figure 4.67. Soot mass versus time of PRF60 under 3 differences oxygen concentration

As shown in Figure 4.68, the soot mass fractions of spray for PRF60 fuel at 3.5 ms ASOI for 3 oxygen levels are computed. The contour is drawn with a red line. With increasing oxygen concentration the soot mass processes shift upstream to nozzle.

The local soot mass (over thickness of 1 mm) present in the jet flame is calculated by Eq. 4.9, along the spray axis. The results are presented in Figure 4.69.

$$m_{soot} = \rho_{soot} \int_{-0.5mm}^{0.5mm} \left(\int_0^R \left(f_v 2\pi \right) dr \right) dx \qquad \textbf{Eq. 4.9}$$

Figure 4.69 shows that increasing the oxygen concentration in ambient gas leads to an increase the peak soot mass and a shift this peak upstream of nozzle. When the oxygen concentration in

ambient gas decreases from 18% to 21%, the soot mass first increases (39-50 mm), then decreases when the oxygen content of 15%.

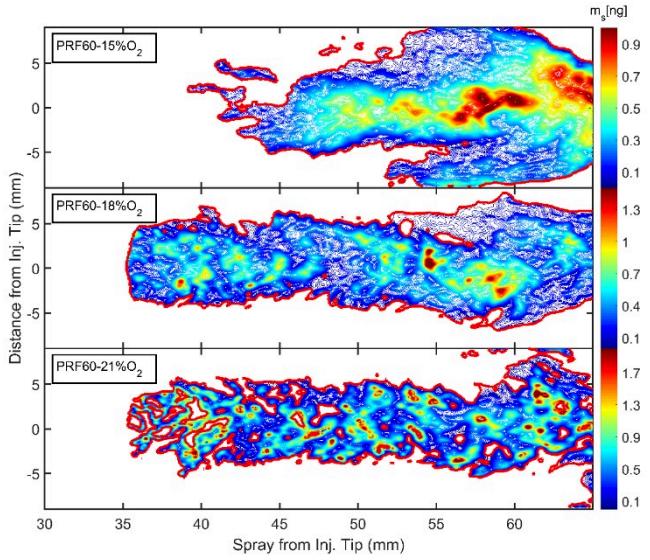

Figure 4.68. The soot mass fraction images at 3.0 ms ASOC for PRF60 fuel and various of oxygen concentration ambient gas

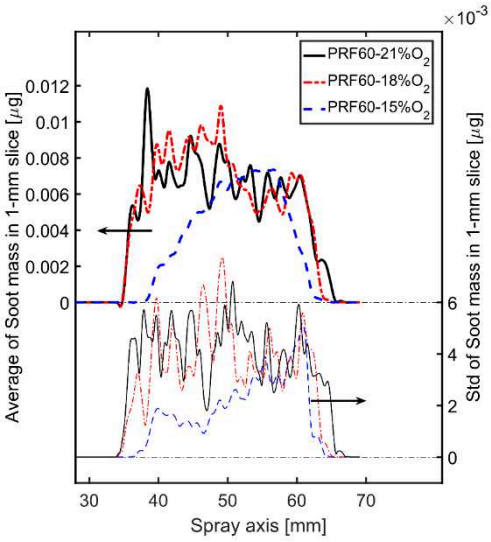

Figure 4.69. Soot mass for PRF60 fuel and various oxygen concentration of ambient gas in thin (1 mm) cross-sections of jet as a function of axis distance

b) PRF70 fuel

For different oxygen concentration in ambient gas, the IXT of soot mass of PRF70 fuel under 900K temperature and 60 bar gas back-pressure is illustrated in Figure 4.70.

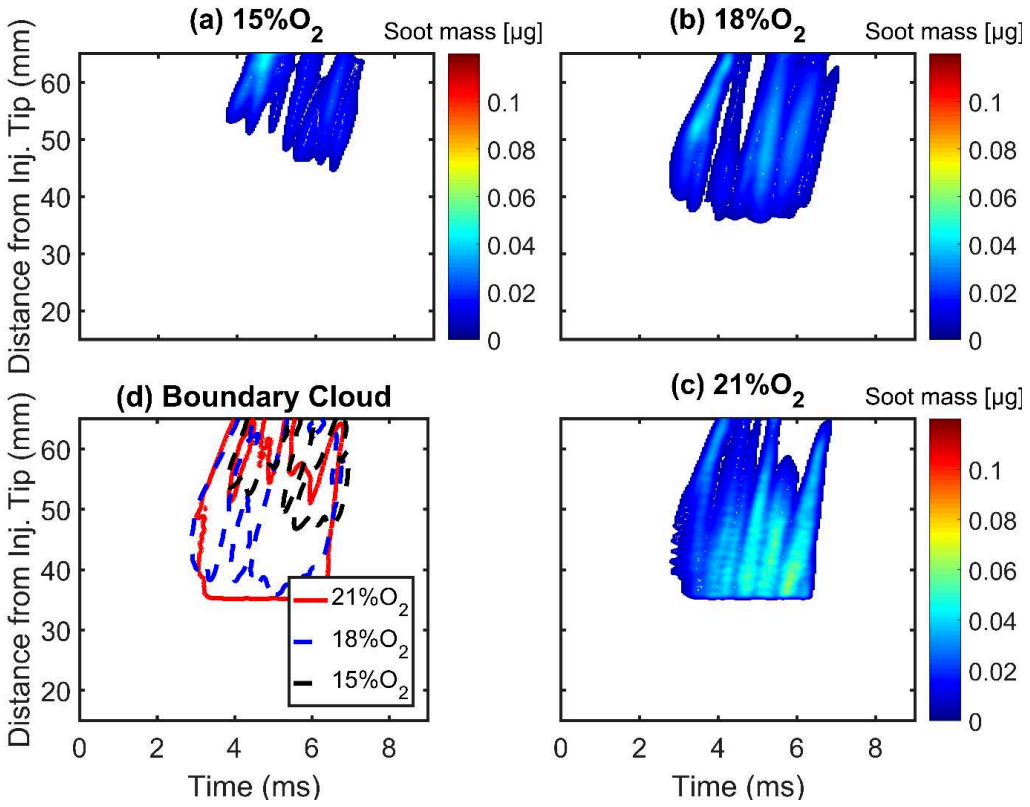

Figure 4.70. Cloud Soot mass of PRF70 under 3 differences oxygen concentration

The soot mass versus time of six tests for PRF70 fuel under 3 different oxygen concentrations are illustrated in Figure 4.71. The no significantly difference is observed between 15 and 18% oxygen. The soot mass is higher under the 21% oxygen.

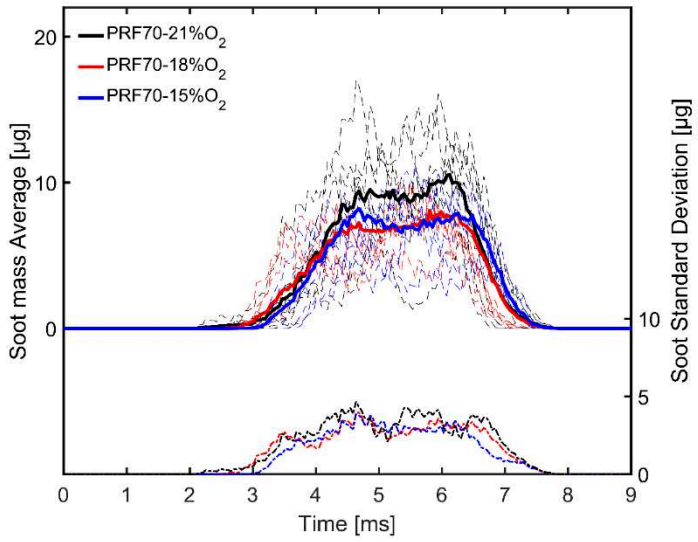

Figure 4.71. Soot mass versus time of PRF70 under 3 differences oxygen concentration

As shown in Figure 4.72, the soot mass fractions of spray for PRF70 fuel at 4.5 ms for 3 oxygen levels are calculated within the area delimited by the red line. Figure 4.73 shows the integrated

soot masses in thin (1 mm) radial cross-sections within the PRF70 jet flame along spray axis for 3 oxygen levels.

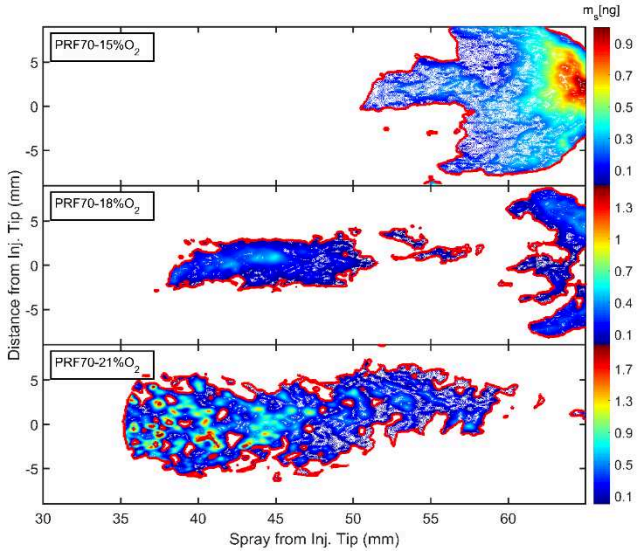

Figure 4.72. The soot mass fraction images at 3.5 ms ASOC for PRF70 fuel and various of oxygen concentration ambient gas

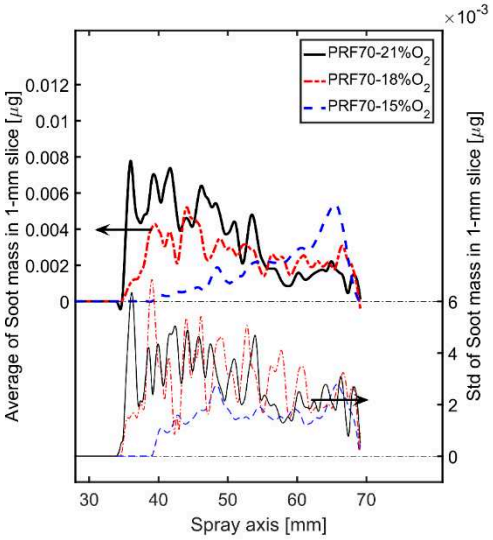

Figure 4.73. Soot mass for PRF70 fuel and various oxygen concentration of ambient gas in thin (1 mm) cross-sections of jet as a function of axis distance

Figure 4.73 shows that decreasing the oxygen concentration in ambient gas causes the peak soot mass to decrease and the peak to shift downstream of the nozzle. The soot mass is reduced as the oxygen concentration decreases.

c) PRF80 fuel

The soot mass versus time of six tests for PRF80 fuel under 3 different oxygen concentrations is illustrated in Figure 4.74. It is clear that the low oxygen concentration in ambient gas produces less soot than cases with higher oxygen concentration.

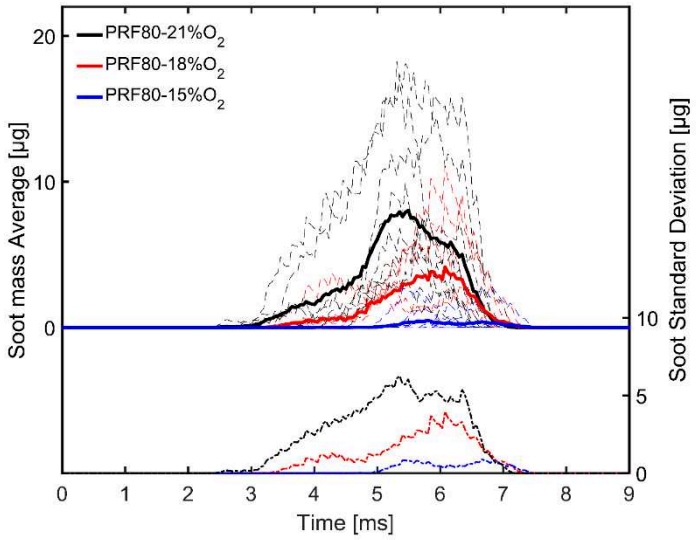

Figure 4.74. Soot mass versus time of PRF80 under 3 differences oxygen concentration

The Figure 4.75 is a contour plot to illustrate the soot mass fractions of spray for PRF80 fuel with 3 oxygen concentration.

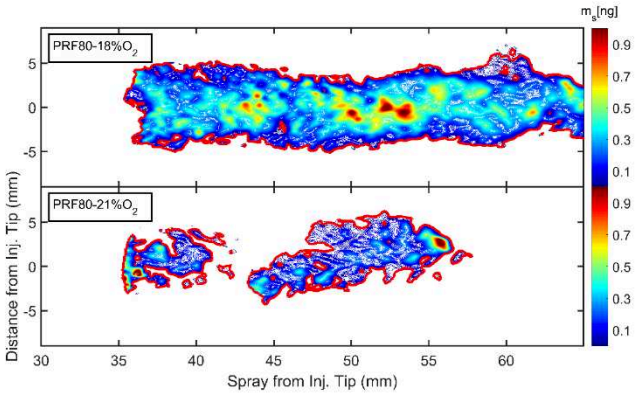

Figure 4.75. The soot mass fraction images at 4.0 ms ASOC for PRF80 fuel and various of oxegen concentration ambient gas

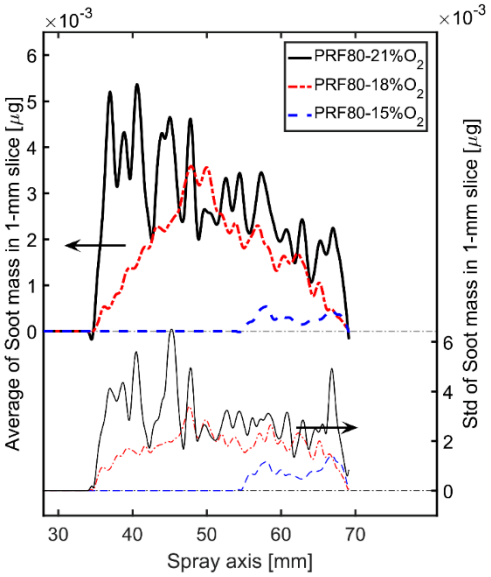

Figure 4.76. Soot mass for PRF80 fuel and various oxygen concentration of ambient gas in thin (1 mm) cross-sections of jet as a function of axis distance

Figure 4.76 shows the integrated soot masses in thin (1 mm) radial cross-sections within the PRF70 jet flame along spray axis for 3 oxygen levels. The trends already observed for FRP70 are more marked.

Under 15% oxygen concentration in ambient gas, only a negligible signal of soot is captured.

4.4.4.2. Effect of octane number of fuel

For PRF80, PRF70 and PRF60 fuels, the IXT of soot mass of 21% oxygen concentration, 900 K temperature and 60 bar gas back-pressure are illustrated in Figure 4.77. The PRF 60 produces more soot and earlier.

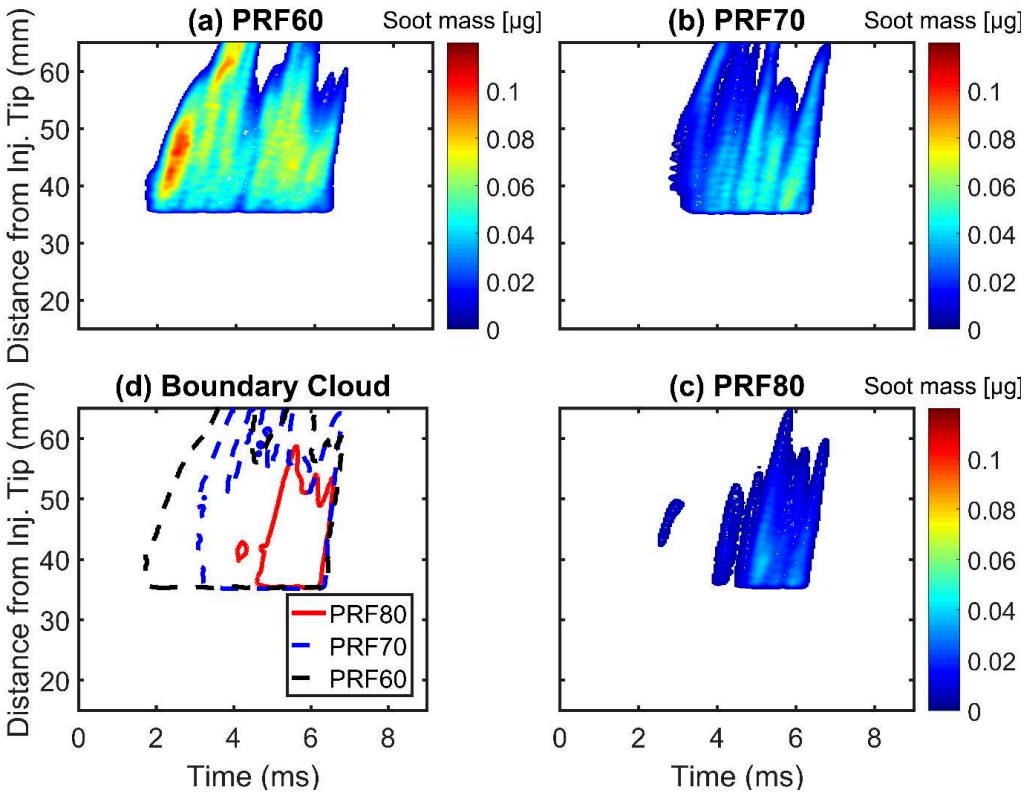

Figure 4.77. Cloud Soot mass of PRF60, PRF70 and PRF80 fuels under 21% oxygen concentration

The soot mass versus time of six tests for PRF60, PRF70 and PRF80 fuels under 21% oxygen concentration are illustrated in Figure 4.78. The soot mass decreases with increasing the octane number of fuel.

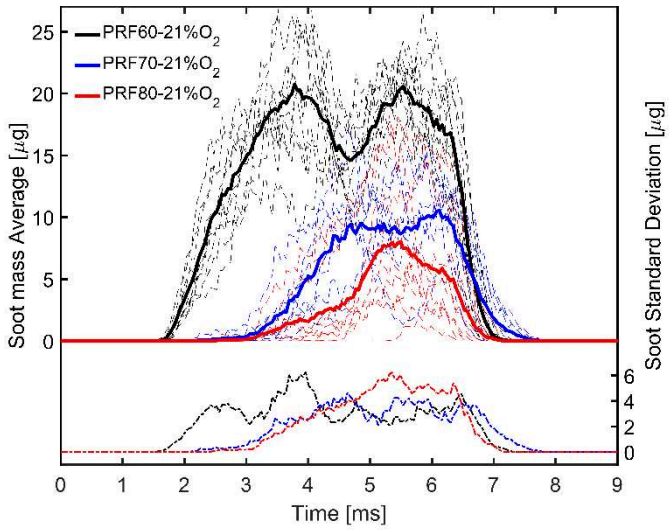

Figure 4.78. Soot mass versus time of PRF80, PRF70 and PRF60 fuels under 21% oxygen concentration

The Figure 4.79 compares the contour plot of soot mass fractions of spray of PRF60, PRF70 and PRF80 fuels with 21% oxygen.

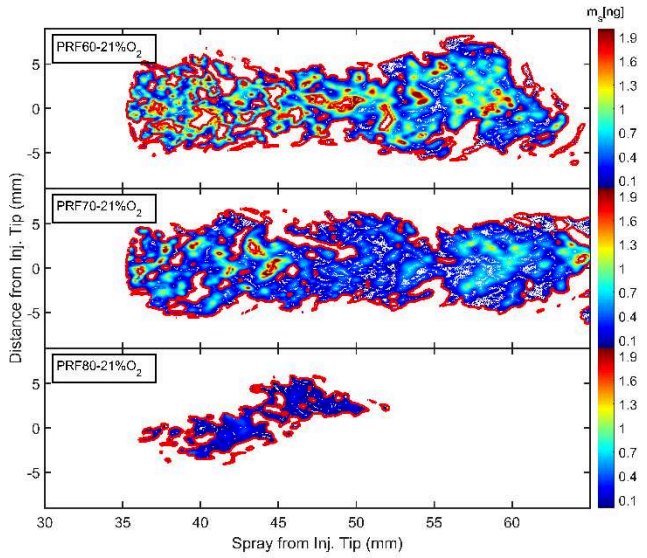

Figure 4.79. The soot mass fraction images at 3.0 ms ASOC for PRF60, PRF70 and PRF80 fuel and 21% of oxygen concentration ambient gas

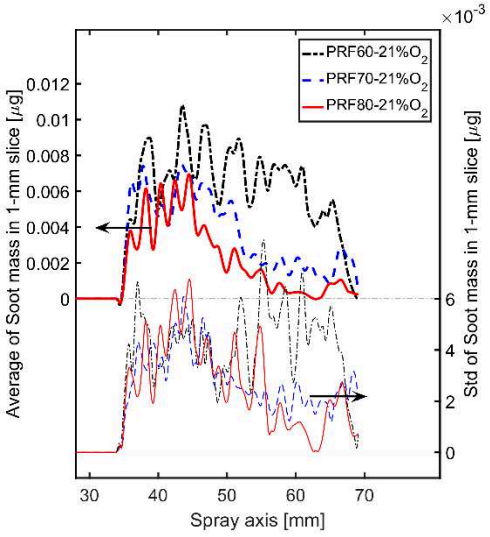

Figure 4.80. Soot mass for PRF80, PRF70 and PRF60 fuels and 21% oxygen concentration of ambient gas in thin (1 mm) cross-sections of jet as a function of axis distance

The integrated soot masses in thin (1 mm) radial cross-sections inside the jet flame of PRF60, PRF70 and PRF80 fuels with 21% oxygen along spray axis are calculated on Figure 4.80. The decrease in the amount of soot with increasing octane number is greater in the tail end of the

spray.

For the PRF80, PRF70 and PRF60 fuels, the IXT of soot mass of 18% of oxygen concentration, 900 K of temperature and 60 bar gas back- pressure are illustrated in Figure 4.81. The similar trend are observed for 21%, 18% and 15% oxygen.

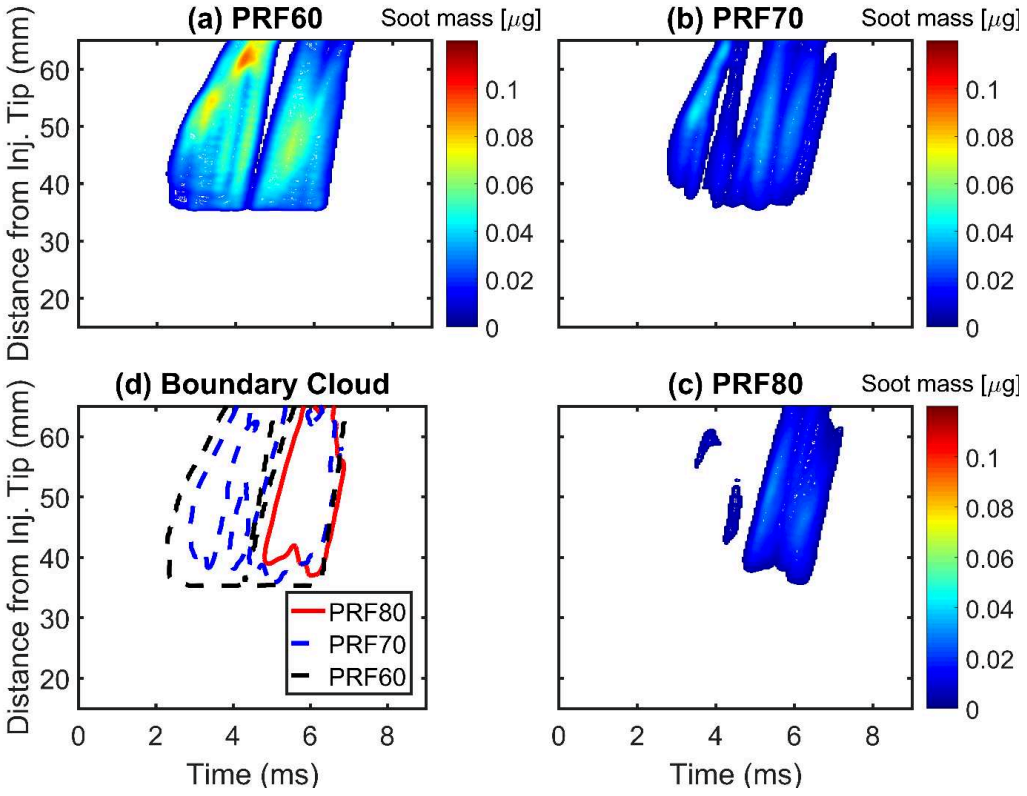

Figure 4.81. Cloud Soot mass of PRF60/PRF70/PRF80 under 18% oxygen concentration

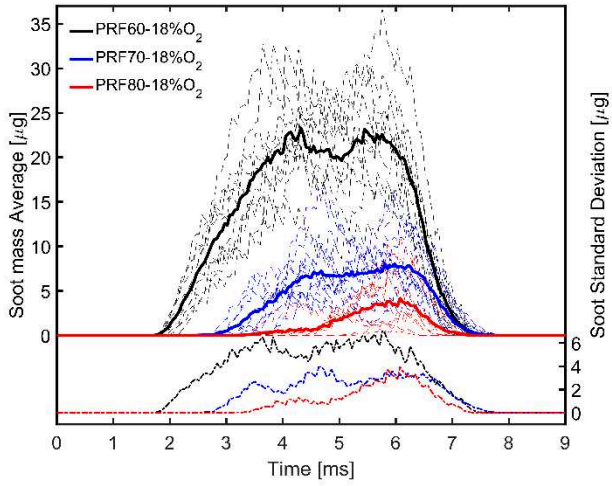

Figure 4.82. Soot mass versus time of PRF80, PRF70 and PRF60 fuels under 21% oxygen concentration

The soot mass versus time of six tests for PRF60, PRF70 and PRF80 fuels under 18% oxygen

concentration is illustrated in Figure 4.82. The soot mass decreases with increasing the octane number of fuel.

4.4.5. Conclusions

Soot mass total as a function of Lift off length, equivalence ratio at LOL for 3 fuels (PRF60, PRF70 and PRF80) and 3 oxygen concentrations (15, 18 and 21%), including the Bu20 and ABE20 with 21% oxygen concentration, is plotted in Figure 4.83.

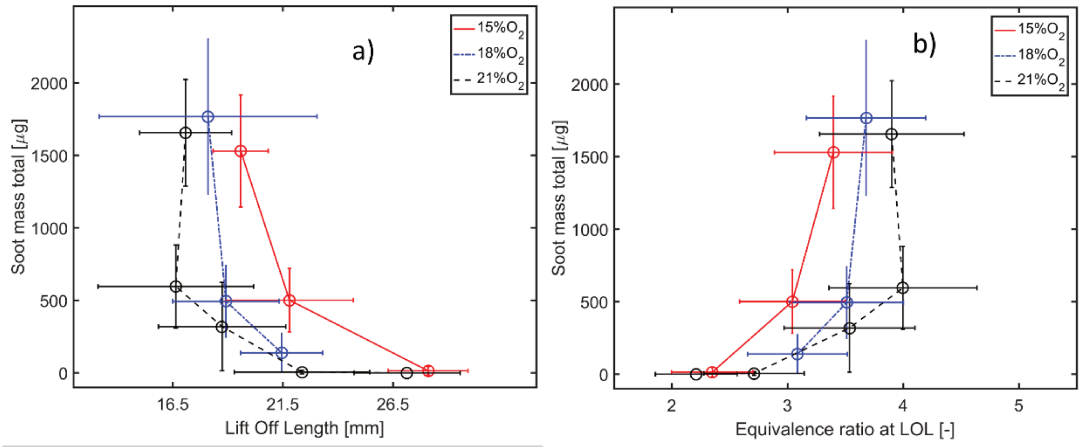

Figure 4.83. Relationship between Soot mass total production and a) Lift Off Length; b) Equivalence ratio at LOL

The result shows that higher oxygen concentration reduces the amount of soot for a similar LOL.

From the soot mass vs. time data set, the start of the soot mass or the mass reached at 1 µg is plotted as a function of fuel octane rating as well as Lift off length and ignition delays. Here, it can be seen that the higher the octane number, the later the soot formation with no clear trend on the impact of oxygen concentration.

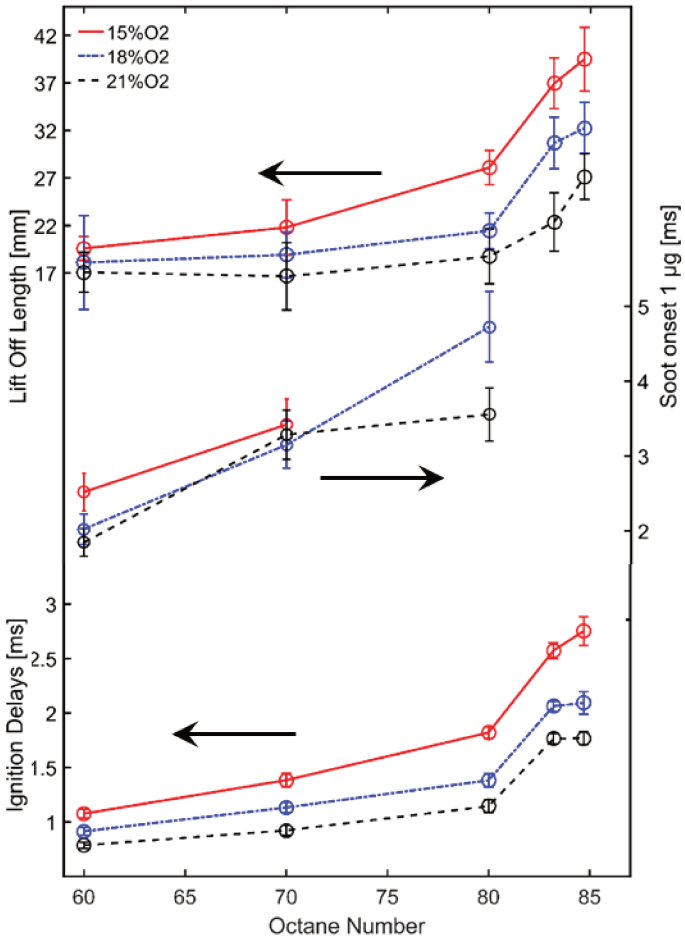

Figure 4.84. Lift off length, Ignition delays and soot onset 1 µg as a function of octane number of fuel

The summary of ignition delays, Lift-Off length, soot mass total and soot mass onset are given in Table 4.11, Table 4.12 and Table 4.13, respectively.

Table 4.11. Summary Ignition delays

Fuel	**Ignition delays (ms)**		
	$15\%O_2$	$18\%O_2$	$21\%O_2$
PRF60	1.08 (±0.04)	0.91 (±0.04)	0.79 (±0.03)
PRF70	1.38 (±0.06)	1.13 (±0.05)	0.92 (±0.05)
PRF80	1.82 (±0.05)	1.38 (±0.06)	1.14 (±0.06)
Bu20	2.57 (±0.07)	2.06 (±0.05)	1.76 (±0.05)
ABE20	2.75 (±0.13)	2.09 (±0.10)	1.77 (±0.06)

Table 4.12. Summary Lift off length

Fuel	**Lift off length (mm)**		
	$15\%O_2$	$18\%O_2$	$21\%O_2$
PRF60	19.6 (±1.3)	18.1 (±4.9)	16.6 (±3.5)

PRF70	21.8 (±2.9)	18.9 (±2.4)	17.1 (±2.1)
PRF80	28.1 (±1.8)	21.4 (±1.9)	18.7 (±2.9)
Bu20	36.9 (±2.7)	30.7 (±2.7)	22.4 (±3.1)
ABE20	39.5 (±3.3)	32.3 (±2.7)	27.1 (±2.4)

Table 4.13. Summary soot mass total

Fuel	**Soot mass total (mg)**		
	15%O_2	18%O_2	21%O_2
PRF60	1.53 (±0.49)	1.77 (±0.53)	1.66 (±0.37)
PRF70	0.50 (±0.22)	0.49 (±0.25)	0.60 (±0.29)
PRF80	0.014 (±0.03)	0.14 (±0.13)	0.32 (±0.30)

Table 4.14. Summary soot mass onset 1 µg

Fuel	**Soot mass onset 1 µg (ms)**		
	15%O_2	18%O_2	21%O_2
PRF60	2.52 (±0.12)	2.03 (±0.10)	1.85 (±0.07)
PRF70	3.42 (±0.13)	3.15 (±0.13)	3.29 (±0.13)
PRF80		4.73 (±0.09)	3.56 (±0.15)
Fuel	**Soot mass onset 1 µg (ASOC ms)**		
	15%O_2	18%O_2	21%O_2
PRF60	1.44	1.12	1.06
PRF70	2.04	2.02	2.37
PRF80		3.35	2.42

The effect of fuel octane number and oxygen concentrations on ignition delays observed in this study is consistent with previous studies.

This section provides additional data on the formation and oxidation of soot under compression ignition conditions for gasoline and butanol/ABE blends.

During the quasi-stationary phase, the soot concentration in a flame jet increases along the spray axis. A high octane number or a lower oxygen concentration reduces the amount of soot.

4.5. Conclusions

The current chapter describes the DBI, Schlieren technique and mass flow rate measurement setups to capture some parameter under inert conditions into the effect of bio-fuel addition on the physical properties of base gasoline-like fuel.

The work performed in this part of the thesis was the first attempt to the measure the liquid

length, vapor spray penetration, ignition delays, Lift off length and soot mass as a function of Octane number fuel.

By understanding the phenomena in inert conditions, helps the research in term of fuel characterization, as specially the alternative of bio-fuels, to enhance sufficient mixing in CI mode engine, as especially for gasoline CI mode, as the advanced LTC mode.

The parts of reacting condition, the Ignition delay, Lift Off Length and soot mass measurement are conducted into the effects of bio-fuel addition on the physics and chemical properties of base gasoline-like fuel. There were a few challenges that is capture data of soot mass of higher Octane number (more than 80).

The low-octane number fuel, as PRF60, PRF70 and PRF80, is conducted to evaluate the soot production in this high-temperature high-pressure conditions.

Chapter 5. SPLIT INJECTION STRATEGY

This chapter presents an experimental investigate of the mixing, penetration and ignition characteristics under condition of high temperature high pressure with gasoline-like (PRF80) and mixture with Ethanol, Butanol and ABE sprays. The experimental investigations are carried in a combustion vessel at ambient temperature 900 K and pressure 6 MPa, with Engine Combustion Network (ECN) mono-orifice nozzles, with two split injection schedules. The first case is a variation of pilot injection duration and second case is a variation of dwell of double injection. The interaction between pilot and main injections events on term of the mixing and combustion process is evaluated.

All injection duration times within the current chapter are defined in terms of current injection duration, and dwell time is the interval between the end of the first injection, which was determined by observation from high speed camera images, and the start of current second injection. One single injection case, with injection duration of 3000 µs, is the reference case.

The range of variation of the command duration is between 400 and 1500 µs and that of the Dwell is from 300 to 2300 µs. The second injection is fixed at 1500 µs. The test matrix is detailed in Table 5.1. 12 cases have been studied named D1-400/700/1000/13000/1500, I2-300/700/1100/1500/1900/2300 and the reference case.

Table 5.1. Summary of split injection strategy

Operating points		**D_1[1] [µs]**	**D_{dwell}[2] [µs]**	**D_2[3] [µs]**
Single injection		3000	-	-
Variation of D_1	D1-400	400	1100	1500
	D1-700	700		
	D1-1000	1000		
	D1-1300	1300		
	D1-1500	1500		
Variation of D_{dwell}	I2-300	1000	300	
	I2-700		700	
	I2-1100		1100	
	I2-1500		1500	
	I2-1900		1900	
	I2-2300		2300	

Operating points	D_1[1] [µs]	D_{dwell}[2] [µs]	D_2[3] [µs]
D_1[1]: Duration of pilot injection; D_{dwell}[2]: dwell time; D_2[3]: Duration of main injection.			

5.1. Split injection strategies under inert atmosphere conditions

5.1.1. Study of reference case: PRF80 fuel

5.1.1.1. The different measure and diagnostic

In inert conditions 3 types of diagnostics are performed as resume in Table 5.2: (1) Mass flow rate; (2) Liquid penetration length and (3) Penetration length of the liquid and vapor spray.

Table 5.2. Summary of diagnostics for inert conditions

Measure	Number of tests	Diagnostics
Mass flow rate	20	Introduction Rate IAV
Liquid penetration length	6	DBI
Vapor spray penetration	6	Schlieren with two threshold level

5.1.1.2. Results of inerting condition for PRF80 fuel

a) Mass flow rate

To study how the first injection affects the second one, the results of second injection shifted to the same time and starts by default at 5 ms. The mass flow rate is shown in Figure 5.1.

The pilot injection period is longer with a longer command signal and this does not impact on main injection. The mass flow rate of the pilot and main injection de not depend significantly on Dwell.

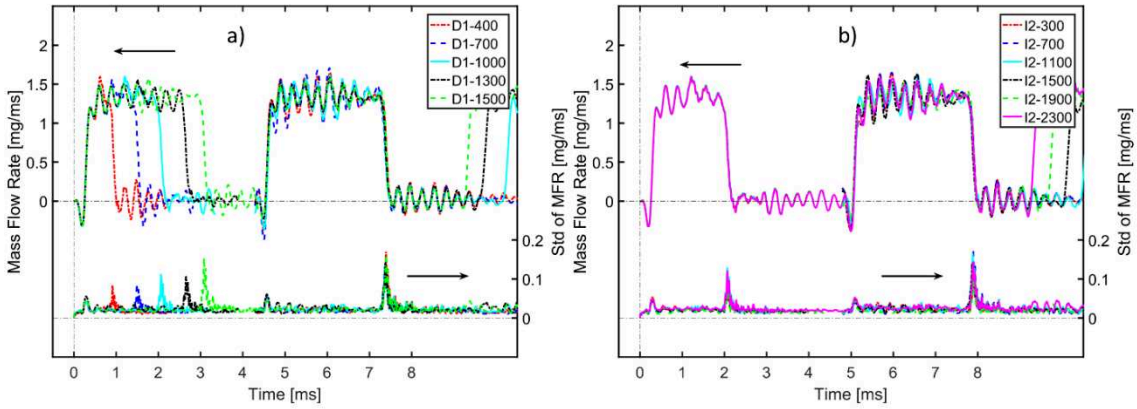

Figure 5.1. Mass flow rate of PRF80 on case double injection, (a) pilot injection duration and (b) Dwell variations

The effective duration of the injection for a 400 µs command is about 1000 µs. The injector thus has time to open completely before closing again. Thus, the injected mass for the pilot injection is a linear function of the injection duration (see Figure 5.2). The standard deviation is about 2%.

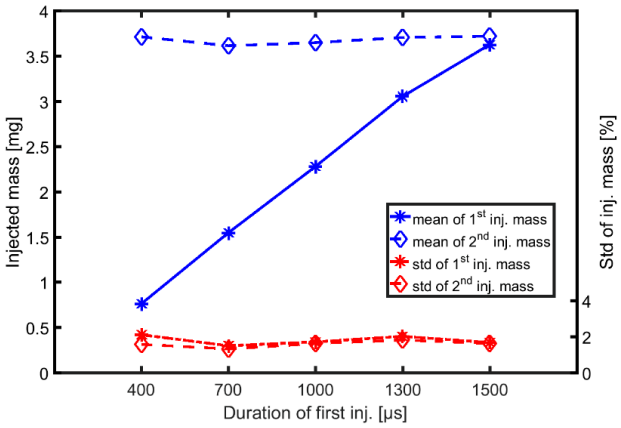

Figure 5.2. Mass of injection as a function of pilot injection duration variation

b) Liquid length

The liquid length of PRF80 fuel on two types of study: pilot injection duration variations and Dwell variations, as shown in Figure 5.3 a) and b), respectively. The main injection has a slightly longer liquid penetration length than the pilot. For example, the delta between the main and the pilot injection for the case D1-1500 about 0.5 mm (6.4%), as shown in Figure 5.4. The evaporation of the pilot injection modifies locally the temperature conditions and the composition of the ambient gases reducing slightly the evaporation performances of the main injection.

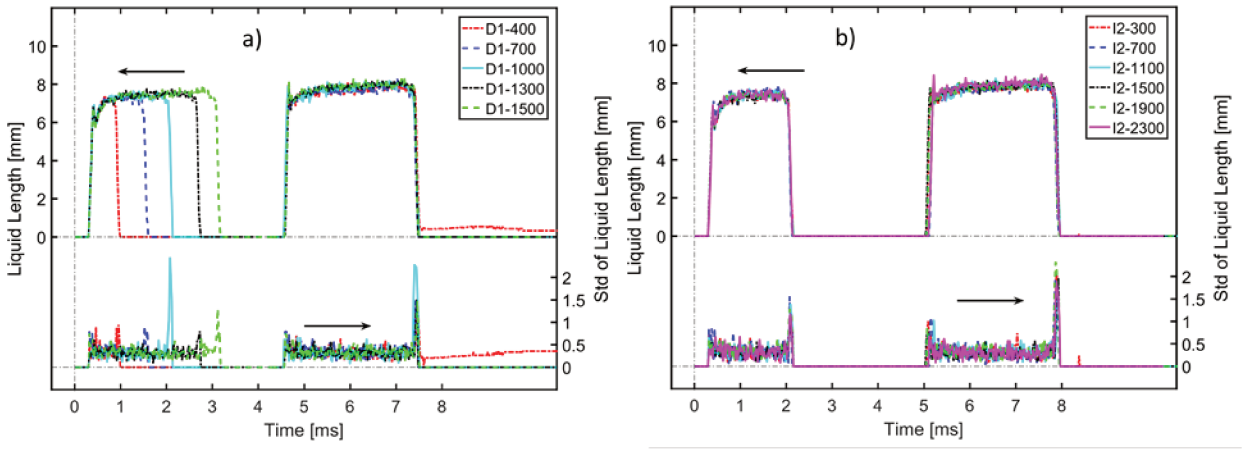

Figure 5.3. Liquid length of PRF80 fuel on two cases split injection, (a) pilot injection duration variations and (b) Dwell variations

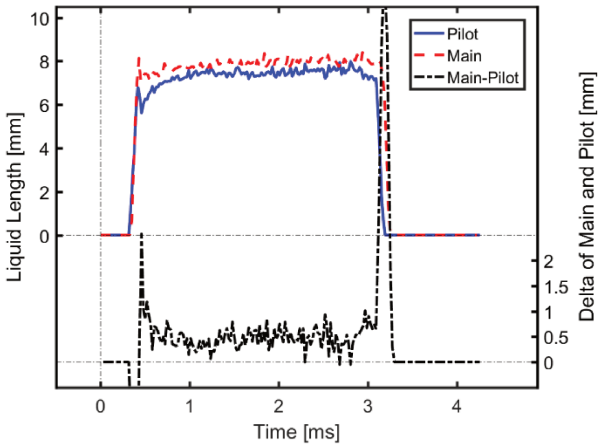

Figure 5.4. Comparison between the liquid length of pilot and main injection on case of D1-1500

c) Spray vapor penetration

The pilot and main injections with pilot duration injection of D1-400, D1-1000 and D1-1500 for PRF80 fuel are shown in Figure 5.5. As we can see, the standard deviation for the pilot and main injections is less than 2 mm. The penetration of main injection for all cases is more rapid than pilot one.

The single injection with 3.0 ms duration is utilized to comparison with split strategies. In Figure 5.6, the comparison of spray vapor penetration between pilot, main and single injection are presented. Between 10 and 40 mm the pilot and the main behave in a way very close to the single injection. Beyond that the pilot penetrates less and the main has an easier penetration. Increasing the velocity of main injection due to gas flow induced by pilot injection could be explained the longer spray vapor penetration length of main injection. Thus, the air entrainment

and the air/fuel ratio will be modified.

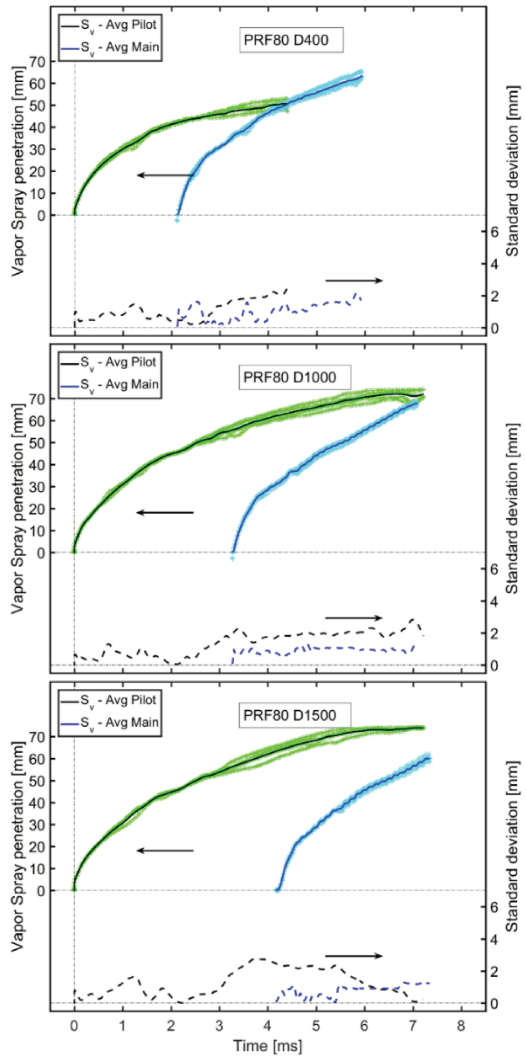

Figure 5.5. Vapor sprays penetration length evolution with time on case duration of pilot injection variation: D1-400, D1-1000 and D1-1500

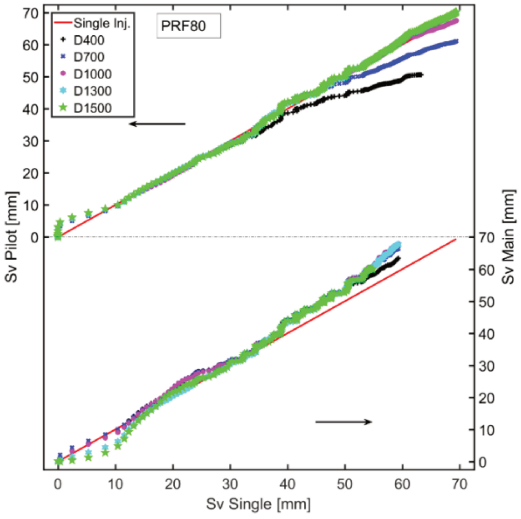

Figure 5.6. Comparison between pilot injection and single injection

5.1.2. Results of inert condition for PRF80 and Alcohols blends

a) MFR for PRF80, Bu60, ABE60 and Et20

The comparison of MFR between PRF80, Bu60, ABE60 and Et20 under 3 cases of split injection: D1-400, D1-1000 and D1-1500, as shown in Figure 5.7.

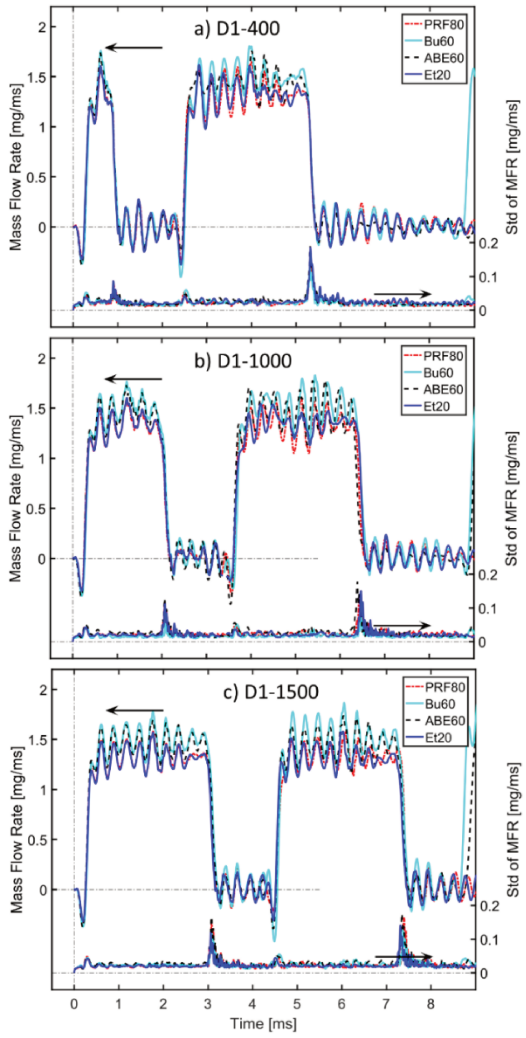

Figure 5.7. Comparison the mass flow rate between PRF80, Butanol, ABE and Ethanol blends under difference of pilot injection duration: D1-400, D1-1000 and D1-1500

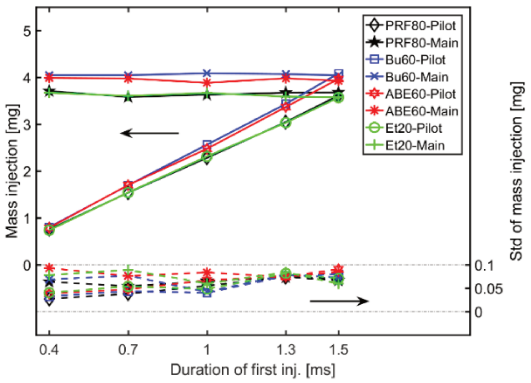

Figure 5.8. Mass of pilot and main injections as a function of pilot injection duration for PRF80, Bu60, ABE60 and Et20

The Bu60 has higher peak value, ABE60, PRF80 and Et20 have similar values. The injected mass of pilot and main injection for PRF80, Bu60, ABE60 and Et20 different durations of pilot injection are shown in Figure 5.8. As found in single injection in chapter 4, whether it is for the pilot or the main injection the mass flow rate or the amount follow the following order: PRF80, Et20, ABE60 and Bu60.

b) Liquid length for Butanol blends

The influence of Butanol blends on Liquid length under 3 cases of split injection with varying

pilot duration: D1-400, D1-1000 and D1-1500, is shown in Figure 5.9. The liquid penetration length of higher butanol ratio in the fuel blends, as shown by similar results with single injection in Chapter 4.

Moreover, for all blend fuels, the main injection has longer liquid length penetration than that of pilot with same the sensibility than PRF80. An example on case of D1-1500 is shown in Figure 5.10, the delta of main and pilot injection liquid length for all test fuels is about 0.5 mm, 0.5-0.6%. The pilot injection has no significantly difference of liquid length with single injection, as found in chapter 4.

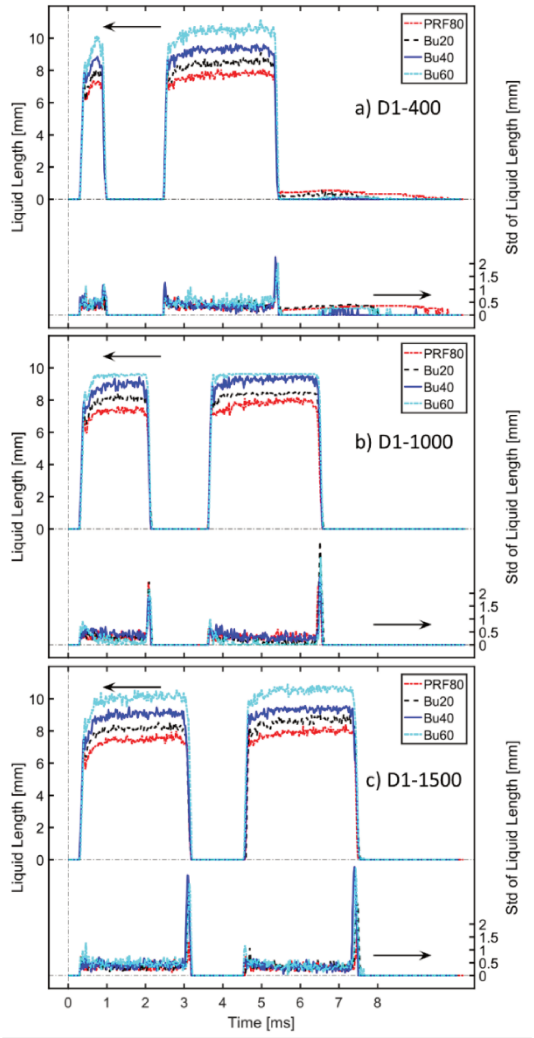

Figure 5.9. Comparison the liquid penetration length between Butanol blends under difference of pilot injection duration: D1-400, D1-1000 and D1-1500

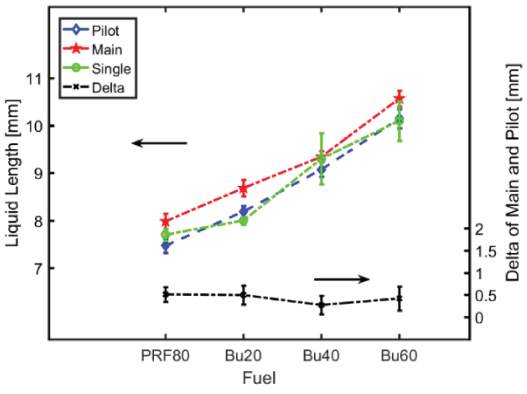

Figure 5.10. Liquid length of pilot and main injections for PRF80 and Butanol blends

c) Spray vapor penetration for PRF80, Butanol blends, ABE blends and Ethanol blend fuels

The Butanol blends (Bu20, Bu40 and Bu60), the ABE blends (ABE20, ABE40 and ABE60), Et20 and PRF80, with 3 different cases of variations of the pilot duration are presented in Figure 5.11. As shown in Figure 5.11, the spray vapor penetration of all blends of pilot and main injections have identical profiles. The impact of bio-fuel on blends is no significantly, as similar results of single injection in Chapter 4.

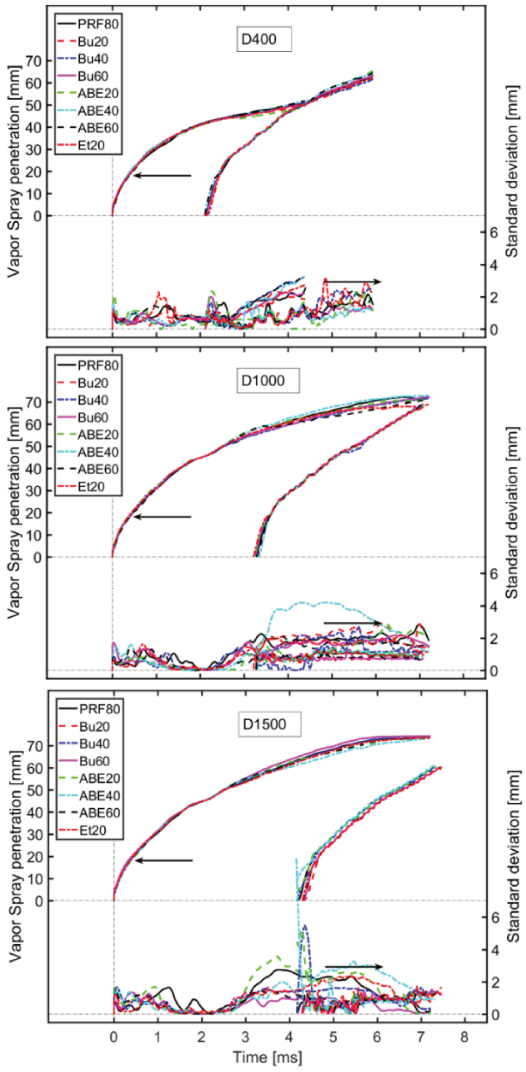

Figure 5.11. Comparison the spray vapor penetration between Butanol, ABE and Et blends under difference of pilot injection duration: D1-400, D1-1000 and D1-1500

5.1.3. Conclusion

The injection characteristics, including mass flow rate, liquid length and spray vapor penetration of split injection strategy were studied in current section. The instantaneous MFR,

liquid length, spray vapor penetration and total fuel mass delivered in each split quantitatively evaluated for PRF80 and Butanol, ABE, Et blends. Whether it is a simple or with another injection strategy (one pilot and one main) the addition of alcohol in the fuel does not modify the effects.

5.2. Split injection strategies under reactive atmosphere conditions for PRF80 fuel

In reactive conditions 3 types of diagnostics are performed as resume in Table 5.3:

Table 5.3. Summary of diagnostics for reacting conditions

Measure	**Number of tests**	**Diagnostics**
HRR	10	In-cylinder pressure
LOL – flame contour	10	OH* Chemiluminescence

5.2.1. Study of reference case: PRF80 fuel and 21% of oxygen

a) In-cylinder pressure signal and estimated HRR for split injection case

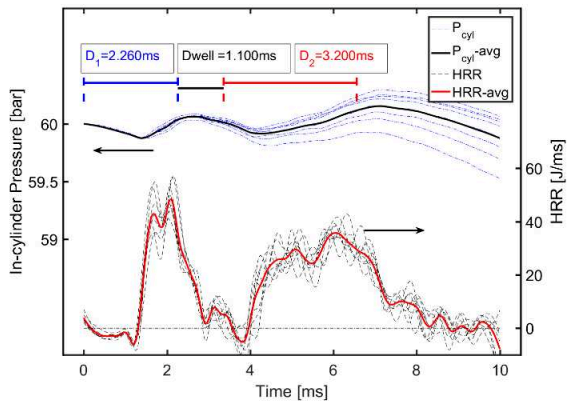

Figure 5.12. Typical In-cylinder Pressure and Heat release rate for PRF80 fuel under conditions: 60 bar, 900 K, 21% Oxygen concentration on case double injection D1-1000 µs, Dwell-1100µs, D2-1500 µs

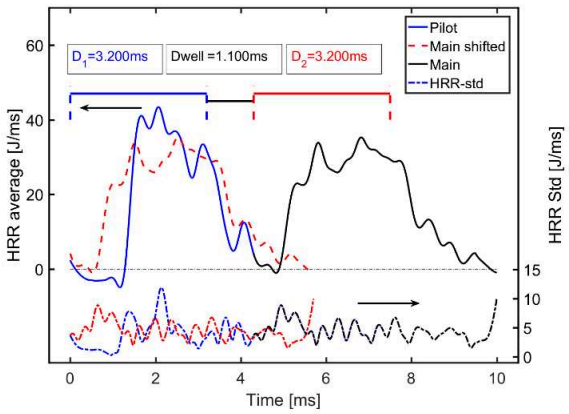

Figure 5.13. Heat release rate comparison of pilot and main spray combustion

The cylinder pressure plot and apparent HRR of 10 tests with the actual injection durations are highlighted in Figure 5.12 for PRF80 fuel under ambient conditions: 60 bar of back-pressure,

900 K temperature, 21% Oxygen concentration in case of split injection D1-1000: Pilot/Dwell/Main: 1000 µs /1100 µs /1500 µs.

The onset of the first or second stage of autoignition is the time when the HRR changes from a negative to a positive value after the start of the first or second injection. They are significantly different with values of 1 (± 0.05) ms and 0.5 (± 0.05) ms, respectively. The auto-ignition delay of the main injection is considerably reduced compared to that of the pilot injection. Therefore, the period of air-fuel mixing before ignition is shorter changing the type of combustion. The pilot injection with its later delay and maximum heat release rate may have a premixed type of combustion phase.

As shown in Figure 5.13, results of heat release average for all test are similar, with difference < 10%. Energy release of pilot and main injections is about 42.5 (± 5) J and 45.5 (± 5) J, respectively. Although the peak heat release rate is lower, the longer combustion time for the main injection explains this gain.

The split injection strategies for different pilot injection durations and different dwell period were investigated under combustion process.

b) Pilot injection variation

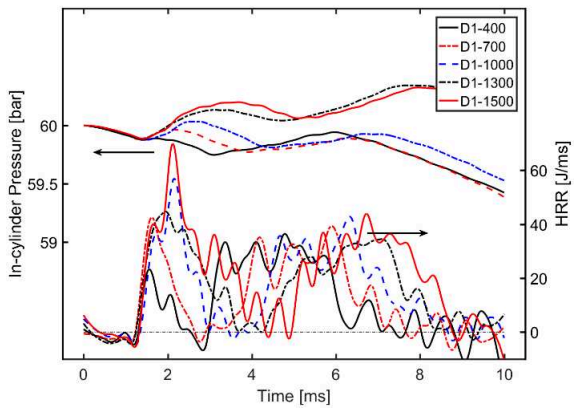

Figure 5.14. Typical of in-cylinder pressure and heat release rate on case variation of pilot injection duration

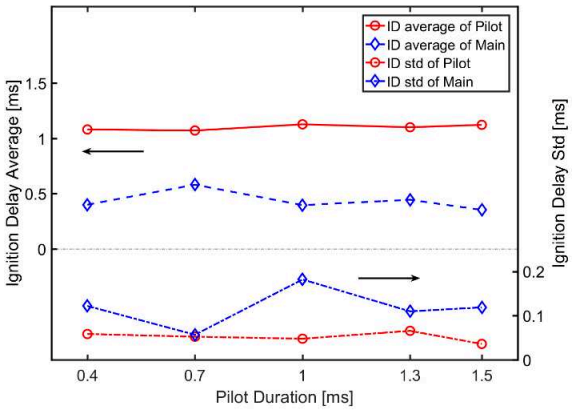

Figure 5.15. Ignition delays of pilot and main injection on case pilot injection duration variation

Figure 5.14 illustrates the cylinder pressure and heat release rate for PRF80 fuel with split injection strategy under reactive atmosphere (ambient gas: 21% O_2 and 79% N_2) as a function of variations in pilot injection duration from 400 µs to 1500 µs.

It was found that by increasing the pilot injection duration from 400 µs to 1500 µs the heat release rate peak increased slightly and was delayed. Fluctuations in the heat release rate profile complicate the interpretation. It seems that the pilot flames show a combination of premixed combustion phase and a mixing-controlled combustion phase, whereas the main flames show a mixing-controlled combustion phase only.

For the pilot injection duration of 400 µs case, the HRR plots shown in Figure 5.14 indicated that the ignition of the pilot injected fuel occurs during the dwell period, after end of pilot injection, heat release of pilot injection mainly driven by premixed combustion. The heat release rate of the main injection is very similar regardless of the duration of the pilot injection.

Figure 5.15 shows the pilot and main injection ignition delay as a function of pilot duration. The pilot and main auto-ignition delay appears to be constant. Although the temperature and pressure conditions at the end of the combustion of the pilot injection are different, the auto-ignition of the main injection occurs at approximately the same time. The presence of burnt gases (NO, NO_2, CO) could accelerates the process.

c) Dwell influence second injection phase

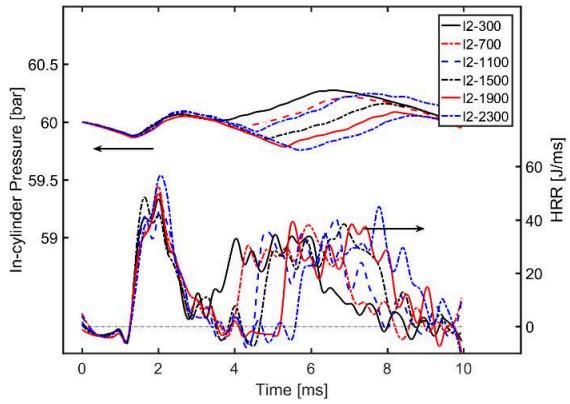

Figure 5.16. Typical of in-cylinder pressure and Heat release rate on case variation of dwell times

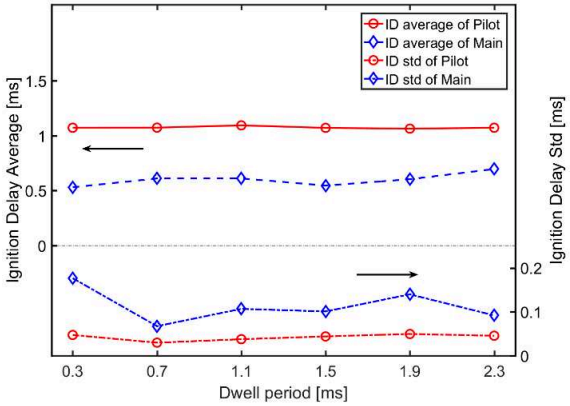

Figure 5.17. Ignition delay of main injection on case dwell variation

This dwell time variation exercise was performed for split injection strategies. The Figure 5.16 exhibits the heat release rate profiles of the injection sequences obtained with varying dwell times, the pilot and main injection durations were kept constant at 1000 µs and 1500 µs, respectively, but the dwell time between them was varied as 300 µs, 700 µs, 1100 µs, 1500 µs,

1900 µs and 2300 µs.

The heat release rate profiles of main flame are similar for all dwell times. As the main injection is shifted the main ignition timing is also later. Although the pressure and temperature is lower when the dwell time increases, the ignition delay is not significantly affected as observed in Figure 5.16. The peaks HRR of main injection burn of these cases are similar, and that is lower than that of pilot one's, indicating reduced premixed of main injection as compare pilot or single injections, seen Figure 4.11 and Figure 5.16 for single and split injection, respectively.

Ignition delays of pilot injection on case of variation dwell period, kept duration of pilot injection 1000 µs, is about 1 (±0.05) ms. The ignition delay of main injection is about 0.6 (±0.1) ms.

5.2.2. Flame Lift off length of split injection

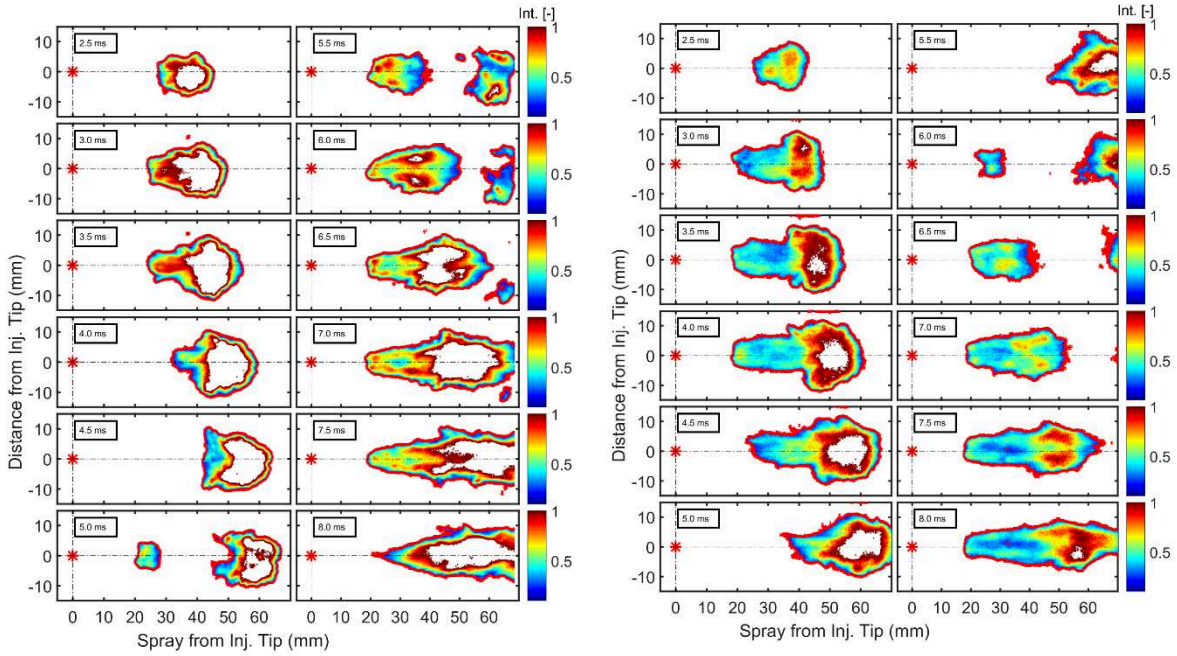

Figure 5.18. Continuous OH* chemiluminescence images under ambient gas of 21% of oxygen concentration, 900 K of temperature and 60 bar of pressure for PRF80 fuel on case of Split injection strategy D1-1000 and D1-1500

Figure 5.18 shows an example of a time resolved OH* chemiluminescence images with boundary in red line, under ambient gas with 21% oxygen concentration, 900 K temperature and 60 bar back-pressure for PRF80 fuel, for D1-1000 Split injection strategy: Pilot 1000 µs, Dwell 1100 µs, Main 1500 µs. The pilot flame is observed between 2.5 ms and 6.5 ms ASOI,

and the main flame from 5.0 ms and 8.0 ms $ASOI_1$ (approximate 0.5 and 3.5 ms $ASOI_2$).

As can be seen Figure 5.18, the location of main flame start (at 5.0 ms $ASOI_1$ or 1.5 ms $ASOI_2$) is further upstream than the pilot flame start (at 2.5 ms $ASOI_1$). The position of the flame base detected in this type of image allows us to determine the LOL of the pilot or main flame.

The main flame lift off length for PRF80 fuel with different quantities injected during the pilot injection under reactive atmosphere condition are show in Figure 5.19. From the figure, it can be seen that the LOL initially starts at a distant point, then slowly approaches and finally quickly moves away from the injector tip. After the auto-ignition the flame moves towards the injector. The process stabilizes and when the injection is completed the flame is convected and the combustion zone narrows.

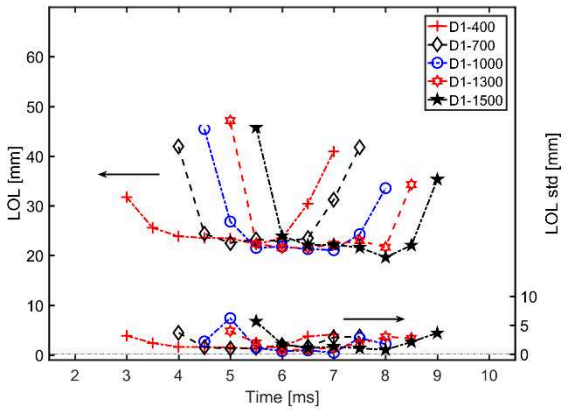

Figure 5.19. Flame Lift off length as a function by time on case variation of duration of pilot injection for PRF80 fuel

For each case of injection strategy, such as D1-400, D1-1000 and D1-1500, the Lift off length obtained from on the pilot and on the main flames is shown in Figure 5.20. The values of the main flame extinction length for each pilot injection duration are shown in Figure 5.19, it can be seen that there is no effect of the pilot injection duration on the LOL. The main flame originates further upstream than the pilot flame but settles closer to the injector tip, as shown in Figure 5.20. Thus, although the auto-ignition time is shorter for the main flame, the auto-ignition zone is further upstream.

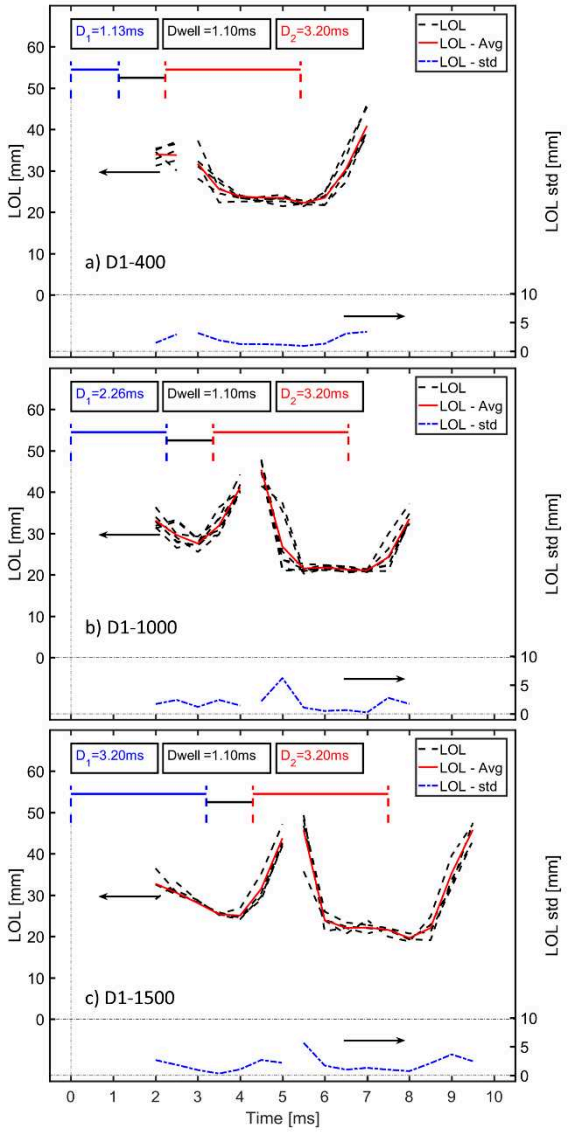

Figure 5.20. Lift off length time-resolved measurement from SOI until EOI under ambient gas of 21% of oxygen concentration, 900 K of temperature and 60 bar of pressure for PRF80 fuel under 3 cases of strategies injection: D1-400; D1-1000 and D1-1500

The LOL of pilot and main flame obtained from OH* chemiluminescence are presented in Figure 5.21, the pilot one was shifted to same injection timing of pilot and main. It can be observed that the main flame has shorter flame lift off length than pilot one's, as LOL of main and pilot flames is 15.8 (±2) mm and 19.2 (±2) mm, respectively. This trend is similar to those of other researchers on Split injection strategy [150–152].

The ignition kernels upstream of main injection that ignite the combustion earlier and thus there, in which the main ignition delay is earlier are closer to the injector tip, thus reducing the main LOL. The influence of the interaction of the pilot's burnt gas and main injection can lead to a shorter main LOL. Another factor that could impact the main flame is the thermal effect

of the hot gas from the burned pilot injection, which influences the spray combustion locally, thus decreasing the main LOL.

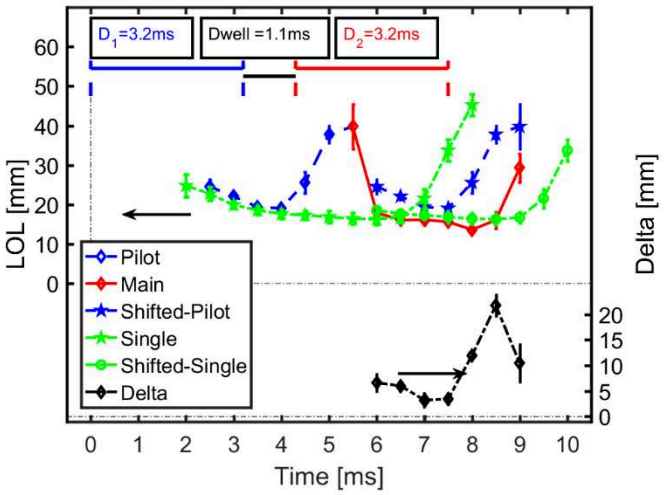

Figure 5.21. Compare between pilot and main injection under ambient gas of 21% of oxygen concentration, 900 K and 60 bar for PRF80 fuel, under case of strategy injection D1-1500

5.2.3. PRF80 with various oxygen concentration in ambient gas

The influence of ambient gas oxygen concentration on the combustion processes for PRF80 fuel under split injection strategy is investigated in this section.

a) Ignition delay

The apparent heat release rate for strategy split injection is studied for 3 cases (D1-400, D1-1000 and D1-1500) and ambient oxygen concentration ranging from 15% to 21%. For these cases, the heat release rate profile shows a double peak, one for each of the two combustion phases. Combustion is delayed at lower oxygen concentration.

Higher oxygen concentration can lead to higher temperature and higher pressure inside the cylinder due to combustion of pilot injection gases, which contributes to the auto-ignition behavior of the main injection. In the case of D1-400, the first and second HRR peaks of 21% O_2 case are highest.

Figure 5.22 shows that the pilot injection has a peak HRR that increases with increasing oxygen concentration or with increasing injection duration from 400 to 1500 µs. This indicates that the net vaporized mass at the time of pilot injection ignition is increased, resulting in an increase in the amounts of fuel burned during premixed combustion increases of the pilot injection.

The addition of oxygen promises ignition for both the pilot and main injection. The main injection ignition is initiated 0.4 ms earlier than the pilot regardless of the oxygen level.

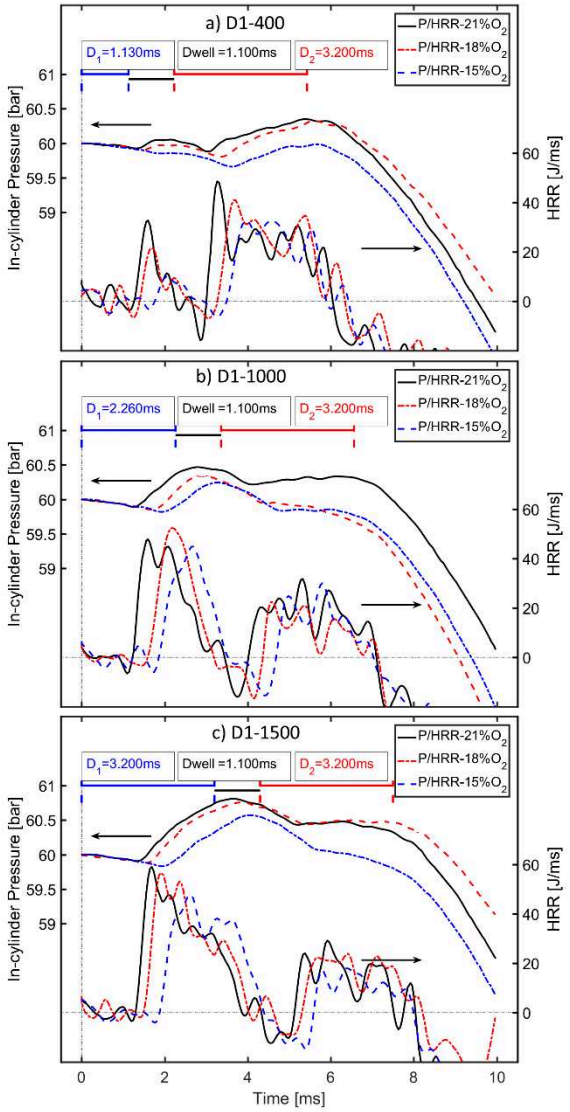

Figure 5.22. In-cylinder pressure and HRR for PRF80 fuel as a function of Oxygen concentration gas under 3 difference cases strategies with variation of pilot injection

The ignition delays for the pilot, main and single injection as a function of ambient gas oxygen concentration are shown in Figure 5.23. The relation presented in Eq. 5.1 and Eq. 5.2, with R_2=0.983 and R_2=0.990, respectively.

Figure 5.23 shows that a change in pilot injection duration from D1-400 to D1-1500 does not help with early auto-ignition of the main injection, for three level of oxygen concentration.

$$ID_1 \propto O_2^{-1.514}[\%] \qquad \textit{Eq. 5.1}$$

$$ID_2 \propto O_2^{-1.520}[\%] \qquad \textit{Eq. 5.2}$$

R^2 for Eq. 5.1 and Eq. 5.2 are 0.996 and 0.955, respectively. The constants shown in Eq. 5.1 and Eq. 5.2 indicate that lower sensitivity of oxygen concentration on main ignition delay.

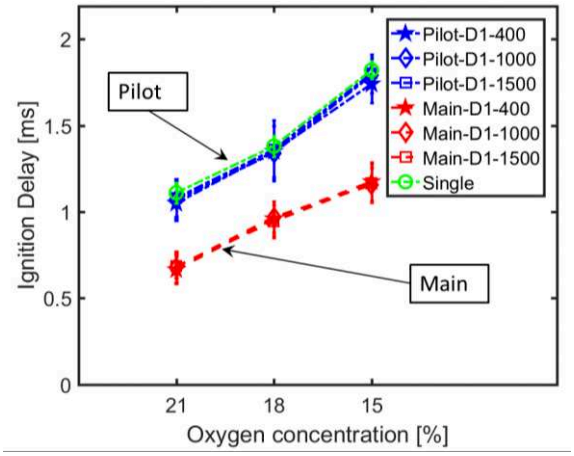

Figure 5.23. The ignition delays of pilot, main and single injection for PRF80 fuel as a function of Oxygen concentration gas

b) Lift off length

For each case of injection strategy, such as D1-400, D1-1000 and D1-1500, the Lift off length obtained from main flame is shown in Figure 5.25. The trend of effect of oxygen concentration on the main flame is similar for all three cases, the lift off takes place in the downstream regions for lower oxygen concentration.

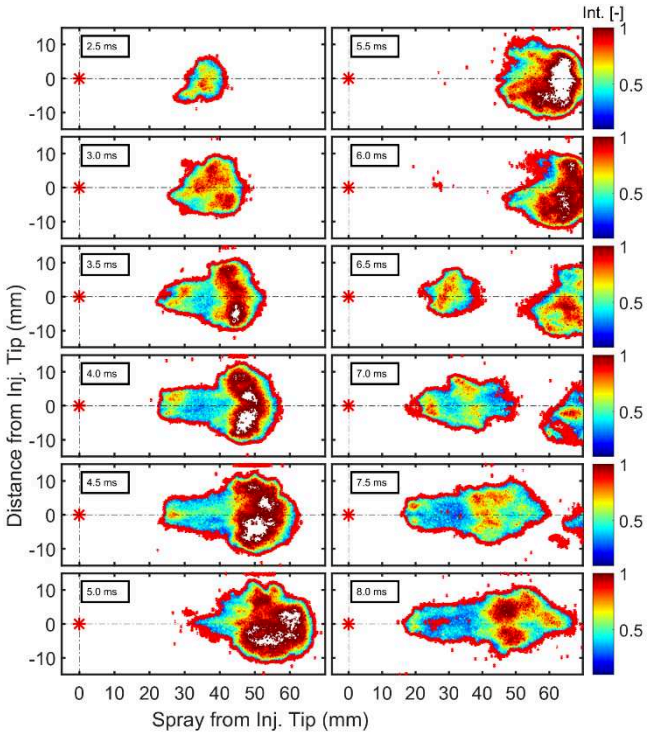

Figure 5.24. Continuous OH* chemiluminescence images under ambient gas of 18% of oxygen concentration, 900 K and 60 bar for PRF80 fuel on case of Split injection strategy D1-1500

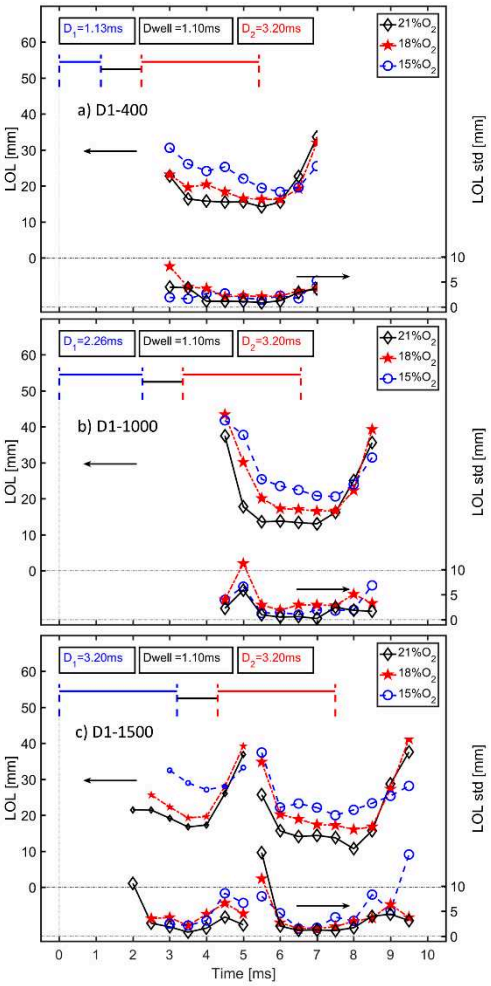

Figure 5.25. Lift off length time-resolved measurement from SOI until EOI under ambient gas of various oxygen concentration (21%O_2, 18%O_2 and 15%O_2), 900 K and 60 bar for PRF80 fuel under 3 cases of strategies injection: D1-400; D1-1000 and D1-1500

The LOL of pilot and main injections obtained 2 images after the start of combustion of pilot and main injections from 2.5 to 3.5 ms of main flame, as a function of oxygen concentration of ambient gas are represented in Figure 5.26.

As can be seen Figure 5.26, the delta between pilot and main LOL for the D1-1000 case is higher than that for D1-1500 case, confirming that longer injection duration results in a shorter LOL for all three oxygen concentration condition.

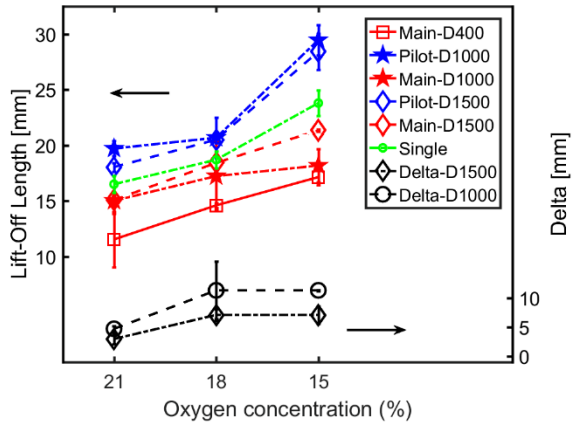

Figure 5.26. Comparison of LOL of pilot, main and single injections under intake gas ambient oxygen concentration various

5.2.4. Conclusion

The split injection strategies are studied under high-Temperature, high-Pressure in NOSE, with the PRF80 fuels. The pilot injection duration, the dwell period between two injections and oxygen concentration of ambient gas are considered to evaluated the interaction of pilot and main injection. The main injection has shorter ignition delays and shorter LOL, as its jet penetrates into the residual reaction zone of the pilot injection. The result is the same regardless of the dwell.

5.3. Effect of Alcohols on Combustion characteristics under double injection

In current section, the influence of Butanol, ABE and Ethanol on combustion process is evaluated under split injection strategy, with two parts: first, impact of Butanol on blend with PRF80 and second, comparison between Bu60, ABE60 and Et20.

5.3.1. Butanol blends

In Figure 5.27, the in-cylinder pressure and the HRR patterns are reported for Butanol blends of Bu20, Bu40 and Bu60 under 3 differences pilot injection duration. As the single injection, the higher butanol ratio, the more delayed the combustion.

In the case of the D1-400 injection strategy, the short dwell, for Bu40 and Bu60 blend fuels, the pilot injection does not ignite before the main injection. The beginning of combustion occurs at main injection. Under D1-1000 and D1-1500, all fuels have two combustion phases for each of the two injections.

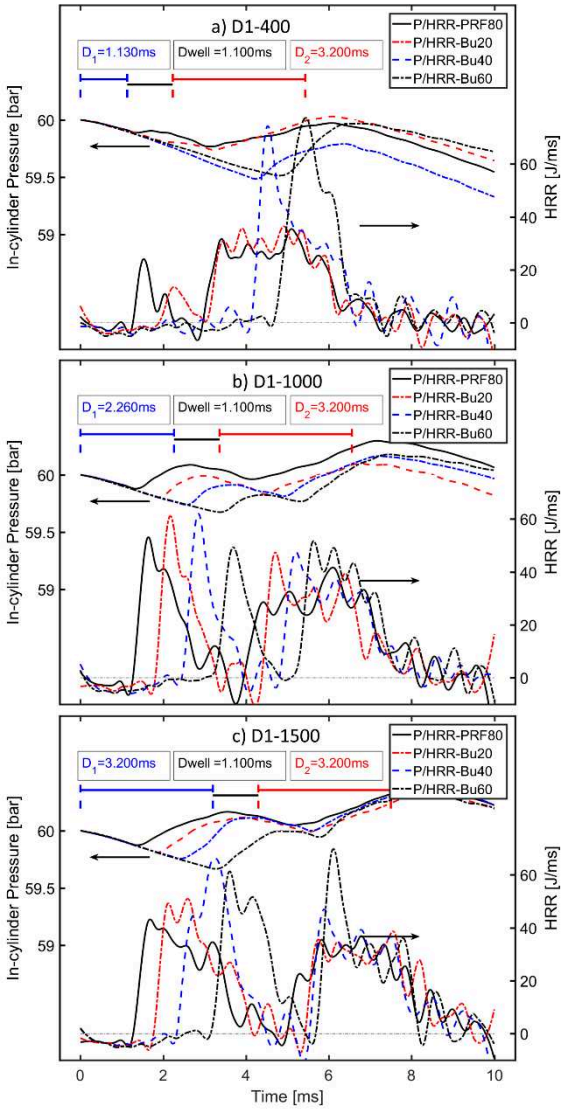

Figure 5.27. In-cylinder pressure and HRR of Butanol blends for 3 different case of split injection strategies

The larger peak HRR during the premixed burn of main injection for Bu40 and Bu60 fuels of case D1-400, see Figure 5.27 a), indicating enhanced premixing of fuel during the longer auto-ignition delay of pilot injection.

Ignition delays of pilot and main injection are shown in Figure 5.28 and Figure 5.29, respectively.

In Figure 5.28 or Figure 5.29, it can be observed that for the pilot or main injection, increasing the butanol ratio increases the delay, as was observed in the previous Chapter 4 for the single injection.

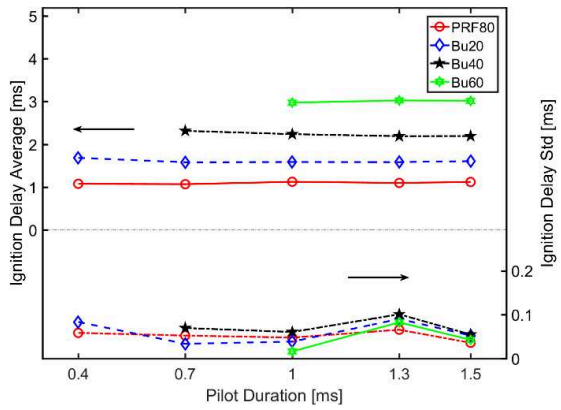

Figure 5.28. Ignition delay of pilot injection for Butanol blend fuels

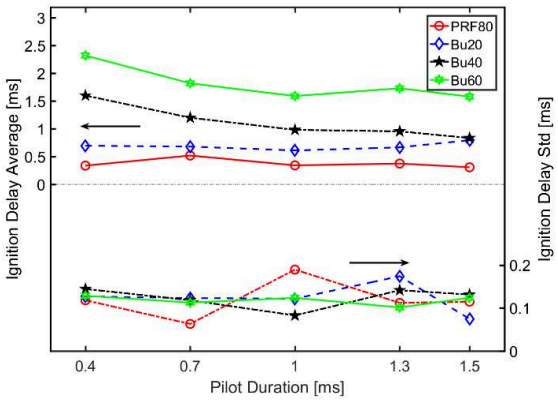

Figure 5.29. Ignition delay of main injection for Butanol blend fuels

When the main injection takes place when the pilot injection is burning the delay is the same whatever the duration of the pilot injection. But when the pilot injection is not burning the quantity injected influences the auto-ignition delay. As shown in Figure 5.29, for Bu60 fuel, the ignition delay for D1-400 is about 4 ms after the start of the pilot injection (compared to 3ms in single injection) in agreement with the observations made by Skeen et al. [153]. The evaporation of the pilot injection cools the ambient gases locally and thus delays combustion. In cases where the pilot injection burns, the combustion of the main injection is prompted by the increase in temperature due to the combustion of the pilot injection.

The Figure 5.30, Figure 5.31 and Figure 5.32 show the imaging OH* Chemiluminescence for Bu20 fuel case under following conditions: 21% of oxygen concentration in ambient gas, 900 K and 60 bar for D1-400, D1-1000 and D1-1500, respectively. The “Bu20” flames occur later than PRF80 fuel and at more downstream region.

On these types of images we can measure the LOL. LOL of main flame versus time and as a function of Butanol blends for 3 cases of pilot injection duration is shown in Figure 5.33.

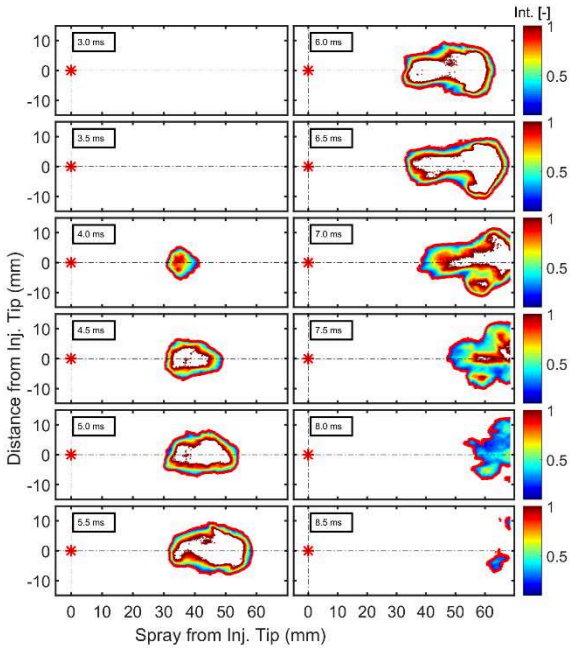

Figure 5.30. Continuous OH* chemiluminescence images under ambient gas of 21% of oxygen concentration, 900 K and 60 bar for Bu20 fuel on case of Split injection strategy D1-400

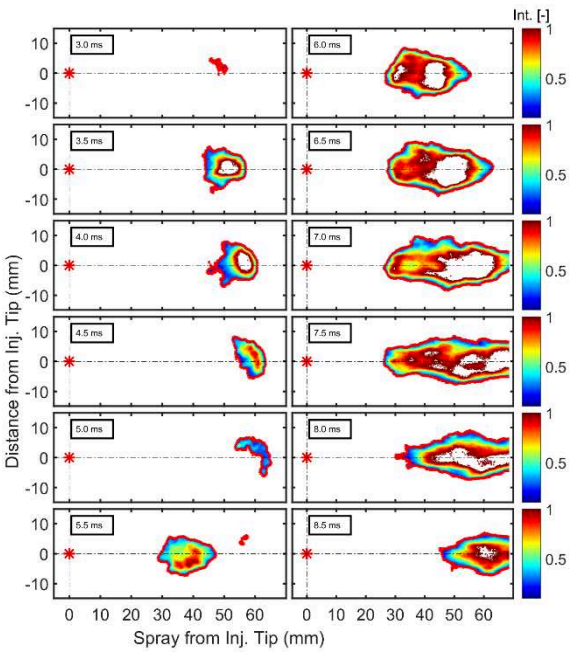

Figure 5.31. Continuous OH* chemiluminescence images under ambient gas of 21% of oxygen concentration, 900 K and 60 bar for Bu20 fuel on case of Split injection strategy D1-1000

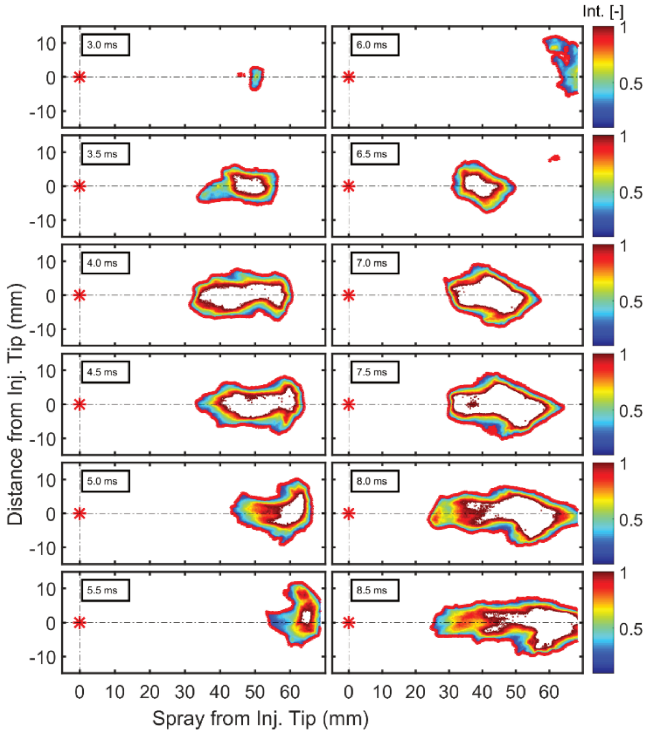

Figure 5.32. Continuous OH* chemiluminescence images under ambient gas of 21% of oxygen concentration, 900 K and 60 bar for Bu20 fuel on case of Split injection strategy D1-1500

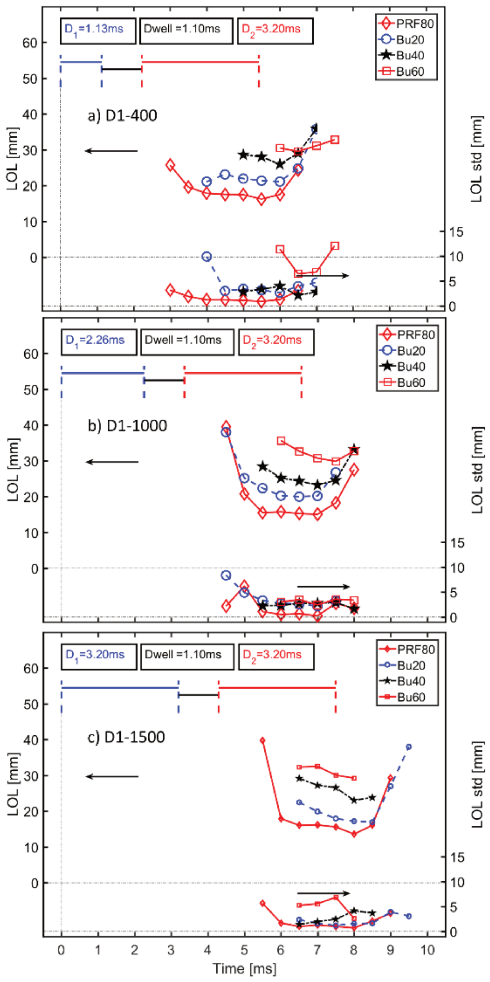

Figure 5.33. Lift off length time-resolved measurement from SOI until EOI under ambient gas of 21% of oxygen concentration, 900 K and 60 bar for PRF80 and Butanol blend fuels under 3 cases of split strategies

The ignition delays the pilot, main and single injections are illustrated in Figure 5.34. Overall, the main ignition delay increases with increasing butanol fraction. The ignition delay for the main injection depends on the type of strategy and whether the pilot combustion is initiated before the main injection starts. Regarding the auto-ignition for pilot injection, the ignition delays of Bu40 and Bu60 fuels are approximate 3.9 and 4.5 ms, respectively, that values are higher than other cases and single injection, about 2.4 and 3 ms, for these fuels. The promoted auto-ignition behavior of the main injection in the case of pilot injection without combustion shows the benefit of split injections, as agree with previous research [153]. The well mixing pilot injection appears to be a reactive environment for early auto-ignition of the main injection.

The main ignition occurs through the controlled mechanism of premixed combustion, as proposed by Felsch et al. [154].

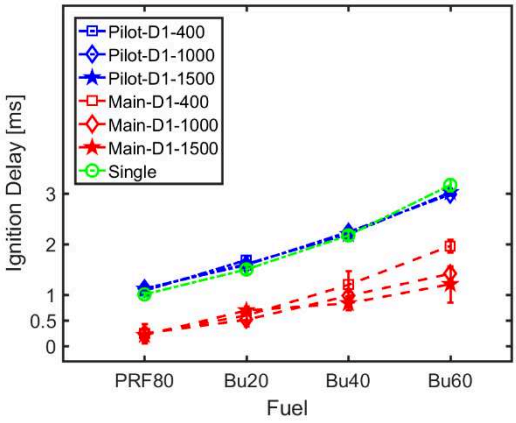

Figure 5.34. Comparison of Ignition delay of pilot, main and single injections for Butanol blends

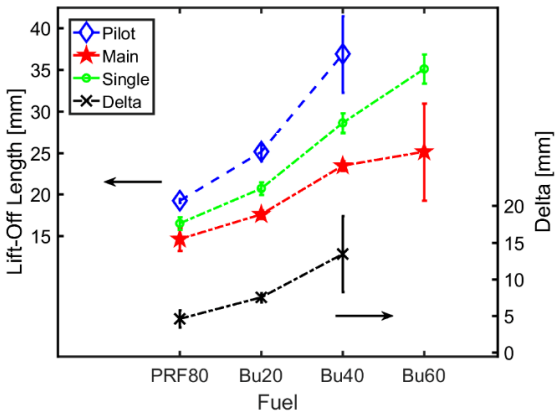

Figure 5.35. Comparison of LOL of pilot, main and single injections for Butanol blends under D1-1500 case

In the case D1-1500, the observed pilot and main flames are in comparison with single injection case, the LOL is illustrated in Figure 5.35. Figure 5.35 shows the LOL of single is shorter than that of pilot because the injection time of the single injection is longer than that of the pilot injection. The delta of LOL of main and pilot increases with increase of butanol fraction on the blends.

5.3.2. Comparison between Bu60, ABE60 and Et20 blends

The cylinder pressure and heat release rate for various pilot injection duration strategies are depicted in Figure 5.36. Under shorter pilot injection duration, the Bu60, ABE60 and Et20 blend fuels have single combustion phase, the mixture air/fuel of pilot injection does not burn before the main injection and hence enhanced premixing of main injection for pilot injection during longer auto-ignition delay to lead the larger peak HRR.

However, the differences are more significant for LOL. In Figure 5.37, LOL versus times for 3 cases of various pilot injection duration, with PRF80, Bu60, ABE60 and Et20 fuels performed in the tests are depicted. For Bu60, ABE60 and Et20, the LOL of main injection appear shorter because of high resistance auto-ignition of these fuels, beside there are not quasi-steady phase of these LOL in which the start of combustion takes place in the downstream regions and thereafter the lift-off position just only travels back towards the injector tip. The relative

position of these curves for three cases of pilot injection duration follows the trend of LOL: PRF80 < Bu60 < Et20 < ABE60.

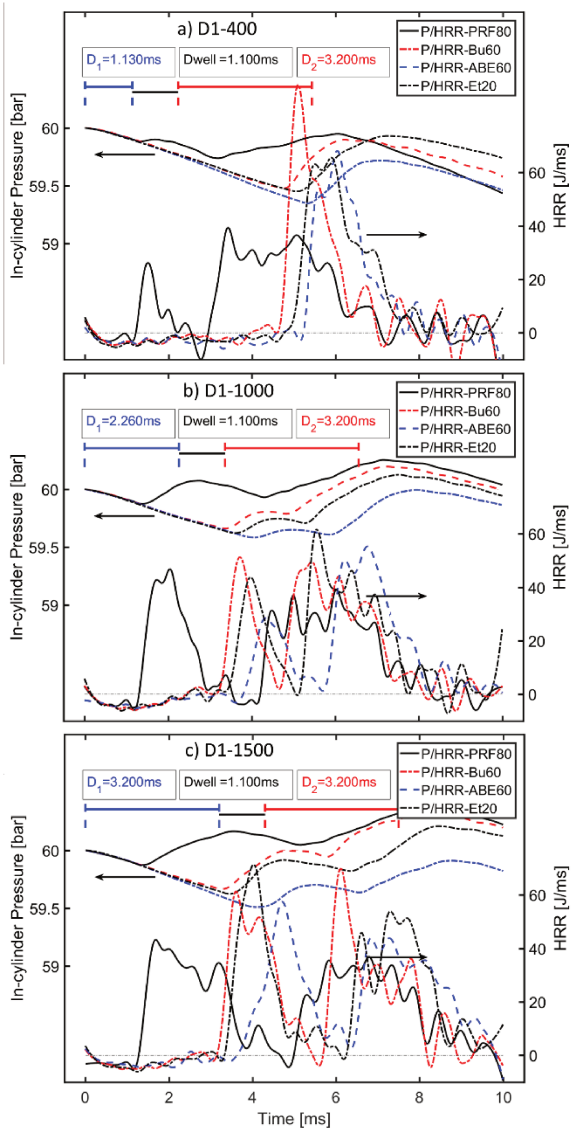

Figure 5.36. In-Cylinder pressure and HRR of PRF80, Bu60, ABE60 and Et20 blends under 3 cases of strategies injections

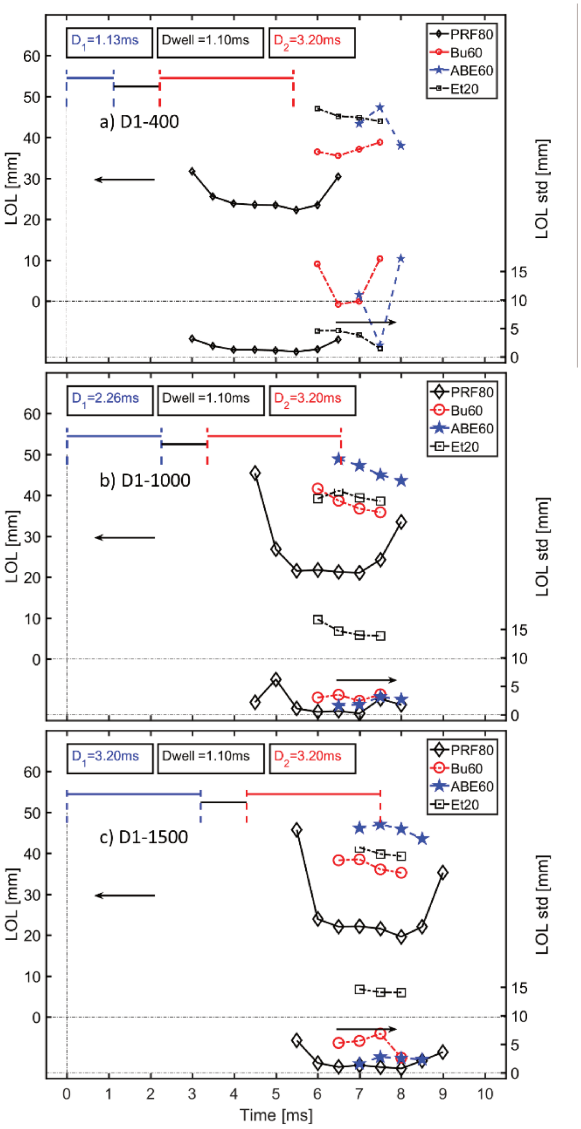

Figure 5.37. Lift off length time-resolved measurement from SOI until EOI of PRF80, Bu60, ABE60 and Et20 blends under 3 cases of strategies injections

The ignition delays of pilot and main injections are shown in Figure 5.38 and Figure 5.39, respectively.

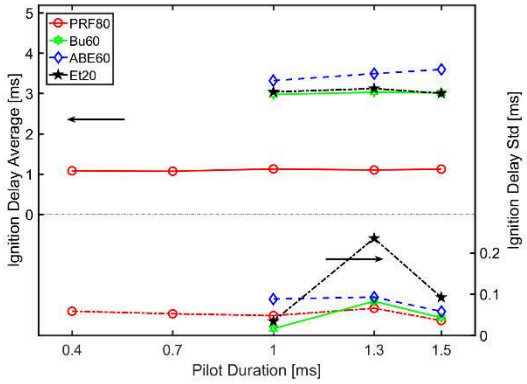

Figure 5.38. Ignition delay of pilot injection for Bu60, ABE60 and Et20

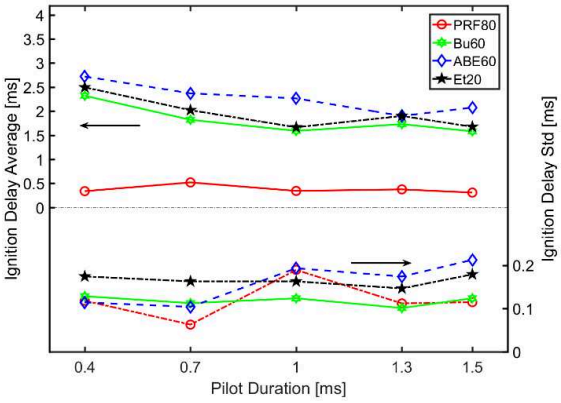

Figure 5.39. Ignition delay of main injection for Bu60, ABE60 and Et20

As the single injection, the ignition delay is longest for ABE60. The Et20 and Bu60 blends have pilot auto-ignition behavior similar, however main auto-ignition of Et20 is more resistance than that of Bu60.

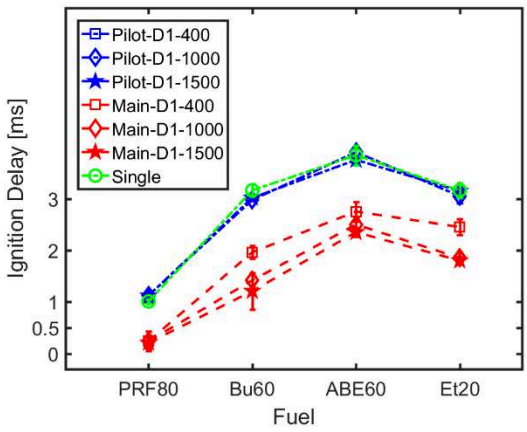

Figure 5.40. Ignition delay of pilot, main and single injections for Bu60, ABE60 and Et20 fuels

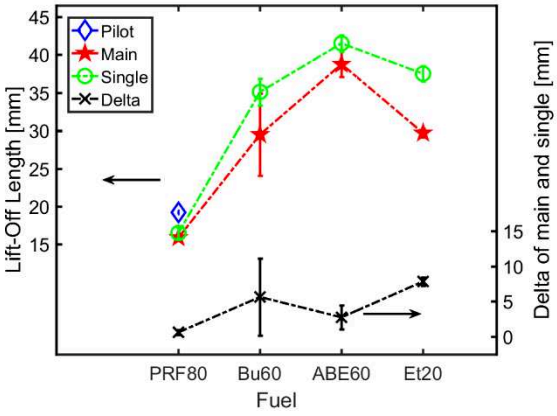

Figure 5.41. Comparison between the LOL of main injection under D1-1500 case and single injection of PRF80, Bu60, ABE60 and Et20 fuels

The main ignition delay is longer for shorter pilot injection duration of case D1-400 for these 3 blends. The pilot and main delays for Et20 fuel are similar to those for Bu60 fuel.

As shown in Figure 5.41, the LOL of single and main of Bu60 and Et60 are similar. The point of pilot LOL was obtained for PRF80 fuel.

The relationship between ignition delays of main and pilot injections is illustrated in Figure 5.42 for all fuels. The fuel with a lower octane number as PRF80, Bu20/40, ABE20/40 are

aligned well. The same linear relationship between pilot injection and main injection self-inflation time exists for 5 blends. This correlation is less good with octane fuels as Bu60, ABE60 and Et20.

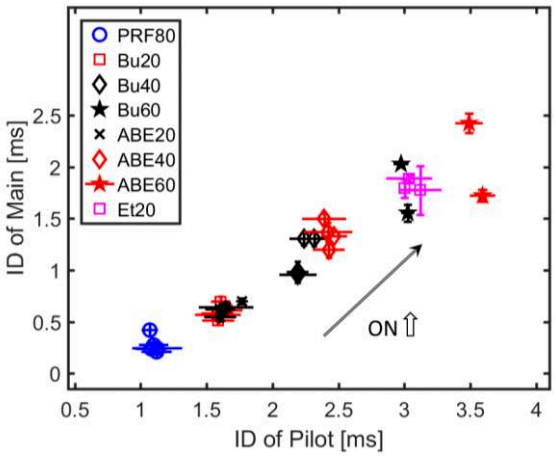

Figure 5.42. Ignition delays of main and pilot injections for Butanol, ABE and Ethanol blends tested fuels

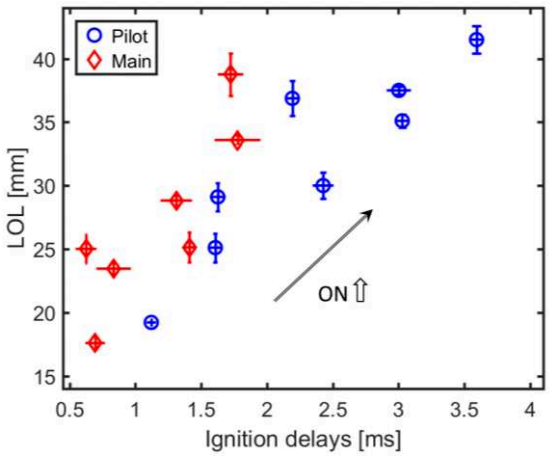

Figure 5.43. Relationship between LOL and ignition delay for both pilot and main injections for Butanol, ABE and Ethanol blends tested fuels

This linear model for Ignition delay of main injection (ID_2) as a function of that of pilot injection (ID_1) is presented in Eq. 5.3, with R_2=0.951. As in the case of a simple injection, the auto-ignition time of the pilot or main injection depends on the fuel characteristic. The pilot combustion time does not influence the auto-ignition time of the main injection. Only the presence or absence of combustion of a pilot injection accelerates the auto-ignition of the main injection.

$$ID_2 = 0.802 * ID_1 - 0.676 \ \text{(ms)} \qquad \textit{Eq. 5.3}$$

Under case D1-1500 of split injection strategy, the LOL and ID of pilot and main of Butanol, ABE and Ethanol blends tested fuels is shown in Figure 5.43. In the case where the LOL has not been measured (ABE60, Bu60, and Et20), the reported value corresponds to the delay and the LOL measured on the single 3 ms injection.

From Figure 5.43, it can be observed that the main flame has a lower ignition delay and shorter lift off length than pilot for Butanol, ABE and Ethanol blends tested fuels. The pilot ignition delays and LOL are higher for higher fraction of butanol, leading to a nearly equally high main

ignition delay and LOL are also almost equally higher. For the same ignition delay, the LOL of main is longer than the LOL of the pilot. For example, in the case of D1-1500 the ignition delay of the pilot injection of Bu20 is close to that of the main injection of ABE60, i.e. 1.6 ms and 1.7 ms respectively. For these 2 fuels the LOL is very different 25 mm for the pilot injection of Bu20 against 37 mm for the main injection of ABE60.

The pilot shows a good correlation of the ignition delay and LOL, see Figure 5.43, as shown in chapter 4 for these tested fuel blends, see Figure 4.50. However, this trend is failing for main injection. The reasons are the main spray enters a much hotter local environment created by the pilot burning, compared to the ambient temperature condition at which the pilot or single injection is found. Moreover, the position of pilot combustion release depends on the auto-ignition delay, hence impact on interaction of main spray and hot burned gas is differed for these blends.

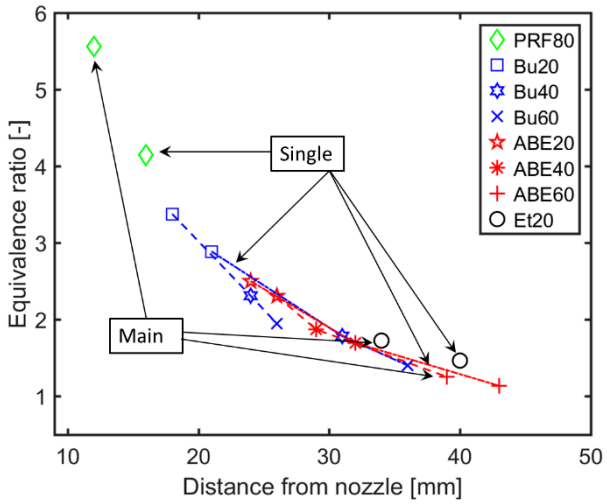

Figure 5.44. Comparison the cross-sectional average equivalence ratio at the LOL between main and single injections of PRF80, Butanol blends, ABE blends, Et blends

The comparison the cross-sectional average equivalence ratio at the LOL between main and single injection of PRF80 and blends is shown in Figure 5.44. The main injection has richer mixture than single for all tested fuels.

As shown in the points for the ABE40, ABE60, Bu60, and Et20 fuels, despite the decrease in main injection LOL of about 3 mm (9%), 4 mm (9%), 9 mm (25%), and 6 mm (15%), respectively, the estimated equivalence ratio at the main injection LOL is approximately the same as that of the single injection. This suggests that the higher oxygen content in the mixtures at the beginning of combustion at the LOL is at the same air/fuel ratio. Thus, these mixtures

will produce little soot while improving auto-ignition behavior.

Summary pilot and main Ignition delays, main LOL and equivalence ratio at main LOL for PRF80, Butanol blends, ABE blends and Ethanol blend fuels is given in Table 5.4.

Table 5.4. Summary pilot and main Ignition delays, main LOL and equivalence ratio at main LOL

Fuel	Ignition delays (ms)		Main LOL (mm)	ER at main LOL
	Pilot	Main		
PRF80	1.08 (±0.04)	0.68 (±0.02)	14.2 (±2.5)	5.56
Bu20	1.65 (±0.05)	0.80 (±0.04)	21.5 (±1.6)	3.38
Bu40	2.23 (±0.06)	0.92 (±0.04)	24.1 (±1.3)	2.31
Bu60	3.02 (±0.06)	1.60 (±0.05)	26.0 (±1.7)	1.95
ABE20	1.70 (±0.05)	0.90 (±0.06)	22.2 (±1.4)	2.50
ABE40	2.42 (±0.06)	1.28 (±0.05)	26.2 (±1.8)	2.31
ABE60	3.85 (±0.08)	2.30 (±0.07)	39.3 (±3.2)	1.25
Et20	3.05 (±0.07)	1.81 (±0.09)	34.1 (±2.1)	1.73

5.4. DBI imaging and measurement soot results

As for the single injection measurements with DBI technique, the fuels and gas conditions are presented in Table 4.9. The matrix of split injection strategies is summarized in Table 5.1.

5.4.1. DBI imagining

In current section, the PRF60 fuels and 18% ambient gas oxygen concentration is used to evaluated the soot production of the split injection strategies.

Sequences of Image of Natural Luminosity and estimated KL of the main flame for cases D1-400, D1-1000 and D1-1500 are presented in Figure 5.45, Figure 5.46 and Figure 5.47, left and right, respectively.

With dwell period of 1.1 ms for all cases, the main combustion started while the pilot combustion was almost extinguished, as seen the first image NL.

For a short pilot injection duration (D1-400), pilot combustion is of the premixed type, characterized by rapid combustion away from the injector tip but occurring later here after the dwell period. As the pilot injection duration becomes longer, the more diffusion combustion fraction can be less dwell time period. Thus, it is probable that the interaction between the main injection and pilot combustion is more aggressive as the pilot injection duration become longer,

which results in slightly higher luminosity.

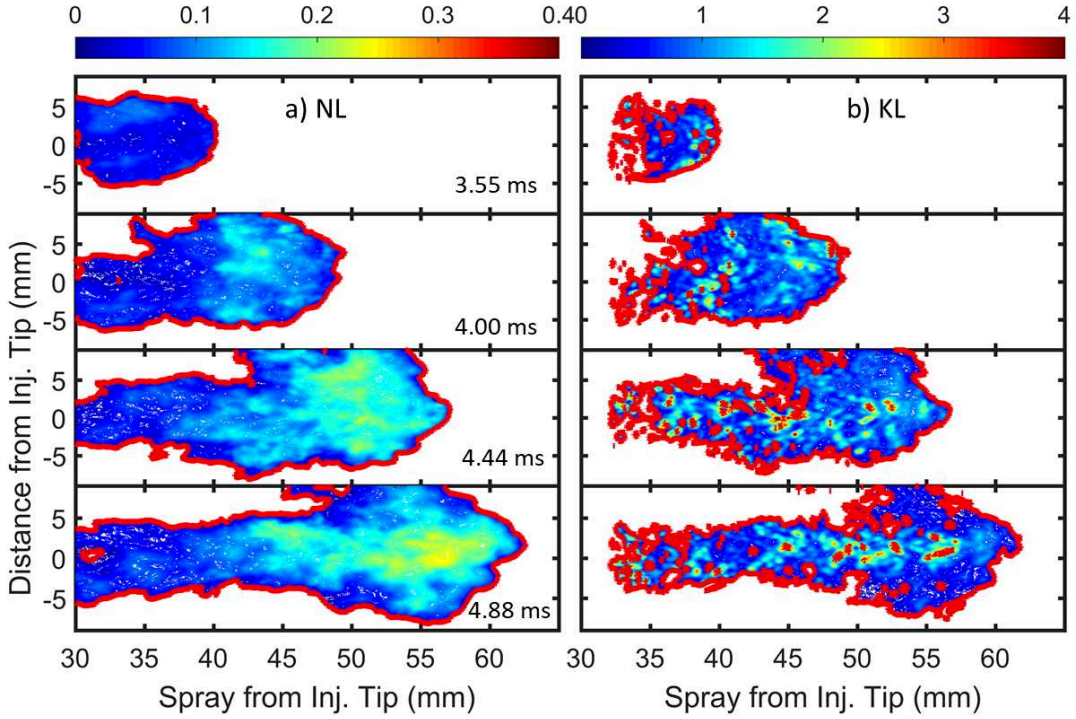

Figure 5.45. Imaging of Natural Luminosity and KL at four times after SOI of PRF60 fuel under ambient gas conditions: 18% of Oxygen concentration, 900 K of temperature and 60 bar of pressure and case split injection of D1-400

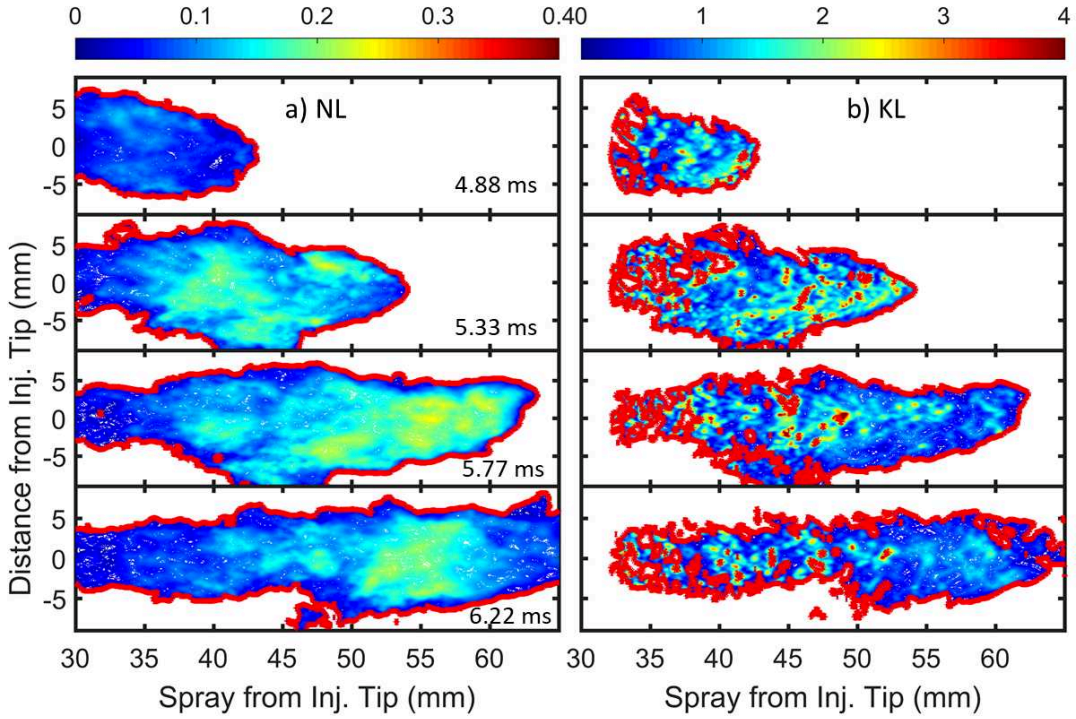

Figure 5.46. Imaging of Natural Luminosity and KL at four times after SOI of PRF60 fuel under ambient gas conditions: 18% of Oxygen concentration, 900 K of temperature and 60 bar of pressure and case split injection of D1-1000

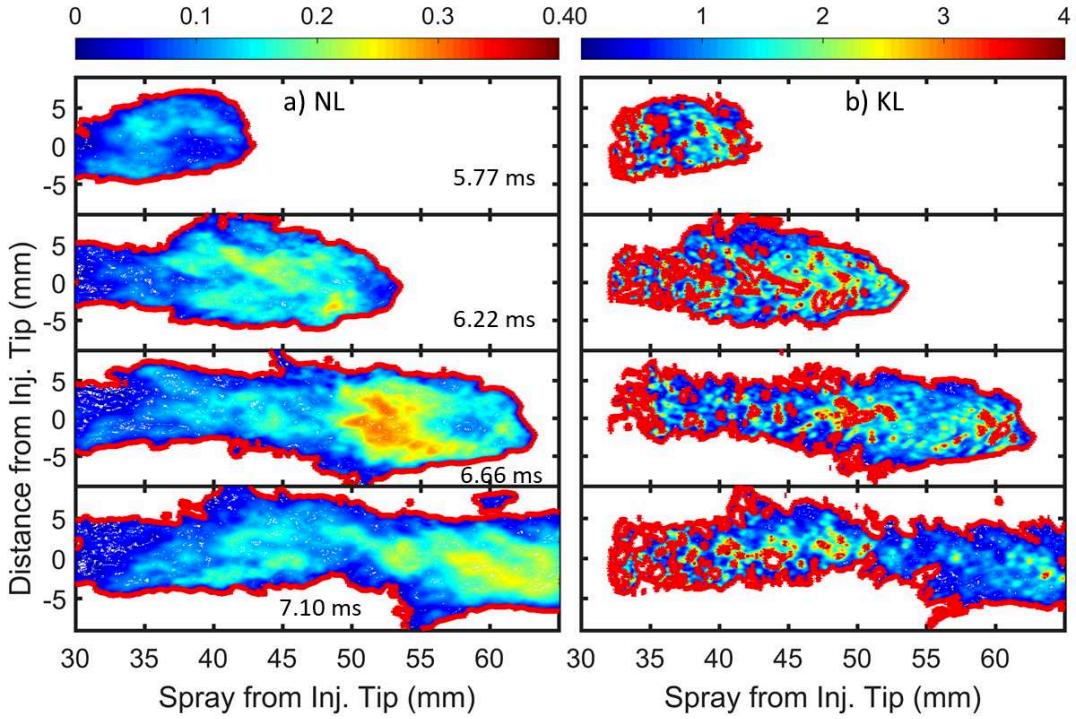

Figure 5.47. Imaging of Natural Luminosity and KL at four times after SOI of PRF60 fuel under ambient gas conditions: 18% of Oxygen concentration, 900 K of temperature and 60 bar of pressure and case split injection of D1-1500

The Natural Luminosity integral is calculated for 6 tests. The mean and the standard derivation for split and single injections are plotted in Figure 5.48.

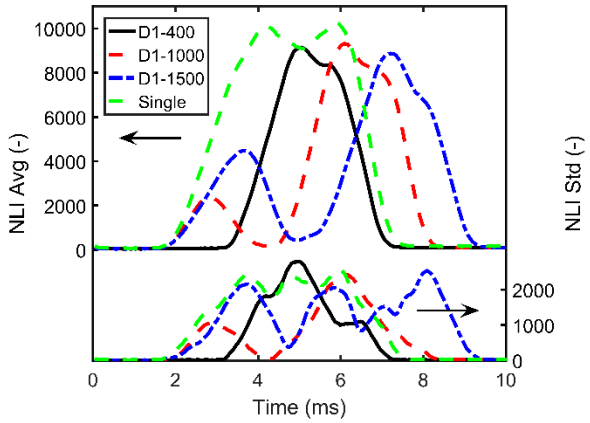

Figure 5.48. Natural Luminosity Integral (NLI) of single and split injections strategies versus times of PRF60 fuel under ambient gas conditions: 18% of Oxygen concentration, 900 K of temperature and 60 bar of pressure

The Normalized of Natural Luminosity Intensity along spray axis and cross-sectional at 50 mm of downstream from nozzle are illustrated in Figure 5.49.

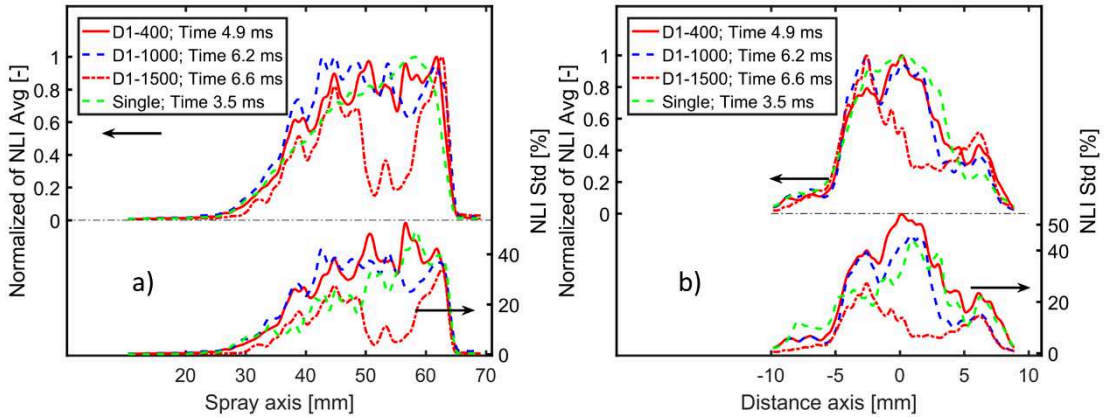

Figure 5.49. Normalized of Natural Luminosity Intensity (NLI) along spray axis and spray cross-sectional at 50 mm of downstream from nozzle of PRF60 fuel under ambient gas conditions: 18% of Oxygen concentration, 900 K of temperature and 60 bar of pressure

The corresponding cylinder pressure and HRR, as well as the average over 6 tests for three split injections cases are shown in Figure 5.50. The evolution of these trends is similar from test to test, and the auto-ignition timing of both pilot and main injections are also repeatable over all tests.

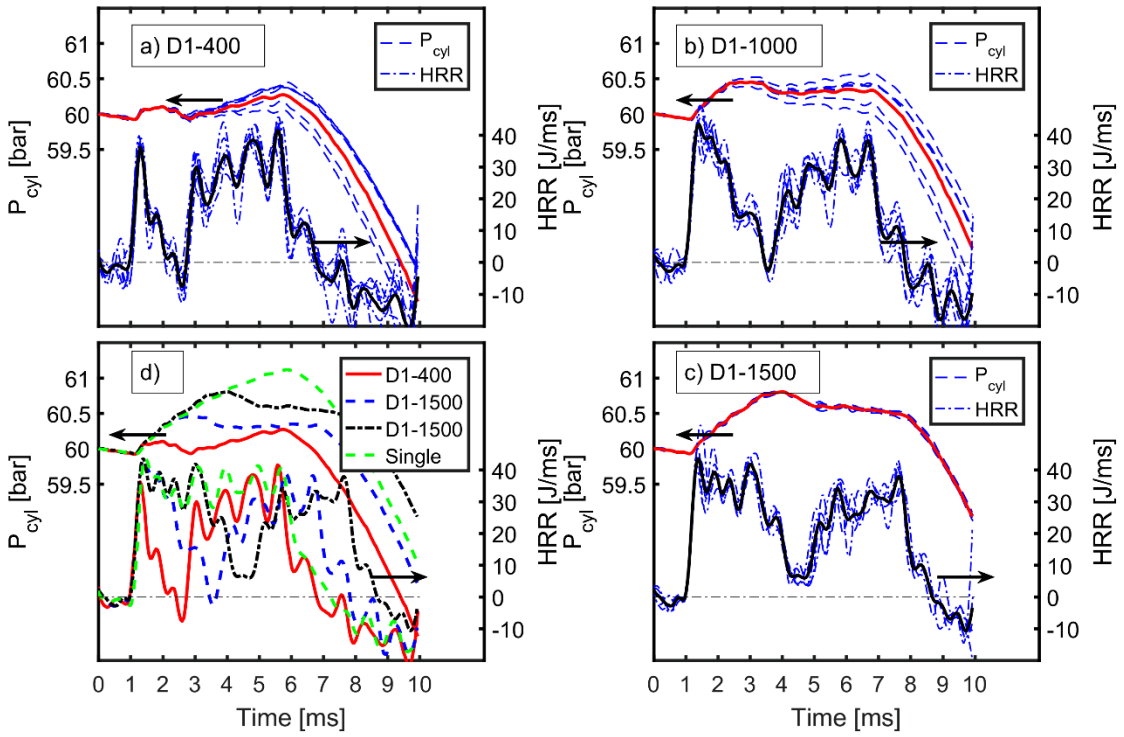

Figure 5.50. Corresponding in-cylinder pressure HRR to Figure 5.48 averaged one over 6 tests

As with the single injections, variations in HRR and spray auto-ignition behavior under this tested condition do not have major impact on the cycle-to-cycle soot variations.

5.4.2. Soot measurement results for split injection strategies

As discussed in chapter 4, it is possible to correctly capture the natural flame luminosity of the PRF60, PRF70 and PRF80. Hence in current section, these fuels were chosen to evaluate the combustion characteristics and the soot production, under various oxygen concentration in ambient gas for different pilot injection times of split strategies, as listed in Table 5.5. Moreover, the combustion characteristics were observed with the ABE20 and Bu20 under 18% and 21% oxygen concentration.

Table 5.5. Fuel and condition test matrix

No.	**Fuel**	**O_2 [%]**	**Pilot duration [µs]**
1	PRF60	15/18	400 (D1-400) 1000 (D1-1000) 1500 (D1-1500)
2	PRF70	15/18/21	
3	PRF80	15/18/21	
4	Bu20	18/21	
4	ABE20	18/21	

5.4.2.1. Ignition delay and Lift off length

The main injection ignition delays of as a function the pilot injection of ignition delays for PRF60, PRF70, PRF80, Bu20 and ABE20 under various ambient gas oxygen concentration (15%, 18% and 21%) for different pilot injection times of split strategies is shown in Figure 5.51. The experimental results presented here are in agreement with previous section on low octane fuels and low gas ambient oxygen concentration, wherein increasing the pilot ignition delay decreased fuel reactivity, leading to longer main ignition delays.

Figure 5.51 shows that Butanol and ABE gave a lower main ignition delays compared to PRF80 fuel, while the pilot ignition delay behavior is similar as the ambient gas oxygen concentration increases for Butanol and ABE blend.

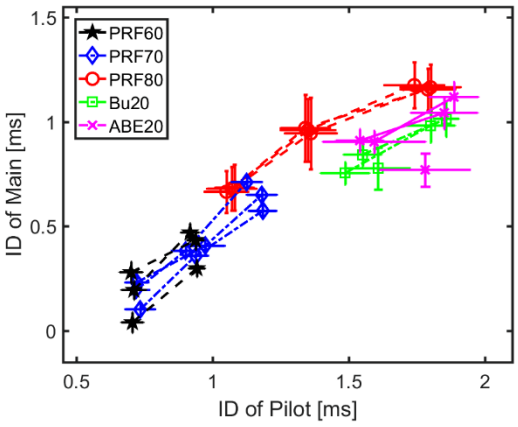

Figure 5.51. Ignition delay of Main and pilot for PRF60, PRF70, PRF80, Bu20 and ABE20 under various oxygen concentration ambient gas (15%, 18% and 21%) for different pilot injection durations of split strategies

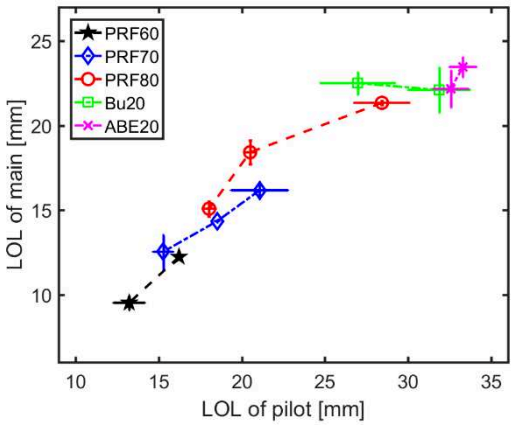

Figure 5.52. LOL of main and pilot, for D1500 case under oxygen concentration various conditions ambient gas (15%, 18% and 21%) for different pilot injection durations of split strategies

A linear model for the main injection ignition delay as a function of pilot injection ignition delay is presented in Eq. 5.4, with R_2=0.857. Compared to Eq. 5.3, the coefficient in Eq. 5.4 is lower than in Eq. 5.3, which shows the inverse impact of ambient gas oxygen concentration on the behavior of main auto-ignition delay.

$$ID_2 = 0.762 * ID_1 - 0.289 \ \text{(ms)} \qquad \textit{Eq. 5.4}$$

In the case of low oxygen concentration and low octane fuels, the relationship obtained is similar to that of high-octane, high-oxygen fuels with an oxygen concentration of 21% of the ambient gas, as seen Figure 5.51.

The main ignition delays are generally dependent on the pilot ignition delays, indicating that the main ignition occurs in the surrounding boundaries, because the main injection has less oxygen to mixture and burn in head portion of vapor spray, where the air is entrained into the pilot spray and then burns and utilizes the local oxygen, as proposed by Moiz et al. [155]. In the surrounding boundaries of main spray, where a lean mixture remains at the end of the pilot spray, the auto-ignition of main injection is promoted. In addition, the main auto-ignition delays are also influenced by hotter gas ambient of pilot flame.

The longer pilot injection duration of D1-1500 provided the pilot flame LOL, which is

compared to the main injection, as shown in Figure 5.52. The pilot LOL has a larger fluctuation due to the transient flame stage due to the short duration of gasoline fuel.

A linear model for LOL of the main injection versus that of the pilot injection is presented in Eq. 5.5, R^2=0.918. In comparison to the linear model for ignition delay, the coefficient of Eq. 5.5 is lowest. The flame LOL are dominated by auto-ignition process, but the pilot flame has longer LOL than single flame, due to the shorter the duration of pilot injection for gasoline fuel.

$$LOL_m = 0.635 * LOL_p + 2.882 \ \text{(mm)} \qquad \textit{Eq. 5.5}$$

A linear model for LOL of main injection versus that of single injection is presented in Eq. 5.6, R^2=0.840, as expected that the observed coefficient is similar to the main auto-ignition delay, see Eq. 5.4.

$$LOL_m = 0.792 * LOL_s - 0.743 \ \text{(mm)} \qquad \textit{Eq. 5.6}$$

The LOL as a function of ignition delay for the main and pilot injections is illustrated in Figure 5.53, it can be observed that the main flame has the advantage of lower ignition delay and shorter LOL than pilot and single injections, in the case of various oxygen concentration and fuel octane number.

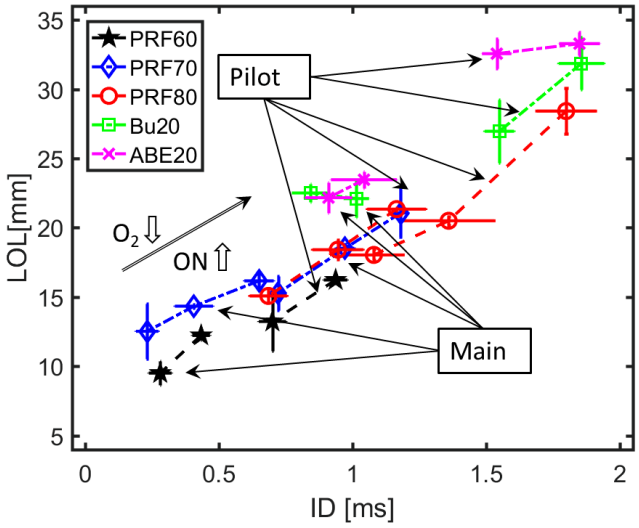

Figure 5.53. LOL and ID of main and pilot injections, for D1500 case under oxygen concentration various conditions

The main LOL is generally dependent on the main auto-ignition behavior. Thus, if combustion

occurs earlier the combustion zone is closer to the injector tip. The flame LOL is influenced by a burnt gas 'reservoir' that surrounds the fuel jet and stabilizes the reaction zone, as suggested Pickett et al. [156].

5.4.2.2. Effect of injection strategies on soot production

a) PRF60 fuel

In Figure 5.54, contours plot show within the boundary plotted in red the spray soot mass fractions for PRF60 fuel under 18% O_2 condition at around 2.0 ms and 2.5 ms ASOC for split and single injections, respectively.

In comparison to the main LOL (about 10 mm of axial length to nozzle), the soot formation begins (about 30 mm of axial length to nozzle) well downstream of the flame lift-off. Soot oxidation continues downstream of 60-65 mm, so the soot concentration decreases. Figure 5.54 shows that that the soot jet of the split flame is higher than that of the single flame at the same time after injection. This increase is due to higher temperature conditions (due to pilot injection combustion) and stabilized combustion on richer mixtures (lower LOL).

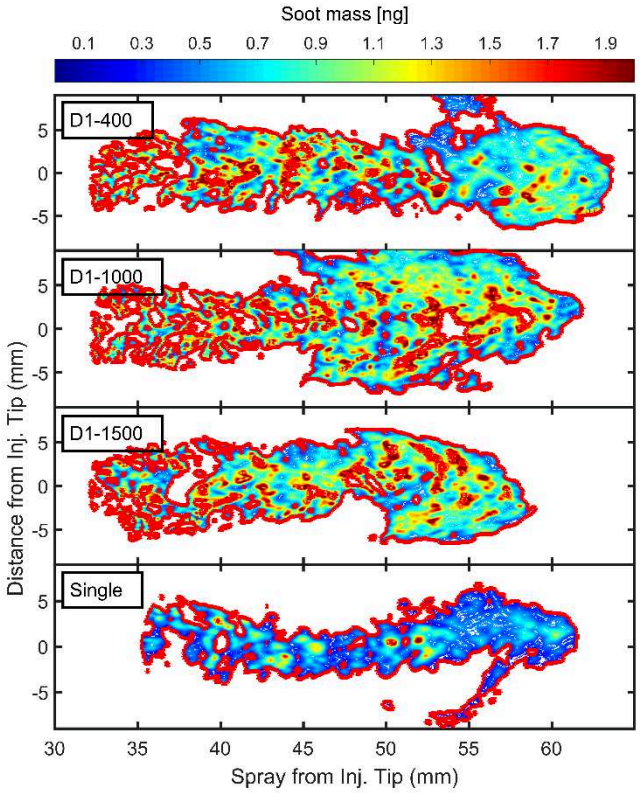

Figure 5.54. The soot mass fraction images for PRF60 fuel, 18% of oxygen concentration ambient gas for single and split injections

The integrated soot masses (according to the Eq. 4.9) in thin radial cross-sections (1 mm) inside the jet flame of PRF60 fuel under ambient gas 18% O_2 are plotted in Figure 5.55. The shorter flame and higher peak of soot mass of D1-1500 case is observed.

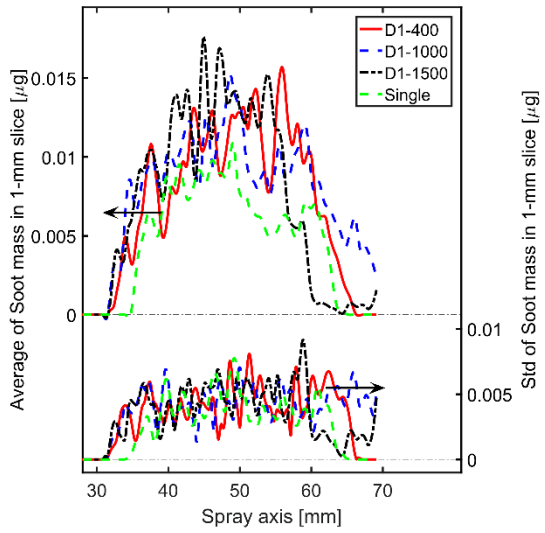

Figure 5.55. Soot mass for PRF60 fuel, 18% oxygen concentration of ambient gas in thin (1 mm) cross-sections of jet as a function of axis distance for single and split injections strategies

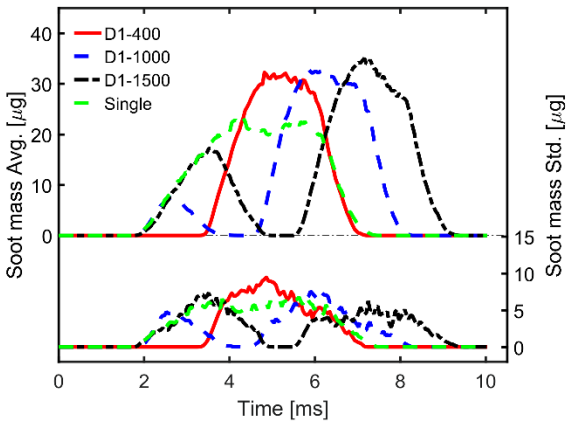

Figure 5.56. Soot mass versus time of PRF60 under 18% oxygen concentration for split injection strategies and single injection

Figure 5.55 shows similar the soot mass peaks for the split injections higher than for single injection. With the D1-1500 case and single injection, the soot process shifts upstream, as shown by the end of the soot mass profile.

As seen in Figure 5.54 and Figure 5.55, the cases of D1-400 and D1-1000 have a longer vertical soot, which implies more mixing with ambient oxygen, which can lead to efficient combustion.

Figure 5.56 shows the average soot mass of six tests as a function of time for the PRF60 fuel under different split injection and single injection strategies under 18% oxygen concentration. The three cases of pilot duration are interesting to study. For the case with the shortest duration (D1-400) the soot is present only on the main injection stage. For the intermediate duration (D1-1000), a small mass of soot is observed during the pilot phase. For longer duration (D1-1500), the soot mass of the pilot injection is significant compared to the main injection.

As seen Figure 5.56, the soot mass of these three split cases are similar and higher than those of single injection.

As can be seen from the soot mass slope, the pilot flame of D1-1000 and D1-1500 and the single injection have similar trends in the early moments.

The small and short of soot mass of pilot injection, see Figure 5.56, show that the influence of main injection on soot process of pilot flame by availing more oxygen, through more ambient gas, to the soot region of pilot flame, hence the soot oxidation from pilot flame, such presented by Moiz et al. [151].

For different pilot injection times of split injection strategies and single injection, the IXT of soot mass of PRF60 fuel under a temperature of 900 K, a pressure of 60 bar and an oxygen concentration of 18% of the ambient gas is illustrated in Figure 5.57. The D1-1000 and D1-1500 cases create two islands on the IXT contour for pilot and main flames. The shape of soot mass cloud of the main combustion does not show significant difference. The intensity level is quite different for the 4 cases.

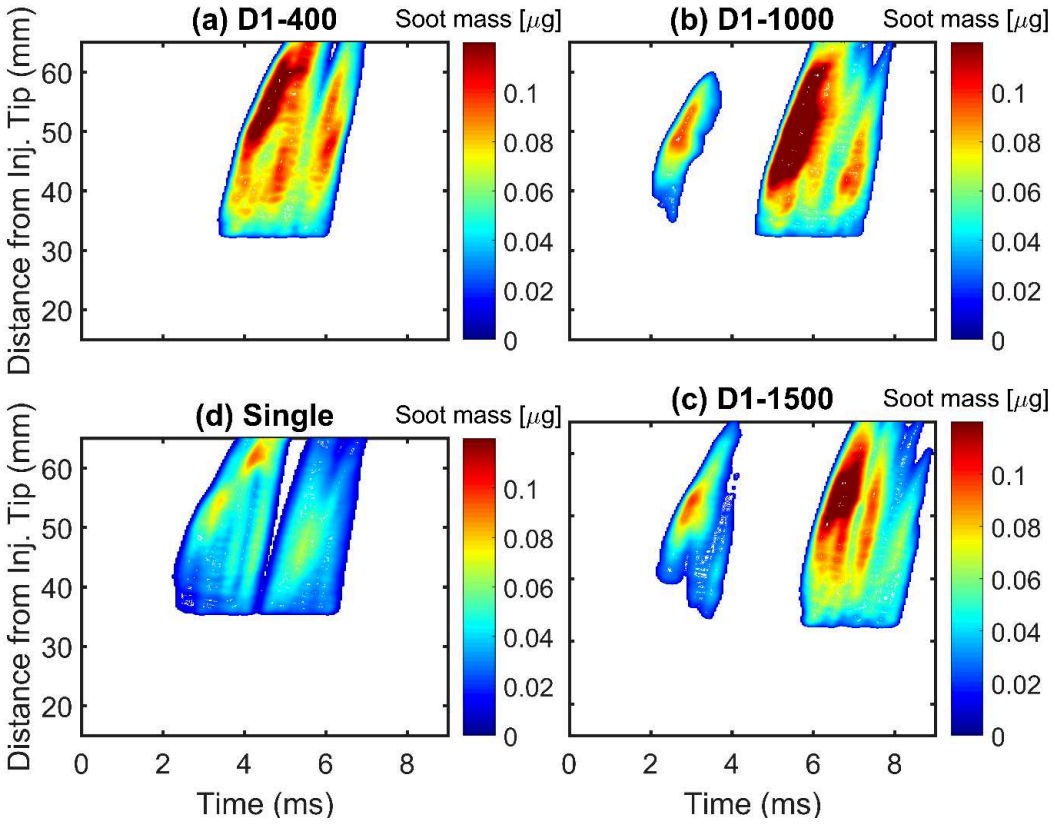

Figure 5.57. Cloud of soot mass of PRF60 fuel under ambient gas of 18% Oxygen concentration, 900 K of temperature and 60 bar of pressure for single and split injections strategies

Thus, the soot mass intensity of the main injection is higher than that of the pilot or single injection. The presence of the pilot flame promotes faster and higher soot production by

improving the mixing.

From the soot mass IXT, the soot initiation time and the axial location of the main flame for PRF60 fuel under 15% and 18% ambient oxygen are given in Table 5.6. The main flame hasve similar soot initiation time after start of combustion and initial axial location of soot for each ambient condition. Compared to the single flame, the axial location of soot initiation is slightly shorter for a similar initiation time for the main flame.

Table 5.6. Soot initiation time and axial location of main flame for PRF60 fuel under 15% and 18% of ambient oxygen

Case	Ambient oxygen [%]	Soot initiation time [ASOC ms]	Soot initiation axial location [mm]
D1-400	15	1.1	42
	18	0.6	33
D1-1000	15	1.2	42
	18	0.5	33
D1-1500	15	1.3	41
	18	0.9	33
Single	15	1	46
	18	0.9	40

b) PRF70 fuel

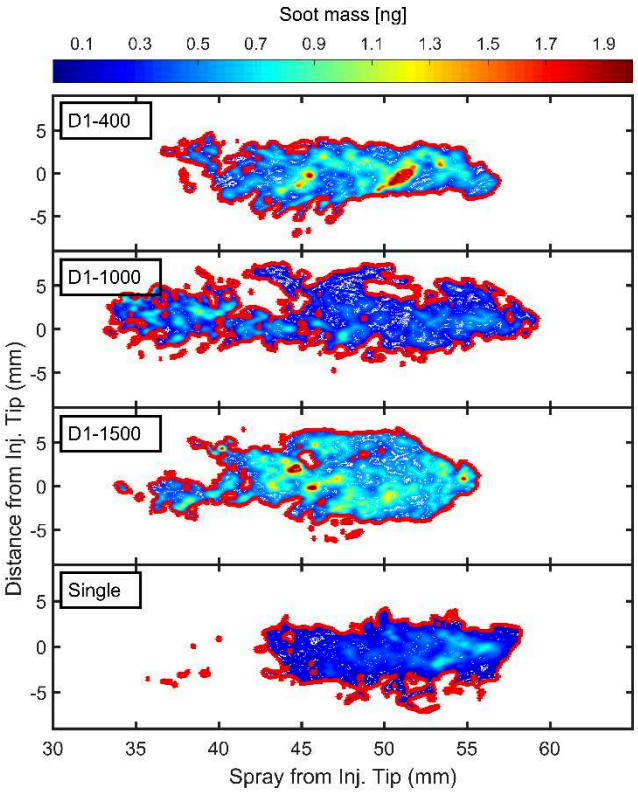

Figure 5.58. The soot mass fraction images for PRF70 fuel, 18% of oxygen concentration ambient gas for single and split injections

In Figure 5.58, contours plot show within the boundary plotted in red the spray soot mass fractions for PR70 fuel under 18% O_2 condition at around 2.0 ms and 2.5 ms ASOC for split and single injections, respectively.

The integrated soot masses in thin radial cross-sections (1 mm) inside the jet flame of PRF70 fuel under ambient gas at 18% O_2 are plotted in Figure 5.59.

Figure 5.59 shows similar soot mass peaks for the split injections higher than for single injection. Similar to PRF60 fuel, a shorter flame is obtained for the D1-1500 case.

The soot mass average of six tests versus time for PRF70 fuel under differences split injection strategies and single injection under 18% oxygen concentration is illustrated in Figure 5.60.

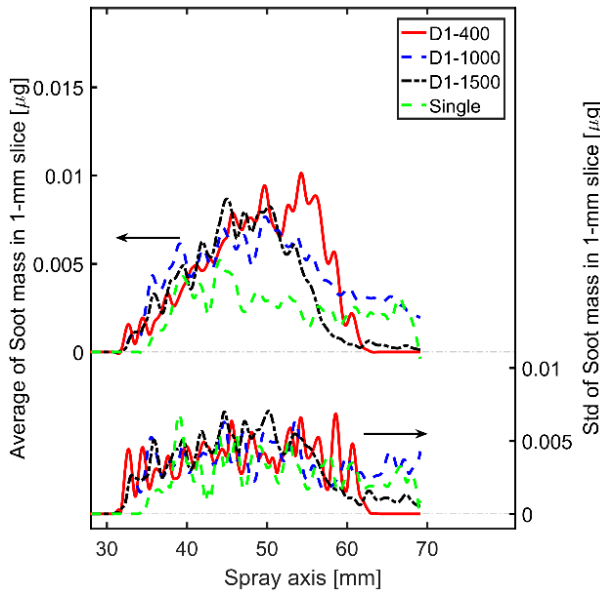

Figure 5.59. Soot mass for PRF70 fuel, 18% oxygen concentration of ambient gas in thin (1 mm) cross-sections of jet as a function of axis distance for single and split injections strategies

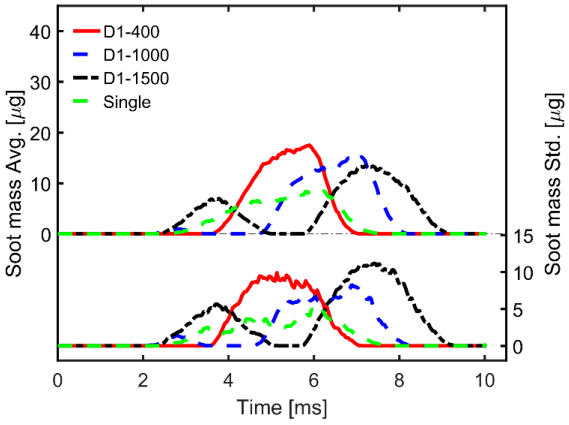

Figure 5.60. Soot mass versus time of PRF70 under 18% oxygen concentration for split injection strategies and single injection

Figure 5.60 shows the average soot mass of six tests as a function of time for the PRF70 fuel under different split injection and single injection strategies under 18% oxygen concentration.

Figure 5.60 shows that the level of soot mass peaks is following: D1-400 > D1-1000 > D1-1500.

The D1-1500 case shows two stages of soot mass profile, corresponding to the two injections while the D1-400 and D1-1000 cases show only one stage, including the more premixed combustion fraction of the pilot injection and the main combustion.

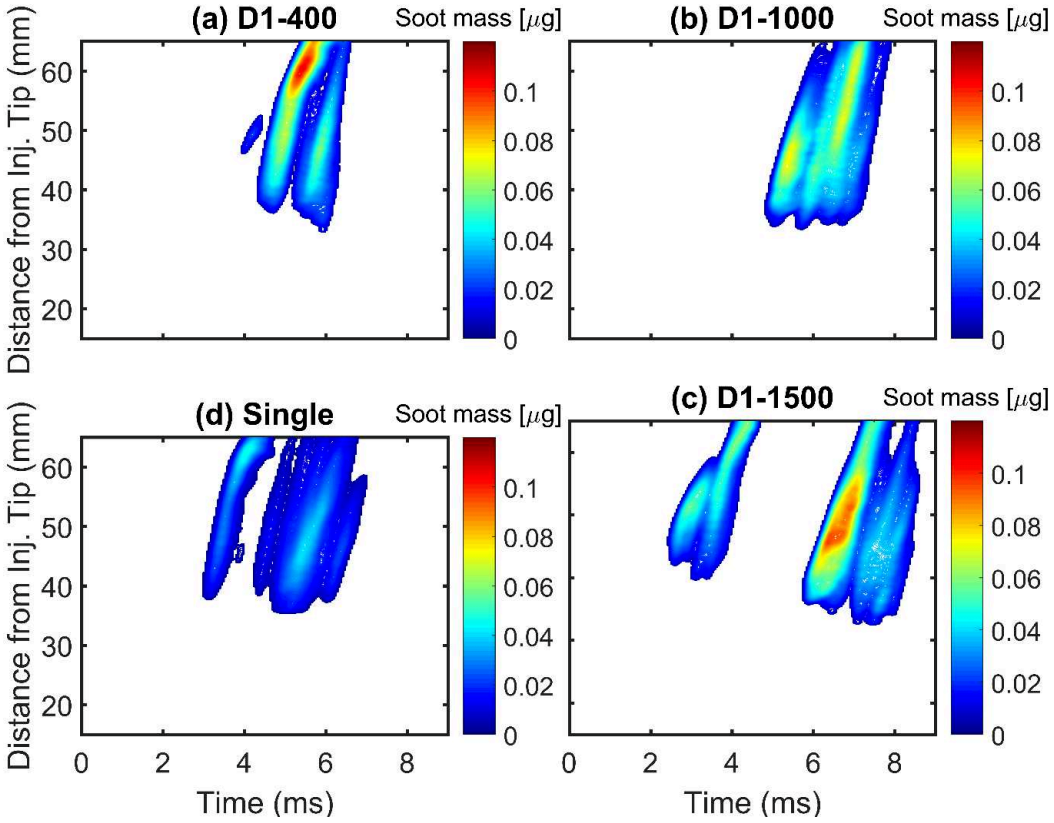

Figure 5.61. Cloud of soot mass of PRF70 fuel under ambient gas of 18% Oxygen concentration, 900 K of temperature and 60 bar of pressure for single and split injections

For different pilot injection times of split injection strategies and single injection, the IXT of soot mass of PRF70 fuel under a temperature of 900 K, a pressure of 60 bar and an oxygen concentration of 18% of the ambient gas is illustrated in Figure 5.61.

Comparing the soot mass fraction of PRF70 fuel to that of PRF60 fuel, the soot concentration is lower and the main flame soot formations are delayed and pushed downstream for all three split cases.

From the soot mass IXT, the soot initiation time and axial location of main flame for PRF70 fuel under 15% and 18% ambient oxygen are given in Table 5.7.

Table 5.7. Soot initiation time and axial location of main flame for PRF70 fuel under 15%, 18% and 21% of ambient oxygen

Case	Ambient	Soot initiation time [ASOC	Soot initiation axial

	oxygen [%]	ms]	location [mm]
D1-400	15	1.1	45
	18	1.3	39
	21	0.5	32
D1-1000	15	1.2	45
	18	0.8	38
	21	0.5	32
D1-1500	15	1.8	50
	18	1.0	36
	21	0.7	32
Single	15	1.5	50
	18	1.3	45
	21	1.2	42

c) PRF80 fuel

In Figure 5.62, contours plot show within the boundary plotted in red the spray soot mass fractions for PR80 fuel under 18% O_2 condition at around 2.0 ms and 2.5 ms ASOC for split and single injections, respectively.

For main flame, the soot mass appears higher than of single flame. The natural luminosity and soot mass concentration of PRF80 fuel show ultra-low soot production.

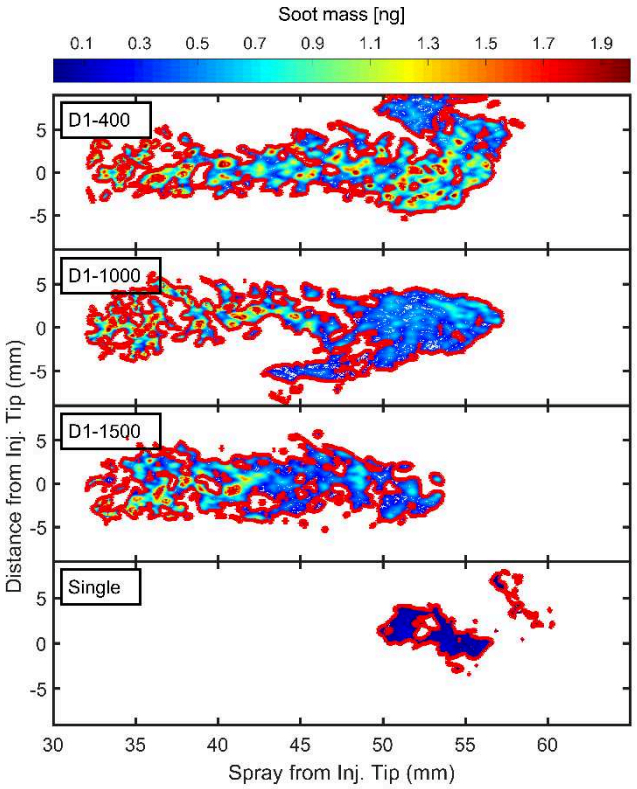

Figure 5.62. The soot mass fraction images for PRF80 fuel, 21% of oxygen concentration

ambient gas for single and split injections

The integrated soot masses in thin radial cross-sections (1 mm) inside the jet flame of PRF80 fuel under ambient gas at 21% O_2 are plotted in Figure 5.63. Figure 5.63 shows similar soot mass peaks for the split injections slightly higher than for single injection. As with the PRF60 and PRF70 fuels, a shorter flame is obtained for the D1-1500 case.

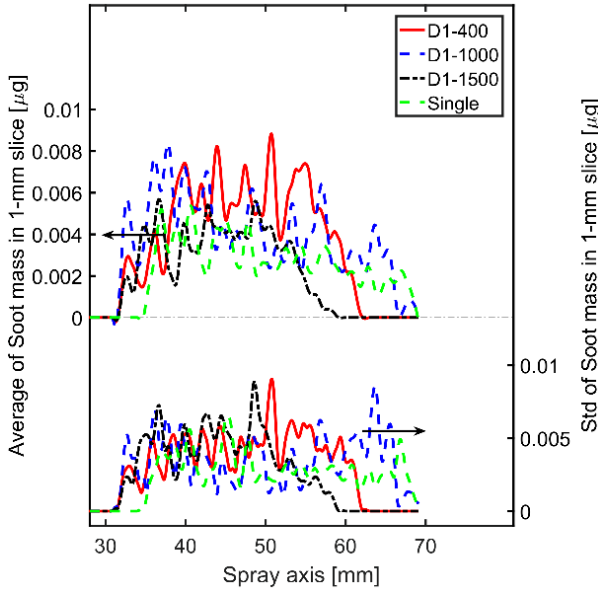

Figure 5.63. Soot mass for PRF80 fuel, 21% oxygen concentration of ambient gas in thin (1 mm) cross-sections of jet as a function of axis distance for single and split injections strategies

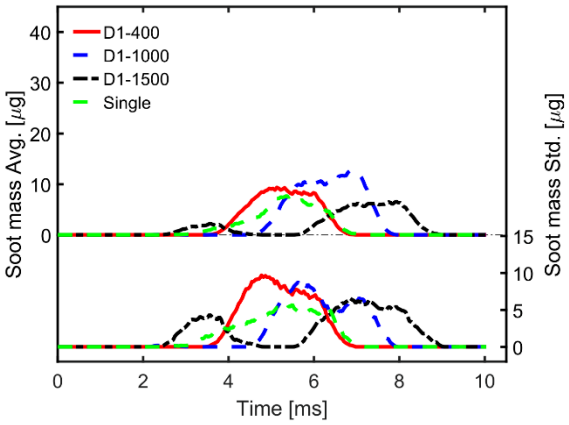

Figure 5.64. Soot mass versus time of PRF80 under 21% oxygen concentration for split injection strategies and single injection

Figure 5.64 shows the average soot mass of six tests as a function of time for the PRF80 fuel under different split injection and single injection strategies under 21% oxygen concentration.

It shows that the level of soot mass peaks follows this order: D1-1000 > D1-400 > D1-1500.

For different pilot injection times of split injection strategies and single injection, the IXT of soot mass of PRF80 fuel under a temperature of 900 K, a pressure of 60 bar and an oxygen concentration of 21% of the ambient gas is illustrated in Figure 5.65.

From the soot mass IXT, the soot initiation time and axial location of main flame for PRF80 fuel under 18% and 21% ambient oxygen are given in Table 5.8. Similar to the ignition delay and LOL of the main injection, the soot initiation time was observed to be shorter for the main flame. But the initial location was not impacted.

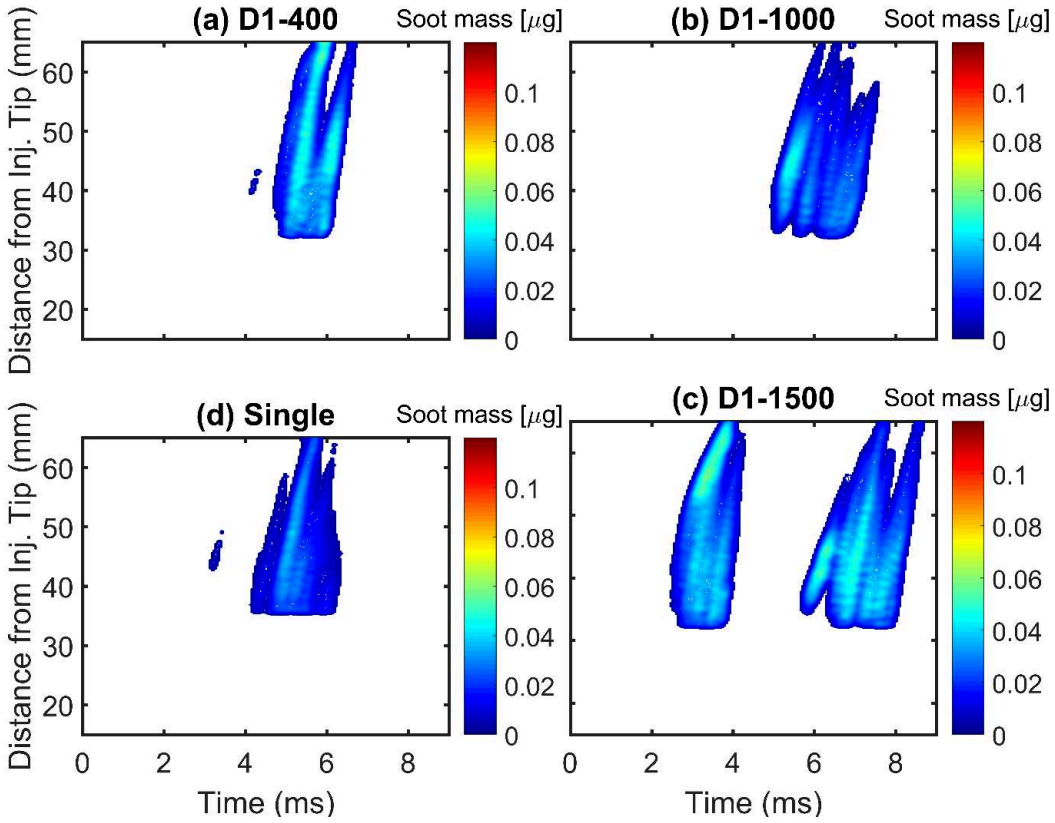

Figure 5.65. Cloud of soot mass of PRF80 fuel under ambient gas of 21% Oxygen concentration, 900 K of temperature and 60bar of pressure for single and split injections

Table 5.8. Soot initiation time and axial location of main flame for PRF80 fuel under 18% and 21% of ambient oxygen

Case	Ambient oxygen [%]	Soot initiation time [ASOC ms]	Soot initiation axial location [mm]
D1-400	18	1.5	46
	21	0.5	38
D1-1000	18	1.7	45
	21	0.8	38
D1-1500	18	1.3	40
	21	0.5	36
Single	18	2.8	46
	21	1.7	33

Two main conclusions can be drawn from the results for PRF60, PRF70 and PRF80 fuels. Consistent with previous studies [152,155], a split injection leads to a higher soot production positioned closer to the injector. Firstly, a longer pilot injection duration leads to a more diffuse combustion phase with a more consequent soot production. Secondly, the presence of local and reactive high temperature radicals caused by the pilot injection combustion promotes the

ignition of the main jet, resulting in a shorter main ignition delay and Lift-off length. The soot creation process in main flame is located in a richer region.

Another finding, the impact of the main injection on pilot soot process as promote oxidation of soot from pilot injection, by availing more oxygen to pilot flame region, for these tested fuels under split injections strategies.

5.4.2.3. Effect of oxygen concentration on soot production

The case D1-1500 is considered to evaluate the influence of oxygen concentration. It can be compared to the simple injection and other strategies.

a) PRF60 fuel

The integrated soot masses in thin radial cross-sections (1 mm) inside the jet flame of PRF60 fuel under ambient gas at 15% and 18% O_2 are plotted in Figure 5.66.

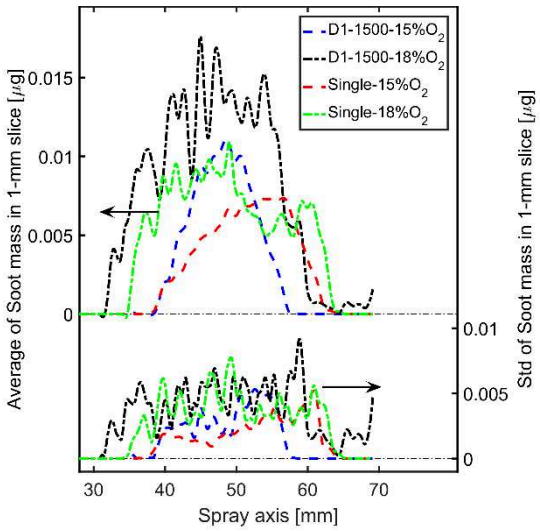

Figure 5.66. Soot mass for PRF60 fuel and various oxygen concentration of ambient gas in thin (1 mm) cross-sections of jet as a function of axis distance for single and case split injection strategy of D1-1500

At 15% oxygen, soot is located further downstream of the nozzle and the amount produced is less than the level observed at 18% oxygen. The formation time of the soot precursors is shorter when the ambient oxygen is higher [78]. Moreover, with a higher oxygen level, the air-fuel stoichiometry is more rapidly expected along the spray and thus the oxygen supply for soot oxidation is reduced. The injection strategy has a strong impact on the levels and positioning of the soot.

The spatiotemporal boundary of the soot for the two oxygen concentrations are compared in

Figure 5.67.

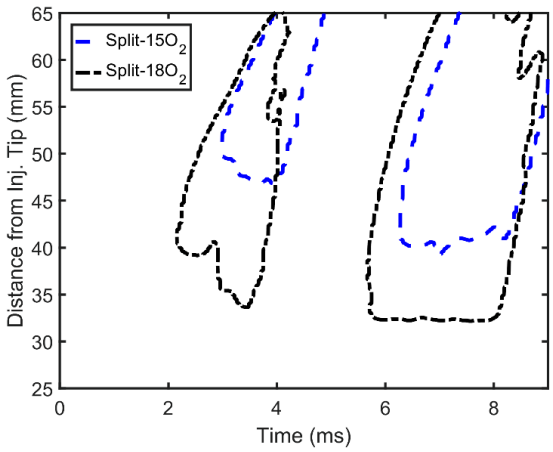

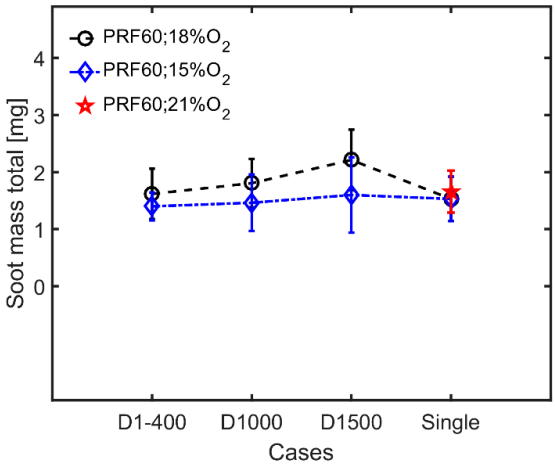

Figure 5.67. Boundary of soot mass of PRF60 fuel under ambient gas of various Oxygen concentration, 900 K of temperature and 60bar of pressure for case split injection of D1-1500

Figure 5.68. Soot mass total as a function of variation pilot injection duration for PRF60 fuel with 15, 18% (21% for single injection) Oxygen concentration of ambient gas

Figure 5.67 that the D1-1500 split injection boundary consists of two islands, one for the pilot flame and one for the main flame. The soot process is pushed downstream of the injector tip and occurs later at 15% oxygen.

Figure 5.68 shows the total soot mass as a function of pilot injection times for split strategies and single injection for PRF60 and various oxygen concentration levels (15 and 18%), including the 21% O_2 for single injection. As ambient oxygen increases, the region of soot formation and oxidation tends to move upstream, and vice versa, as we found in the previous chapter for the single injection. In other words, the oxygen entrained in the spray at the takeoff length and above is less. The impact of oxygen concentration on soot production is greater for split injection than for single injection (see Figure 5.68). With the decrease in ambient oxygen from 18% to 15%, the soot mass is reduced by about 22%, from 1.85 mg to 1.45 mg. The total soot mass is independent of the injection time.

The ambient oxygen of 15%, the soot mass observed is no significantly between difference of pilot injection duration, causing of more premixed combustion fraction of pilot and main injections, lower soot formation of main spray under the less reactive environment of pilot generated.

b) PRF70 fuel

The integrated soot masses in thin radial cross-sections (1 mm) inside the jet flame of PRF60 fuel under ambient gas at 15%, 18% and 21% O_2 are plotted in Figure 5.69. The ambient oxygen has significant impact on for PRF70 fuel, in both split and single injections. Because of higher auto-ignition resistance of PRF70 compared to PRF60, when ambient oxygen decreases to 15%, the soot mass is downstream on a low level.

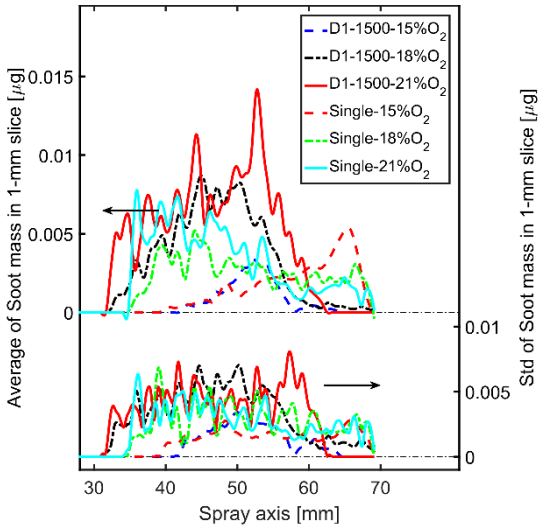

Figure 5.69. Soot mass for PRF70 fuel and various oxygen concentration of ambient gas in thin (1 mm) cross-sections of jet as a function of axis distance for single and case split injection strategy of D1-1500

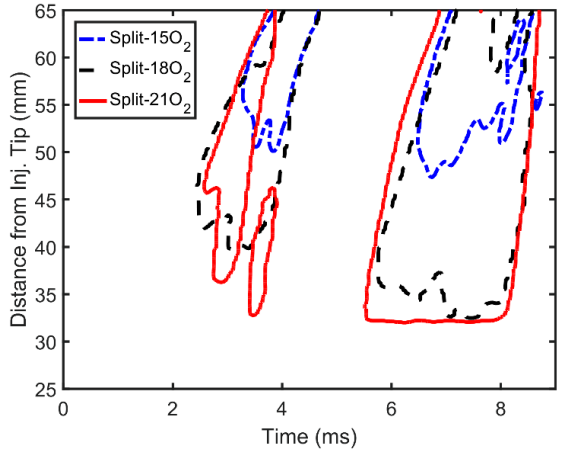

Figure 5.70. Boundary of soot mass of PRF70 fuel under ambient gas of various Oxygen concentration, 900 K of temperature and 60 bar of pressure for case D1-1500

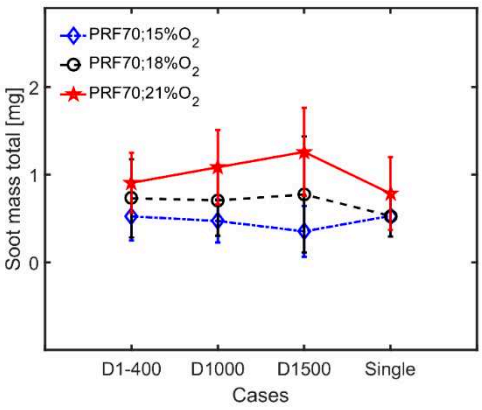

Figure 5.71. Soot mass total as a function of variation pilot injection duration for PRF70 fuel with 15, 18% and 21% Oxygen concentration of ambient gas

The spatiotemporal boundary of the soot for the tree oxygen concentrations are compared in Figure 5.70. Figure 5.70 shows that the split injection boundary consists of two islands one for pilot and the other for main flame, with soot being pushed downstream and later as ambient oxygen decreases.

Figure 5.71 shows the total soot mass as a function of pilot injection duration and the single injection case for PRF70 over different oxygen concentration levels.

The soot mass observed for split injection is higher than for single injection for 18% and 21% ambient oxygen, it is similar for 15% ambient oxygen. In the case of 21% ambient oxygen, the combustion is dominated by the diffusion phase concerning the split injections. The main injection burns in the more reactive environment generated by the pilot injection combustion generated, resulting in more soot.

The decrease in ambient oxygen from 21% to 18% and 18% to 15%, the soot mass is reduced by about 33%, from 1.05 mg to 0.7 mg, and 35% from 0.7 mg to 0.45 mg, respectively.

In conclusion, the impact of ambient oxygen on soot processes of split injections strategies for PRF60 and PRF70 fuels is the decrease in soot mass production with decrease in ambient oxygen. For higher octane number of PRF70 fuel, the effect of reduced pilot injection of the main ignition delays, the main LOL and thus the observed soot mass are lower.

5.4.2.4. Effect of octane number fuel on soot production

The spray soot mass fractions for PRF60 and PRF70 fuels under 18% O_2 condition and PRF80 under 21% O_2 condition at 2.5 ms ASOC for each pilot and main of D1-1500 case are illustrated in Figure 5.72 and Figure 5.73, respectively. The main injection of each fuel causes auto-ignition in a rich mixture zone, resulting in a higher soot concentration and larger soot formation zone.

As seen Figure 5.72 and Figure 5.73, the soot mass concentration for the pilot and main injections of PRF80 fuel appears to be less significant.

The integrated soot masses in thin (1 mm) radial cross-sections inside the jet flame of PRF60, PRF70 and PRF80 fuels under 18% (21% O_2 for PRF80) condition for case D1-1500 and single injections are shown in Figure 5.74. The cross-sectional area of the soot mass reaches its maximum at about 45-50 mm from the nozzle, and decreases with increasing fuel octane or decreasing ambient oxygen.

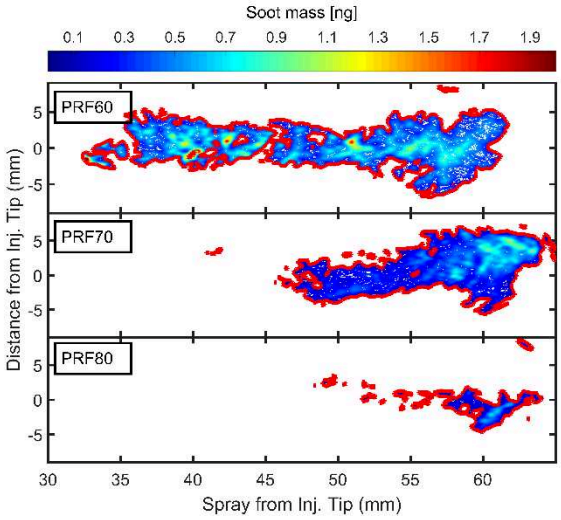

Figure 5.72. The soot mass fraction images of pilot injection for PRF60, PRF70 and PRF80 fuels, 18% (for PRF60 and PRF70), 21% (for PRF80) of oxygen concentration ambient gas for case D1-1500

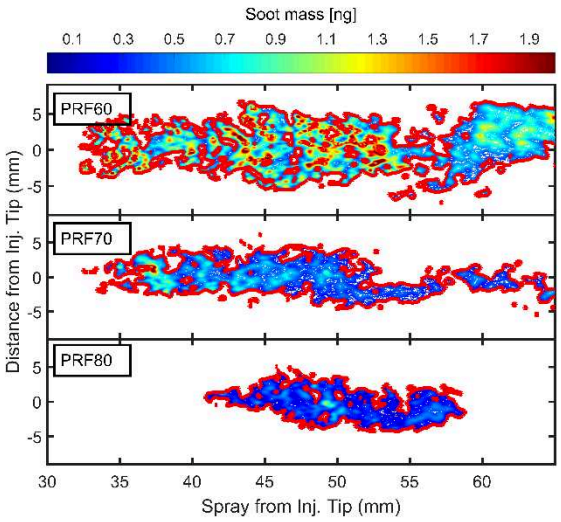

Figure 5.73. The soot mass fraction images of main injection for PRF60, PRF70 and PRF80 fuels, 18% (for PRF60 and PRF70), 21% (for PRF80) of oxygen concentration ambient gas for case D1-1500

The comparison between these tested fuels shows that the PRF60 fuel has a lower resistance ignition, hence the higher presence of reactive pilot species and their location which can lead to a high level of soot formation resulting from the main ignition in rich mixture. The higher ignition resistance, as in the case of PRF80 fuel, 18% O_2, promoted, as expected less soot production, as seen Figure 5.74 and Figure 5.75.

Figure 5.75 shows the evolution of the soot mass for case D1-1500 of split injection strategy for PRF60, PRF70 and PRF80 under 18% (21% for PRF80) ambient oxygen. The peak soot mass levels of the pilot and main injections are in order: PRF60 (18%O_2) > PRF70 (18%O_2) > PRF80 (21%O_2) > PRF80 (18%O_2). As expected, increasing fuel octane number or decreasing ambient oxygen can be reduce the soot mass production in GCI mode.

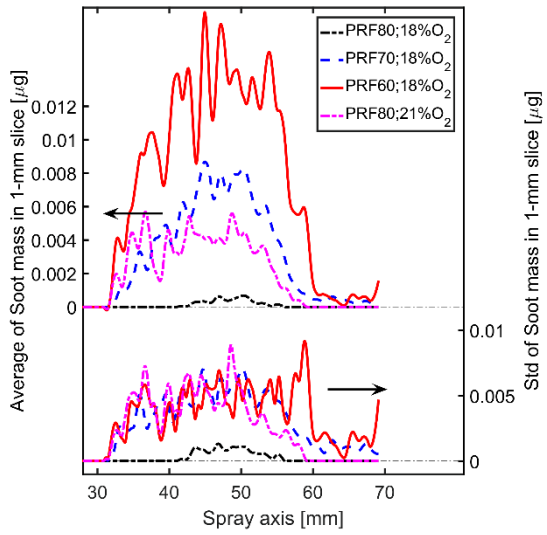

Figure 5.74. Soot mass for PRF60, PRF70 and PRF80 fuel and 18% oxygen concentration of ambient gas, including 21% for PRF80, in thin (1 mm) cross-sections of jet as a function of axis distance for case D1-1500

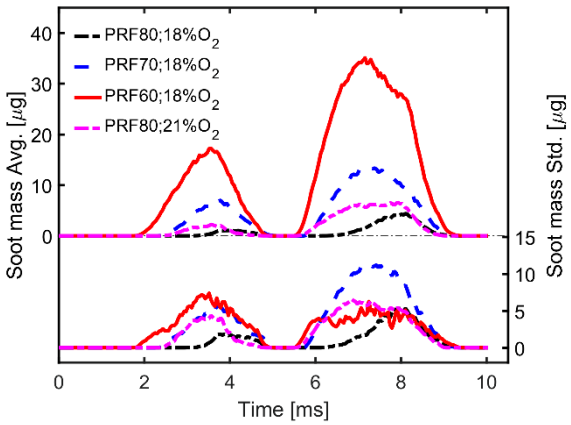

Figure 5.75. Soot mass versus time of PRF60, PRF70 and PRF80 under 18% (21% for PRF80) oxygen concentration for case D1-1500 of split injection strategy

The comparison the boundary of IXT of soot between the of PRF60 and PRF70 fuels under 18% oxygen concentration of ambient gas for the case of D1-1500 of split injection strategies, are shown in Figure 5.76. The soot region is closer to the nozzle for the lower octane fuels, as seen in the pilot boundary for PRF60 and PRF70 fuels. The PRF80 fuel has a single island, which appears later and farther from nozzle than that of PRF60 and PRF70 fuels.

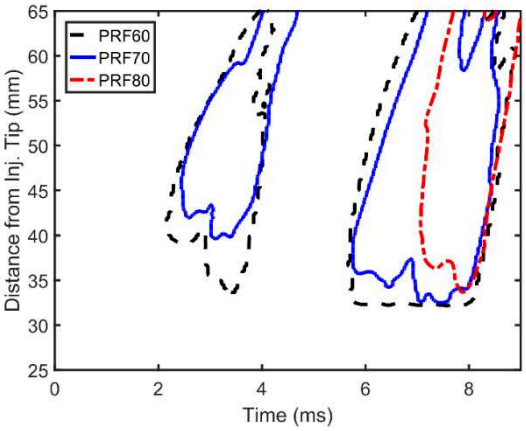

Figure 5.76. Boundary of soot mass of PRF60, PRF70 and PRF80 fuels under ambient gas of 18% Oxygen concentration,

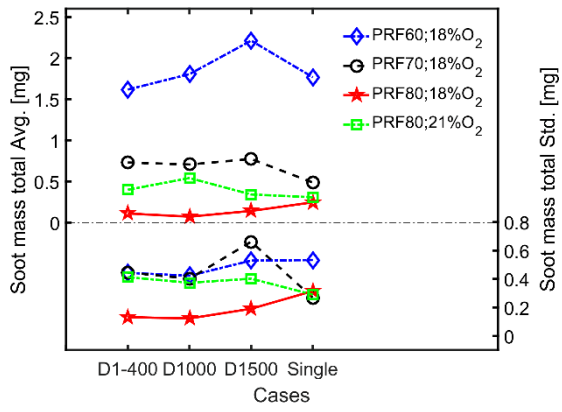

Figure 5.77. Soot mass total as a function of variation pilot injection duration for PRF60, PRF70 and PRF80 fuels with 18%

900 K of temperature and 60bar of pressure for case split injection strategy of D1-1500

(21% for PRF80) Oxygen concentration of ambient gas

Figure 5.77 shows the total soot mass as a function of pilot injection duration for the split injection and single injection strategies for the PRF60, PRF70, and PRF80 fuels under an oxygen concentration of 18%, and 21% O_2 for PRF80.

As in the similar case of D1-1500, the effects of the pilot injection variation on the soot mass production can be ranked as: PRF60 (18%O_2) > PRF70 (18%O_2) > PRF80 (21%O_2) > PRF80 (18%O_2). Under 18% O_2, PRF80 with a split injection strategy has the advantage of a very low soot mass level, lower than that of single injection. This is due to more premixed type combustion in a leaner mixture.

As shown in Figure 5.77, the PRF60 fuel case is characterized by the highest soot mass, with this mass increasing with the amount of fuel injected during pilot injection.

In conclusion, high octane or low cetane fuels tend to have a greater resistance to auto-ignition behavior, thus more time for air-fuel mixing leading to the reduction of soot mass, similar to the single injection flames of the previous chapter, which can be extended to split injection strategies [157]. PRF80 fuel with a higher octane rating has longer ignition delays and LOLs. This fuel was found to have less than 18% oxygen a lower soot concentration for the split injection strategy.

5.4.3. Conclusions

Soot mass total as a function of Lift off length for 3 fuels (PRF60, PRF70 and PRF80) and 3 oxygen concentration levels (15, 18 and 21%), under 3 cases of pilot injection duration, is plotted in Figure 5.78.

We have discussed in previous sections, the relationships between auto-ignition behavior and lift-off length flame, soot process under various pilot injection duration, ambient oxygen and fuel octane number. In this section, observations are provided of the relationship between lift-off length and soot in a gasoline fuel jet.

Figure 5.78 clearly shows a general trend of decreasing soot mass with increasing LOL, or decreasing the ambient oxygen or increasing the fuel octane number, under three split injections strategies. This trend for main injection is similar to the trend for single injection that

was demonstrated in the previous chapter.

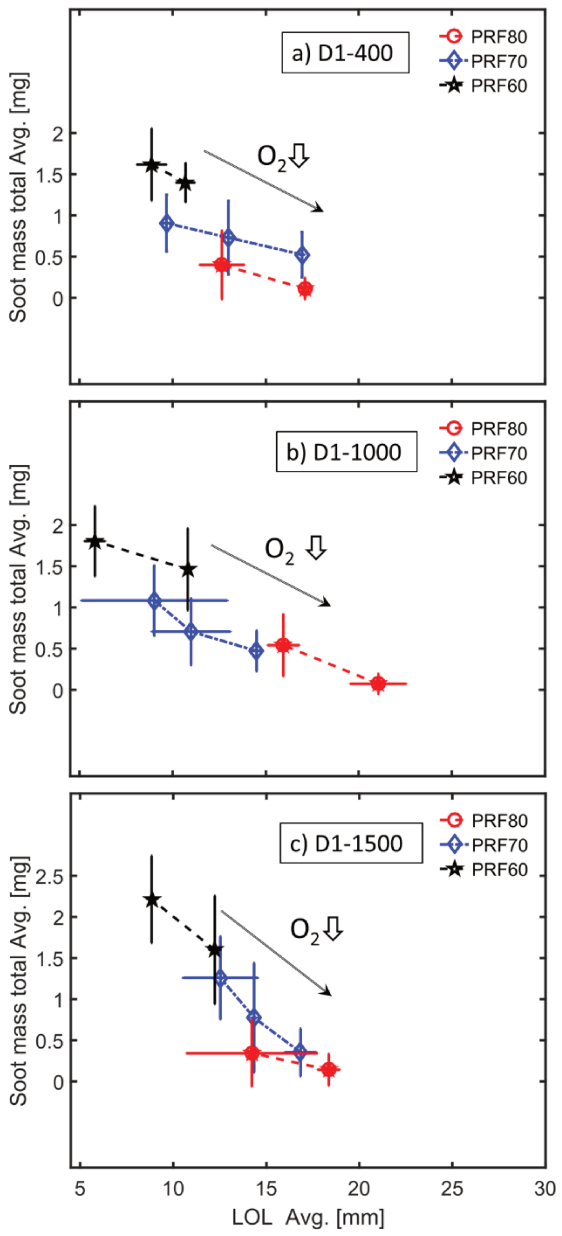

Figure 5.78. The trend of soot mass total versus LOL for PRF60, PRF70, PRF80 fuels with various Oxygen concentration of ambient gas, under three cases injections strategies

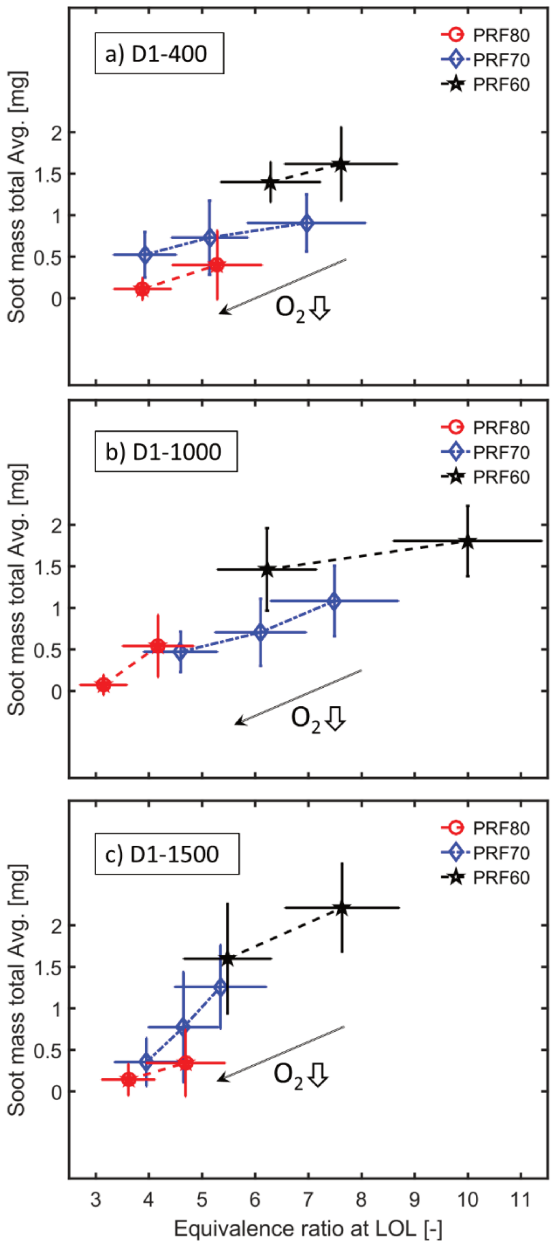

Figure 5.79. The trend of soot mass total versus equivalence ratio at LOL for PRF60, PRF70, PRF80 fuels with various Oxygen concentration of ambient gas, under three cases injections strategies

The shorter Lift-Off length of main flames than the pilot flames is one reasons for faster and higher soot formation that takes place in rich air-fuel mixture regions [151].

For all three cases, the sensitivity of the LOL impact on soot mass is ranked as follows: D1-

400 < D1-1000 < D1-1500. The higher fraction of premixed combustion occurring in the pilot coupled with more oxygen entrained in the main flame at a shorter pilot injection duration may explain this order. Moreover, the longer pilot injection duration, the more the propagation towards the upstream nozzle leads to a pilot flame region closer to the injector tip, thus less oxygen entrained in the main injection promoting the soot formation process.

The PRF80 fuel shows that soot mass is substantially reduced to a very low level in all case of split injection strategies and under both ambient oxygen condition, due to better fuel-air mixing.

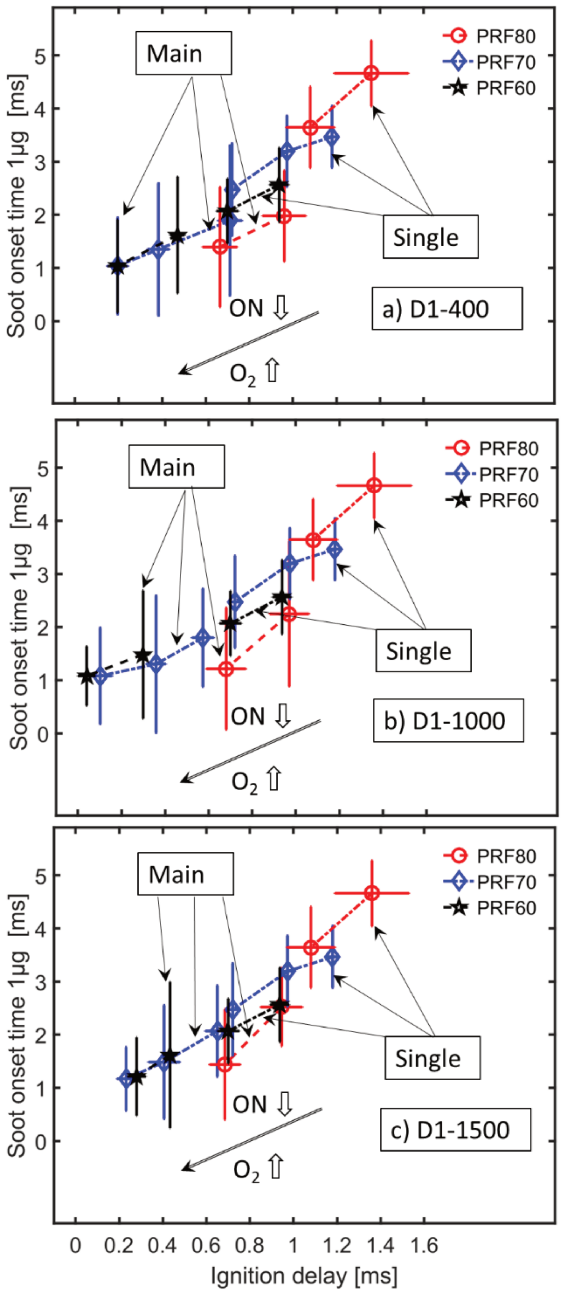

Figure 5.80. Soot onset time 1 µg as a function of ignition delay for main and single injections of PRF60, PRF70 and PRF80 under ambient oxygen variation

Figure 5.80 gives the soot onset time 1 µg as a function of ignition delay for single injection and main injection with different pilot amounts of PRF60, PRF70 and PRF80 under various ambient oxygen. The soot onset time of the main flame is earlier than that of single flame for these tested fuels and ambient condition, as expected. The pilot injection duration does not appear to have an impact on the soot onset time for tested each case. In agreement with previous results with a single injection, increasing ambient oxygen or decreasing fuel octane number

leads to an earlier soot onset time.

The main results of this chapter are summarized in Table 5.9, Table 5.10, Table 5.11 and Table 5.12.

Table 5.9. Summary pilot and main Ignition delays under D1-1500 case

Fuel	**Pilot ignition delays (ms)**			**Main ignition delays (ms)**		
	$15\%O_2$	$18\%O_2$	$21\%O_2$	$15\%O_2$	$18\%O_2$	$21\%O_2$
PRF60	0.94 (±0.04)	0.70 (±0.04)	-	0.43 (±0.02)	0.30 (±0.02)	-
PRF70	1.20 (±0.06)	0.98 (±0.05)	0.73 (±0.05)	0.65 (±0.02)	0.39 (±0.02)	0.25 (±0.02)
PRF80	1.60 (±0.05)	1.35 (±0.06)	1.08 (±0.06)	1.17 (±0.02)	0.95 (±0.02)	0.68 (±0.02)
Bu20	-	1.86 (±0.06)	1.65 (±0.06)	-	1.05 (±0.06)	0.80 (±0.06)
ABE20	-	1.83 (±0.10)	1.51 (±0.06)	-	1.22 (±0.06)	0.90 (±0.06)

Table 5.10. Summary Main Lift off length under D1-1500 case

Fuel	**Main Lift off length (mm)**			**Equivalence ratio at LOL**		
	$15\%O_2$	$18\%O_2$	$21\%O_2$	$15\%O_2$	$18\%O_2$	$21\%O_2$
PRF60	12.2 (±0.3)	8.8 (±0.1)	-	5.5 (±0.8)	7.6 (±0.9)	-
PRF70	16.8 (±0.9)	14.3 (±0.2)	12.5 (±2.0)	4.0 (±0.5)	4.6 (±0.6)	5.3 (±0.8)
PRF80	-	18.4 (±0.6)	14.2 (±3.5)	-	3.6 (±0.5)	4.7 (±0.5)
Bu20	-	22.1 (±1.3)	21.5 (±0.6)	-	2.7 (±0.3)	3.1 (±0.4)
ABE20	-	23.5 (±0.6)	22.2 (±1.1)	-	2.6 (±0.3)	2.7 (±0.4)

Table 5.11. Summary soot mass total for split injection strategy

Fuel	**Soot mass total (mg)**								
	D1-400			**D1-1000**			**D1-1500**		
	$15\%O_2$	$18\%O_2$	$21\%O_2$	$15\%O_2$	$18\%O_2$	$21\%O_2$	$15\%O_2$	$18\%O_2$	$21\%O_2$
PRF60	1.40 (±0.24)	1.62 (±0.44)	-	1.46 (±0.50)	1.81 (±0.42)	-	1.66 (±0.37)	2.21 (±0.53)	-
PRF70	0.52 (±0.22)	0.73 (±0.44)	0.91 (±0.29)	0.47 (±0.24)	0.71 (±0.40)	1.08 (±0.42)	0.35 (±0.28)	0.77 (±0.66)	1.26 (±0.50)

PRF80	-	0.11 (±0.13)	0.40 (±0.41)	-	0.07 (±0.12)	0.54 (±0.37)	-	0.14 (±0.19)	0.34 (±0.40)

Table 5.12. Summary soot onset time 1 µg for split injection strategy

Fuel	**Soot onset time 1 µg (ms)**								
	D1-400			**D1-1000**			**D1-1500**		
	15%O_2	18%O_2	21%O_2	15%O_2	18%O_2	21%O_2	15%O_2	18%O_2	21%O_2
PRF60	1.62 (±0.55)	1.04 (±0.44)	-	1.49 (±0.50)	1.08 (±0.23)	-	1.62 (±0.37)	1.21 (±0.35)	-
PRF70	1.89 (±0.70)	1.35 (±0.67)	1.04 (±0.45)	1.80 (±0.48)	1.31 (±0.64)	1.08 (±0.45)	2.07 (±0.42)	1.49 (±0.50)	1.17 (±0.30)
PRF80	-	1.98 (±0.43)	1.40 (±0.56)	-	2.25 (±0.73)	1.22 (±0.57)	-	2.52 (±0.37)	1.44 (±0.57)
Fuel	**Soot onset time 1 µg (ASOC ms)**								
	D1-400			**D1-1000**			**D1-1500**		
	15%O_2	18%O_2	21%O_2	15%O_2	18%O_2	21%O_2	15%O_2	18%O_2	21%O_2
PRF60	1.21	0.66	-	1.06	0.62	-	1.19	0.91	-
PRF70	0.69	0.37	0.31	0.60	0.33	0.35	0.87	0.51	0.44
PRF80	-	1.03	0.72	-	1.30	0.54	-	1.57	0.76

A split injection strategy with different pilot injection durations was adopted with PRF60, PRF70, PRF80, Bu20 and ABE20 as fuels, under various ambient oxygen, some more detailed conclusions may be drawn as well:

- The auto-ignition delay and flame lift off length were improved for main injection for all tested fuel and split injection strategy, but promoting higher soot mass production for PRF60 and PRF70 fuels. The benefits of higher fuel octane number, such as PRF80 fuels, under split injections are early ignition compared to a single injection and very low soot production regardless of the pilot amount injected.

- The impact of ambient oxygen and fuel octane number on ignition delay and lift-off length was observed for the main injection. Hence, the auto-ignition and lift-off length of the main injection are mainly influence the soot production process.

- The pilot quantity significantly affects the soot mass production for PRF60 fuel at 18% ambient oxygen condition, but the trends for PRF70 and PRF80 fuels at 15%, 18% and 21% ambient oxygen condition are not well defined.

5.5. Conclusions

In current chapter, the split injections generating spray-flame were investigated for gasoline fuels under GCI conditions of high temperature and high pressure. Detailed results were analyzed based on the inert conditions (mass flow rate, liquid length and spray vapor penetration), reactive conditions (Heat release rate, ignition delay and lift-off length) and soot production process.

The conclusion of this chapter is summarized as follows:

*) For the mass flow rate measurement of split injection strategies, the pilot and main injection have similar peak velocity for each tested fuel.

*) For inert condition, the liquid and vapor spray penetrations of the main spray are faster with higher momentum than pilot injection, which helps to well air-fuel mixing of main injection. This behavior is noticed for all tested fuels and its sensitivity does not depend on the blend tested fuels.

*) For the reactive condition, HRR profile showed two stages for each injection time for low octane number, especially, the HRR profile showed a one-stage combustion when the fuel octane number is high, or when ambient oxygen is low.

- Ignition delays of main injection were reduced for these ambient oxygen conditions and these tested fuels, as expected due to the high temperature of burned gas of pilot injection or reactive species in the low temperature reaction behavior.

*) For the soot mass measurement, the soot mass was reduced for the pilot and main when fuel octane number is higher, or when ambient oxygen is low, due to a longer mixing period. In the case of PRF80 fuel, the soot concentration was significantly reduced under 18% ambient oxygen. The main auto-ignition improvement is achieved in case of low ambient oxygen for high fuel octane number of blends with PRF80 base fuel, such as Bu20 and ABE20, with ultra-low soot production. However, for lower fuel octane number, such as PRF60 and PRF70, the ignition and Lift-off length of main injection shift upstream, resulting in more upstream soot formation and higher soot production.

Based on the results obtained with split injection strategy with gasoline sprays, this more efficient mixing of main injection with higher momentum, combined with the presence of species from the combustion reaction of the pilot injection promotes ignition of the main injection and the flame approaches the nozzle, which is observed for all tested fuels. Thus, the

trends observed as a function of fuel type are the same regardless the injection strategy and single injection.

CONCLUSION

This section aims to summarize the main conclusions and important contributions of this PhD thesis. Some recommendations for future work are provided also.

The understanding the physicochemical phenomena on spray for gasoline type fuel under high temperature-high pressure conditions, including the chemical on HCCI mode, in term of bio-alcohols fuel characterization is still required to optimize the use of bio-fuels for clean ICE

The results of the investigation of the effects of Ethanol, Butanol and ABE blends on chemical properties of PRF80 based fuel in HCCI combustion mode show the great potential of these biofuels to contribute to decrease global CO_2. The experiment results suggest that alcohols fuels, especially ethanol and n-butanol, but also ABE are promising alternative fuel for HCCI combustion mode. Then, a parametric study investigating the effects of several control parameters, such as intake temperature, intake pressure, equivalence ratio, EGR ratio, fuel properties on the combustion characteristics of HCCI combustion mode was performed.

The Ethanol, Butanol and ABE blends with PRF80 were investigated the mixing, ignition and combustion behavior in an optically accessible New One Shot Engine under GCI relevant conditions with single and split injections. The results of single injection, the slight difference of mass flow rate, the longer liquid length with higher blends fraction, and similar vapor spray penetrations were first provided. The longer auto-ignition delay and LOL with higher blends fraction can improved the fuel-air mixing, combustion efficiency and reduction soot production, as expected.

The results of split injection strategies, the longer liquid length and spray vapor penetration are observed for the main injection under inert and reactant conditions. The auto-ignition occurs earlier when the LOL is shortened for main injection, induce higher equivalence ratios at the LOL and hence, higher soot formation.

This PhD work is the first one where systematically the global strategies of injection condition for gasoline type fuel for Compression Ignition combustion mode were identified, including the fuel-air mixing control, the combustion and the soot production.

From these measurements, a database was developed that can help improve the accuracy of CFD modelling and the design of multiple injection strategies especially in the case of bio-fuels, such as ethanol, n-butanol and ABE. The results showed a promising future for ABE-

gasoline mixture as an alternative transportation fuel, with lower cost of ABE production. Some key features of ABE-gasoline mixture for LTC mode are following:

- Overall longer ignition delays of both single and main injections lead to the increase of the premixed combustion phase fraction

- The longer LOL of both single and main injections lead to leaner mixture at auto-ignition region, hence soot concentration would be lower.

Based on the research mentioned in this thesis, the following recommendations can be made:

- The investigation will look into conditions similar to wall-spray, the knowledge will give an expanded view on closer engine-relevant condition. Addition, the metal and optical engine experiments would be conducted to confirm some tendencies, first identified or assumed in this thesis.

- The engine performance and emissions under GCI mode with ABE60 has to be investigated in comparison to pure gasoline.

- The other alcohols with higher reactivity, viscosity and energy density, which contain more carbon atoms in molecule, such as heptane and octane, could be blended also in gasoline and require investigation under GCI combustion mode.

REFERENCE

[1] Wu M, Wang M, Liu J, Huo H. Review : Bioseparations and Assessment of Potential Life-Cycle Energy and Greenhouse Gas Emission Effects. Biotechnol Prog 2008:1204–14. https://doi.org/10.1021/bp.71.

[2] Summary SPM for Policymakers n.d. https://www.ipcc.ch/site/assets/uploads/2018/02/WG1AR5_SPM_FINAL.pdf.

[3] https://data.giss.nasa.gov/gistemp/ n.d.

[4] Rhodes JS, Keith DW. Biomass with capture: Negative emissions within social and environmental constraints: An editorial comment. Clim Change 2008. https://doi.org/10.1007/s10584-007-9387-4.

[5] Roser HR and M. CO_2 and Greenhouse Gas Emissions n.d. https://ourworldindata.org/grapher/global-carbon-dioxide-emissions-by-sector.

[6] McKinsey & Company. Global Energy Perspective 2019 : Reference Case. Energy Insights 2019:31.

[7] Hubbert peak theory n.d. https://en.wikipedia.org/wiki/Hubbert_peak_theory.

[8] Stanton DW. Systematic Development of Highly Efficient and Clean Engines to Meet Future Commercial Vehicle Greenhouse Gas Regulations. SAE Int J Engines 2013;6:1395–480. https://doi.org/10.4271/2013-01-2421.

[9] Yao M, Zheng Z, Liu H. Progress and recent trends in homogeneous charge compression ignition (HCCI) engines. Prog Energy Combust Sci 2009. https://doi.org/10.1016/j.pecs.2009.05.001.

[10] Saxena S, Bedoya ID. Fundamental phenomena affecting low temperature combustion and HCCI engines, high load limits and strategies for extending these limits. Prog Energy Combust Sci 2013. https://doi.org/10.1016/j.pecs.2013.05.002 Review.

[11] Musculus MPB, Miles PC, Pickett LM. Conceptual models for partially premixed low-temperature diesel combustion. Prog Energy Combust Sci 2013. https://doi.org/10.1016/j.pecs.2012.09.001.

[12] Tuner M. Review and Benchmarking of Alternative Fuels in Conventional and

Advanced Engine Concepts with Emphasis on Efficiency, CO2, and Regulated Emissions. SAE Tech. Pap., 2016. https://doi.org/10.4271/2016-01-0882.

[13] Dernotte J, Mounaim-Rousselle C, Halter F, Seers P. Évaluation De Mélange Butanol-Essence Dans Un Moteur À Allumage Commandé À Injection Indirecte. Oil Gas Sci Technol 2010;65:345–51. https://doi.org/10.2516/ogst/2009034.

[14] Yu X, Guo Z, He L, Dong W, Sun P, Shi W, et al. Effect of gasoline / n-butanol blends on gaseous and particle emissions from an SI direct injection engine. Fuel 2018;229:1–10. https://doi.org/10.1016/j.fuel.2018.05.003.

[15] Nithyanandan K, Zhang J, Li Y, Wu H, Lee TH, Lin Y, et al. Improved SI engine efficiency using Acetone-Butanol-Ethanol (ABE). Fuel 2016;174:333–43. https://doi.org/10.1016/j.fuel.2016.01.001.

[16] Ribeiro MD, Bimbato AM, Zanardi MA. a preliminary study on simulations of a single jet from the ECN " spray g " test case 2016.

[17] Kuo KK, Acharya R. Fundamentals of Turbulent Multi-Phase Combustion. 2012. https://doi.org/10.1002/9781118107683.

[18] Bjørgen KOP. Optical Study of Soot Characteristics of Biofuel Spray Combustion. 2019.

[19] Espey C, Dec JE. The effect of TDC temperature and density on the liquid-phase fuel penetration in a D. I. diesel engine. SAE Tech Pap 1995. https://doi.org/10.4271/952456.

[20] Siebers DL. Liquid-phase fuel penetration in diesel sprays. SAE Tech Pap 1998. https://doi.org/10.4271/980809.

[21] Senecal PK, Pomraning E, Richards KJ, Briggs TE, Choi CY, McDavid RM, et al. Multi-dimensional modeling of direct-injection diesel spray liquid length and flame lift-off length using cfd and parallel detailed chemistry. SAE Tech Pap 2003. https://doi.org/10.4271/2003-01-1043.

[22] dos Santos F, le Moyne L. Spray atomization models in engine applications, from correlations to direct numerical simulations. Oil Gas Sci Technol 2011;66:801–22. https://doi.org/10.2516/ogst/2011116.

[23] Yue Z, Reitz RD. An equilibrium phase spray model for high-pressure fuel injection and

engine combustion simulations. Int J Engine Res 2017;20:203–15. https://doi.org/10.1177/1468087417744144.

[24] Browne KR, Partridge IM, Greeves G. Fuel Property Effects on Fuel/Air Mixing in an Experimental Diesel Engine 1986. https://doi.org/10.4271/860223.

[25] Higgins B, Siebers D, Mueller C, Aradi A. Effects of an ignition-enhancing, diesel-fuel additive on diesel-spray evaporation, mixing, ignition, and combustion. Symp. Combust., 1998. https://doi.org/10.1016/S0082-0784(98)80030-1.

[26] Canaan RE, Dec JE, Green RM, Daly DT. The influence of fuel volatility on the liquid-phase fuel penetration in a heavy-duty D.I. Diesel engine. SAE Tech Pap 1998. https://doi.org/10.4271/980510.

[27] Dernotte, J. F. Foucher, C. Hespel, C. Mounaim-Rouselle SH. Influence of fuel properties on the spray development characteristics in a Diesel optical access engine. 10th Int. Symp. Combust. Diagnostics, 2012, p. 6–13.

[28] Matsuoka H, Yamashita H, Hayashi T, Kitano K. Effects of fuel properties on diesel spray behavior under high temperature and high pressure conditions. SAE Tech Pap 2009. https://doi.org/10.4271/2009-01-0834.

[29] Higgins BS, Mueller CJ, Siebers DL. Measurements of fuel effects on liquid-phase penetration in di sprays 1. SAE Tech Pap 1999. https://doi.org/10.4271/1999-01-0519.

[30] Pastor J V., García-Oliver JM, Nerva JG, Giménez B. Fuel effect on the liquid-phase penetration of an evaporating spray under transient diesel-like conditions. Fuel 2011;90:3369–81. https://doi.org/10.1016/j.fuel.2011.05.006.

[31] Kook S, Pickett LM. Liquid length and vapor penetration of conventional, Fischer-Tropsch, coal-derived, and surrogate fuel sprays at high-temperature and high-pressure ambient conditions. Fuel 2012;93:539–48. https://doi.org/10.1016/j.fuel.2011.10.004.

[32] Chehroudi B, Chen SH, Bracco F V., Onuma Y. On the intact core of full-cone sprays. SAE Tech. Pap., 1985. https://doi.org/10.4271/850126.

[33] Beale JC, Reitz RD. Modeling Spray Atomization with the Kelvin-Helmholtz/Rayleigh-Taylor Hybrid Model. At Sprays 1999;9:623–50.

[34] Su TF, Patterson MA, Reitz RD, Farrell P V. Experimental and numerical studies of

high pressure multiple injection sprays. SAE Tech. Pap., 1996. https://doi.org/10.4271/960861.

[35] Hiroyasu H, Arai M. Structures of fuel sprays in diesel engines. SAE Tech. Pap., 1990. https://doi.org/10.4271/900475.

[36] Siebers DL. Scaling liquid-phase fuel penetration in diesel sprays based on mixing-limited vaporization. SAE Tech Pap 1999. https://doi.org/10.4271/1999-01-0528.

[37] López JJ, García-Oliver JM, García A, Domenech V. Gasoline effects on spray characteristics, mixing and auto-ignition processes in a CI engine under Partially Premixed Combustion conditions. Appl Therm Eng 2014;70:996–1006. https://doi.org/10.1016/j.applthermaleng.2014.06.027.

[38] Payri R, Garcia-Oliver JM, Manin J, Bardi M. Fuel temperature influence on Diesel sprays in reacting conditions. ILASS-Americas 23rd Annu Conf Liq At Spray Syst 2011.

[39] WAKURI Y, FUJII M, AMITANI T, TSUNEYA R. Studies on the Penetration of Fuel Spray of Diesel Engine. Trans Japan Soc Mech Eng 1959;25:820–6. https://doi.org/10.1299/kikai1938.25.820.

[40] Dent JC. A basis for the comparison of various experimental methods for studying spray penetration. SAE Tech. Pap., 1971. https://doi.org/10.4271/710571.

[41] Levich VG. Physicochemical Hydrodynamics. Prentice-Hall; 1962.

[42] Schihl P, Bryzik W, Atreya A. Analysis of current spray penetration models and proposal of a phenomenological cone penetration model. SAE Tech. Pap., 1996. https://doi.org/10.4271/960773.

[43] Arrègle J, Pastor J V., Ruiz S. The influence of injection parameters on diesel spray characteristics. SAE Tech. Pap., 1999. https://doi.org/10.4271/1999-01-0200.

[44] Naber JD, Siebers DL. Effects of gas density and vaporization on penetration and dispersion of diesel sprays. SAE Tech. Pap., SAE International; 1996. https://doi.org/10.4271/960034.

[45] Pastor JM V., Javier López J, García JM, Pastor JM V. A 1D model for the description of mixing-controlled inert diesel sprays. Fuel 2008;87:2871–85. https://doi.org/10.1016/j.fuel.2008.04.017.

[46] Bruneaux G. Combustion structure of free and wall-impinging diesel jets by simultaneous laser-induced fluorescence of formaldehyde, poly-aromatic hydrocarbons, and hydroxides. Int J Engine Res 2008. https://doi.org/10.1243/14680874JER00108.

[47] Assanis DN, Filipi ZS, Fiveland SB, Syrimis M. A predictive ignition delay correlation under steady-state and transient operation of a direct injection diesel engine. J Eng Gas Turbines Power 2003. https://doi.org/10.1115/1.1563238.

[48] Payri R, Salvador FJ, De la Morena J, Pagano V. Using a one-dimensional spray model to improve liquid length and ignition delay estimations for diesel flames. Appl Therm Eng 2017;124:1090–102. https://doi.org/10.1016/j.applthermaleng.2017.06.102.

[49] Liu Y, Yuan Z, Ma Y, Fu J, Huang R, Liu J. Analysis of spray combustion characteristics of diesel, biodiesel and their n-pentanol blends based on a one-dimensional semi-phenomenological model. Appl Energy 2019;238:996–1009. https://doi.org/10.1016/j.apenergy.2019.01.176.

[50] Burgess CP, Lawn CJ. The premixture model of turbulent burning to describe lifted jet flames. Combust Flame 1999;119:95–108. https://doi.org/10.1016/S0010-2180(99)00037-1.

[51] Peters N. Turbulent Combustion. 2000. https://doi.org/10.1017/cbo9780511612701.

[52] Siebers D, Higgins B. Flame lift-off on direct-injection diesel sprays under quiescent conditions. SAE Tech Pap 2001. https://doi.org/10.4271/2001-01-0530.

[53] Siebers D, Higgins B, Pickett L. Flame lift-off on direct-injection diesel fuel jets: Oxygen concentration effects. SAE Tech. Pap., 2002. https://doi.org/10.4271/2002-01-0890.

[54] Tagliante-saracino F. Combined study by direct numerical simulation and optical diagnostics of the flame stabilization in a Diesel spray. 2019.

[55] Higgins B, Siebers D. Measurement of the flame lift-off location on di diesel sprays using OH chemiluminescence. SAE Tech. Pap., 2001. https://doi.org/10.4271/2001-01-0918.

[56] Payri R, García A, Domenech V, Durrett R, Plazas AH. An experimental study of gasoline effects on injection rate, momentum flux and spray characteristics using a

common rail diesel injection system. Fuel 2012. https://doi.org/10.1016/j.fuel.2011.11.065.

[57] Payri R, Viera JP, Gopalakrishnan V, Szymkowicz PG. The effect of nozzle geometry over ignition delay and flame lift-off of reacting direct-injection sprays for three different fuels. Fuel 2017;199:76–90. https://doi.org/10.1016/j.fuel.2017.02.075.

[58] Payri R, Salvador FJ, Gimeno J, Peraza JE. Experimental study of the injection conditions influence over n-dodecane and diesel sprays with two ECN single-hole nozzles. Part II: Reactive atmosphere. Energy Convers Manag 2016;126:1157–67. https://doi.org/10.1016/j.enconman.2016.07.079.

[59] Payri R, Salvador FJ, Manin J, Viera A. Diesel ignition delay and lift-off length through different methodologies using a multi-hole injector. Appl Energy 2016;162:541–50. https://doi.org/10.1016/j.apenergy.2015.10.118.

[60] Persson H, Andersson Ö, Egnell R. Fuel effects on flame lift-off under diesel conditions. Combust Flame 2011;158:91–7. https://doi.org/10.1016/j.combustflame.2010.07.020.

[61] Musculus MPB. Effects of the in-cylinder environment on diffusion flame lift-off in a di diesel engine. SAE Tech. Pap., 2003. https://doi.org/10.4271/2003-01-0074.

[62] Rusly AM, Le MK, Kook S, Hawkes ER. The shortening of lift-off length associated with jet-wall and jet-jet interaction in a small-bore optical diesel engine. Fuel 2014;125:1–14. https://doi.org/10.1016/j.fuel.2014.02.004.

[63] Lequien G, Li Z, Andersson O, Richter M. Lift-Off Length in an Optical Heavy-Duty Diesel Engine: Effects of Swirl and Jet-Jet Interactions. SAE Int J Engines 2015. https://doi.org/10.4271/2015-24-2442.

[64] Pickett LM, Siebers DL, Idicheria CA. Relationship between ignition processes and the lift-off length of diesel fuel jets. SAE Tech Pap 2005. https://doi.org/10.4271/2005-01-3843.

[65] Pastor J V., Garcia-Oliver JM, Lopez JJ, Vera-Tudela W. An experimental study of the effects of fuel properties on reactive spray evolution using Primary Reference Fuels. Fuel 2016;163:260–70. https://doi.org/10.1016/j.fuel.2015.09.064.

[66] Lundgren M, Matamis A, Wang Z, Garcia Valladolid P, Richter M, Andersson O, et al.

Lift-Off Lengths in an Optical Heavy-Duty Engine Operated at High Load with Low and High Octane Number Fuels. SAE Tech Pap 2018;2018-April:1–9. https://doi.org/10.4271/2018-01-0245.

[67] Kitamura T, Ito T, Kitamura Y, Ueda M, Senda J, Fujimoto H. Soot kinetic modeling and empirical validation on smokeless diesel combustion with oxygenated fuels. SAE Tech. Pap., 2003. https://doi.org/10.4271/2003-01-1789.

[68] Westbrook CK, Pitz WJ, Curran HJ. Chemical kinetic modeling study of the effects of oxygenated hydrocarbons on soot emissions from diesel engines. J Phys Chem A 2006. https://doi.org/10.1021/jp056362g.

[69] Manin J, Skeen S, Pickett L, Kurtz E, Anderson JE, Manin, J., Skeen, S., Pickett, L., Kurtz, E., & Anderson JE. Effects of Oxygenated Fuels on Combustion and Soot Formation/Oxidation Processes. SAE Int J Fuels Lubr 2014;7:704–17. https://doi.org/10.4271/2014-01-2657.

[70] Jain SK, Aggarwal SK. Compositional effects on the ignition and combustion of low octane fuels under diesel conditions. Fuel 2018;220:654–70. https://doi.org/10.1016/j.fuel.2018.02.015.

[71] Smith OI. Fundamentals of soot formation in flames with application to diesel engine particulate emissions. Prog Energy Combust Sci 1981. https://doi.org/10.1016/0360-1285(81)90002-2.

[72] Manin J, Pickett LM, Skeen SA. Two-Color Diffused Back-Illumination Imaging as a Diagnostic for Time-Resolved Soot Measurements in Reacting Sprays. SAE Int J Engines 2013;6. https://doi.org/10.4271/2013-01-2548.

[73] Xuan T, Desantes JM, Pastor J V., Garcia-Oliver JM. Soot temperature characterization of spray a flames by combined extinction and radiation methodology. Combust Flame 2019:290–303. https://doi.org/10.1016/j.combustflame.2019.03.023.

[74] Skeen SA, Manin J, Pickett LM, Cenker E, Bruneaux G, Kondo K, et al. A Progress Review on Soot Experiments and Modeling in the Engine Combustion Network (ECN). SAE Int J Engines 2016;9. https://doi.org/10.4271/2016-01-0734.

[75] Westlye FR, Penney K, Ivarsson A, Pickett LM, Manin J, Skeen SA. Diffuse back-illumination setup for high temporally resolved extinction imaging. Appl Opt

2017;56:5028. https://doi.org/10.1364/ao.56.005028.

[76] Frenklach M, Wang H. Detailed Mechanism and Modeling of Soot Particle Formation BT - Soot Formation in Combustion: Mechanisms and Models. In: Bockhorn H, editor., Berlin, Heidelberg: Springer Berlin Heidelberg; 1994, p. 165–92. https://doi.org/10.1007/978-3-642-85167-4_10.

[77] Frenklach M, Wang H. Detailed modeling of soot particle nucleation and growth. Symp Combust 1991. https://doi.org/10.1016/S0082-0784(06)80426-1.

[78] Idicheria CA, Pickett LM. Soot formation in diesel combustion under high-EGR conditions. SAE Tech Pap 2005. https://doi.org/10.4271/2005-01-3834.

[79] Pickett LM, Siebers DL. Soot in diesel fuel jets: Effects of ambient temperature, ambient density, and injection pressure. Combust Flame 2004;138:114–35. https://doi.org/10.1016/j.combustflame.2004.04.006.

[80] Payri R, Gimeno J, Cardona S, Ayyapureddi S. Experimental study of the influence of the fuel and boundary conditions over the soot formation in multi-hole diesel injectors using high-speed color diffused back-illumination technique. Appl Therm Eng 2019;158:113746. https://doi.org/10.1016/j.applthermaleng.2019.113746.

[81] Xuan T, Cao J, He Z, Wang Q, Zhong W, Leng X, et al. A study of soot quantification in diesel flame with hydrogenated catalytic biodiesel in a constant volume combustion chamber. Energy 2018;145:691–9. https://doi.org/10.1016/j.energy.2017.12.106.

[82] Pickett LM, Siebers DL. Fuel Effects on Soot Processes of Fuel Jets at DI Diesel Conditions. SAE Tech. Pap., 2003. https://doi.org/10.4271/2003-01-3080.

[83] Pickett LM, Siebers DL. Soot formation in diesel fuel jets near the lift-off length. Int J Engine Res 2006;7:103–30. https://doi.org/10.1243/146808705X57793.

[84] Menkiel B, Donkerbroek A, Uitz R, Cracknell R, Ganippa L. Combustion and soot processes of diesel and rapeseed methyl ester in an optical diesel engine. Fuel 2014;118:406–15. https://doi.org/10.1016/j.fuel.2013.10.074.

[85] Ito T, Kitamura T, Ueda M, Matsumoto T, Senda J, Fujimoto H. Effects of flame lift-off and flame temperature on soot formation in oxygenated fuel sprays. SAE Tech. Pap., 2003. https://doi.org/10.4271/2003-01-0073.

[86] Donkerbroek AJ, Boot MD, Luijten CCM, Dam NJ, ter Meulen JJ. Flame lift-off length and soot production of oxygenated fuels in relation with ignition delay in a DI heavy-duty diesel engine. Combust Flame 2011;158:525–38. https://doi.org/10.1016/j.combustflame.2010.10.003.

[87] Payri R, Gimeno J, Bracho G, Vaquerizo D. Study of liquid and vapor phase behavior on Diesel sprays for heavy duty engine nozzles. Appl Therm Eng 2016. https://doi.org/10.1016/j.applthermaleng.2016.06.159.

[88] Desantes JM, Pastor JVM, Payri R, Pastor JVM, Gimeno J. Experimental Characterization of Internal Nozzle Flow and Diesel Spray Behavior. Part Ii: Evaporative Conditions. At Sprays 2005;15:517–44. https://doi.org/10.1615/atomizspr.v15.i5.20.

[89] Payri R, Gimeno J, Viera JP, Plazas AH. Needle lift profile influence on the vapor phase penetration for a prototype diesel direct acting piezoelectric injector. Fuel 2013;113:257–65. https://doi.org/10.1016/j.fuel.2013.05.057.

[90] Idicheria CA, Pickett LM. Ignition, soot formation, and end-of-combustion transients in diesel combustion under high-EGR conditions. Int J Engine Res 2011;12:376–92. https://doi.org/10.1177/1468087411399505.

[91] Kook S, Pickett LM. Soot Volume Fraction and Morphology of Conventional, Fischer-Tropsch, Coal-Derived, and Surrogate Fuel at Diesel Conditions. SAE Int J Fuels Lubr 2012;5:647–64. https://doi.org/10.4271/2012-01-0678.

[92] Cenker E, Bruneaux G, Pickett L, Schulz C. Study of soot formation and oxidation in the engine combustion network (ECN), spray A: Effects of ambient temperature and oxygen concentration. SAE Int J Engines 2013;6:352–65. https://doi.org/10.4271/2013-01-0901.

[93] Skeen SA, Manin J, Dalen K, Pickett LM. Extinction-based imaging of soot processes over a range of diesel operating conditions. 8th US Natl Combust Meet 2013 2013;3:1981–93.

[94] Dernotte J, Hespe C, HouilÍe S, Foucher F, Mounäim-Rousselle C. Influence of fuel properties on the diesel injection process in nonvaporizing conditions. At Sprays 2012. https://doi.org/10.1615/AtomizSpr.2012004401.

[95] Hattori H, Narumiya K, Tsue M, Kadota T. Analysis of initial breakup mechanism of diesel spray injected into high-pressure ambience. SAE Tech. Pap., 2004. https://doi.org/10.4271/2004-01-0528.

[96] Payri R, García-Oliver JM, Bardi M, Manin J. Fuel temperature influence on diesel sprays in inert and reacting conditions. Appl Therm Eng 2012;35:185–95. https://doi.org/10.1016/j.applthermaleng.2011.10.027.

[97] Jin C, Yao M, Liu H, Lee CFF, Ji J. Progress in the production and application of n-butanol as a biofuel. Renew Sustain Energy Rev 2011. https://doi.org/10.1016/j.rser.2011.06.001.

[98] Zheng J, Tashiro Y, Wang Q, Sonomoto K. Recent advances to improve fermentative butanol production: Genetic engineering and fermentation technology. J Biosci Bioeng 2015. https://doi.org/10.1016/j.jbiosc.2014.05.023.

[99] Karimi K, Tabatabaei M, Horváth IS, Kumar R. Recent trends in acetone, butanol, and ethanol (ABE) production. Biofuel Res J 2015. https://doi.org/10.18331/BRJ2015.2.4.4.

[100] Li Y, Tang W, Chen Y, Liu J, Lee C fon F. Potential of acetone-butanol-ethanol (ABE) as a biofuel. Fuel 2019. https://doi.org/10.1016/j.fuel.2019.01.063.

[101] No SY. Application of biobutanol in advanced CI engines – A review. Fuel 2016;183:641–58. https://doi.org/10.1016/j.fuel.2016.06.121.

[102] Cheng X, LI S, Yang J, Dong S, Bao Z. Effect of N-butanol-Diesel Blends on Partially Premixed Combustion and Emission Characteristics in a Light-duty Engine. SAE Tech Pap 2014;2014-Octob. https://doi.org/10.4271/2014-01-2675.

[103] Zhang Q, Yao M, Zheng Z, Liu H, Xu J. Experimental study of n-butanol addition on performance and emissions with diesel low temperature combustion. Energy 2012;47:515–21. https://doi.org/10.1016/j.energy.2012.09.020.

[104] Valentino G, Corcione FE, Iannuzzi SE, Serra S. Experimental study on performance and emissions of a high speed diesel engine fuelled with n-butanol diesel blends under premixed low temperature combustion. Fuel 2012;92:295–307. https://doi.org/10.1016/j.fuel.2011.07.035.

[105] Han X, Zheng M, Wang J. Fuel suitability for low temperature combustion in

compression ignition engines. Fuel 2013;109:336–49. https://doi.org/10.1016/j.fuel.2013.01.049.

[106] Yang B, Yao M, Cheng WK, Zheng Z, Yue L. Regulated and unregulated emissions from a compression ignition engine under low temperature combustion fuelled with gasoline and n-butanol/gasoline blends. Fuel 2014;120:163–70. https://doi.org/10.1016/j.fuel.2013.11.058.

[107] Wu H, Nithyanandan K, Zhang J, Lin Y, Lee TH, Lee C fon F, et al. Impacts of Acetone-Butanol-Ethanol (ABE) ratio on spray and combustion characteristics of ABE-diesel blends. Appl Energy 2015;149:367–78. https://doi.org/10.1016/j.apenergy.2014.11.053.

[108] Zhou N, Huo M, Wu H, Nithyanandan K, Lee C fon F, Wang Q. Low temperature spray combustion of acetone-butanol-ethanol (ABE) and diesel blends. Appl Energy 2014;117:104–15. https://doi.org/10.1016/j.apenergy.2013.11.035.

[109] Wu H, Nithyanandan K, Zhou N, Lee TH, Lee CFF, Zhang C. Impacts of acetone on the spray combustion of Acetone-Butanol-Ethanol (ABE)-Diesel blends under low ambient temperature. Fuel 2015. https://doi.org/10.1016/j.fuel.2014.10.009.

[110] Nilaphai O, Hespel C, Chanchaona S, Mounaïm-Rousselle C. Spray and combustion characterizations of ABE/Dodecane blend in comparison to alcohol/Dodecane blends at high-pressure and high-temperature conditions. Fuel 2018;225:542–53. https://doi.org/10.1016/j.fuel.2018.03.184.

[111] Cuoci A, Frassoldati A, Faravelli T, Ranzi E. OpenSMOKE++: An object-oriented framework for the numerical modeling of reactive systems with detailed kinetic mechanisms. Comput Phys Commun 2015. https://doi.org/10.1016/j.cpc.2015.02.014.

[112] Masurier J. Etude expérimentale de la combustion HCCI par l'ajout d'espèces chimiques oxydantes minoritaires. 2016.

[113] Woschni G. A universally applicable equation for the instantaneous heat transfer coefficient in the internal combustion engine. SAE Tech. Pap., 1967. https://doi.org/10.4271/670931.

[114] Chang J, Güralp O, Filipi Z, Assanis D, Kuo T, Najt P, et al. New Heat Transfer Correlation for an HCCI Engine Derived from Measurements of Instantaneous Surface Heat Flux. SAE Tech Pap 2004. https://doi.org/10.4271/2004-01-2996.

[115] Eng JA. Characterization of Pressure Waves in HCCI Combustion. SAE Tech. Pap., 2002. https://doi.org/10.4271/2002-01-2859.

[116] Anderson JE, Dicicco DM, Ginder JM, Kramer U, Leone TG, Raney-Pablo HE, et al. High octane number ethanol-gasoline blends: Quantifying the potential benefits in the United States. Fuel 2012. https://doi.org/10.1016/j.fuel.2012.03.017.

[117] Anderson JE, Leone TG, Shelby MH, Wallington TJ, Bizub JJ, Foster M, et al. Octane numbers of ethanol-gasoline blends: Measurements and novel estimation method from molar composition. SAE Tech. Pap., 2012. https://doi.org/10.4271/2012-01-1274.

[118] Anderson JE, Kramer U, Mueller SA, Wallington TJ. Octane numbers of ethanol- and methanol-gasoline blends estimated from molar concentrations. Energy and Fuels 2010. https://doi.org/10.1021/ef101125c.

[119] Anderson JE, Wallington TJ. Novel Method to Estimate the Octane Ratings of Ethanol-Gasoline Mixtures Using Base Fuel Properties. Energy and Fuels 2020. https://doi.org/10.1021/acs.energyfuels.9b04204.

[120] Sjöberg M, Dec JE. Comparing late-cycle autoignition stability for single- and two-stage ignition fuels in HCCI engines. Proc Combust Inst 2007;31 II:2895–902. https://doi.org/10.1016/j.proci.2006.08.010.

[121] Sjöberg M, Dec JE. Influence of fuel autoignition reactivity on the high-load limits of HCCI engines. SAE Int J Engines 2009. https://doi.org/10.4271/2008-01-0054.

[122] Frassoldati A, Cuoci A, Faravelli T, Ranzi E. Kinetic modeling of the oxidation of ethanol and gasoline surrogate mixtures. Combust Sci Technol 2010. https://doi.org/10.1080/00102200903466368.

[123] Vuilleumier D, Atef N, Kukkadapu G, Wolk B, Selim H, Kozarac D, et al. The Influence of Intake Pressure and Ethanol Addition to Gasoline on Single- and Dual-Stage Autoignition in an HCCI Engine. Energy and Fuels 2018;32:9822–37. https://doi.org/10.1021/acs.energyfuels.8b00887.

[124] Sjöberg M, Dec JE. Influence of EGR quality and unmixedness on the high-load limits of HCCI engines. SAE Int J Engines 2009;2:492–510. https://doi.org/10.4271/2009-01-0666.

[125] Masurier JB, Foucher F, Dayma G, Dagaut P. Homogeneous charge compression ignition combustion of primary reference fuels influenced by ozone addition. Energy and Fuels 2013;27:5495–505. https://doi.org/10.1021/ef401009x.

[126] Masurier JB, Foucher F, Dayma G, Dagaut P. Ozone applied to the homogeneous charge compression ignition engine to control alcohol fuels combustion. Appl Energy 2015. https://doi.org/10.1016/j.apenergy.2015.08.004.

[127] Pochet M, Dias V, Jeanmart H, Verhelst S, Blondeau J, Contino F. Multifuel HCCI engine: numerical study of the operating range for hydrogen, ammonia, methane, methanol and their blends. Energy & Fuels 2017:?

[128] Saxena S. Maximizing Power Output in Homogeneous Charge Compression Ignition (HCCI) Engines and Enabling Effective Control of Combustion Timing. 2011.

[129] Maas JWU, Dibble RW. Combustion: Physical and Chemical Fundamentals, Modeling and Simulation, Experiments, Pollutant Formation. Springer; 2006.

[130] Rockstroh T, Fridlyand A, Ciatti S, Cannella W, Goldsborough SS. Autoignition behavior of a full boiling-range gasoline: Observations in RCM and GCI engine environments. Combust Flame 2019;209:239–55. https://doi.org/10.1016/j.combustflame.2019.07.013.

[131] Wang Z, Zhang L, Moshammer K, Popolan-Vaida DM, Shankar VSB, Lucassen A, et al. Additional chain-branching pathways in the low-temperature oxidation of branched alkanes. Combust Flame 2016. https://doi.org/10.1016/j.combustflame.2015.11.035.

[132] Truedsson I, Tuner M, Johansson B, Cannella W. Pressure sensitivity of HCCI auto-ignition temperature for oxygenated reference fuels. J Eng Gas Turbines Power 2013;135. https://doi.org/10.1115/1.4023614.

[133] Cheng S, Kang D, Fridlyand A, Goldsborough SS, Saggese C, Wagnon S, et al. Autoignition behavior of gasoline/ethanol blends at engine-relevant conditions. Combust Flame 2020;216:369–84. https://doi.org/10.1016/j.combustflame.2020.02.032.

[134] Truedsson I. The HCCI Fuel Number Measuring and Describing Auto-ignition for HCCI. 2016.

[135] Lü X, Ji L, Zu L, Hou Y, Huang C, Huang Z. Experimental study and chemical analysis of n-heptane homogeneous charge compression ignition combustion with port injection of reaction inhibitors. Combust Flame 2007. https://doi.org/10.1016/j.combustflame.2007.01.002.

[136] Andrae JCG, Head RA. HCCI experiments with gasoline surrogate fuels modeled by a semidetailed chemical kinetic model. Combust Flame 2009. https://doi.org/10.1016/j.combustflame.2008.10.002.

[137] Barraza-Botet CL, Wooldridge MS. Combustion chemistry of iso-octane/ethanol blends: Effects on ignition and reaction pathways. Combust Flame 2018;188:324–36. https://doi.org/10.1016/j.combustflame.2017.10.011.

[138] Bogin GE, Luecke J, Ratcliff MA, Osecky E, Zigler BT. Effects of iso-octane/ethanol blend ratios on the observance of negative temperature coefficient behavior within the Ignition Quality Tester. Fuel 2016;186:82–90. https://doi.org/10.1016/j.fuel.2016.08.021.

[139] He BQ, Liu M Bin, Zhao H. Comparison of combustion characteristics of n-butanol/ethanol-gasoline blends in a HCCI engine. Energy Convers Manag 2015;95:101–9. https://doi.org/10.1016/j.enconman.2015.02.019.

[140] Dagaut P, Togbé C. Oxidation kinetics of mixtures of iso-octane with ethanol or butanol in a jet-stirred reactor: Experimental and modeling study. Combust. Sci. Technol., 2012. https://doi.org/10.1080/00102202.2012.663993.

[141] Rousselle C, Bruneaux G, Hespel C, Ben Houidi M, Ajrouche H, Foucher F, et al. Characterization of the ECN spray A in different facilities. Part 1: boundary conditions characterization. Oil Gas Sci Technol 2020;75. https://doi.org/10.2516/ogst/2020070.

[142] Nilaphai O. Vaporization and Combustion Processes of Alcohols and Acetone-Butanol-Ethanol (ABE) blended in n-Dodecane for High Pressure-High Temperature Conditions. 2019.

[143] Nilaphai O, Hespel C, Moreau B, Contino F, Bourgeois N, Chanchaona S, et al. New High-Pressure and High-Temperature Chamber for Diesel Spray Characterization. ILASS – Eur. 2016, Brighton UK: 2016, p. 4–5.

[144] ECN. Engine Combustion Network 2013. https://ecn.sandia.gov/.

[145] Zhao H, Ladommatos N. Optical diagnostics for soot and temperature measurement in diesel engines. Prog Energy Combust Sci 1998;24:221–55. https://doi.org/10.1016/S0360-1285(97)00033-6.

[146] Pickett LM, Idicheria CA. Effects of ambient temperature and density on soot formation under high EGR conditions. Thermo- Fluid-Dynamic Process. Diesel Engines, 2006, p. 1–13.

[147] Settles, G, Covert, E. Schlieren and Shadowgraph Techniques: Visualizing Phenomena in Transport Media. Appl Mech Rev 2002. https://doi.org/10.1115/1.1483362.

[148] Benajes J, Payri R, Bardi M, Martí-Aldaraví P. Experimental characterization of diesel ignition and lift-off length using a single-hole ECN injector. Appl Therm Eng 2013;58:554–63. https://doi.org/10.1016/j.applthermaleng.2013.04.044.

[149] Kook S, Pickett LM, Musculus MPB, Kattke K, Gehmlich RK. Liquid-phase diesel spray penetration during end-of-injection transient. Proc 7th Int Conf Model Diagnostics Adv Engine Syst COMODIA 2008 2008:413–20.

[150] Cung K, Moiz A, Johnson J, Lee SY, Kweon CB, Montanaro A. Spray-combustion interaction mechanism of multiple-injection under diesel engine conditions. Proc Combust Inst 2015;35:3061–8. https://doi.org/10.1016/j.proci.2014.07.054.

[151] Moiz AA, Cung KD, Lee SY. Ignition, lift-off, and soot formation studies in n-dodecane split injection spray-flames. Int J Engine Res 2017;18:1077–87. https://doi.org/10.1177/1468087417700778.

[152] Desantes JM, García-Oliver JM, García A, Xuan T. Optical study on characteristics of non-reacting and reacting diesel spray with different strategies of split injection. Int J Engine Res 2019;20:606–23. https://doi.org/10.1177/1468087418773012.

[153] Skeen S, Manin J, Pickett LM. Visualization of Ignition Processes in High-Pressure Sprays with Multiple Injections of n-Dodecane. SAE Int J Engines 2015;8:696–715. https://doi.org/10.4271/2015-01-0799.

[154] Felsch C, Gauding M, Hasse C, Vogel S, Peters N. An extended flamelet model for multiple injections in DI Diesel engines. Proc Combust Inst 2009;32:2775–83. https://doi.org/10.1016/J.PROCI.2008.05.053.

[155] Moiz AA. Low Temperature Split Injection Spray Combustion : Ignition , Flame Stabilization and Soot Formation Characteristics in Diesel Engine Conditions. 2016.

[156] Pickett LM, Kook S, Persson H, Andersson Ö. Diesel fuel jet lift-off stabilization in the presence of laser-induced plasma ignition. Proc Combust Inst 2009. https://doi.org/10.1016/j.proci.2008.06.082.

[157] Cung KD, Ciatti SA, Tanov S, Andersson Ö. Low-Temperature Combustion of High Octane Fuels in a Gasoline Compression Ignition Engine. Front Mech Eng 2017;3:1–14. https://doi.org/10.3389/fmech.2017.00022.

Tung Lam NGUYEN

Caractérisation de la combustion partiellement prémélangée du bio-carburant Acetone-Butanol-Ethanol pour les moteurs thermiques

Aujourd'hui, en raison des exigences législatives et politiques en matière de réduction des émissions de NOx, de particules (PM) et de CO_2 (liés à la consommation de carburant), de nouveaux concepts de combustion avancés, tels que la combustion à basse température (LTC), sont à considérer. Les bio-alcools, en particulier le méthanol, l'éthanol et le butanol, ont reçu beaucoup d'attention en tant que futurs carburants potentiels alternatifs à l'essence pure. Comme le bio-butanol contient 30 % d'énergie de plus que l'éthanol, l'utilisation du n-bio-butanol comme carburant pour les moteurs peut permettre d'économiser 39 à 56 % d'énergie fossile tout en réduisant les émissions de gaz à effet de serre jusqu'à 48 % à partir d'une analyse du cycle de vie. De plus, le bio-butanol peut être plus facilement mélangé à l'essence ou au diesel que le méthanol ou l'éthanol. Mais même si le bio-butanol présente plusieurs avantages par rapport à l'éthanol et au méthanol, le principal problème qui empêche l'utilisation du n-butanol dans les moteurs modernes reste son coût de production élevé. L'acétone-butanol-éthanol (ABE), le produit intermédiaire du processus de fermentation de la production de bio-butanol, est de plus en plus considéré comme un autre carburant alternatif. Cette étude examine les propriétés de l'ABE en comparaison avec les alcools, éthanol et butanol, mélangés avec un carburant de substitution typé essence (PRF80) sur deux modes de combustion avancée : le mode de combustion HCCI (Homogeneous Charge Compression Ignition) et le mode GCI (Gasoline Compression Ignition).

Mots clés : Mélange acétone-butanol-éthanol, mélange d'alcools, mode HCCI, mode GCI, caractéristiques du spray, longueur de stabilisation, délai d'inflammation.

Characterization of the partially premixed combustion of Acetone-Butanol-Ethanol bio-fuel for thermal engines

Nowadays, due to legislative demands for reduction the emissions of NOx, Particulate Matter (PM) and CO_2 (reduce fuel consumption), new advanced combustion concepts, such as Low-Temperature combustion (LTC) are considered. Bio-alcohols have received a lot of attention as potential future alternative fuels to pure gasoline. Due to the higher energy content in comparison to ethanol (30% more), the use of bio-butanol as a transportation fuel can save 39-56% fossil energy while reducing greenhouse gas emissions by up to 48%, based on a life cycle analysis. Even if bio-butanol has several advantages compared to ethanol and methanol, the main issue preventing bio-butanol's use in modern engines is its relatively high production costs. Acetone-Butanol-Ethanol (ABE), one intermediate product from the fermentation process of bio-butanol production, is more and more considering as another alternative fuel. In this context, the study investigates the characterization of the combustion of Acetone-Butanol-Ethanol (ABE), compared to alcohols, i.e. Ethanol and Butanol, blended with a gasoline surrogate fuel (PRF80) on 2 advanced combustion concepts: Homogeneous Charge Compression Ignition (HCCI) and Gasoline Compression Ignition (GCI).

Keywords: Acetone-Butanol-Ethanol blend, Alcohol blend, HCCI mode, GCI mode, Spray Characteristics, Lift-Off Length, Ignition Delay, High-Pressure High-Temperature Conditions.

PRISME
Laboratoire Pluridisciplinaire de Recherche Ingénierie des Systèmes, Mécanique, Énergétique

UNIVERSITE D'ORLEANS